UNIVERSITY OF CALIFORNIA SAN DIEGO

Development of a Test Bed and Prototype Blades for an Open-Centered Hydrokinetic Turbine

A thesis submitted in partial satisfaction of the
requirements for the degree of Master of Science

in

Engineering Sciences (Mechanical Engineering)

by

Spencer R. Ellis

Committee in charge:

Professor John Kosmatka, Chair
Professor Hyonny Kim
Professor Frank Talke

2018

The Thesis of Spencer R. Ellis is approved, and is acceptable in quality and form for publication on microfilm and electronically:

_____

_____

_____
Chair

University of California San Diego

2018

Table of Contents

List of Figures

List of Tables

Abstract of the Thesis

Development of a Test Bed and Prototype Blades for an Open-Centered Hydrokinetic Turbine

by

Spencer R. Ellis

Master of Science in Engineering Sciences (Mechanical Engineering)

University of California San Diego, 2018

Professor John Kosmatka, Chair

As the world transitions towards carbon free energy sources there remains enormous untapped potential for hydropower generation. Hydrokinetic turbines have shown significant potential to harness this resource at a variety of scales. A unique open-centered turbine geared towards pico-scale power generation is introduced. A robust prototype with an annulus outer diameter of 0.40 m is assembled to serve as a

test bed for continuing blade optimization studies. Benefits of the open-center type turbine include: improved blade structural efficiency as blades mounted on the annular rotor have reduced spans compared to a traditional rotor covering the same area, ability for aquatic life and debris to pass through, potential for hub to augment flow through the center.

The completed system is outfitted with additive manufactured (AM) polylactic acid (PLA) blades and an above-water generator. Current blade geometry was developed by Oceana Energy Company for a grid scale hydrokinetic turbine. Successful tow tests conducted over a range from 1 m/s to 3.2 m/s demonstrate moderate AM PLA blade performance. Approximately 600 W of power was produced at the top test speed of 3.2 m/s. Maximum hydrodynamic efficiency, after accounting for electromechanical losses in the powertrain, is found to be 25%. Experimental performance compares favorably with a blade element momentum theory (BEMT) code developed for application to open-centered turbines.

Chapter 1. Introduction

1.1 Motivation

In 2014, worldwide electricity demand was 20,557 terrawatt hours (TWh). The International Energy Agency projects that this figure will swell by 70% to 34,250 TWh by 2040 [11]. Where this value saturates, and in turn our ability to meet these demands with available resources, is heavily dependent on population size and human development. Examining the correlation between the United Nations Human Development Index (HDI)—an indicator that accounts for life expectancy, education level, and income—and per capita electricity consumption suggests that HDI plateaus when energy consumption per capita reaches 4,000 kilowatt hours (KWh) per year [12]. Furthermore, the rate at which per capita energy access increases is correlated with population growth rate. Finally, countries with high standards of living, as measured by indices like HDI, have very low to zero growth rates [13]. With population growth, energy consumption, and quality of life all intertwined there is a logical incentive to rapidly expand energy access.

However, with this increasing demand comes an even greater need to reduce the carbon intensity of our energy sources. A 2 $^{\circ}$C global mean temperature rise has been identified by both world leaders and scientific experts as a target to limit global warming [14]. In order to achieve this goal with at least 66% probability of success, cumulative CO_2 emissions must be kept below 2,900 gigatonnes of CO_2 ($GtCO_2$). It's estimated that world emissions totaled 1,890 $GtCO_2$ from 1870 to 2011 [14].

Meanwhile, the global greenhouse gas emission rate in 2010 was equal to 49 gigatonnes CO_2 equivalent per year ($GtCO_2eq/year$) [15]. Thus, given the current trajectory and looming target, the impetus for a rapid transition to carbon free energy sources is clear. There is no single renewable energy source currently capable of being reasonably scaled to meet future energy demand. The energy generation portfolio of the future is likely to comprise a variety of sources depending on what is available locally.

For coastal and riverine communities, hydrokinetic energy converters offer a viable source of renewable energy. It is estimated stream current energy in the U.S. comprises 120 TWh-year of recoverable energy in the riverine system [16], 49 TWh-year of recoverable energy in the Gulf Stream system [17], and 445 TWh-year total tidal stream energy along the U.S. coast [18]. If 20% of the available tidal stream energy can be extracted, hydrokinetic turbines have the potential to supply roughly 258 TWh-year. This is equivalent to 6% of the total utility scale electricity generation by the U.S. in 2016 [19].

What they lack in potential magnitude hydrokinetic turbines (HKTs) make up for in consistency by potentially operating 24 hours a day. In order to fully integrate wind and solar resources, which are capable in magnitude, with our electrical grid the issue of intermittency must be addressed. Although hydrokinetic energy is not capable of rapidly ramping to meet unforeseen load variation, its predictable capacity allows grid operators to more accurately characterize available power at any given time and subsequently manage the high variability inherent in hybrid renewable

generation systems [20]. HKTs also have the inherent ability to operate in remote areas and contribute to distributed generation schemes [10].

1.2 Classifying Hydrokinetic Energy Converters

Hydrokinetic energy devices differ from classic hydrostatic plants in that they do not require large reservoirs of water to create artificial, or in some locations natural, pressure heads to drive a turbine. Instead they capture the kinetic energy of fluid streams directly [21]. Because little to no alterations to the natural stream are necessary to deploy a hydrokinetic turbine, both the environmental impact and economic costs can be reduced. Hydrokinetic systems are typically designed to operate in rivers, tidal estuaries, ocean currents, waves, and man-made channels [21]. They can also be operated in a variety of other flows environments as long as there if sufficient velocity.

Devices for extracting hydrokinetic energy from free-streams can be classified into two general categories, turbine and non-turbine systems. Although the non-turbine family employs an interesting range of energy conversion methods such as vortex induced vibration, piezoelectric generation, and drag inducing sails, the focus of this work is on the more traditional class of turbine devices [10]. Turbine systems, or HKTs, are further subdivided based on their operating principle. Table 1.1 provides a summary current conversion typologies and some of their advantage/disadvantages. Examples of each type are pictured in fig. 1.1 [1–4].

Table 1.1: Hydrokinetic Turbine Systems

Type	Defining Characteristics	Advantages	Disadvantages
Horizontal Axis	•rotor axis of rotation oriented parallel to the direction of flow [10] •lift or drag type blades [10]	•self-starting [10] •potential for active pitch control, allowing for improved efficiency and safe operating range [5] •optimum performance at higher rotational speeds allows for reduced gearing [5]	•high generator costs due to underwater placement [10]
Vertical Axis	•rotor axis of rotation is perpendicular to both the water surface and the direction of flow [10] •lift or drag type blades [10]	•low generator costs due to more natural above water placement (Khan, Bhuyan, Iqbal, & Quaicoe, 2009) •improved performance when subject to velocity gradient across turbine or bidirectional flow [5,10] •reduced blade tip losses and noise [5,10]	•low starting torque, low efficiency, poor starting performance [10]
Cross-flow	•rotor axis of rotation parallel to water surface, but perpendicular to flow [10] •typically drag type [10]	•Well suited for bi-directional operation	•lower efficiencies [20]
Ducted	•employs choke or shroud to accelerate flow across rotor disk [10]	•higher speed operation can eliminated need for gearbox [5] •can exceed the Betz limit of 59.3% efficiency [22,23]	•not easily deployed for floating applications [5]

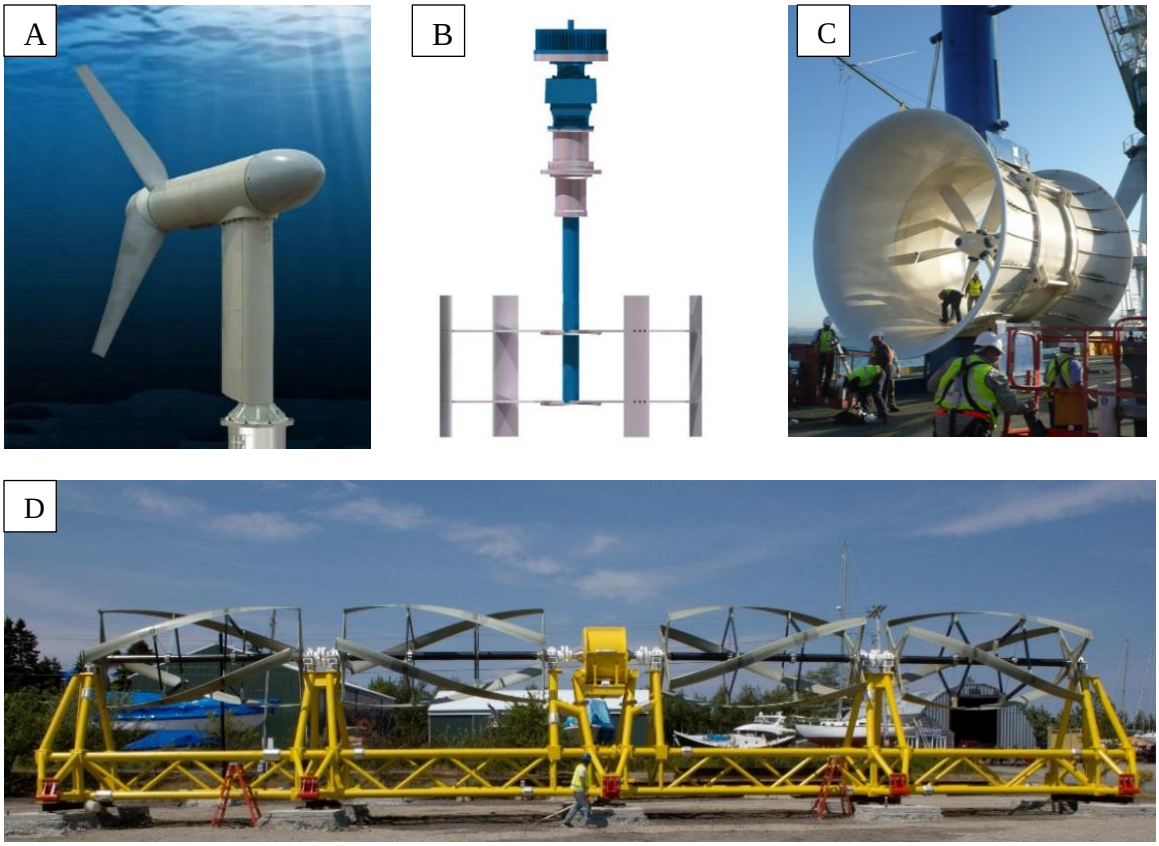

Figure 1.1: A) Verdant Power's horizontal axis turbine [1] B) EnCurrent vertical axis turbine [2] C) Atlantis Solon ducted turbine [3] D) Ocean Renewable Power Company TidGen cross-flow turbine [4].

Hydrokinetic turbines that operate in rivers or artificial waterways are referred to as river current turbines (RCTs), while those designed to work in tidal or ocean currents are often called marine hydrokinetic turbines (MHKTs) or marine current turbines (MCTs). Tidal currents are naturally bi-directional so tidal MCTs are designed to function in both directions using one the following methods: yawing the turbine into the flow, adjusting blade pitch by 180 degrees, or leveraging symmetric foils so that the rotor can reverse direction with the flow [24]. River current turbines, on the other hand, forgo this additional complexity by operating in uni-directional flows.

1.3 River Current Turbines

Horizontal axis and cross-flow turbines are the two most common designs for small RCTs. Horizontal axis turbines, which have their axis of rotation aligned parallel to the fluid flow, are the marine counterpart to the typical land-based wind turbines. There are several operational configurations for these types of devices pictured in fig. 1.2. The inclined axis in fig. 1.2 (i) is frequently studied for river applications, while configurations (ii), (iii), and (iv) are more commonly associated with lager tidal stream generators [5]. The primary advantages of axial-flow turbines are their low starting toque and self-starting capability, the ability for pitch control to improve performance and expand operational range, and their faster rotational speeds that require less gearing to couple with the generator [5,10]. However, the expensive underwater generators and associated cabling are major disadvantage [10].

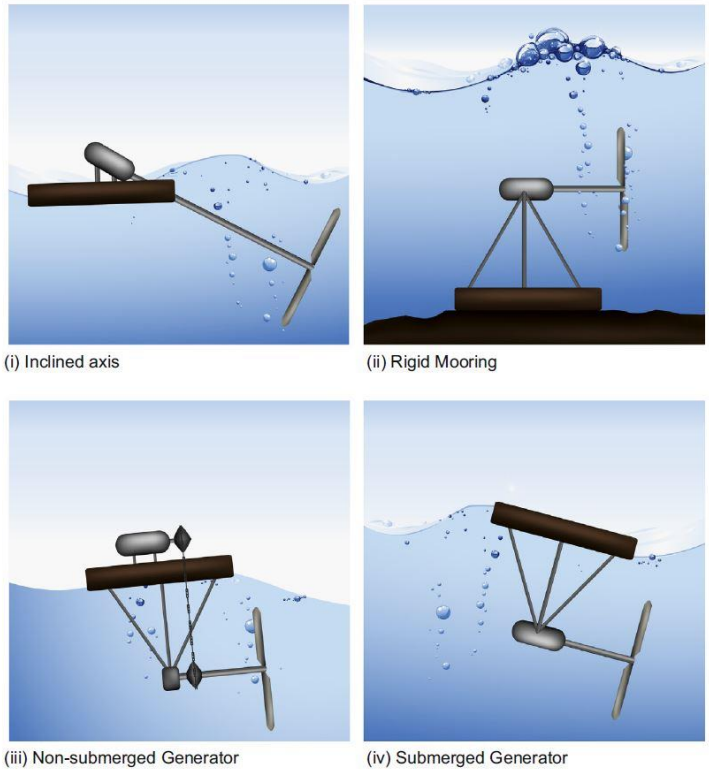

Figure 1.2: Operational configurations for horizontal or axial-flow turbines [5].

Cross-flow turbines rotate on an axis that is perpendicular to the direction of flow. They can be oriented vertically Fig. 1.3 (ii)-(vi) or horizontally (in-plane) Fig. 1.3 (i) with respect to the water surface. The in-plane devices are similar to old fashioned waterwheels, are typically drag based, and exhibit lower efficiencies [5]. The vertical axis turbines in (ii)-(vi) have the distinct advantage of being able to operate horizontally as well as the vertical orientation shown (though the axis of rotation is always perpendicular to the flow of water). Cross-flow turbines are able to capture energy from all directions at low speeds [21]. They are also less sensitive to velocity gradients in the fluid profile, which is an advantage in low-flow or shallow river conditions. However, their performance is limited by lower efficiencies,

tendency for higher fatigue loading, cavitation, cyclic rippling in torque output, and poor starting capabilities [10].

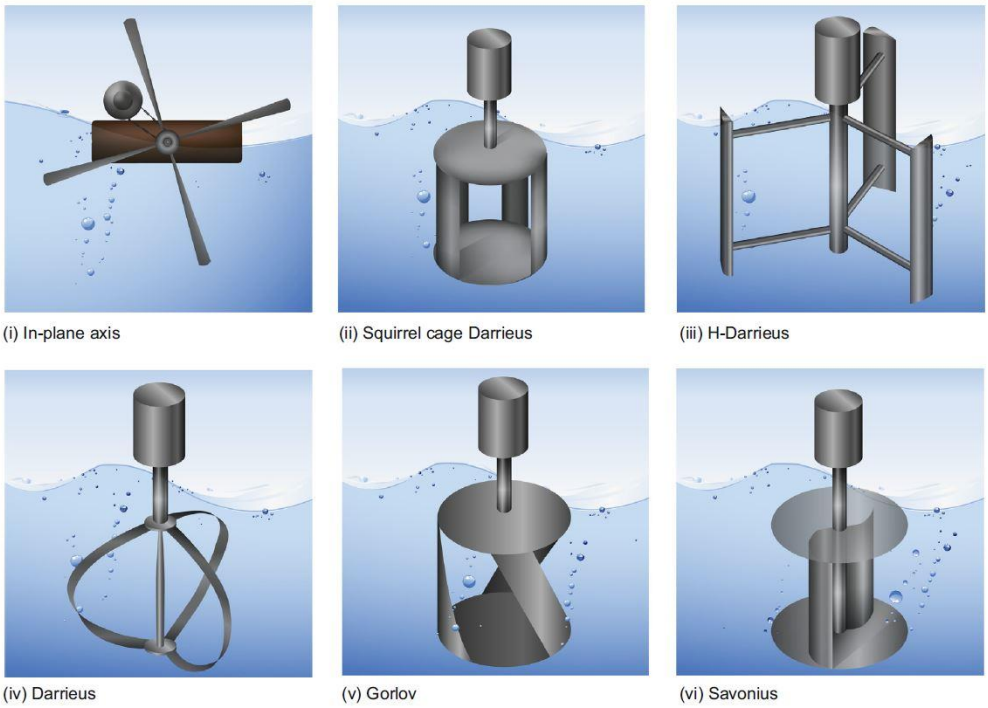

Figure 1.3: Variations of cross-flow turbines, including both (i) in-plain and (ii)-(vi) vertical axis turbines [5].

1.4 Open-centered Hydrokinetic Turbines

The current open-centered turbine concept originates with Herbert Williams and OpenHydro Group Ltd. [25,26]. OpenHydro removed the central turbine hub, as shown in fig. 1.4A, and attached the blades to an annular rotor that spins within a duct. Total drag on the turbine structure is subsequently reduced by eliminating the central hub [26]. The unobstructed flow through the center can improve the turbine performance by creating a low-pressure region that helps accelerate flow through the

turbine [27]. This accelerated flow may also facilitate the passage of debris and aquatic life through the turbine, but further research is needed to confirm this. Instead of extracting power through a central shaft it's generated through a direct-drive permanent magnet generator built into duct. Since 2006, they have accrued over 10,000 hours of run time on 6 m (outer diameter) models at the European Marine Energy Center (EMEC) test site off the coast of Scotland. Deployments in 2016 demonstrated successful operation of MW scale OpenHydro turbines in Nova Scotia, Canada and Paimpol-Bréhat, France [6,25].

Oceana Energy Company has recently developed a unique open-centered turbine, pictured in fig. 1.4B, with blades that extend radially from both sides of the annular rotor to increase performance [7,28–32]. Oceana worked closely with engineers at the Naval Surface Warfare Center, Carderock Division under a Cooperative Research and Development Agreement (CRADA) to optimize the hydrodynamic design. During testing in the Carderock tow tank the roughly 2 m (tip-to-tip diameter) HKT was able to produce over 8 kW of power [7]. Additional testing was conducted in 2014 and 2015, in partnership with the University of Alaska and the Alaska Energy Authority, through deployments in the Tenana River in Nenana, Alaska.

A) B)

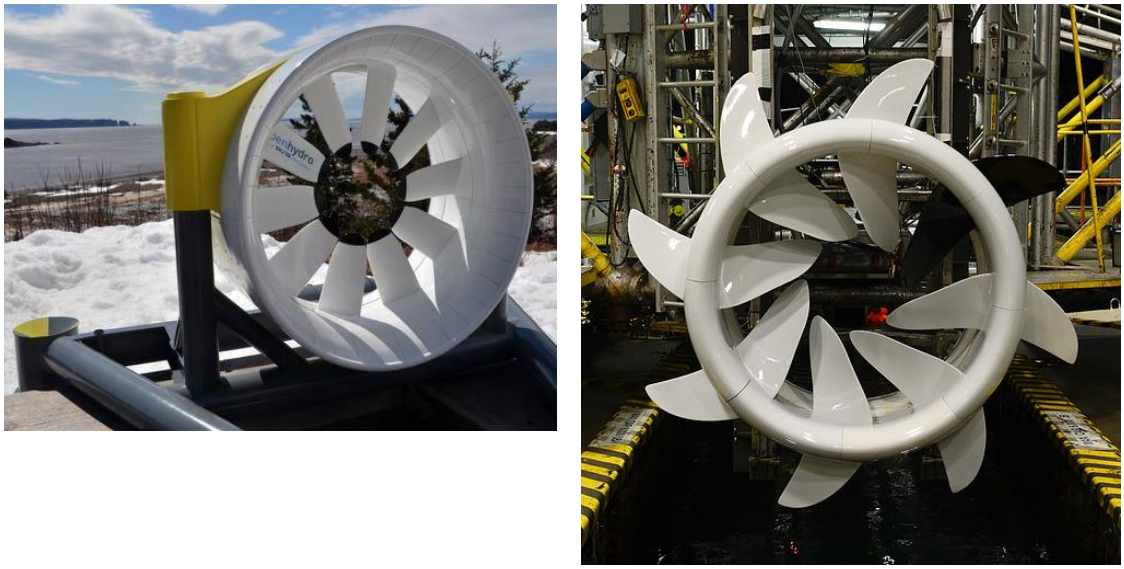

Figure 1.4: A) A photograph of OpenHydro's HKT [6]. B) A photograph of Oceana Energy Company's open centered RCT [7].

For a given turbine area, Oceana's design offers greater blade structural efficiency than other turbine architectures. Mounting blades to the annular rotor makes it possible to shorten the length of the cantilevered blades without significantly impacting the rotor area. Considering the significant loads generated by flowing water, shorter blades provide substantial opportunity for material cost savings without sacrificing on power capacity. The only moving part in the entire Oceana system is the annular rotor, which travels on magnetic bearings to eliminate the wear and friction associated with mechanical bearings. A specially designed direct-drive permanent magnet generator is built directly into the turbine so no gearbox is required. The end result is a more efficient and more durable device with an expected operating lifetime of 30 years [7].

1.5 Current Pico Hydro Regime

Oceana's highly scalable design is conducive to rapid field assembly and low-maintenance operation. A small portable version could have far ranging applications from permanent installations in remote rural areas or emergency electrification, to powering mobile military encampments. This section explores the potential applications and current commercial market for small scale HKTs.

Small-scale hydro power has been identified as a highly robust, environmentally benign, and cost-effective technology for bringing power to rural communities [33]. Considering that most populous regions around the world are located within close proximity to rivers [34], the potential for micro-hydro to provide sustainable energy access is enormous. Average annual energy use for a U.S. household is 10,720 kWh/year [35]. This demand could realistically be met by coupling a 1.5-2 kW HKT with a battery bank sized to meet peak load. Grid optimization studies have found small hydro power to be extremely capable in off-grid hybrid power systems [36–38]. In one specific example, it was determined that the integration of 78% hydro and 22% wind with battery storage was sufficient to meet the 24 hour power demand of an entire village without the need for an auxiliary diesel generator [36].

A small portable generation system capable of rapid deployment has applications in emergency preparedness and disaster relief. Location permitting, this unit would be ideal for powering critical electronic systems (lamp~10 W, radio~1 W [39], cell phone battery~6.5 Wh [39], etc.) during major grid disruptions. The

possibility of extreme weather events occurring with increasing frequency and severity, due to climate change, poses a growing hazard human to infrastructure [40]. Basic needs such as water, food, shelter, and sanitation are often the immediate focus of relief, however the coordination of these humanitarian efforts can benefit from reliable power that doesn't require a source of diesel fuel.

Temporary military encampments could also benefit from an ultraportable drop-in micro-hydrokinetic generator. Portable photovoltaic systems currently exist—the Marines have developed a system called the Ground Renewable Expeditionary System (GREENS)—that could benefit from a complimentary hydro system to generate power in low-light and nighttime conditions [41].

While there is no universal definition in the literature [33], small scale hydropower can be roughly classified by their output capacity as follows in table 1.2. The test bed device developed in the current work will be considered pico scale hydro.

Table 1.2: Small Turbine Classifications

Class	Rating [MW]	Reference
Small	1-30	[5]
Mini	0.1-1	[5]
Micro	<0.01	[5]
Pico	<0.005	[42–45]

The choice of turbine in this class depends on the size of available hydrostatic head, with propeller turbines usually being used in low head applications [44]. Common turbines for medium to high head applications—classified as hydrostatic power schemes—include the Pelton, Turgo, and Francis type [46]. These devices are

generally simple, robust, and cost-effective though they may require additional infrastructure to generate the required head.

Hydrokinetic schemes do not depend on the availability of head and are capable of operating in any location with sufficient flow velocity. Being drop-in ready, or deployable without the addition of significant infrastructure, makes them highly versatile. Depending on the application and power needs, these turbines can be coupled with either an induction generator, an alternator, or a permanent magnet alternator (PMA) [43].

Current pico hydro devices and their operating characteristics exhibit significant variety with a dominant design yet to emerge. A sampling of current commercial devices operating in the low to zero head regime is included for comparative purposes. Stated efficiencies (power coefficients) were estimated from power curves published by each company based on the rotor speed, diameter, and power output. Relative costs are compared in dollars per watt by dividing the cost with the maximum rated output power.

The PowerPal, developed by Asian Phoenix Resources Ltd. for use in high and low head conditions, is a hydrostatic propeller-type turbine coupled with a single-phase AC brushless PMA. The PowerPal shown in fig. 1.5 comes in a range of sizes starting at 200 W with the 200 W, 500 W, and 1 KW models in widespread use [43]. To generate power, water enters through the sides of the base and travels down the draft tube to drive the propeller (red in fig. 1.5). Modified implementations of this device have adjustable flumes to control flow rate [8]. These devices are very simple to operate and maintain. They also have the benefit of being relatively inexpensive

at $2/W. However, they are designed to operate within a specific range of head and flow rates. Minor infrastructure additions—such as troughs, channels, or small dams—may be necessary prior to installation.

Figure 1.5: PowerPal 200 W, 500 W, and 1000 W generation systems [8].

A fully submersed horizontal axis turbine called the UW 100 is sold by Seamap (formerly sold by Ampair). The UW 100 pictured in fig. 1.6, which has a propeller diameter of 312 mm, is capable of operating in depths of 0.4 m or more. It has a cut in speed of 1.5 m/s and generates 100 W in flows of 4 m/s [47]. The UW 100 is available with either a 12 V or 24 V DC power system. Watt&Sea makes a very similar turbine (fig. 1.7) with a 240 mm propeller that runs in speeds from 1 m/s to 5 m/s. It has a built-in alternator with a maximum output of 40 V AC. They sell both a 300 W and a 600 W model. A high-performance version of the 600 W model comes with computer controlled variable-pitch blades [48]. The Watt&Sea and UW 100 turbines appear to have moderate efficiencies between 20-30% though they come at the cost

of nearly $12/W and $13/W respectively. A downside of these devices is that it takes significant flow speeds, 4 m/s for the UW 100 and 5 m/s for the Watt&Sea, to reach their nominal output.

Figure 1.6: Seamap UW 100 generation system [47].

Figure 1.7: Watt&Sea Cruising 300 axial flow turbine [48].

Idénergie produces a cross-flow horizontal axis RCT (fig. 1.8) that generates between 100 W and 500 W. It has a low cut in speed of 1 m/s and can operates at a minimum 0.6 m depth. The maximum operating speed is 3 m/s. It has a built-in 48 V three-phase alternator to generate power. Total turbine area is 0.73 m, with overall dimensions of 0.55 m by 1.32 m and a weight of 131 kg [49]. The device exhibits only moderate efficiency for a cost of nearly $20/W. Idénergie's RCT does generate significant power at low current speeds and benefits from operating near maximum output power at flow speeds of 2.5 m/s.

Figure 1.8: Idénergie's cross-flow river turbine [49].

Smart Hydro Power makes a series of turbines (fig. 1.9) for application in rivers and canals [9]. They are horizontal axis RCTs with a 1 m rotor diameter designed for either surface or riverbed installation. Power output ranges from 250 W to 5,000 W. Portability is limited for both models as they weigh over 300 kg. The Free Stream model operates at minimum depths of 1.1 m while the Monofloat model requires at least 2.0 m of depth. Curved blades designed to help shed debris work along with built-in protective cabling to prevent damage from passing debris. The Free Stream and Monofloat are highly efficient. The Monofloat appears to operate at up to 58% efficiency due to its ducted design. Costing between $3/W and $4/W, they are also relatively cheap compared to the other models identified here.

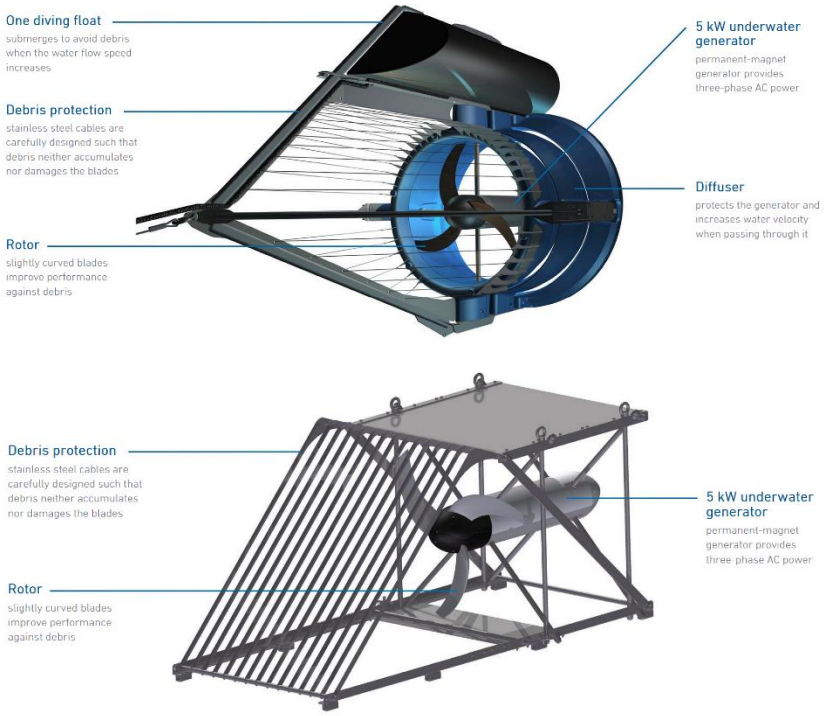

Figure 1.9: Smart Hydro Power's Monofloat (top) and Free Stream (bottom) turbines [9].

Ibasei currently produces a ducted horizontal axis turbine called the Cappa [50]. It's only available to the Japanese market now, though Ibasei hints at wider release in the future. Based on images in fig. 1.10 and dimensions provided for the outer structure it has a rotor diameter of approximately 0.5 m. The maximum output power of 160 W is achieved at a low flow speed of 1.75 m/s. Unfortunately, the Cappa's versatility is limited by the narrow operating flow speed range of 1.5-2.0 m/s.

Figure 1.10: Ibasei's Cappa turbine (top) from the front and (bottom) from the side [50].

Finally, there are the low power ultra-portable devices marketed by Blue Freedom and Seaformatics [51,52]. Both are intended to be tethered with a cable and dropped in moving water to charge batteries or small portable electronics. Blue Freedom's portable horizontal axis turbine pictured in fig 1.11 has a rotor diameter of 0.12 m and weighs only 0.69 kg. Its power output is limited to 5 W at a premium of $74/W.

Figure 1.11: Blue Freedom's portable turbine [51].

Seaformatics' WaterLily, shown in fig. 1.12, is a similarly styled horizontal axis turbine with a rotor diameter of 1.8 m and weight of 1.3 kg. A maximum rated power of 15 W and lower unit price make the WaterLily more price competitive $11/W. In addition to reaching 15 W at flow speeds of only 1.5 m/s, the WaterLily also benefits from a wide operating range with a cut-in flow speed of 0.28 m/s and a maximum flow speed of 3.1 m/s. It's also a solid performer with an apparent efficiency of 28%.

Figure 1.12: Seaformatic's WaterLily turbine [52].

A summary of available information on each of these commercial turbines is presented in table 1.3. For those with data available, a range of efficiencies is plotted as a fraction of the Betz limit (59%) in fig. 1.13. Flow speed conditions used to calculate the efficiencies are noted in the figure legend. The goal of the current work is to build an open-centered turbine test bed and evaluate the design of a portable RCT derived from Oceana Energy Company's utility scale device. The prototype pico scale turbine established in this thesis is included in table 1.3 for context. It's differentiated by its portability—the test bed prototype weighs about 30 kg but a commercial version could weigh even less—and its high output capacity of 1000 W.

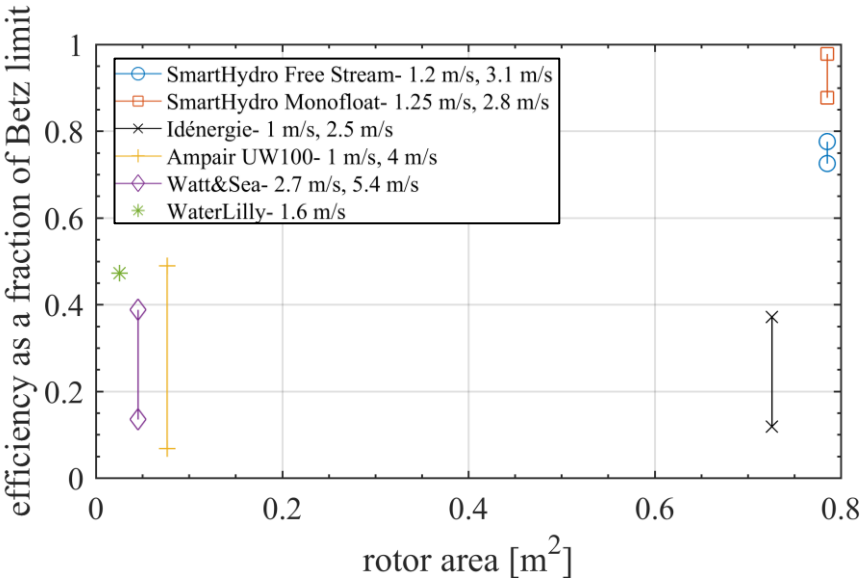

Figure 1.13: Relative efficiency of select surveyed small hydro devices as a function of rotor area.

Table 1.3: Small Hydro Market Survey

Company	Oceana Energy Company	Smart Hydro Power	Smart Hydro Power	Idénergie	Watt&Sea
Model	UCSD Pico Prototype	MonoFloat	Free Stream	River Turbine	Cruising 300
Type	HKT- open-center horizontal axis	HKT- shrouded horizontal axis	HKT- horizontal axis	HKT- horizontal darrieus cross-flow	HKT- horizontal axis
Directionality	uni-directional	uni-directional	uni-directional	uni-directional	uni-directional
Dimensions [m]	0.56 (rotor diameter)	1 (rotor diameter)	1 (rotor diameter)	1.32 x 0.55 (width x height)	0.240 (rotor diameter)
Number of Blades	8	3	3	3	3
Minimum Depth [m]	0.7	2	1.1	0.6	0.47
Weight [kg]	28	380	300	131	6.3
Cut in speed/Cut out speed [m/s]	1.0/3.5	1.0/2.8	1.0/3.1	1.0/3.5	1.0/7.7
Nominal Power [W]	250	5000	5000	-	300
Flow speed at nominal power [m/s]	2.4	2.8	3.1	-	4.9
Max Rated Power [W]	1500	5000	5000	500	300
Flow speed [m/s] / Power [W] / **Estimated Power Coefficient**	-	1.25/401/**0.52**, 2.25/2485/**0.56**, 2.62/4006/**0.57**, 2.8/5000/**0.58**	1.2/310/**0.46**, 2.4/2355/**0.43**, 2.8/3746/**0.43**, 3.1/5000/**0.43**	1/95.8/**0.22**, 1.5/195.8/**0.13**, 2/325/**0.09**, 2.5/483.3/**0.07**	1.5/16/**0.19**, 2.7/100/**0.23,** 4.1/212/**0.13,** 5.4/300/**0.08**
Cost [usd]	-	$18,001.00	$15,420.00	$9,689.00	$3,575.00

Table 1.3: Small Hydro Market Survey Cont.

Company	ibasei	Seamap/Ampair	Asian Phoenix Resources Ltd.	Blue Freedom	WaterLily
Model	Cappa (Japanese Model)	UW 100	PowerPal MHG-200LH	Portable	WaterLily Turbine
Type	HKT- shrouded horizontal axis	HKT- horizontal axis	Hydrostatic turbine-propeller	HKT- horizontal axis	HKT- horizontal axis
Directionality	uni-directional	bi-directional	uni-directional	uni-directional	uni-directional
Dimensions [m]	0.832 x 0.770 x 0.665 (width x depth x height)	0.312 (rotor diameter)	0.2 (rotor diameter)	0.12 (rotor diameter)	0.180 (rotor diameter)
Number of Blades	2	3	-	8	3
Minimum Depth [m]	0.5	0.4	0.2	-	0.18
Weight [kg]	57	10	16	0.69	1.3
Cut in speed/Cut out speed [m/s]	1.5/2.0	1.5/-	35 liters/s (0.54 m/s @ 1.5 m head)/-	-/-	0.28/3.1
Nominal Power [W]	160	100	200	5	15
Flow speed at nominal power [m/s]	1.75	4.0	35 liters/s	-	1.6
Max Rated Power [W]	-	-	250	5	15
Flow speed [m/s] / Power [W] / **Estimated Power Coefficient**	-	1.0/12/**0.29**, 2.1/50/**0.15**, 3.1/79/**0.07**, 4/100/**0.04**	-	-	0.6/0.6/**0.28**, 1.1/4.9/**0.28**, 1.4/9.5/**0.28**, 1.6/15/**0.28**
Cost [usd]	-	$1,288.00	$425.00	$369.00	$159.00

1.6 Locating Turbines

There are three different placement options for a hydrokinetic turbine in a natural or manmade waterway. They are shown schematically in fig. 1.14 as a moored surface float, a near surface structure such as a dock, and a bottom surface fixture. Each mounting option has its drawbacks, so the best option will likely be site-specific. The greatest energy is contained in the faster moving surface waters, but any surface mounted device also has to deal with increased debris and other waterway activity. This is in contrast to the bottom surface mount which is the most convenient and least energetic [10]. The current open-centered HKT test bed is designed for operation near the surface to keep electrical components above water. Therefore, all physical testing was conducted from a floating structure.

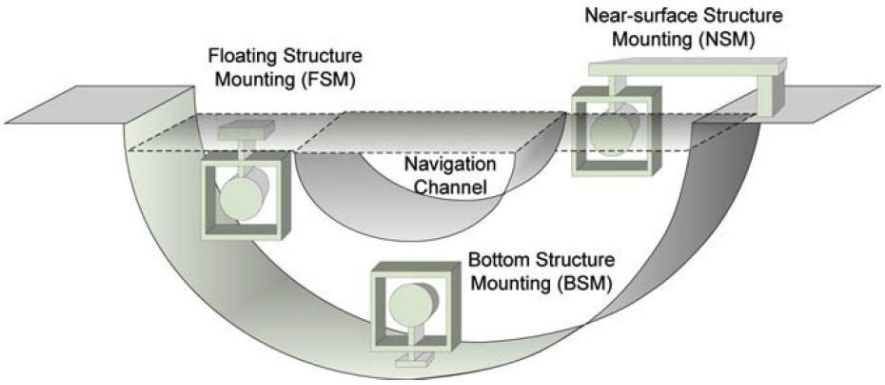

Figure 1.14: Turbine placement options for river or waterway that leave an open navigation channel [10].

1.7 Thesis Outline

This thesis is divided into six parts that cover the development and fabrication of an open-centered pico-scale hydrokinetic turbine test bed. A model of the turbine prototype is shown in fig. 1.15. The unique test bed is designed to be robust and highly modular so that components can be easily modified or swapped out to accommodate new developments. The completed test bed is outfitted with scaled Oceana blades and their performance is measured through a series of tow tests. Experimental results are subsequently compared with results from an analytical model of the open-centered test bed turbine.

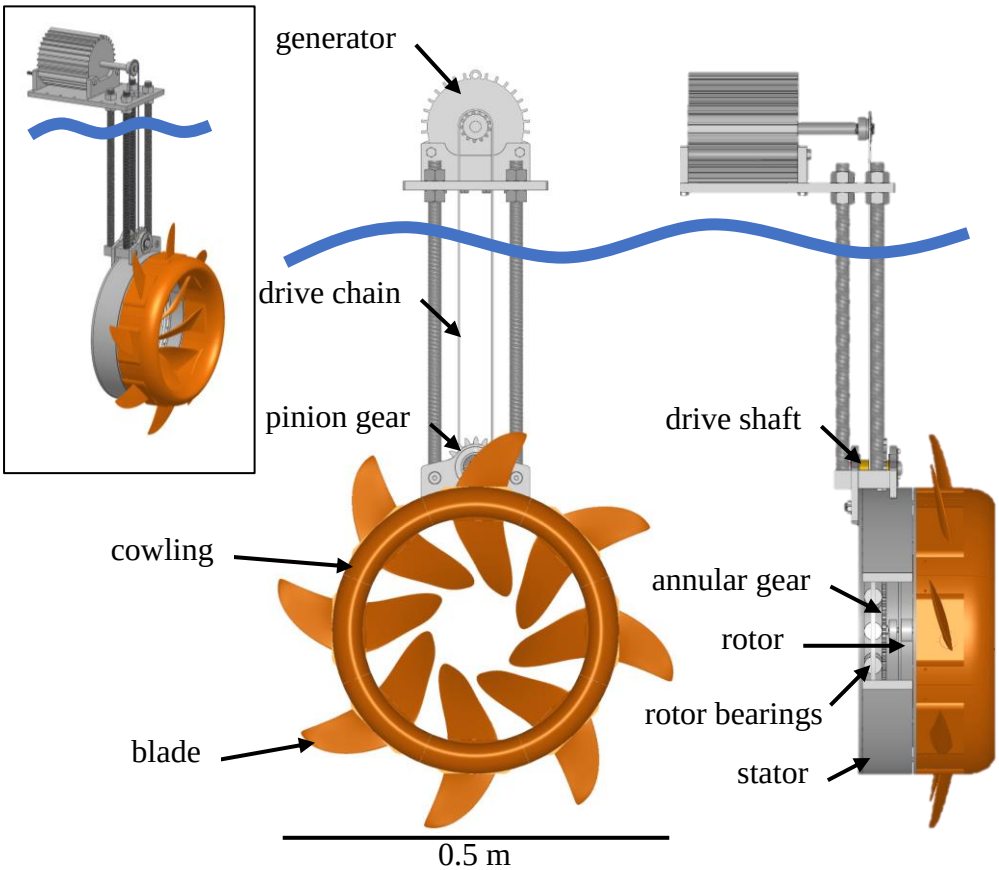

Figure 1.15: A rendering of the full test bed system with a cutaway in the stator to show internal components.

The materials and machine elements that comprise the turbine test bed are explained in Chapter 2. There is a description of the design process for important metallic turbine features, including the stator, the rotor (including the annular gear), the drive chain, the drive shaft, and the pinion gear. This is followed by a brief discussion of the drive shaft bearings and the rotor bearings. The chapter closes with an examination of the generator selection process.

Chapter 3 introduces the additive manufacturing process called fusion deposition modeling (FDM). Material property testing is conducted to compare polylactic acid (PLA) with Acrylonitrile butadiene styrene (ABS), two common materials used in FDM. The effect of infill orientation angle on material properties is explored to quantify the anisotropic nature of the finished parts. This characterization is critical for designing experimental blade sets used during testing.

A basic hydrodynamic model for a turbine is summarized in Chapter 4. Blade element momentum theory (BEMT) is introduced along with modifications for its application to open-centered turbines. A Matlab code based on BEMT is developed to analyze open-centered turbines. The code is then applied to the pico Oceana device to predict turbine performance and blade loading.

In Chapter 5 the material properties established in Chapter 3 are used along with the hydrodynamic loads found in Chapter 4 to build finite element models of PLA blades manufactured by FDM. Blade prototypes are built to perform a combination of static and dynamic load tests. The PLA blades are subsequently evaluated for their potential utility.

Experimental work demonstrating the fully assembled turbine test bed is summarized in Chapter 6. Generator and drivetrain efficiency is measured through a series of lab bench tests. Next, a simple data acquisition system is built to monitor the turbine operation during tow testing. Results from the tow testing are discussed and compared against predicted performance characteristics from Chapter 4.

This thesis concludes with a summary of completed work and a discussion of future avenues to explore within the project. Recommendations for future work focus on improving the hydrodynamic model and expanding data acquisition capabilities. Additional testing with the Oceana blade set is called for, along with development of blades optimized for the pico-scale device that can be demonstrated on the test rig.

Chapter 2. Hydrokinetic Turbine Test Bed Overview

The following chapter presents an overview of the design and engineering analysis process for the open-center hydrokinetic test bed. Figure 2.1 shows an exploded view of the complete test bed system for visual orientation. Metallic features are rendered in light gray for steel alloys and gold for bronze. Polymers are colored with an off-white, while components produced using additive manufacturing are rendered orange. Labels are provided for all major elements of the test bed system.

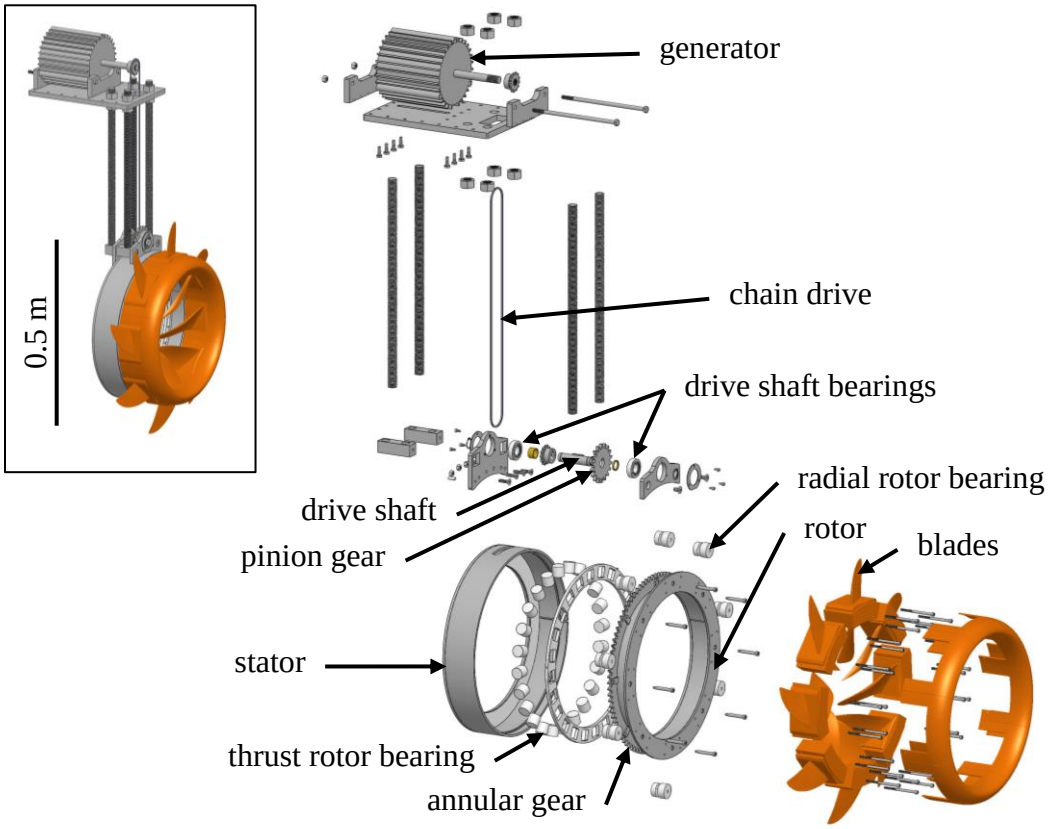

Figure 2.1: An exploded view the test bed system.

To begin, material selection is discussed for the primary turbine structure and bearings. Powertrain elements—including the annular rotor gear, pinion gear, and

drive chain—are sized to maximize power capacity according to material and geometric constraints. Power ratings for the gears are used to size the drive shaft and drive shaft bearings. Rotor thrust bearings are designed based on the maximum drag load. Finally, a commercially available generator with suitable output capacity is identified.

2.1 Material Selection for the Test Bed

The experimental turbine system is intended primarily for testing in freshwater. However, the flexibility to test in marine or brackish water requires the consideration of galvanic corrosion. The potential for any galvanic corrosion was eliminated by designing all the turbine components with a single material. Although in some respects this drove the design to be overly conservative, the use of a single material greatly simplified the manufacturing process. 316 stainless steel was used as the primary structural material for the turbine because it offers sufficient strength and hardness to incorporate a gear into the rotor design. It's also naturally resistant to corrosion.

Non-metallic materials—excepting PLA, which is detailed in Chapter 3—were also chosen specifically for their stability in the marine environment. Delrin was used in the bearings to take advantage of its favorable wear resistance, dimensional stability in water and relatively low coefficient of friction that allow it to operate without lubrication [53].

2.2 Required Powertrain Capacity

The full-scale open-centered device operates between 30% and 50% efficiency. Required power rating for the powertrain was approximated using the kinetic energy of the water passing through the rotor plane with an assumed efficiency η of 40%, calculated as

$$P = \eta\left(\frac{1}{2}\rho A U^3\right) \tag{2.1}$$

where ρ is the water density, A is the swept area of the turbine, and U is the water velocity [54]. Swept rotor area for an open-centered turbine is defined

$$A = \pi\left(r_4^2 - r_1^2\right) \tag{2.2}$$

where r_4 is the radius at the tip of the outer blades and r_1 is the radius at the tip of the inner blades. For traditional rotors with a central hub r_1=0.

Figure 2.2 shows the available power density (P/A) as a function of water speed, at the nominal water density of 1000 kg/m^3, for a range of efficiencies. Operating power densities for select pico HKTs detailed in table 1.3 are plotted as well to demonstrate their relative efficiency at different flow speeds. Typical speeds for a comfortable walk (0-1.5 m/s), fast walk (1.5-2.5 m/s), and a jog or run (2.5-5 m/s) are included for scale [55,56]. Particularly high efficiencies demonstrated by the SmartHydro Monofloat result from a diffuser that augments flow across the rotor, which theoretically allows it to exceed the Betz limit.

The current powertrain operates in currents up to 4 m/s to test through a range of realistic and extreme conditions. Table 2.1 contains a limited sample of hydrokinetic resource assessments to illustrate some common flow speeds in both man-made and natural flows. Sites are listed in order of ascending mean discharge, or mean transport for the ocean and tidal sites, to give an approximate measure of flow scale. Mean flow speed across the sites ranges from 0.7 m/s to 3.23 m/s. The highest flow speed reported was 7.25 m/s at the KwaZulu-Natal site, though none of the other sites experienced anything greater than 3.5 m/s. An operating limit of 4 m/s is sufficient for most sites, which at 40% efficiency translates to 3 kW for the current rotor area of 0.24 m^2.

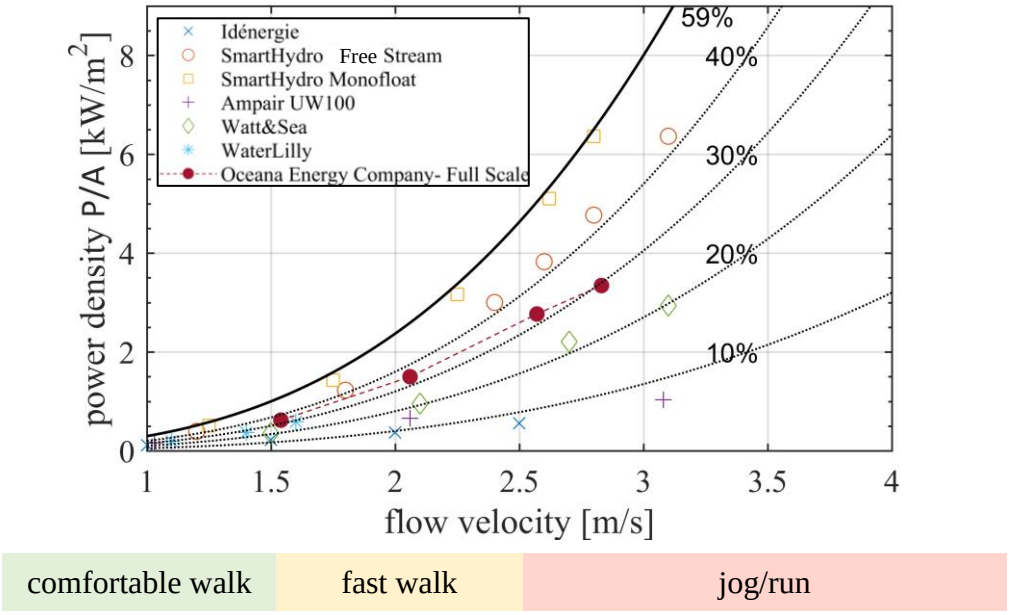

Figure 2.2: Power density as a function of flow velocity for different conversion efficiencies. The theoretical maximum efficiency (Betz limit) is shown with a solid line. Operating points for select pico-scale HKTs are plotted as well.

Table 2.1: Hydrokinetic Resource Assessments

Resource	Site ID	Location	Minimum flow speed [m/s]	Mean flow speed [m/s]	Maximum flow speed [m/s]	Mean discharge or transport [m^3/s]	Source
River	2	KwaZulu-Natal, South Africa	1.41	3.23	7.25	31	[57]
Irrigation Channel	-	Roza Canal, Yakima, WA	-	2	-	53	[58]
River	Vilnius	Neris River, Lithuania	0.48	0.7	1.67	179	[59]
Tidal	RITE	East River Tidal Strait, New York, NY	0	1.4	3.5	310	[60,61]
River	-	Tanana river, Nenana, AK	-	1.5	1.9	693	[62,63]
Ocean Current	B2	Florida Current, south east coast, FL	0.43	1.6	2.49	32,000	[64,65]

2.3 Power Transfer Mechanism

Figure 2.3 shows a model of the key powertrain components. The rotor is designed with an annular ring gear (seen in the fig. 2.3 cutaway) to transmit the torque produced by the blades. A smaller pinion gear meshes with the annular rotor gear through a slot in the stator housing with a 5:1 gear ratio. Common off-the-shelf alternators require shaft speeds greater than the 50-300 rpm expected from the rotor to produce significant power. Gearing up by a factor of 5 makes the task of matching an efficient alternator to the turbine significantly easier. While not technically enclosed, the gear train and accompanying drive shaft elements are referred to as the gearbox.

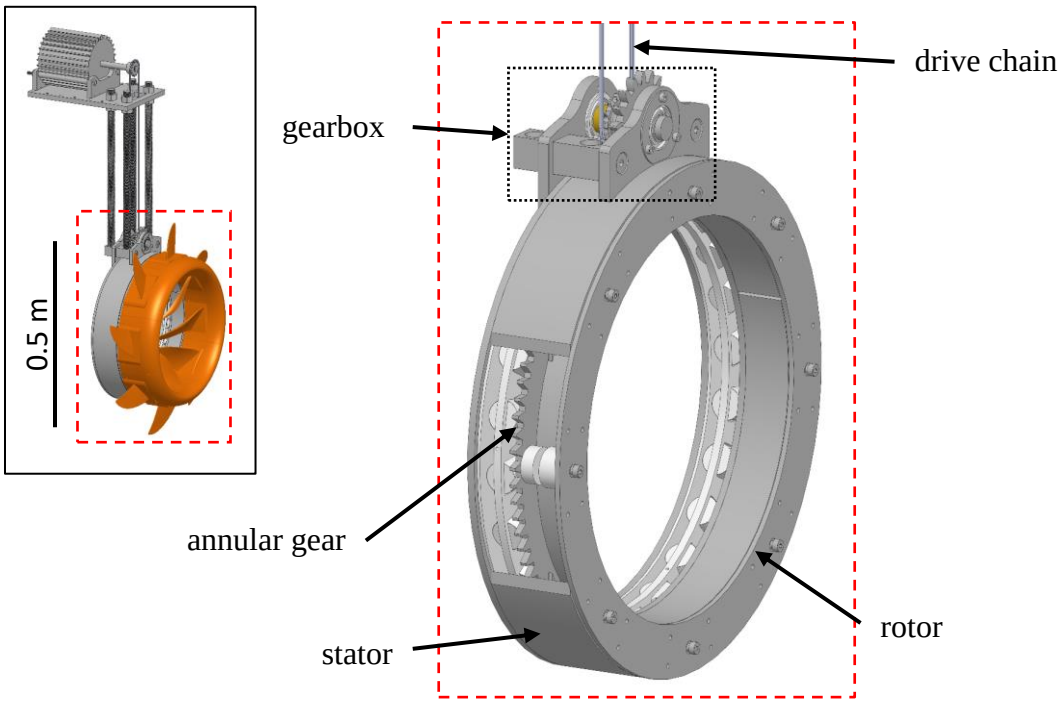

Figure 2.3: A rendering of key turbine powertrain components with a stator cutaway to show internal gearing.

A detailed picture of the gearbox is provided in fig. 2.4. The stator slot, through which the pinion meshes with the annular gear, is aligned with the center of the gearbox. Power is transferred to the generator via the drive chain and sprockets at the gearbox and generator shaft. The sprocket at the generator currently has the same number of teeth as the one in the gear box. However, the ability to easily change the tooth ratio between the sprockets provides flexibility in tuning the total gear ratio of the powertrain.

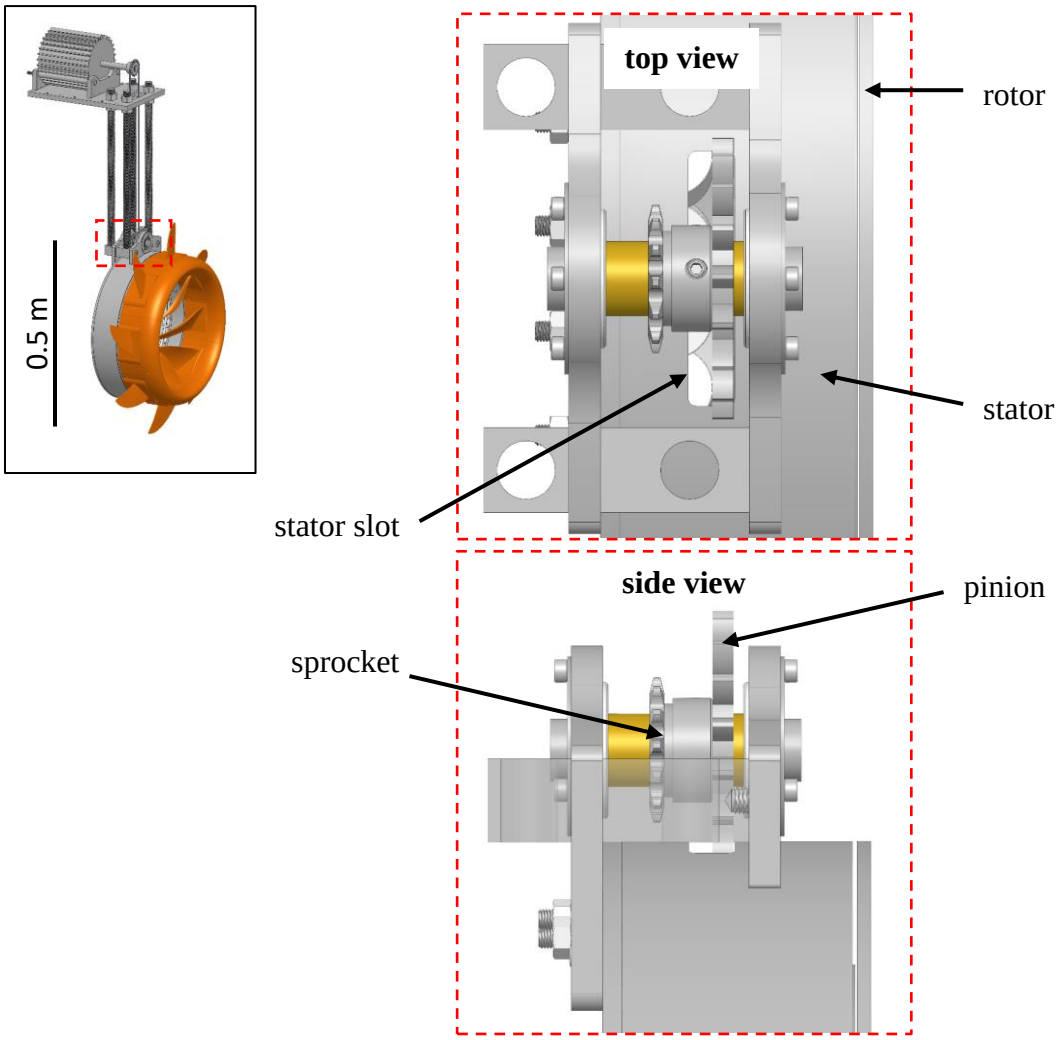

Figure 2.4: Detailed model views of the turbine gear box from the top and side perspective. Note that the outer part of the gear box has been made transparent in the side view to more clearly show all the shaft components.

2.4 Gear Design

Power capacity was the primary driver in designing the gears, which are identified in fig 2.5. Sizing and material for the gears accounts for both contact and bending stresses on the teeth using guidelines published by the American Gear Manufacturers Association (AGMA) [66]. Operation of the test turbine is intended for low-cycle intermittent operation so a life of 10 million cycles—approximately 1,670 hours of operation at 100 rpm—with 99% reliability was targeted in the stress analysis. The annular gear will be identified throughout this section using a subscript 1 while the pinion will be identified with a subscript 2.

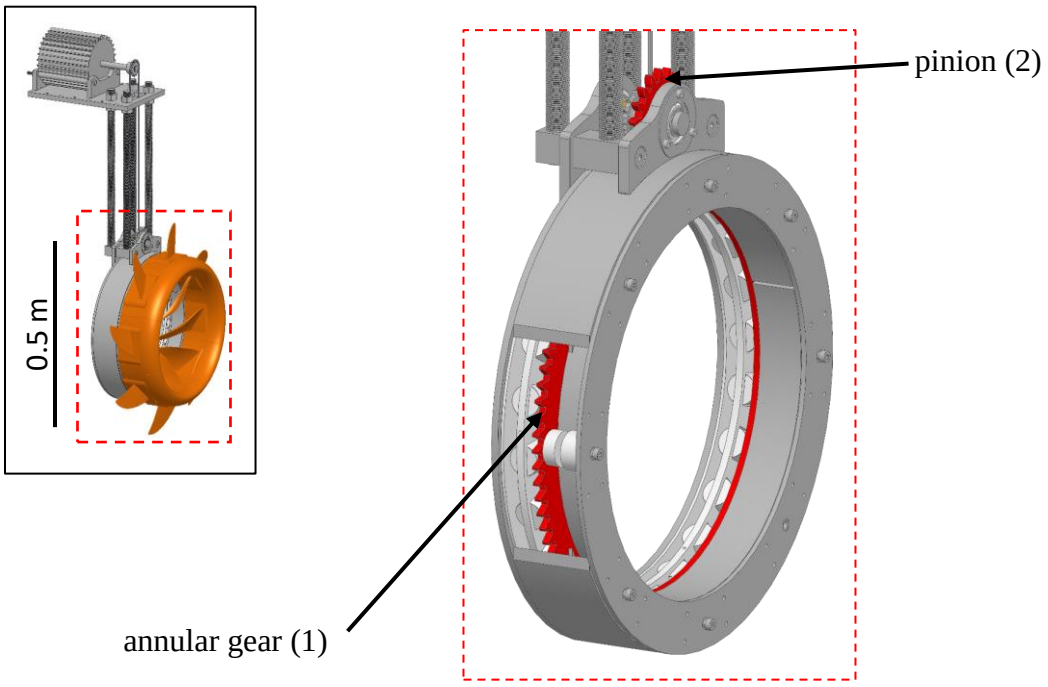

Figure 2.5: A rendering of the turbine showing the pinion and a cutaway revealing the annular gear.

Figure 2.6 is a free body diagram of the two gears showing the force exerted on the pinion by the annular gear F_{12}. The force on the annular gear exerted by the pinion F_{21} has been omitted for clarity. Force F_{12}, which acts at along the pressure angle of the gears ϕ_p, is resolved into a radial component W_r and tangential component W_t. Tangential load W_t is calculated simply as the transmitted power P in W divided by the pitch line velocity V in m/s

$$W_t = \frac{P}{V} \ . \tag{2.3}$$

Pitch line velocity is found using the rotational speed ω and pitch radius r_p

$$V = \omega r_p \tag{2.4}$$

where pitch diameter d_p is the product of gear module m in meters—a unit measure of gear size that must be equal gears to mesh—and the number of teeth N

$$d_p = mN \tag{2.5}$$

and thus

$$r_p = \frac{mN}{2} \ . \tag{2.6}$$

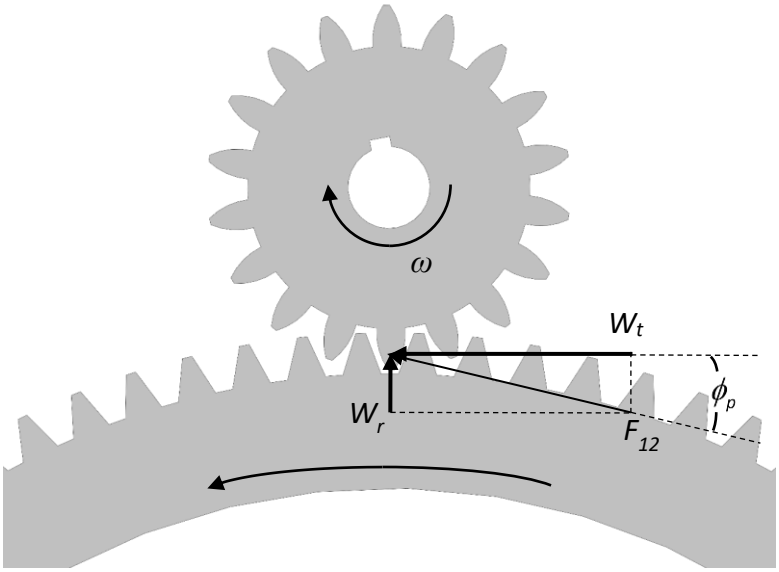

Figure 2.6: A freebody diagram of gear forces.

Bending stress is found by modeling a gear tooth as a cantilevered beam. The maximum stress σ_{max} at the root of the tooth for a simplified uniform rectangular cross-section (shown in fig. 2.7A) is

$$\sigma_{\max} = \frac{My}{I_z}\bigg|_{t/2} = \frac{6lW_t}{bt^2} \tag{2.7}$$

where l is the length of the tooth, t is the width, and b is the face width (thickness). It's assumed that the maximum stress occurs within the fillet at the base of the tooth profile, at point A in fig. 2.7B, and by similar triangles it's found that [67]

$$\frac{t/2}{l_o} = \frac{l}{t/2} \tag{2.8}$$

rearranging,

$$l_o = \frac{t^2}{4l} \ . \tag{2.9}$$

The Lewis bending equation can be found by multiplying eq. (2.7) by circular pitch p_c [67]

$$\sigma_{\max} = \sigma_b = \frac{6 p_c l W_t}{p_c b t^2}, \tag{2.10}$$

where the circular pitch is equal to

$$p_c = \pi m. \tag{2.11}$$

Substituting eq. (2.9) and eq. (2.11) into eq. (2.10) and rearranging yields

$$\sigma_b = \frac{3\pi m W_t}{2\pi m b l_o}. \tag{2.12}$$

A Lewis form factor Y_L can then be defined [67]

$$Y_L = \frac{2 l_o}{3m} \tag{2.13}$$

to produce the Lewis bending equation in terms of gear module m,

$$\sigma_b = \frac{W_t}{b m Y_L}. \tag{2.14}$$

A detailed derivation of the Lewis equation can be found in mechanical design handbooks such as [67,68].

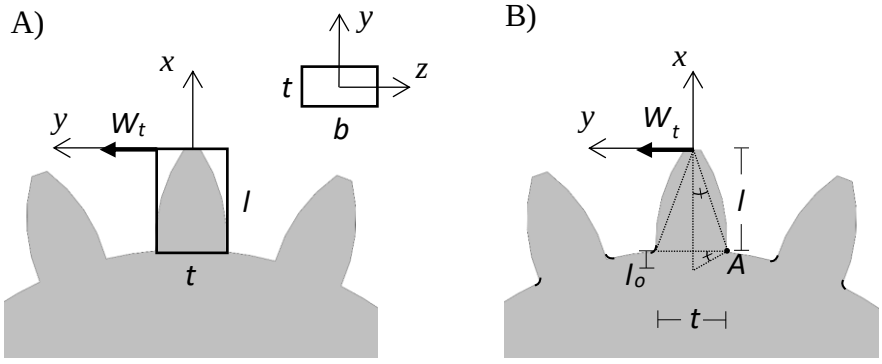

Figure 2.7: Gear tooth modeled as a cantilevered beam.

The American Gear Manufacturers Association (AGMA) uses a similar approach to calculate tooth bending stress. They introduce a geometry factor Y_J, analogous but not equal to the Lewis form factor Y_L, along with a series of additional design factors intended to help improve overall reliability. The AGMA expression for bending stress [66] is

$$\sigma_b = \left(\frac{W_t}{bmY_J} \right) K_O K_V K_S K_H K_B \ . \tag{2.15}$$

Here Y_J is the geometry factor, m is the gear module, b is the face width, K_O is the overload factor, K_v is the dynamic factor, K_s is the size factor, K_H is the load distribution factor, and K_B is the rim-thickness factor. Equation (2.15) can be written in terms of transmitted power and rotational speed using eqs. (2.3)-(2.4)

$$\sigma_b = \left(\frac{2P}{\omega d_p bmY_J} \right) K_O K_V K_S K_H K_B \tag{2.16}$$

or in with the speed n in terms of rpm

$$\sigma_b = \left(\frac{60P}{\pi n d_p bmY_J} \right) K_O K_V K_S K_H K_B \ . \tag{2.17}$$

It's worth stressing that the rotational speed n in eq. (2.17) is the gear speed. The annular gear speed and rotor speed are equivalent, but the pinion speed differs by a factor five.

Overload factor K_O is used to account for variation in the maximum transmitted load. A value of 1.0 was used due to the fairly smooth operating conditions associated with slowly ramping the turbine up and down in speed with a fixed load.

Dynamic factor K_V quantifies the effect of manufacturing quality on gear stresses based on a quality control number Q_V. The quality control rating is defined on a scale from 3 to 15. Higher numbers require increasingly tighter geometric tolerances [69]. In this case, the gears are estimated to be of low-medium quality (Q_V=5) based on of the accuracy of the water-jet machine from which they were cut [69]. Dynamic factor K_V is then calculated by [67]

$$K_V = \left(\frac{A + \sqrt{200V}}{A} \right) B \tag{2.18}$$

with

$$A = 50 + 56\left(1 - B\right) \tag{2.19}$$

and

$$B = \frac{\left(12 - Q_V\right)^{\frac{2}{3}}}{4} \tag{2.20}$$

where V is the pitch line velocity found by eq. (2.4).

The size factor K_S can be used to incorporate non-uniformities in material properties if the size of the gear warrants it [67]. It is set to 1 for this design's relatively thin face width. Load distribution factor K_H accounts for non-uniform contact lines between teeth that occur due to shaft misalignment or deflection under load [67]. For this geometry and configuration—the pinion is straddle mounted between bearings—K_H is equal to [67]

$$K_H = 1 + C_{mc}\left(C_{pf}C_{pm} + C_{ma}C_e\right). \tag{2.21}$$

For uncrowned gear teeth C_{mc}= 1 [67]. The face width b is less than 25.4 mm and the ratio $b/(10d_p)$ is less than 0.05, where d_p is the pitch diameter determined by eq. (2.5), therefore C_{pf} is equal to 0.025 [67]. The centerline of the pinion is offset from the center of the shaft by approximately 14.33 mm, or 26.5% of the full shaft span. As per the standard when the offset is greater than or equal to 17.5% C_{pm} is set to 1.1 [67]. The mesh alignment factor C_{ma} for open gearing is 0.251 [67]. No lapping or refinement has been performed on the gears so C_e is left at unity [67].

Rim thickness factor K_B is set to 1, as the rim thickness is greater than 1.2 times the tooth depth [67]. Geometry factor Y_J accounts for the tooth profile and load sharing ratio of the gear set. It's approximated as 0.42 for the annular gear and 0.325 for the pinion using the AGMA plot of standard values for 20° pressure angle spur gears in fig. 2.8 [70].

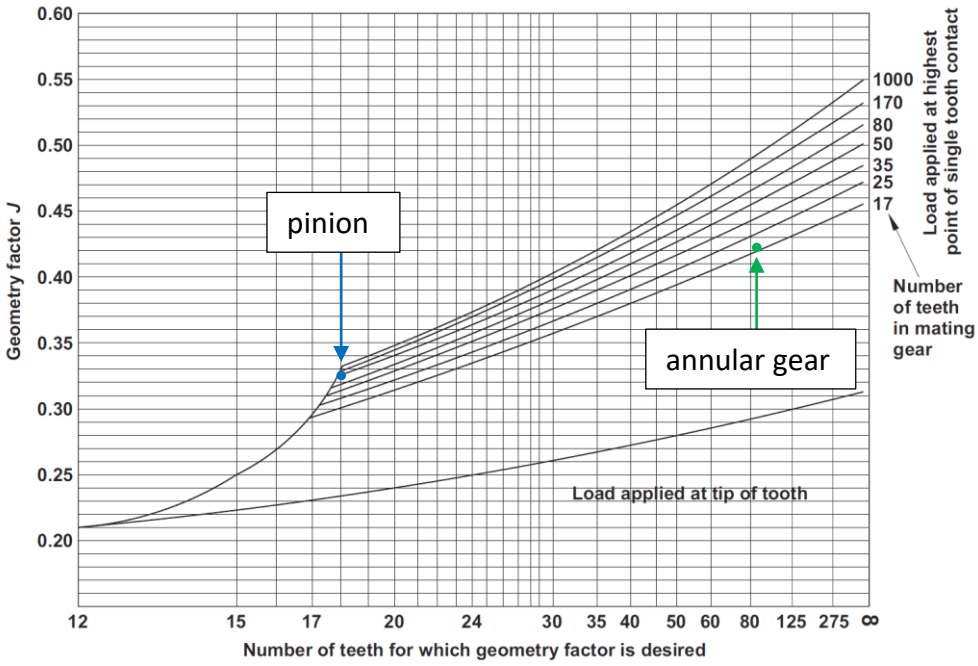

Figure 2.8: Bending stress geometry factor Y_J for spur gears with 20 degree pressure angle [70].

Allowable bending stress F_E is reduced from the fatigue endurance limit of 316 stainless steel reported in [71] using Marin factors [67]. The resulting allowable stress is 167 MPa for the annular gear and 170 MPa for the pinion. Details on the Marin factors used to de-rate the endurance strength are provided in Appendix A. Equation (2.17) is solved to find the maximum transmitted power as a function of gear speed when the margin of safety is equal (MS) to 0

$$P_{bend} = nF_E\left(\frac{\pi d_p bmY_J}{60K_O K_V K_S K_H K_B}\right). \tag{2.22}$$

Equation (2.22) is evaluated for expected rotor speeds up to 300 rpm and plotted in fig. 2.9 to define the safe operating regime—according to the allowable bending stress—of the gear train.

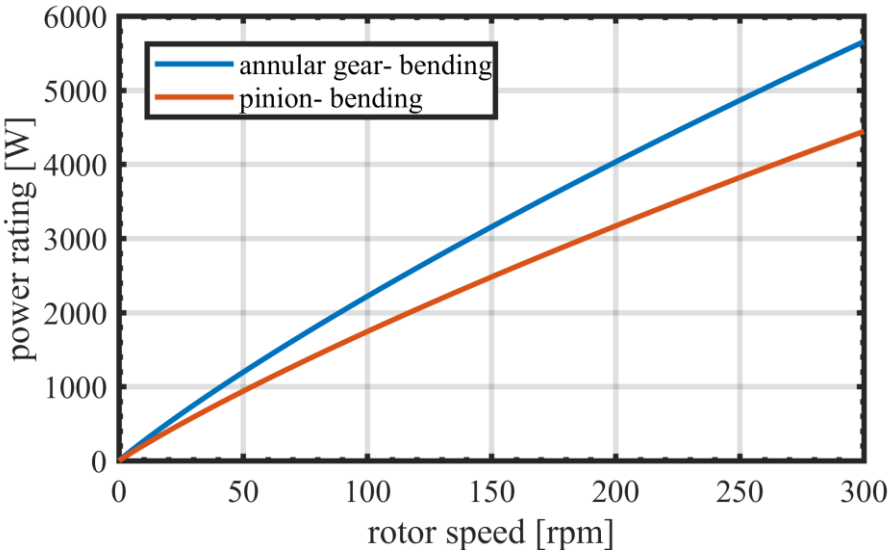

Figure 2.9: Maximum transmitted power (MS=0) for bending stress in the pinion (orange) and annular gear (blue) teeth for a given rotor speed.

Contact stress between the gears was calculated to evaluate surface durability of the teeth. Maximum pressure, or compressive stress, at the surface of two contacting cylinders, both of length L, can be found by the Hertz model [67]

$$P_{max} = \sigma_{max} = \frac{2F}{\pi w L} \tag{2.23}$$

where F is the contact force and w is the half-width of the rectangular contact area exhibited in fig. 2.10. The half-width w of the contact area is defined as [67]

$$w = \left[\frac{2F}{\pi L} \frac{\left(\frac{1-\nu_A^2}{E_A} + \frac{1-\nu_B^2}{E_B} \right)}{\left(\frac{1}{d_A} + \frac{1}{d_B} \right)} \right]^{1/2} \tag{2.24}$$

with subscripts A and B used to differentiate each cylinder's Young's modulus E, Poisson's ratio ν, and diameter d.

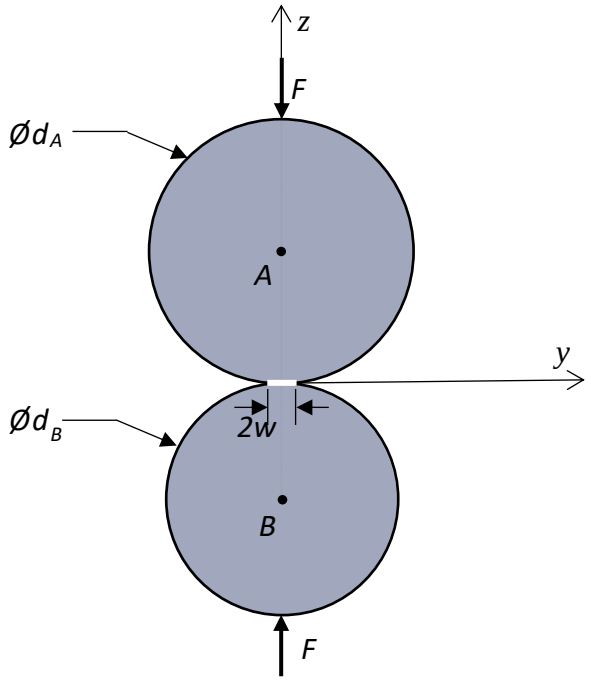

Figure 2.10: Cross-section of two contacting cylinders.

Equation (2.23) can be applied to gear teeth by relating the force F to the transmitted load by

$$F = \frac{W_t}{\cos\phi} \tag{2.25}$$

and substituting face width b for the length L. It's also convenient to substitute radii $2r_1$ and $2r_2$ for diameters d_1 and d_2, where subscripts A and B have been replaced with 1 and 2 to indicate that these equations now refer to the two gears. With some manipulation eq. (2.23) becomes [67]

$$\sigma_{\max} = \sigma_c = \left[\frac{W_t}{\pi b \cos\phi} \frac{\left(\frac{1}{r_1} + \frac{1}{r_2}\right)}{\left(\frac{1-\nu_1^2}{E_1} + \frac{1-\nu_2^2}{E_2}\right)} \right]^{1/2} \tag{2.26}$$

or by defining the elastic coefficient Z_E

$$Z_E = \left[\pi \left(\frac{1-\nu_1^{\,2}}{E_1} + \frac{1-\nu_2^{\,2}}{E_2} \right) \right]^{-1/2} \tag{2.27}$$

the resulting contact stress is

$$\sigma_C = Z_E \left[\frac{W_t}{b\cos\phi} \left(\frac{1}{r_1} + \frac{1}{r_2} \right) \right]^{1/2} . \tag{2.28}$$

The radii of curvature at the point of contact r_1 and r_2 are defined as [67]

$$r_1 = r_{p1} \sin\phi_p \tag{2.29}$$

and

$$r_2 = r_{p2} \sin\phi_p . \tag{2.30}$$

where respective pitch radii r_{p1} and r_{p2} are calculated with eq. (2.6). The radius of curvature at the point of contact for two generic gears in mesh is illustrated in fig. 2.11. Base radius r_b is the radius from which the gear's involute profile originates. It's related to the pitch radius by the cosine of the pressure angle

$$r_b = r_p \cos\phi \ . \tag{2.31}$$

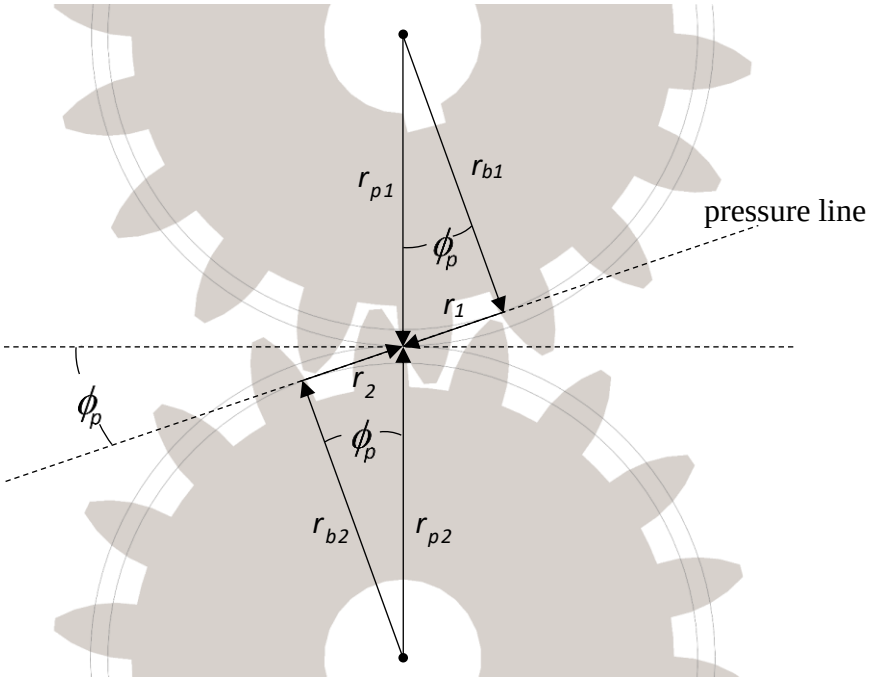

Figure 2.11: Point of contact for two gears in mesh.

The AGMA formula for determining contact stress is derived from Hertz theory as well, resulting in a modified form of eq. (2.28) [66,67]

$$\sigma_c = Z_E \left(\frac{W_t K_O K_V K_S K_H Z_R}{b d_{p2} Z_I} \right)^{1/2} \tag{2.32}$$

where the new terms include the surface condition factor Z_R, the pitch diameter of the pinion d_{p2}, and the geometry factor for pitting resistance Z_I. Elastic coefficient Z_E was

established by eq. (2.27). Factors K_O, K_V (eq. (2.18)), K_S, and K_H (eq.(2.21)) are defined the same as in the AGMA bending stress eq. (2.15). Equation (2.32) can be written in terms of transmitted power and rotational speed using eqs. (2.3) and (2.4)

$$\sigma_c = Z_E \left(\frac{30 P K_O K_V K_S K_H Z_R}{\pi r_p n b d_{p2} Z_I} \right)^{1/2} \tag{2.33}$$

where the gear speed n has units of rpm.

For 316 stainless steel, using properties from [72], Z_E is evaluated to be 179 $\sqrt{MPa}$. Surface condition factor Z_R is used to de-rate the gear for any surface quality issues that may make it less resistant to surface pitting, though since the relative effect of various surface conditions is yet to be standardized Z_R is kept at unity [67]. Finally, Z_I is geometry factor for pitting resistance which for external spur gearing is determined using the gear speed ratio m_g and the pressure angle ϕ_p [67]

$$Z_I = \frac{\cos\phi_p \sin\phi_p}{2} \frac{m_g}{m_g + 1}. \tag{2.34}$$

The AGMA surface fatigue strength F_{SF} for steels is approximated in ksi based on a hardness H in HB [67]

$$F_{SF} \approx 0.327H + 26 \tag{2.35}$$

for a lifetime of 10 million cycles with 99% reliability. Using the minimum hardness for 316 stainless steel of 143 HB [73] results in a surface stress allowable of 72.76 ksi (502 MPa). Table 2.2 presents a summary of all the gear parameters and AGMA design factors used for designing the turbine gear set.

Maximum power as a function of gear speed is found using eq. (2.33) by solving for the power at which the MS=0, yielding

$$P_{contact} = n\left(\frac{F_{SF}}{Z_E}\right)^2\left(\frac{30 r_p b d_{p2} Z_I}{\pi K_O K_V K_S K_H Z_R}\right). \tag{2.36}$$

The rated power curve for contact stress is plotted up to 300 rpm in fig. 2.12.

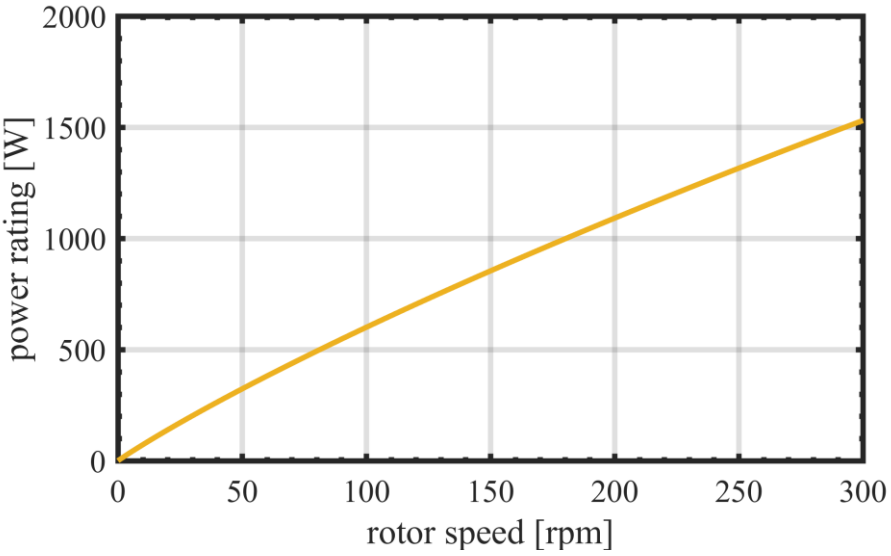

Figure 2.12: Maximum transmitted power (MS=0) for contact stress (yellow) in the pinion and annular gear teeth.

The module was fixed to fit the stator geometry and maintain an advantageous gear ratio. Face width of the gears was manipulated to get positive margins of safety for both contact and bending stresses in flows up to 3 m/s—which translates to roughly 1.3 kW of capacity at a 40% efficiency—at expected rotor speeds between 50 and 300 rpm. Above 3.17 m/s, or 1.5 kW capacity at 40% efficiency, contact stress and tooth durability become the limiting factor. This is deemed an acceptable trade-

off to maintain a compact 6.35 mm face width given that testing at flow speeds exceeding 3.17 m/s would only occur for a short period of time, both gears are accessible for inspection, and a limited number of operational cycles is required.

Table 2.2: Gear Design Parameters

	Variable	Value	Unit	Source
Face width	b	6.35	mm	
Module	m	4.233	mm	
Pressure angle	ϕ_p	20	degrees	
Number of annular gear teeth	N_1	90		
Number of pinion teeth	N_2	18		
Backlash	-	0.305	mm	
Young's modulus 316 SS	E	186	GPa	[72]
Poisson's ratio 316 SS	ν	0.27		[72]
Hardiness 316 SS	H	143	HB	[73]
B-basis ultimate strength 316 SS	F_{ut}	889	MPa	[72]
Endurance strength 316 SS	F_e'	269	MPa	[71]
Marin endurance strength- gear	F_{E1}	167	MPa	
Marin endurance strength- pinion	F_{E2}	170	MPa	
Surface fatigue strength	F_{SF}	502	MPa	
Overload factor	K_O	1		
Quality Number	Q_v	5		[69]
Size factor	K_S	1		
Load distribution factor	K_H	1.279		
Rim thickness factor	K_B	1		
Geometry factor for bending- gear	Y_{J1}	0.420		
Geometry factor for bending- pinion	Y_{J2}	0.325		
Geometry factor for contact	Z_I	0.134		
Elastic coefficient	Z_E	179	$\sqrt{\text{MPa}}$	
Surface condition factor	Z_R	1		

2.5 Drive Chain Selection

Roller chain, identified in fig. 2.13, was selected for the drivetrain to provide up to 3 kW of capacity at rotor speeds below 300 rpm. A surface treated steel was used in place of a stainless-steel for the chain. While the surface treatment provides less corrosion resistance, the load capacity is more than 9 times greater than equivalent sized stainless-steel chain [74].

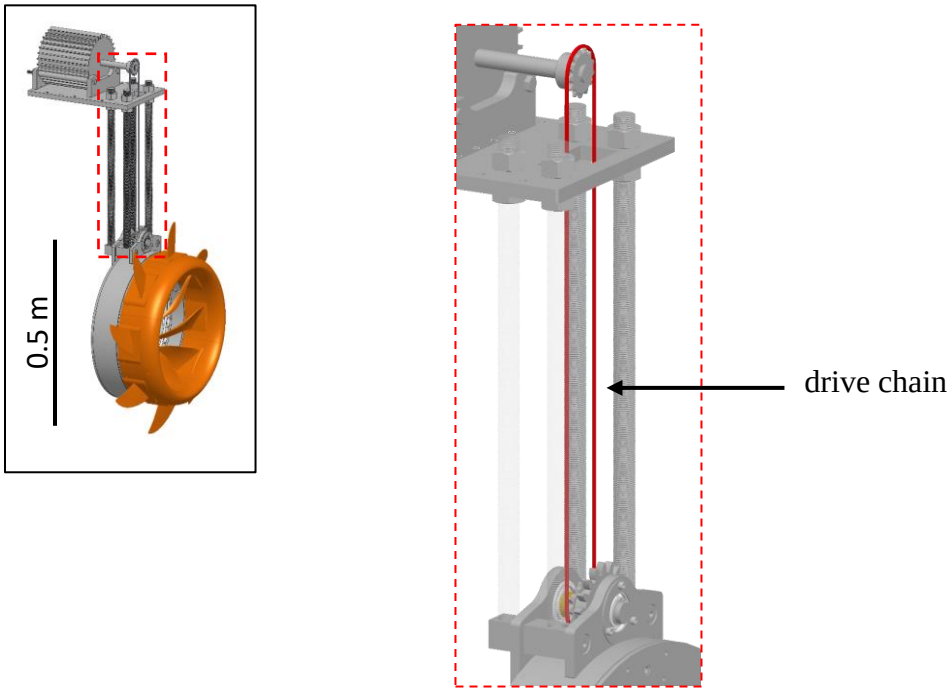

Figure 2.13: A rendering of the turbine highlighting the drive chain.

Figure 2.14 is a basic schematic of the drive train arrangement. Chain tension is calculated according to the power transmitted P and the velocity of the chain V by [75]

$$F_t = \frac{P}{V}\ , \tag{2.37}$$

with roller chain velocity determined by the rotational speed of the sprocket n in units of rpm, the number of teeth N, and the pitch p [75]

$$V = nNp\ . \tag{2.38}$$

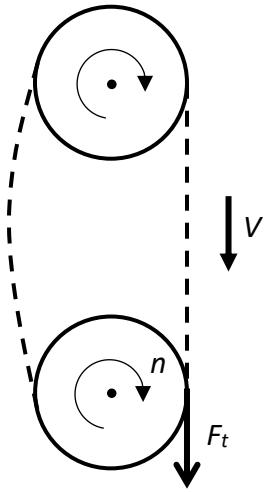

Figure 2.14: Illustration of tension in roller chain.

If the allowable chain tension is Ft^* then the maximum transmitted power, with a MS=0, is found using eq. (2.37)

$$P_{chain} = n\left(\frac{NpF_t^*}{K_X}\right)\ . \tag{2.39}$$

Where a service factor K_X has been introduced to accommodate fluctuations in the load. A moderate service factor of 1.3 was used in case of turbulence or unexpected variations in flow speed during testing [75]. American National Standards Institute (ANSI) number 35 chain with 3/8 in. (9.53 mm) pitch with an allowable working load of 2,491 N was selected [74]. Relevant chain specifications are provided in table 2.3.

Table 2.3: Chain Specifications

	Variable	Value	Units	Source
ANSI number		35		
Pitch	p	3/8	in	
Pitch (converted)	p	9.53	mm	
Allowable chain tension	F_t^*	2,491	N	[74]
Service factor	K_X	1.3		
Number of sprocket teeth- drive shaft	N	13		
Number of sprocket teeth- generator	N	13		

A plot of the maximum power capacity for rotor speeds up to 350 rpm is shown in fig. 2.15. The chain exceeds 1 kW of capacity at 50 rpm and meets the target capacity of 3 kW at 150 rpm. Power ratings for the gears are shown together with the chain rating in fig. 2.16. It's evident that the wear free operating regime of the test powertrain is defined by the gear contact stress and the pinion bending stress as the chain capacity exceeds both these limits.

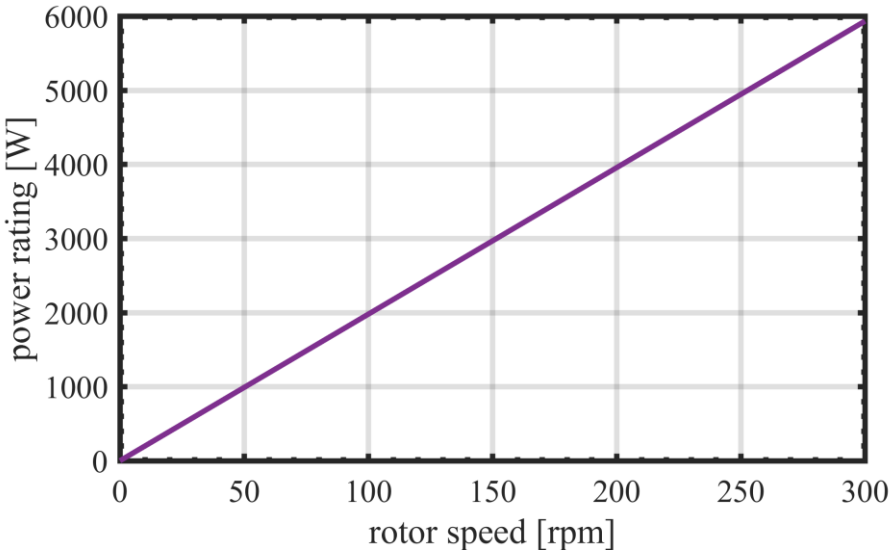

Figure 2.15: Maximum transmitted power as a function of rotor speed such that chain tension does not exceed the safe working limit.

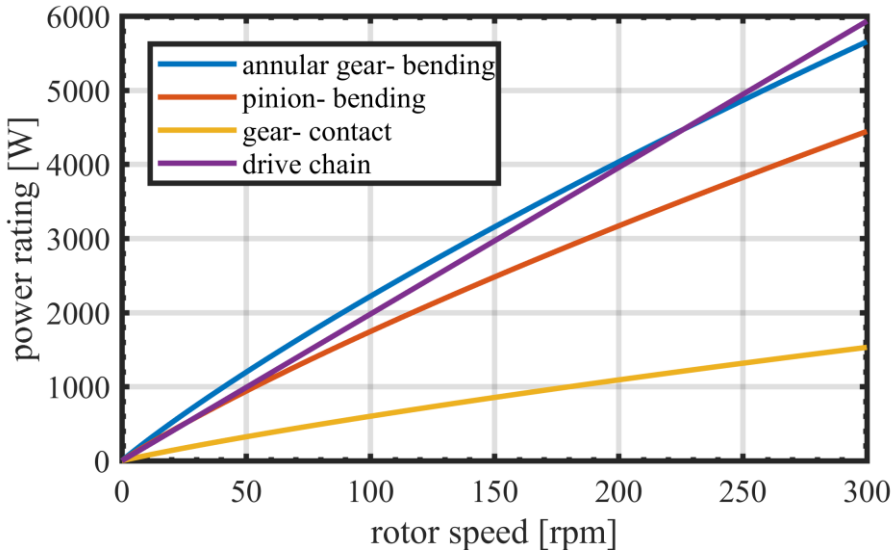

Figure 2.16: Maximum transmitted power (MS=0) for bending stress in the pinion (orange) and annular gear (blue) teeth, contact stress (yellow) between gear teeth, and drive chain load capacity (purple).

2.6 Shaft Elements

The drive shaft and bearings evaluated in this section are highlighted in fig. 2.17 for reference. Surrounding parts of the gearbox have been made transparent for clarity. The drive shaft was initially sized to meet the strength requirements imposed by the maximum transmitted power-rpm curve of fig 2.9 for the pinion tooth in bending (orange curve). Ideally the turbine will never be tested above the contact stress power-rpm curve in fig 2.12, however the extra capacity—equivalent to the difference between the pinion bending rating (orange curve) and the contact rating (yellow curve) seen in fig. 2.16—is included for greater flexibility.

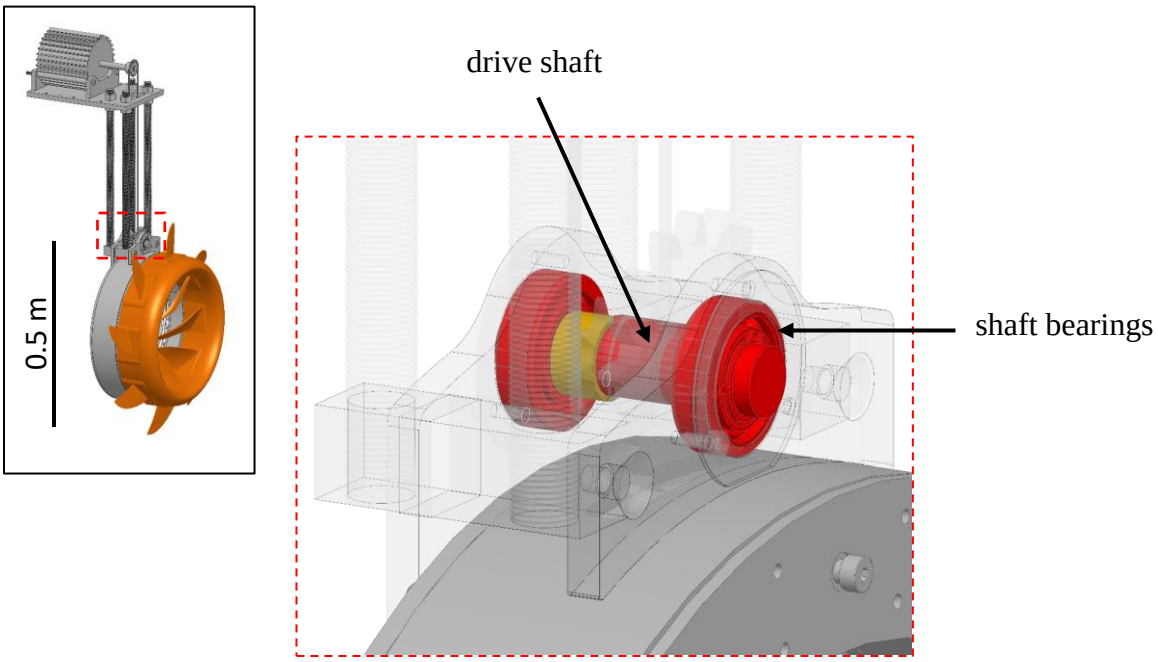

Figure 2.17: A rendering of the turbine highlighting the drive shaft.

Torque T_m transmitted by the shaft is determined by the amount of power transferred and the rotational speed of the shaft. Alternating moments—in the reference frame of the shaft—are generated on the shaft due to forces exerted by the pinion, which transfers both a horizontal and vertical force, and the sprocket, which transmits only a vertical force via tension in the chain. Forces generated by the pinion are labeled with a subscript 2 while those resulting from the chain sprocket are labeled with a subscript 3. They are calculated as follows:

$$F_{y2} = W_t \tag{2.40}$$

$$F_{z2} = W_t \tan\phi_p - m_2 g \tag{2.41}$$

$$F_{z3} = F_t - m_3 g \tag{2.42}$$

in which W_t is defined by eq. (2.3), F_t is defined by eq. (2.37), m_2 is the mass of the pinion, m_3 is the mass of the sprocket, and g is the acceleration due to Earth's gravity. A free body diagram of the shaft is shown in fig. 2.18.

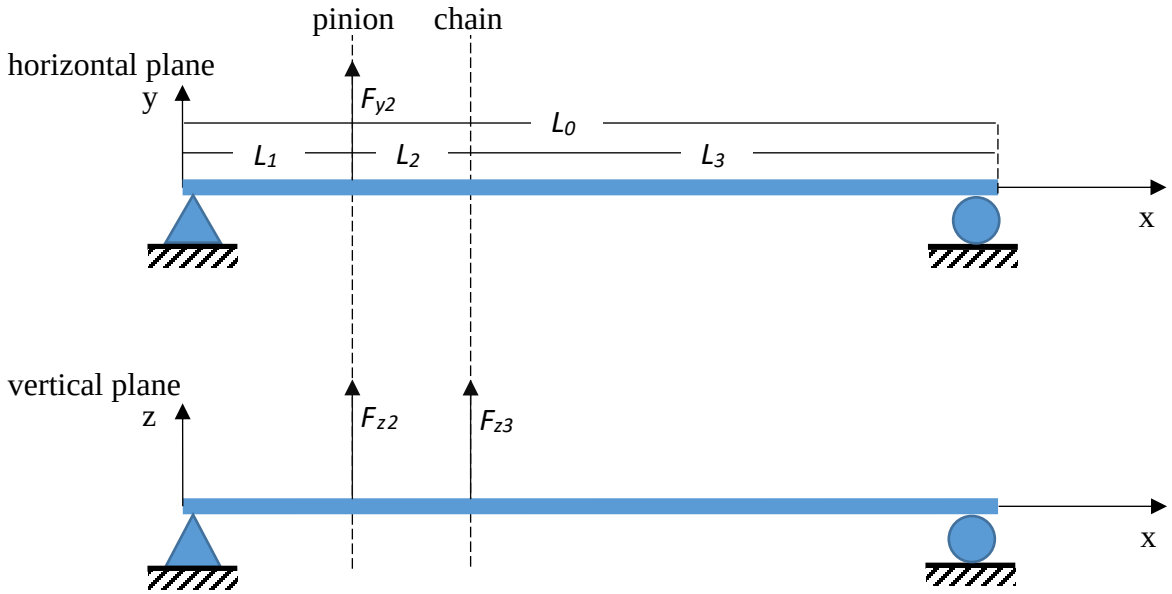

Figure 2.18: Free body diagram of simply supported transmission shaft with length L_0 loaded by a pinion at x=L_1 and a sprocket at x=L_1+L_2.

A disortion energy-elliptic failure criterion was applied to evaluate shaft strength [67]

$$\left(\frac{n_{sf}\sigma_a}{F_{ES}}\right)^2+\left(\frac{n_{sf}\sigma_m}{F_{yt}}\right)^2=1 \tag{2.43}$$

where σ_a is the alternating von Mises stress-amplitude and σ_m is the midrange von Mises stress. Endurance strength F_{ES} is the reduced Marin endurance strength described in Appendix A. B-basis yield F_{yt} is taken from the Metallic Materials Properties Development and Standardization report (MMPDS-11) [72].

For a rotating shaft with a steady applied torque—with alternating normal stress σ_{xxa} due to reversed bending moment M_a and shear τ_{xym} due to the torque T_m—the non-zero von Mises stress components at the surface of the shaft ($r=d/2$) [67]

$$\sigma_a = \left(\sigma_{xxa}^2\right)^{1/2} = \frac{K_f M_a d}{2I} \tag{2.44}$$

and

$$\sigma_m = \left(3\tau_{xym}^2\right)^{1/2} = \sqrt{3}\frac{K_{fs} T_m d}{2J} \tag{2.45}$$

where d is the shaft diameter, I is the area moment of inertia, and J is the polar moment of inertia. Factors K_f and K_{fs} are introduced as fatigue stress concentration factors to address the keyway in the shaft and set conservatively at 2.14 and 2.62 respectively [67].

Substituting eq. (2.44) and eq. (2.45) into the failure criterion eq. (2.43)

$$\left(\frac{n_{sf} K_f M_a d}{2F_{ES} I}\right)^2 + 3\left(\frac{n_{sf} K_{fs} T_m d}{2F_{yt} J}\right)^2 = 1.\,, \tag{2.46}$$

introducing equivalent sectional properties for the shaft

$$\left(\frac{32 n_{sf}}{\pi}\frac{K_f M_a}{F_{ES} d^3}\right)^2 + 3\left(\frac{16 n_{fs}}{\pi}\frac{K_{fs} T_m}{F_{yt} d^3}\right)^2 = 1 \tag{2.47}$$

and solving for the diameter yields [67]

$$d = \left\{\frac{16 n_{sf}}{\pi}\left[4\left(\frac{K_f M_a}{F_{ES}}\right)^2 + 3\left(\frac{K_{fs} T_m}{F_{yt}}\right)^2\right]^{1/2}\right\}^{1/3}. \tag{2.48}$$

Maximum moment M_a and torque T_m were determined for each operating point along the maximum transmitted power-rpm curve for the pinion tooth in bending (orange curve in fig. 2.16).

Equation (2.48) was then used to find the minimum shaft diameter required with safety factor of 1.5. High shaft torque generated at low speeds dictates an increasinly large shaft diamter as the rotor speed approaches zero. The minimum shaft diameter was found to be 18.3 mm, but rounded up to to 19.05 mm to get a standard 0.75 in. shaft.

This diameter was subsequently checked for stiffness to ensure that the slope of the shaft at the bearings and where the teeth mesh does not exceed safe limits. Slope at the bearings was limited to 0.0087 rad while slope at the mesh point of the gears was constrained to less than 0.0005 rad per guidelines in [67]. Displacement of a simply supported beam under any number of point loads F_i at $x=a_i$ can be written by the principle of superposition [76]

$$\Delta = \frac{1}{6lEI}\left[-x\sum_{i=1}^{k} F_i a_i \left(2l - a_i\right)\left(l - a_i\right) + x^3 \sum_{i=1}^{k} F_i \left(l - a_i\right) - l\sum_{i=1}^{k} F_i \left\langle x - a_i \right\rangle^3 \right] . \qquad (2.49)$$

The slope of the shaft is then found by taking the derivitive of the Δ with respect to x

$$\frac{\partial \Delta}{\partial x} = \theta = \frac{1}{6lEI}\left[-\sum_{i=1}^{k} F_i a_i \left(2l - a_i\right)\left(l - a_i\right) + 3x^2 \sum_{i=1}^{k} F_i \left(l - a_i\right) - 3l\sum_{i=1}^{k} F_i \left\langle x - a_i \right\rangle^2 \right]. \qquad (2.50)$$

Angle brackets are used to indicate the use of a unit step function such that

$$\left\langle x - a \right\rangle^2 = \begin{cases} 0 & x < a \\ undefined & x = 0 \\ \left(x - a\right)^2 & x > a \end{cases} . \qquad (2.51)$$

Table 2.4 summarizes the critical design information for a rotor speed of 20 rpm and maximum rated power of 405 W as an example. This is expected to be near the lower limit of turbine operability, below which extremely low conversion efficiencies and outright stall occur. The range of efficiency operating speeds is

explored in detail in Chapter 4. Displacement and slope magnitudes represent the vector sum of the horizontal and vertical components.

Table 2.4: Shaft Calculation Summary

	Variable	Value	Unit	Source
Rotor speed		20	rpm	
Maximum power for pinion bending	P	405	W	
Endurance strength	F_e'	269	MPa	[71]
Marin endurance strength- shaft	F_{ES}	148	MPa	
B-basis yield strength	F_{yt}	572	MPa	[72]
Safety factor	n_{sf}	1.5		
Fatigue stress concentration factor	K_f	2.14		[67]
Fatigue shear stress concentration factor	K_{fs}	2.62		[67]
Maximum moment	M_a	22.44	N-m	
Torque	T_m	38.67	N-m	
Minimum diameter by DE-elliptic	d_m	17.6	mm	
Displacement magnitude at mesh point		0.0039	mm	
Slope magnitude at pinion side	$\theta\|_{x=0}$	0.00034	radians	
Slope magnitude at mesh point	$\theta\|_{x=L_1}$	0.00025	radians	
Slope magnitude at sprocket side	$\theta\|_{x=l}$	0.00035	radians	

Reactions forces for the 20 rpm test case in table 2.4 were summed at each bearing to get a maximum resultant of 1,309 N applied to the ball bearing on the pinion side of the shaft. The required dynamic load rating for the bearings was calculated using the basic rating life equation. Required dynamic load rating C for ball bearings is determined by [67]

$$C = F_r \left(\frac{L_t}{10^6} \right)^{\frac{1}{3}} \tag{2.52}$$

with F_r being the resultant at the bearing and L_t the operational life in millions of cycles. For a minimum operational lifetime of 10 million cycle the required dynamic load rating is 2,820 N. Full ceramic bearings with a dynamic load rating of 3,126 N and speed rating of 1,750 rpm were selected for their resistance to corrosion. Ceramic bearings are also able to operate without a lubricant, which makes them well suited for operating underwater where a lubricant is difficult to maintain [77].

The same exercise performed at the maximum rotor speed of 300 rpm (1,500 rpm at the shaft), for which the pinion bending rating (orange curve in fig. 2.16) allows 4,444 W of power, yields a smaller load of 957 N on the bearings. Given the load rating C=3,126 N, eq. (2.52) can be solved for the bearing lifetime at a rotor speed of 300 rpm. The resulting 387 hours is the minimum expected lifetime for the bearings.

A shorter lifetime is acceptable considering that the test rig isn't expected to operate continuously for an extended duration of time. Bearing lifetime increases significantly at lower speeds which means actual operating time should exceed 387 hours. Figure 2.19 is a plot of bearing lifetime versus rotor rpm according to eq. (2.52) for the maximum power defined by the pinion bending rating, which is also shown on the plot for reference.

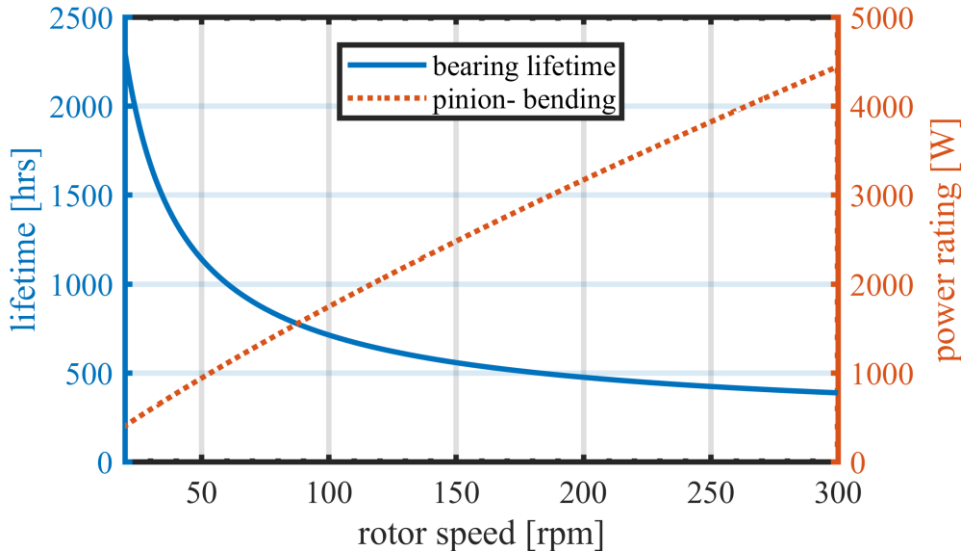

Figure 2.19: The shaft bearing lifetime is plotted as a function of rotor speed. Maximum rated power according to bending strength of the pinion teeth is shown with a dashed line.

2.7 Rotor Bearings

Inside the stator, identified in fig. 2.20, are two sets of cylindrical roller bearings made from Delrin. The thrust bearings bear most the load during operation while the axial bearings serve primarily to maintain rotor alignment. Ideally, predicting failure due to contact stresses in roller bearings would be carried out using the contact endurance strength and one of the fatigue failure theories. However, because this data is not as prevalent for Delrin as with steels the static von Mises failure theory was applied instead with a safety factor of 2.0.

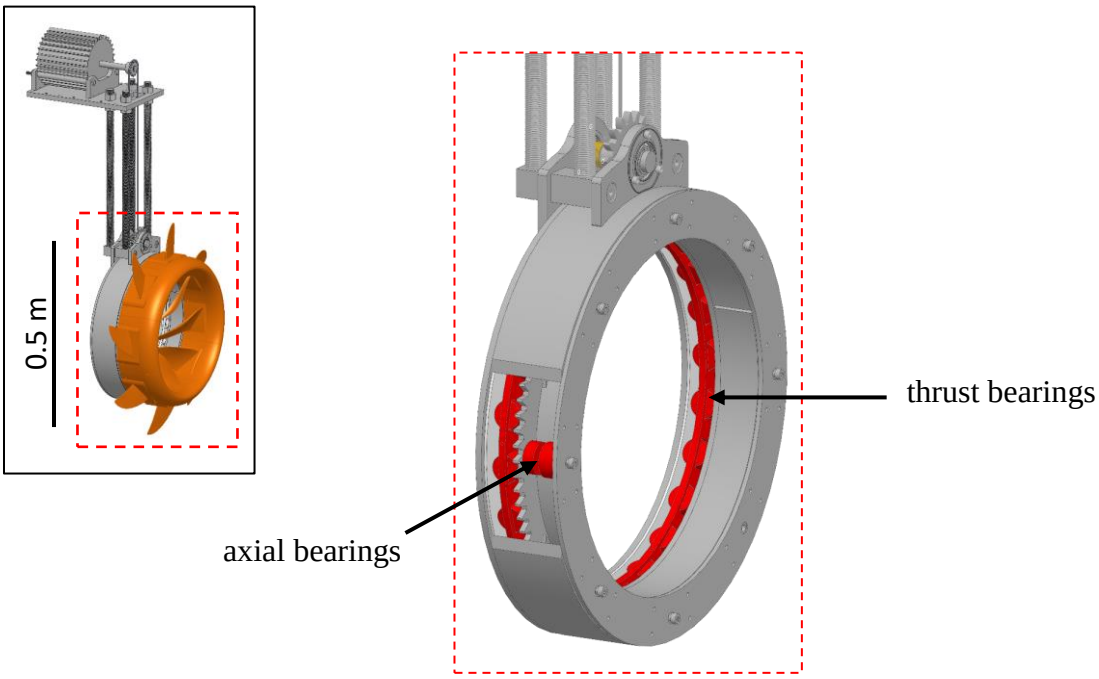

Figure 2.20: A rendering of the turbine highlighting the primary roller bearings.

Hertzian contact stresses were calculated to find the size and number of rollers required. Subscripts A and B are used identify respective properties of the contacting bodies, including the Young's modulus E, the Poisson's ratio ν, the length of the roller L_A. The letter A will always be used to refer to the rolling element while B will refer to the surface it contacts.

The stress state in element A at distance z from the surface of two contacting cylinders, illustrated in fig. 2.10, is calculated along the z-axis as [67]

$$\sigma_x = -2\nu_A P_{\max}\left(\sqrt{1+\frac{z^2}{w^2}} - \left|\frac{z}{w}\right|\right) \tag{2.53}$$

$$\sigma_y = -P_{\max}\left(\frac{1+2\frac{z^2}{w^2}}{\sqrt{1+\frac{z^2}{w^2}}} - 2\left|\frac{z}{w}\right|\right) \tag{2.54}$$

$$\sigma_z = -P_{\max}\frac{1}{\sqrt{1+\frac{z^2}{w^2}}} \tag{2.55}$$

where the maximum surface pressure P_{max} is defined by eq. (2.23) and the half-width of the contact area w is again

$$w = \left[\frac{2F}{\pi L}\frac{\left(\frac{1-\nu_A^2}{E_A}+\frac{1-\nu_B^2}{E_B}\right)}{\left(\frac{1}{d_A}+\frac{1}{d_B}\right)}\right]^{1/2} \tag{2.56}$$

Maximum deformation of the roller along the z-axis can also be calculated according to Hertz's theory [77]

$$\Delta z = \frac{2Fr_A}{\pi L_A E_{eq} r_{eq}}\left[\ln\left(\frac{2\pi L_A E_{eq} r_{eq}}{F}\right)-1\right] \tag{2.57}$$

where the equivalent modulus E_{eq} is defined as

$$E_{AB} = 2\left(\frac{1-\nu_A{}^2}{E_A}+\frac{1-\nu_B{}^2}{E_B}\right)^{-1}. \tag{2.58}$$

The equivalent contact radius r_{eq} is defined according to the geometry of the surface in contact with the bearing. In the case of the thrust bearing where roller contacts a flat surface, illustrated in fig. 2.21, the diameter d_B is effectively infinite and the equivalent contact radius is equal to the radius of the roller (r_{eq}=r_A).

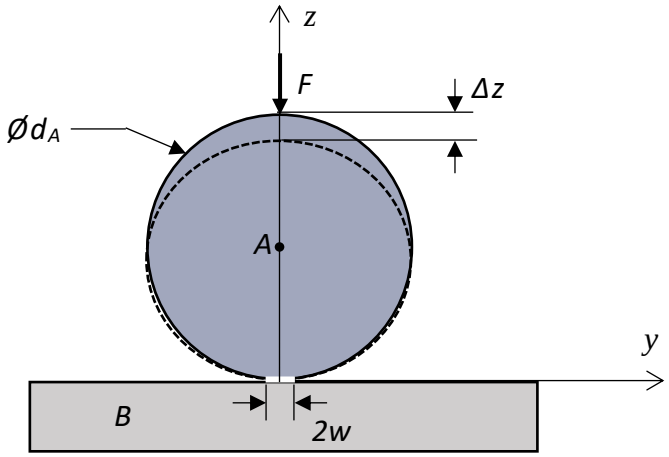

Figure 2.21: Cross-section of cylinder in contact with flat surface.

For the concave contact surface of the radial bearings depicted in fig. 2.22, equivalent radius is determined by the sum of curvatures [77]

$$\frac{1}{r_{eq}} = \frac{1}{r_A} + \frac{1}{r_B} \ . \tag{2.59}$$

The diameter and radius of the concave body are assigned negative values in eq. (2.56) and (2.59).

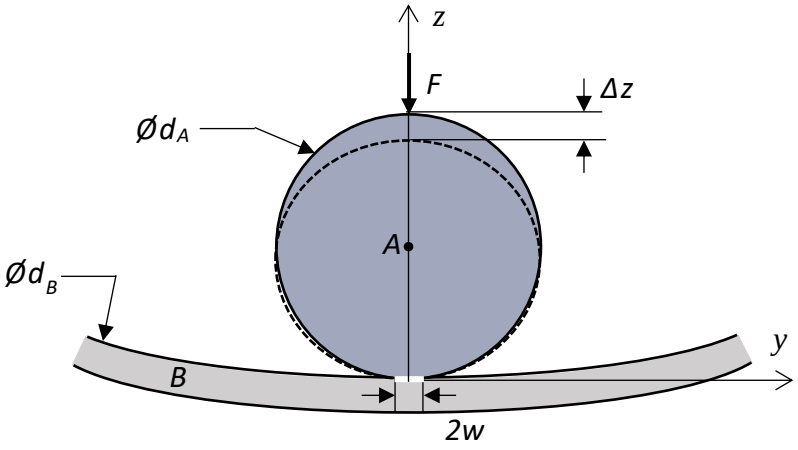

Figure 2.22: Cross-section of cylinder in contact with concave surface.

24 thrust rollers—with a diameter of 24 mm and an effective length of 22 mm—were included to limit the deflection under load and maintain proper gear mesh alignment. The maximum thrust load on the turbine was taken as the approximate drag generated if the turbine were to lock rotation with water flowing at 4 m/s. For a conservative estimate the drag coefficient for a three-dimensional disk, C_d=1.17 [78] is used with the rotor area of the open-centered test bed system (A=0.24 m^2)

$$D = \frac{1}{2}\rho C_d A U^2 \tag{2.60}$$

which resulting in a design capacity of 2,253 N. Force F on each thrust roller is then the total drag divided by the number of rollers N_t

$$F = \frac{D}{N_t}\ , \tag{2.61}$$

which is approximately 94 N.

The maximum von Mises stress is 10.0 MPa at 0.11 mm below the surface of the roller. Von Mises stress along the z-axis within the roller is shown in fig. 2.23. Given the allowable yield strength of 34.5 MPa [53] there is large margin of safety (MS=2.5) in the final design. This extra margin is accepted as a buffer against fatigue failure or unforeseen shock loads. Maximum displacement in the z-direction due to roller deformation is limited to a negligible 0.004 mm.

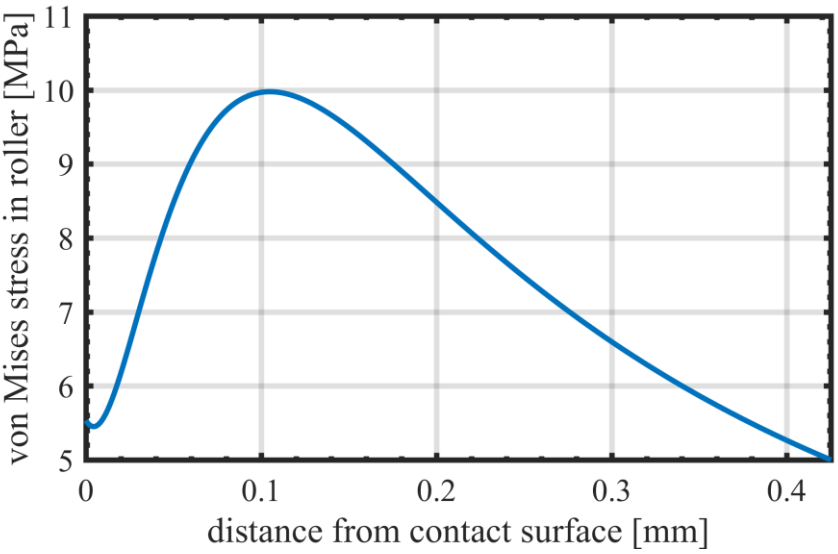

Figure 2.23: Von Mises stress within the thrust rollers plotted along the z-axis (perpendicular to the contact surface).

The radial rollers keep the rotor aligned by reacting the radial component W_r, as shown in fig. 2.6, of the load transmitted by the annular gear. Assuming no load distribution amongst rollers, the force on each radial roller is

$$F = W_r = W_t \tan\phi_p \tag{2.62}$$

where tangential component W_t is found by eq. (2.3). Maximum tangential load was extracted from the speed-power conditions of the pinion bending rating (orange curve in fig. 2.16) to determine the maximum radial component of 409 N. This resulted in a peak von Mises stress of 21.3 MPa at a depth of 0.32 mm inside the roller and a minimum MS of 0.62. Von Mises stress near the surface is plotted in fig. 2.24. Radial roller deformation Δz at 409 N is 0.016 mm, which should minimally impact the gear mesh. A summary of all the rotor bearing design variables is provided in table 2.5.

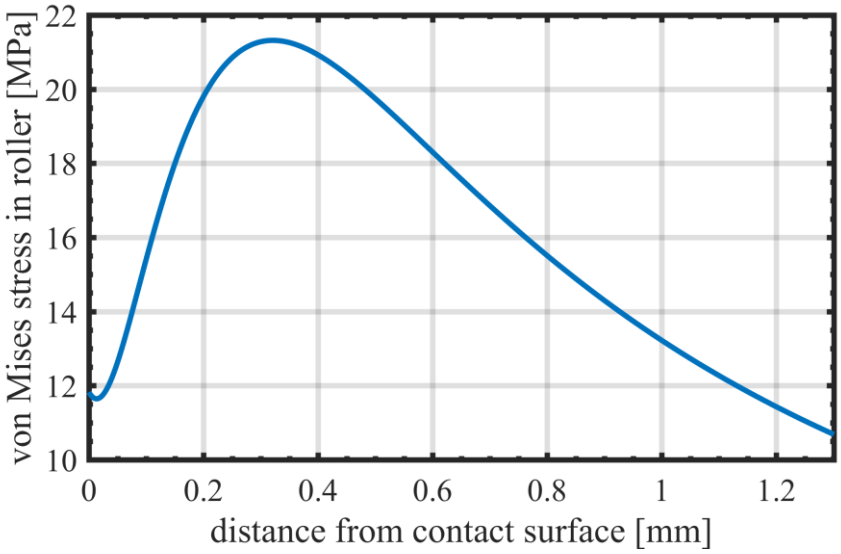

Figure 2.24: Von Mises stress within the radial rollers plotted along the z-axis (perpendicular to the contact surface).

Table 2.5: Rotor Bearing Data

	Variable	Value	Unit	Source
Young's modulus- 316 SS	E_B	186	GPa	[72]
Poisson's ratio- 316 SS	v_B	0.27		[72]
Young's modulus- Delrin	E_A	2.8	GPa	[53]
Poisson's ratio- Delrin	v_A	0.35		[53]
Yield strength- Delrin	F_{yt}	69	MPa	[53]
Safety factor	n_{sf}	2		
Drag load	D	2,253	N	
Radial load	W_r	409	N	
Number of thrust rollers	N_r	24		
Diameter thrust rollers	d_r	24.1	mm	
Length thrust rollers	L_r	22.9	mm	
Number of radial rollers	N_r	8		
Diameter radial rollers	d_r	31.8	mm	
Length radial rollers	L_r	15.2	mm	
Inner diameter of stator	d_s	-392.7	mm	

2.8 Generator Selection

This section briefly details the electrical generator for test rig modeled in fig. 2.25. The generator serves to convert mechanical power from the rotor into electrical power. A load band bank is attached to the generator to serve as a dummy load during testing. Rotor speed can be controlled by changing the size of the load, which is a critical function for investigating the overall performance of the rotor and its blades. A commercial permanent magnet alternator (PMA), specifically designed for low-rpm operation on a small wind turbine, was selected based on cost, availability, and rated output capacity.

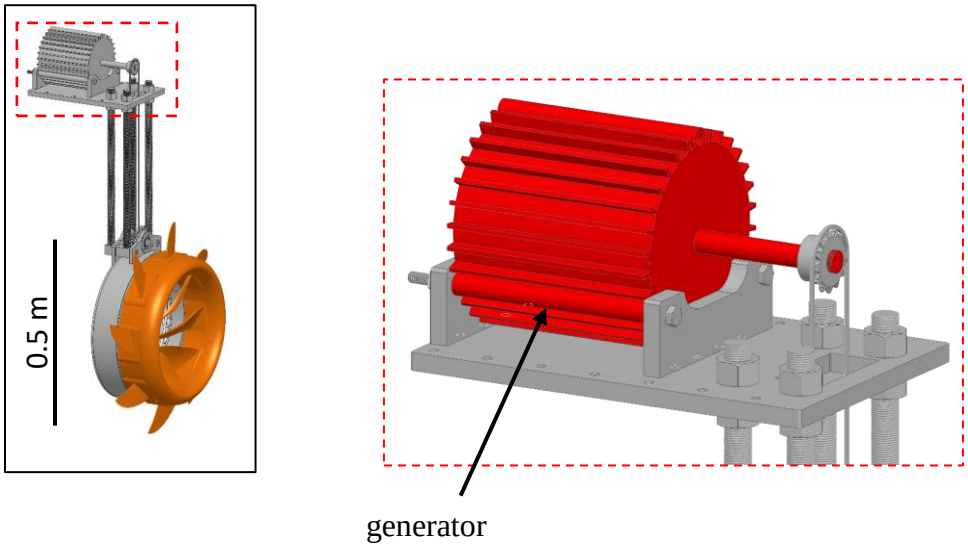

Figure 2.25: A rendering of the turbine highlighting the generator.

It generates three-phase AC at speeds up to 3000 rpm. The housing is made from a combination of stainless-steel and aluminum for outdoor operation. Sealed bearings and an epoxy coated rotor provide additional resistance against corrosion.

The generator is rated for a maximum continuous output of 2 kW. This covers flow speeds up to 3.5 m/s at a conversion efficiency of 40%. It also includes the entire wear free operating regime defined by the gear contact rating (fig. 2.12) under which most of the testing will occur. At more extreme flow speeds the speed of the rotor can be managed to actively reduce the efficiency. If the conversion efficiency is reduced to 26% then the turbine can operate in flows up to 4 m/s before exceeding 2 kW.

Chapter 3. Material Performance Studies

The additive manufacturing (AM) method known as fusion deposition modeling (FDM) was used to produce the turbine blades and cowling. The following chapter provides a brief introduction to FDM and an evaluation of two materials, PLA and ABS, that are common to the process. A detailed study of PLA is conducted to establish its mechanical properties. These properties are used to predict the elastic response of FDM manufactured coupon using classical laminate theory. The relative anisotropy, specific strength, and specific stiffness of FDM produced PLA components are compared with other engineering materials for perspective.

3.1 Background

The prototype turbine blades—intended for short duration performance studies—can be manufactured using a variety of processes including machining, molding, casting, or additive manufacturing. Both casting and molding require a mold of the blade, which is costly and time consuming for fundamental research and development. Any change to the blade design entails creating new molds. Machining is more attractive for one off production runs, but machine time is costly and cut-away material is wasted. Additive manufacturing processes are well suited for research and development with reduced lead times that facilitate rapid prototyping. AM inherently makes efficient use of raw material, requires no additional tooling, and provides greater flexibility than cut-away machining in the geometry it can

produce [79]. However, AM material costs can be significant compared to the cost of raw materials for the other manufacturing processes [80].

Fusion deposition modeling (FDM) is a type of AM in which a heated thermoplastic material is extruded to construct the part layer by layer. FDM machines, or printers, have demonstrated accuracies up to ±0.05 mm [79]. Moderately priced materials, ranging from 15-50 $/kg [80], available for FDM make it a viable option for production of prototype turbine blades. Before designing the blades, it is necessary to establish accurate material properties for parts manufactured with FDM.

Many interrelated factors influence the material properties for an FDM part, though infill orientation, build orientation, layer height, and percent infill are most commonly studied [81–86]. Figure 3.1A is an illustration of single FDM part layer. The outline that maintains layer geometry is generally referred to as the shell with everything inside the shell called the infill. Infill orientation can describe either the pattern or angle of infill material with respect to the printer axes, which for this discussion is taken to be the x-axis. Build orientation references the parts orientation with respect to the print axis. Examples of build orientations in the x-direction (1), y-direction (2), and z-direction (3) are given in fig. 3.1B. Layer height, demonstrated in fig. 3.1C, is essentially print resolution. Smaller layer heights allow for greater dimensional accuracy at the cost of increased build time. Infill percentage controls the density of the finished part. Figure 3.1D shows the difference between 50% infill and 100% infill for a single layer. Weight and material cost savings can be realized by strategically reducing the density, though for this work infill percentage is set to 100% to produce a solid part.

Other parameters affect part strength but may be less meaningful to characterize because they vary based on the technical specifications of the printer. For example, the optimal extrusion temperature can be difficult to compare across low cost 3D printers as the location and calibration of the thermistor measuring extruder temperature can vary [81]. The present lack of a standard test for measuring the material properties of FDM materials, allowing for variation in both coupon geometry and the previously described process parameters, has led to a wide range in the limited properties reported in literature.

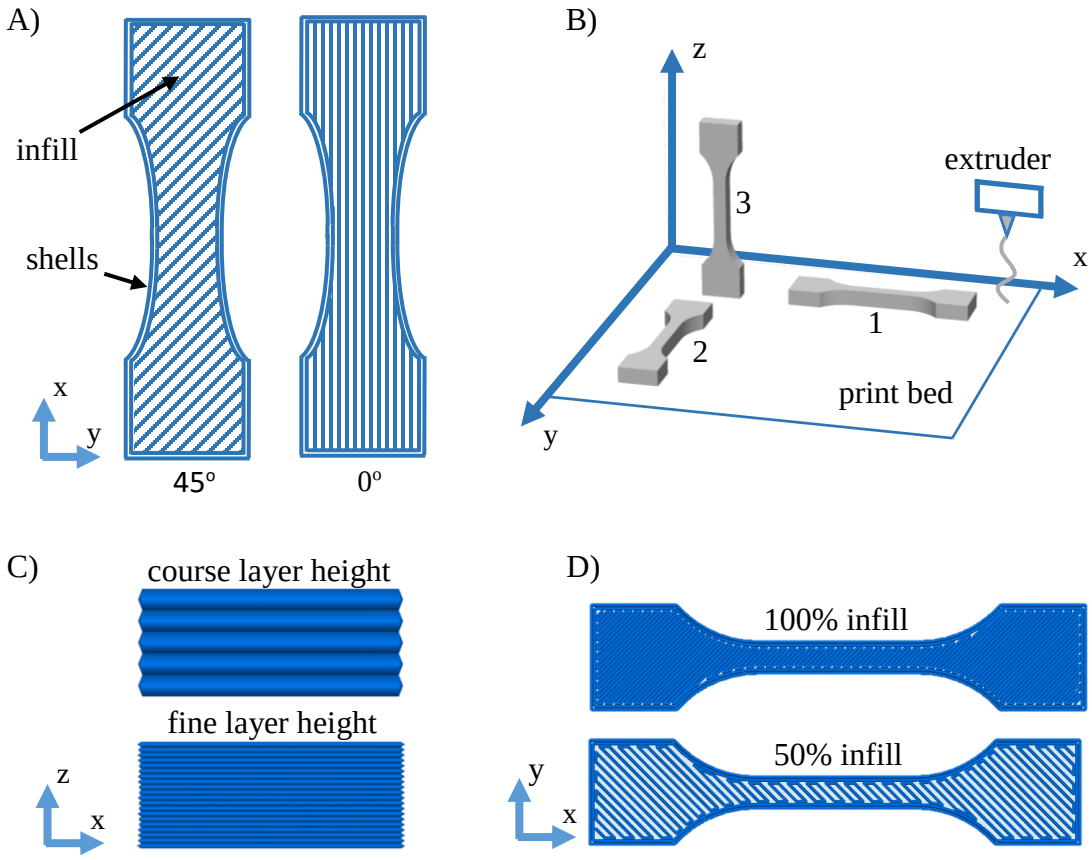

Figure 3.1: A) Raster or infill orientation, B) print orientation, C) layer height, and D) infill percentage all shown with respect to the printer axes.

Polylactic acid (PLA) has become a popular material for use in low cost FDM printers due to a convenient melting temperature between 150 ˚C and 160 ˚C [87], which is low enough to work with in consumer printers while still high enough to maintain form under normal environmental conditions [81]. Studies investigating the ultimate tensile strength of PLA have found average values ranging from 31.43 MPa to 56.6 MPa and elastic moduli from 1,246 MPa to 3,368 MPa [81,83,84].

PLA is a biodegradable thermoplastic which is fine for prototype development, but will require some type of protective coating to prevent degradation from extended environmental exposure [88]. In 13 ˚C water the onset of material fragmentation, in which bits of material are solubilized, occurs around 24 months and biodegradation follows at 48 months [89]. This process is known to erode mechanical properties including yield stress, yield strain, and ultimate strain [90]. Acidic environments are known to accelerate degradation [91] but no sources were found discussing the specific effects of basic (salt water) environments.

Additives to color PLA have been shown to affect materials properties. In a study comparing the ultimate strength and maximum strain of natural, black, grey, blue, and white PLA the natural PLA exhibited superior performance [92]. Grey performed the worst with the maximum strength declining by 11% and the maximum strain declining by 16%. As compared to the natural PLA, blue had the greatest strength with only a 5.3% reduction and white exhibited the greatest maximum strain with a 5.5% drop.

Acrylonitrile butadiene styrene (ABS) is another common material choice, though it is softer and limited in strength compared to PLA. Previous studies have

established a range for the ultimate tensile strength of ABS under different print conditions from 10 MPa to 28.5 MPa with elastic moduli between 1,000 MPa and 1,807 MPa [81,82,93,94]. The ultimate strength of ABS is a limitation in the current application. Despite concerns with long-term environmental stability, PLA is currently a more desirable build material for the load bearing structures of a hydro turbine due to its greater stiffness and strength.

In our current project, three different printers were used to establish materials properties. PLA specimens were printed on a Makerbot Replicator 2 and a HICTop Prusa I3 desktop printer. ABS specimens were printed using a Stratsys Dimension SST 1200es. Tensile and compressive tests were performed according to ASTM D638-14 and ASTM D695-10 standards to establish process specific material properties. Standard print parameters were 100% infill, 0.25 mm layer height (considered a medium resolution), and a range from 0 to 5 shells. Coupons were all manufactured using a build orientation that aligned the load axis of the specimen with the x-axis of the print bed as shown in fig. 3.1B-1.

3.2 A Comparison of PLA and ABS Material Properties

A baseline series of tensile tests were performed on un-extruded PLA (orange) and ABS (green) filaments with a 1.75 mm diameter to directly compare their respective mechanical properties. The tests were conducted on an MTS Criterion-43 with a 30 kN load cell. Samples were displaced at a rate of 4.8 mm/min. Displacement

was measured with an extensometer until the load peaked, at which point the test was paused and the extensometer was removed. Loading was subsequently resumed until failure. Post-processing was conducted in Matlab. Modulus was determined using a least-square fit of the initial linear region of the stress-strain response. Yield strength was identified using a 0.2% strain offset.

Stress-strain curves for the PLA and ABS filaments are shown together in fig. 3.2 with individual plots and fitted modulus lines provided in Appendix B. Strength and elastic modulus results are summarized in table 3.1. The PLA filament had a 41% higher ultimate strength, though calculated yield strengths were roughly equal, while also exhibiting a 45% greater elastic modulus.

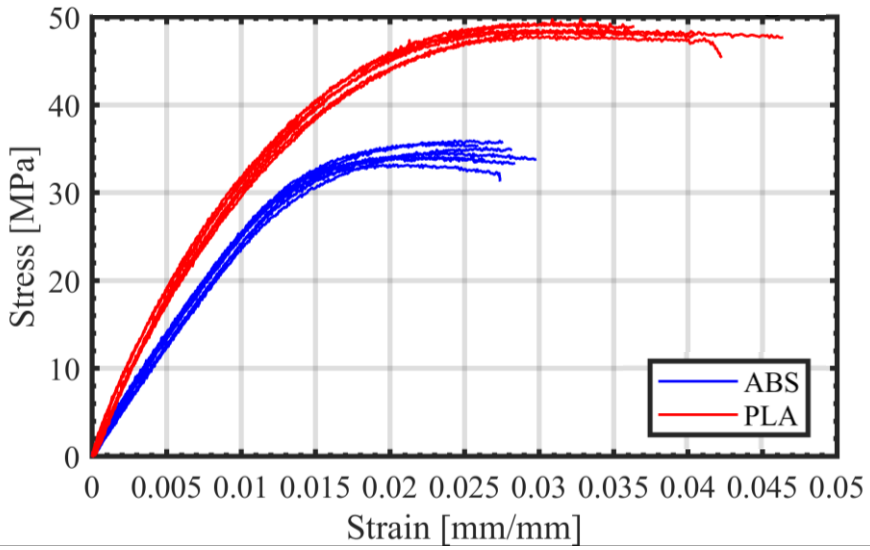

Figure 3.2: Stress-strain curves for PLA (red) and ABS (blue) filaments.

Table 3.1: Filament Properties of ABS and PLA [MPa]

A) ABS- 7 Samples	Minimum	Average	Maximum	Standard Deviation	B-Basis
Yield Strength	26.7	29.3	31.5	1.8	24.4
Ultimate Strength	33.2	34.7	36.0	1.0	32.1
Modulus	2426	2710	3098	269	

B) PLA- 6 Samples	Minimum	Average	Maximum	Standard Deviation	B-Basis
Yield Strength	26.3	29.9	32.2	2.0	23.8
Ultimate Strength	47.8	48.8	49.8	0.7	46.7
Modulus	3624	3928	4449	301	

Coupons were also printed in both PLA and ABS to compare their relative properties. Print orientation was held constant and the default slicers for each printer were allowed to determine the infill orientation. Angles are all referenced to the longitudinal (or specimen loading) axis. The resulting layer-by-layer infill orientation generated by MakerWare, which comes packaged with the MakerBot printer, for the tensile PLA coupons was [45/-45/45/-45/90/0/90/0/90/-45/45/-45/45] and will be abbreviated as $[\pm 45_2/90/0/\overline{90}]_s$. CatalystEX, the Stratsys printer's default operating software, generated an angle-ply stack up [45/-45/45/-45/45/-45/45/-45/45/-45/45/-45/45] for the infill orientation which will be abbreviated as $[\pm 45_3/\overline{45}]_s$. Cylindrical compression specimens, stipulated in ASTM D695-10, were also printed on their side such that the x-axis of the printer, and subsequently the direction of most continuous filaments, would align with the loading axis [95]. Infill orientation for the PLA specimens alternated 0/90 through the thickness while orientation for the ABS coupons alternated +45/-45 through the thickness.

In lieu of a built-in heated plate, an external heating element was used to warm the build plate for prints on the MakerBot. This significantly improves first layer adhesion. The heater also helped maintain a stable temperature within the build chamber to reduce warping of the long tensile coupons and prevent them from curling off the build plate.

Print quality was excellent for the initial group of PLA tensile coupons pictured in fig. 3.3. The side of compressive PLA samples touching the build plate proved to be too steep of an overhanging geometry for the MakerBot to print without support material. As shown in fig. 3.4 the resulting print fidelity suffered. It is therefore assumed that the compressive strengths found for this orientation are conservative, but also representative of the FDM process for this type of geometry. The print quality of the ABS samples from the commercial Stratsys machine (figs. 3.3-3.4) was markedly better than the Makerbot's, though this is unsurprising given the substantial difference in cost. Micrographs of the fractured coupon cross-sections in fig. 3.5 and fig. 3.6 further demonstrate the difference in layer composition and print quality between the two machines.

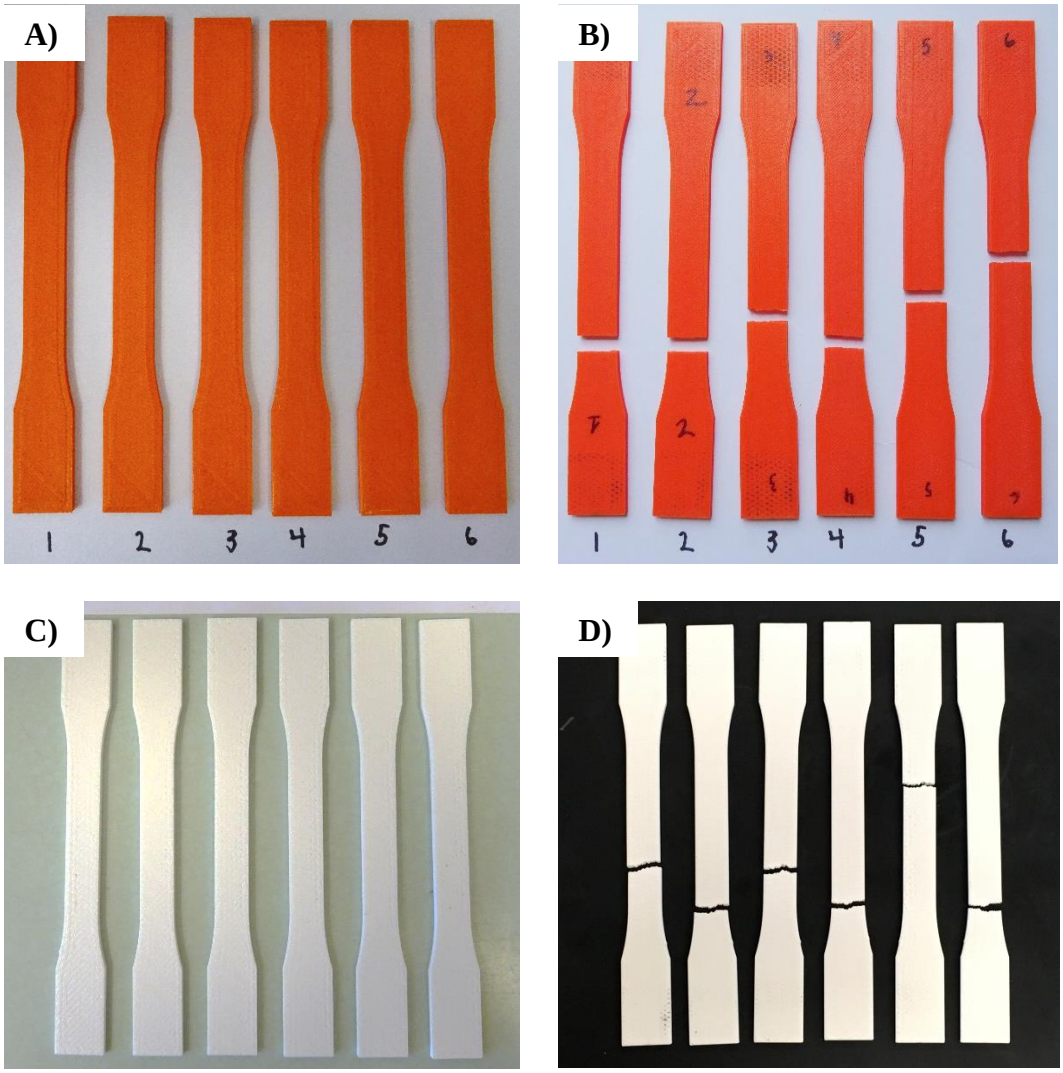

Figure 3.3: PLA coupons for tension tests a) before testing and b) after failure. Samples that failed near the clamping fixture had ultimate strength values comparable to those where the sample broke in the middle of the narrow section. ABS coupons a) before and b) after testing. Failure occurred at or near the clamping fixture for nearly all samples with this geometry.

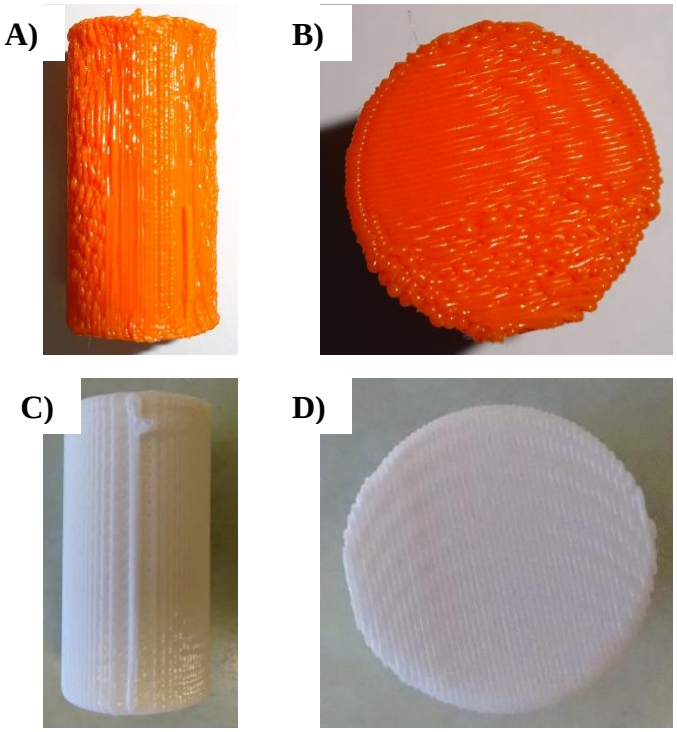

Figure 3.4: PLA samples for compression tests showing A) the plate facing side and b) the free face. Note the rough quality on the lower face of B). Similarly, ABS samples showing C) plate side and D) the free face print quality.

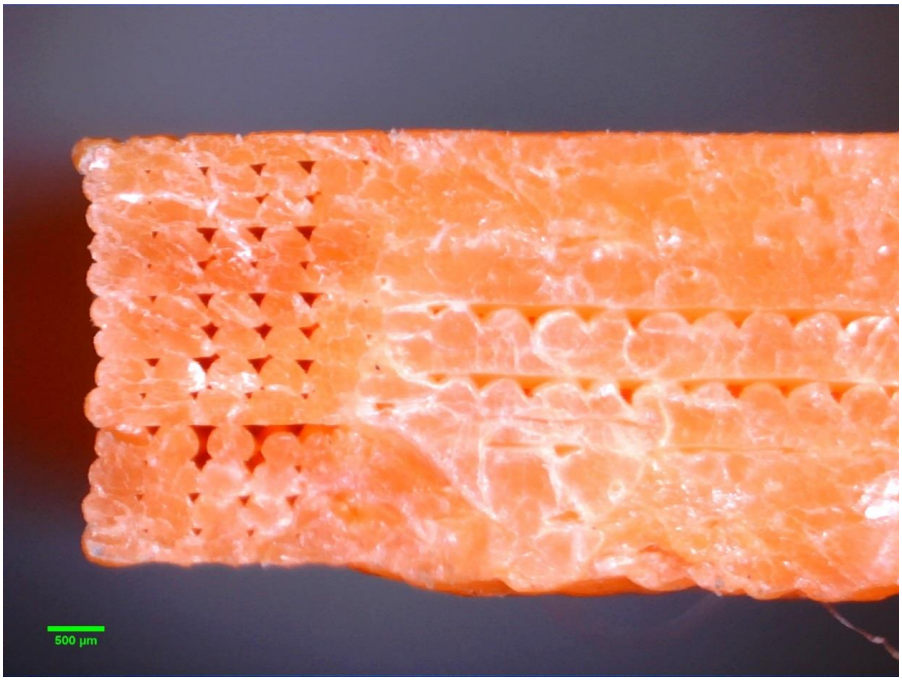

Figure 3.5: Micrograph of PLA coupon after testing to failure. Shell layers are visible on the left side. 0 and 90-degree layers are clearly visible in the center.

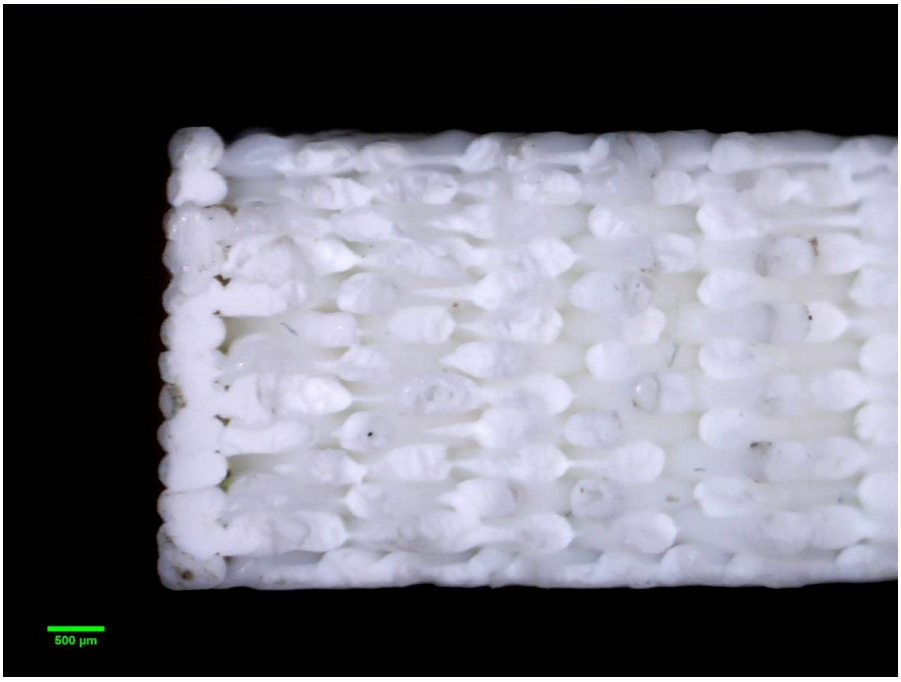

Figure 3.6: Micrograph of ABS coupon after testing to failure. A single shell layer is visible on the left side. Internal layers alternate at +45 and -45 degrees.

Coupons were displaced at a rate of 5 mm/min. It's noted that the differing infill orientation and shell number used for each material have a definite effect on the properties so the results in table 3.2. can only be used for approximate comparison. Figures 3.7 and 3.8 show tensile stress-strain curves overlaid with the fitted modulus and yield strength for PLA and ABS respectively. Similarly, figs. 3.9 and 3.10 present stress-strain curves from the compression samples. PLA was found to be significantly stronger and stiffer than ABS. PLA was chosen for further testing to determine the relative anisotropy of the printed parts.

Table 3.2: Preliminary Coupon Testing

Material	PLA	PLA	ABS	ABS
Print Orientation	x axis	x axis	x axis	x axis
Printer	Makerbot Replicator 2	Makerbot Replicator 2	Stratsys Dimension SST 1200es	Stratsys Dimension SST 1200es
Layer Orientation	$[\pm 45_2/90/0/\overline{90}]_s$	$[0/90]_{20s}$	$[\pm 45_3/\overline{45}]_s$	$[\pm 45]_{23s}$
Test Type	tension	compression	tension	compression
Yield Strength [MPa]	49.56	76.95	28.97	43.11
Ultimate Strength [MPa]	57.08	82.37	33.5	50.53
Modulus [MPa]	3,303	1,896	2,188	1,523
Crosshead Strain at Ultimate [mm/mm]	0.0217	0.0641	0.0231	-

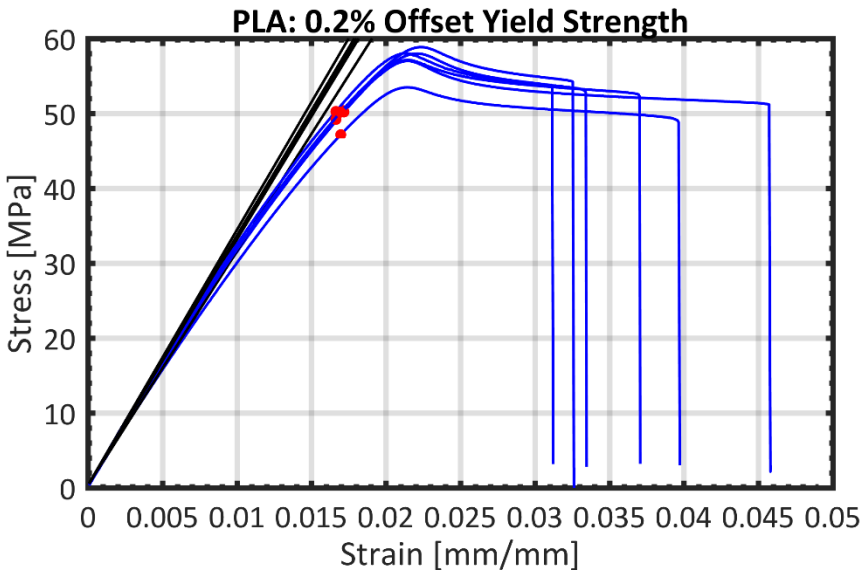

Figure 3.7: Stress-strain curves for 6 PLA $[\pm 45_2/90/0/\overline{90}]_s$ coupons overlaid for comparison. As above, the fit modulus lines are plotted in black and the 0.2% offset yield is noted with a pink dot.

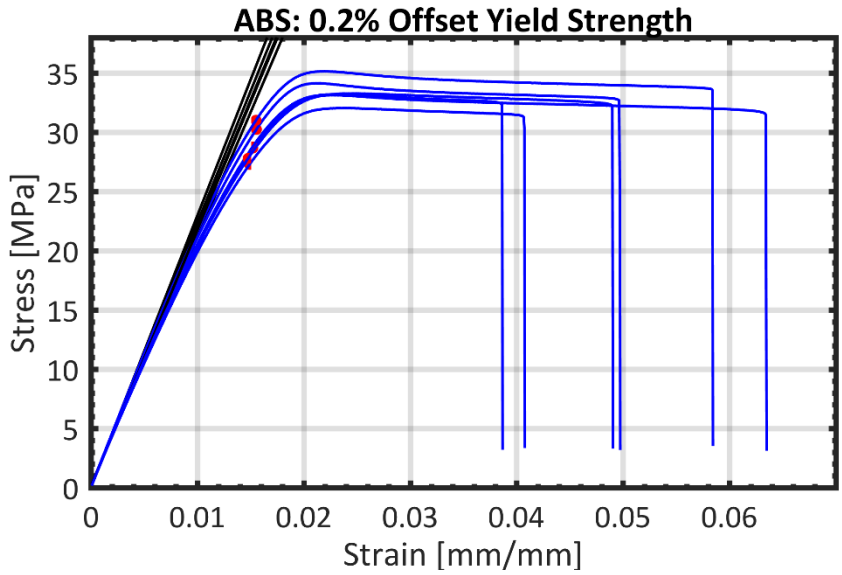

Figure 3.8: Stress-strain curves for 6 $[\pm 45_3/\overline{45}]_s$ ABS coupons overlaid for comparison. As above, the fit modulus lines are plotted in black and the 0.2% offset yield is noted with a pink dot.

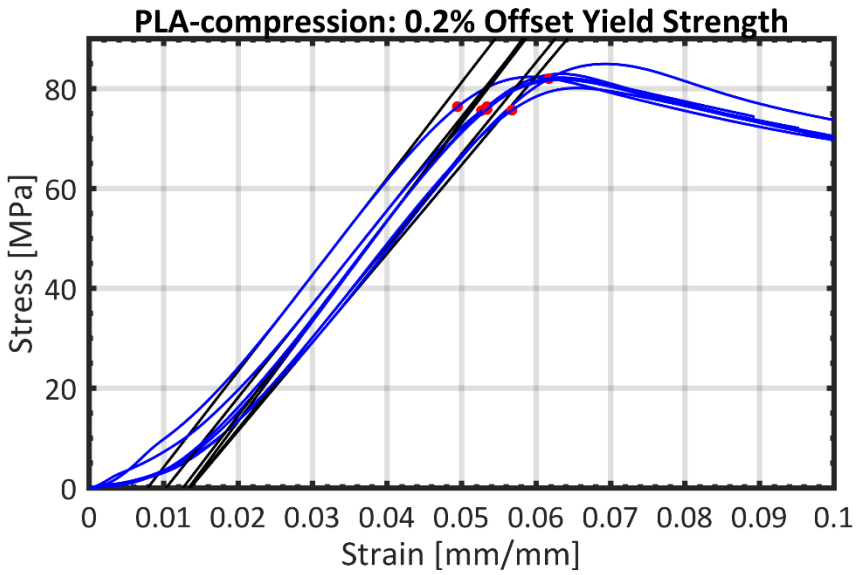

Figure 3.9: Stress-strain curves for compression specimens with $[0/90]_{20s}$ infill orientation and 5 shells overlaid for comparison. Fitted modulus lines are plotted in black and the 0.2% offset yield is noted with a pink dot.

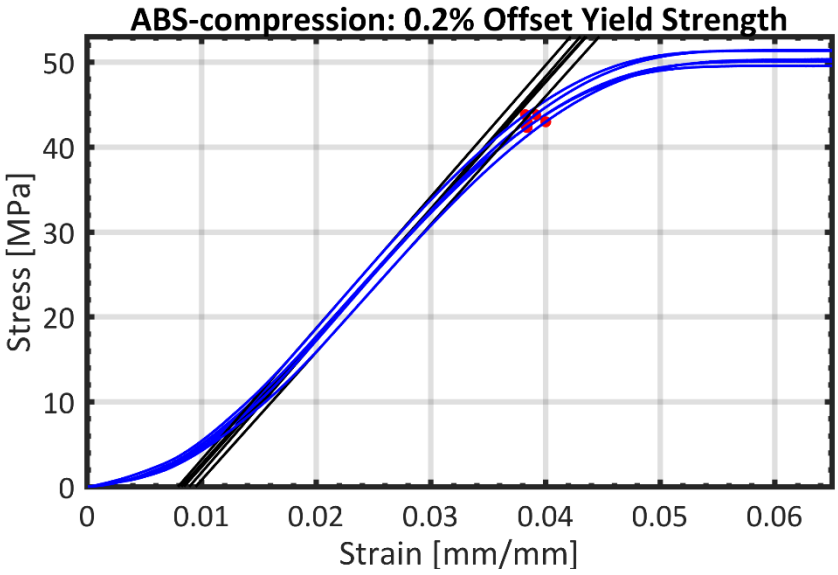

Figure 3.10: Stress-strain curves for ABS specimens with $[\pm 45]_{23s}$ infill orientation and 1 shell overlaid for comparison. Fitted modulus lines are plotted in black and the 0.2% offset yield is noted with a pink dot.

3.3 Infill Orientation

Anisotropy in FDM parts is anticipated due to the nature of the manufacturing process, which builds the part layer by layer at different angles with respect to the structural frame. As a result they exhibit anisotropic behavior and efforts to accurately model them typically employ classical laminate plate theory (CLPT) [82,85,93,96]. Additional coupons were printed with 0, 45, 60, and 90-degree infill orientations to further develop in-plane properties of printed 3-D printed PLA. Prints were made with 100% infill and 0.25 mm layer height using both the Makerbot and the HICTop printers. Coupons were again aligned with the x-axis of the print bed. Angle specimens did not have 0-degree outer shells as demonstrated by the coupon models in fig. 3.11. Simplify3D was used as the slicer to control infill orientation on a layer by layer basis.

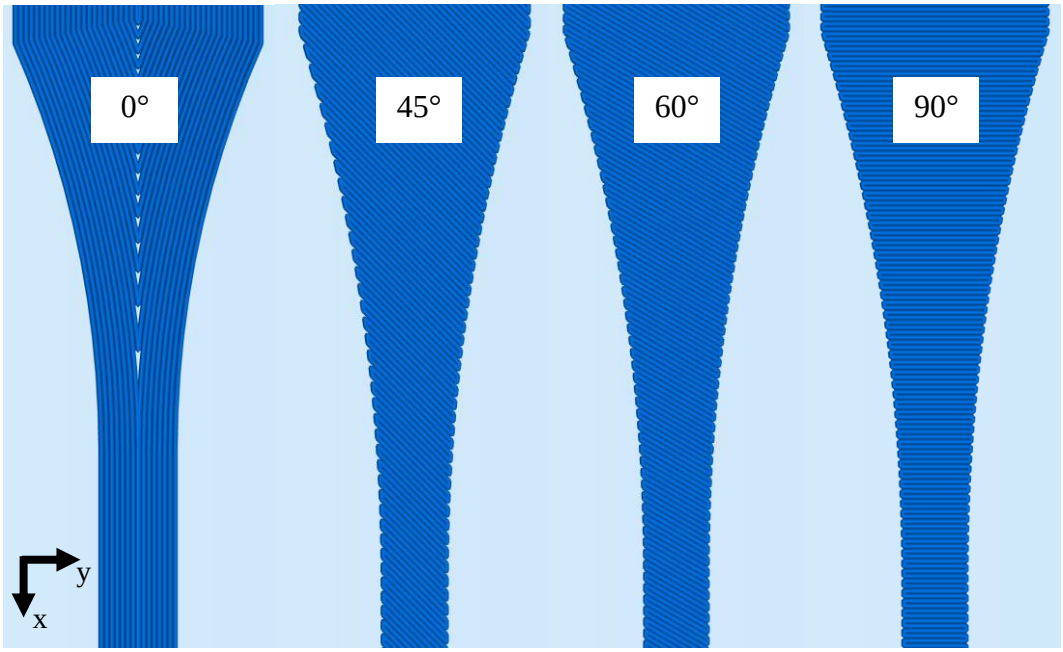

Figure 3.11: Model representations of the different infill orientations as printed for coupon testing.

There was a consistent problem, as evidenced in fig. 3.3, with coupons breaking at the start of the filleted portion. Stress concentrations are generated along the edges of the sample when adjacent filaments don't fully fuse. A modified coupon geometry—similar to the one used in Lanzotti et al. [84]—was developed to alleviate this problem. Large conic fillets were added to the ASTM D638-14 type II sample [97]. The successful geometry is dimensioned in fig. 3.12. Subsequent tests resulted in reliable failure within the constant width section of the coupons. Figure 3.13 exhibits a typical set with the modified geometry that failed within the gauge section.

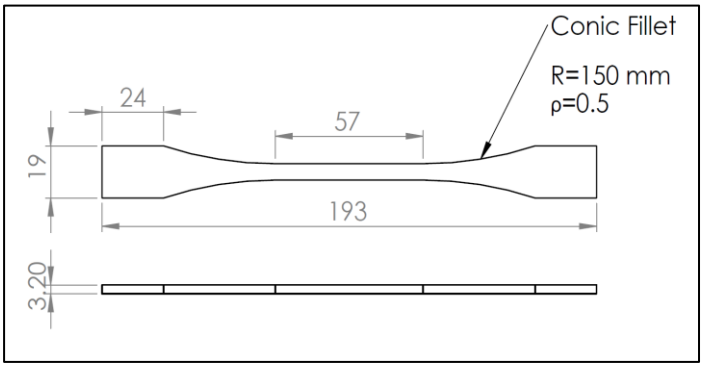

Figure 3.12: Dimensions in mm for modified ASTM coupons that achieved reliable failure in the desired constant width region.

Figure 3.13: Failed samples of modified geometry. Note that they all broke within the 25 mm gauge region.

A 25 mm contact-type extensometer was used to measure axial strain in all but a subset of the 90-degree coupons. Three of the seven 90-degree test runs were conducted without the extensometer. The strain data for these samples were adjusted to account for the added stiffness in the crosshead measurement and included in properties summary. Reported average strain to failure for the 90-degree coupons excludes the three samples in which the extensometer was not used since the moduli-based adjustment doesn't accurately capture the plastic behavior. The justification for this adjustment is presented in section 3.4, with supporting data in Appendix D. B-basis values are reported for yield strength and failure strength, along with all other relevant properties, in table 3.3. Compiled stress-strain curves for each sample angle are presented in figs. 3.14-3.18. Individual plots are provided in Appendix C.

Table 3.3: Tensile Properties of PLA Specimens Printed on Makerbot and HICTop Printers

A)		Yield Strength [MPa]					Strain	Modulus [MPa]
Infill [degrees]	Number of Samples	Min.	Avg.	Max.	SD	B-Basis	% to Yield	E_x
0	5	53.99	55.58	57.35	1.10	51.85	1.84	3,396
45	8	28.25	31.13	33.15	1.67	26.82	1.39	2,626
60	9	29.33	33.08	35.59	1.87	28.49	1.37	2,815
90	7	23.58	27.71	31.78	2.85	19.86	1.25	2,618

B)		Ultimate Strength [MPa]					Strain
Infill [degrees]	Number of Samples	Min.	Avg.	Max.	SD	B-Basis	% to Failure
0	5	56.79	58.56	60.95	1.61	53.07	6.41
45	8	31.25	35.09	37.91	2.15	29.53	2.76
60	9	32.58	37.03	39.74	2.16	31.73	2.79
90	7	26.20	30.94	35.07	3.20	22.12	2.05*

*Based on 4 samples tested with extensometer

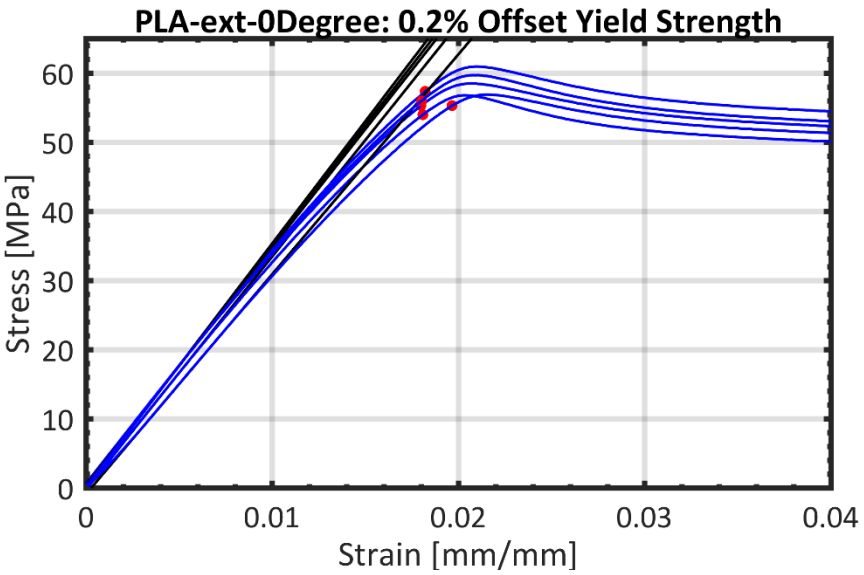

Figure 3.14: Stress-strain curves of all 0-degree coupons overlaid for comparison. Fitted modulus lines are plotted in black and the 0.2% offset yield is noted with a pink dot.

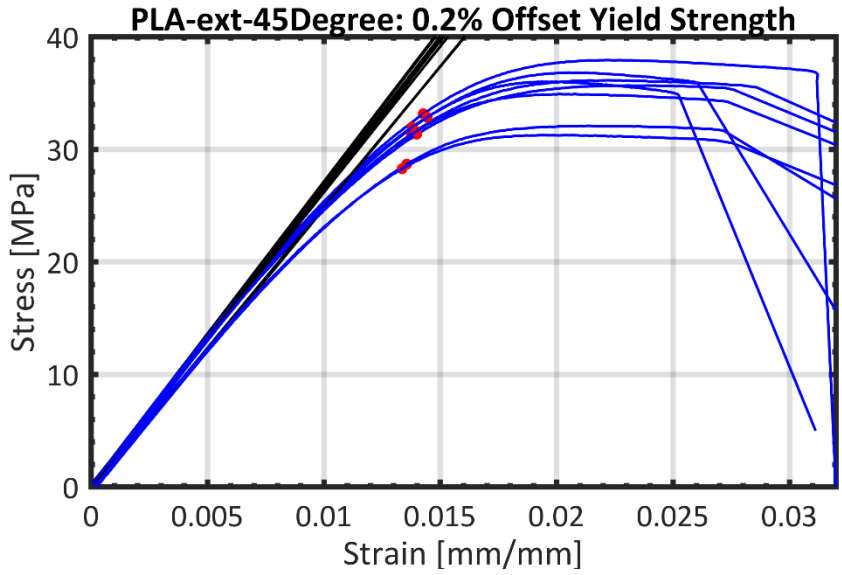

Figure 3.15: Stress-strain curves of all 45-degree coupons overlaid for comparison. Fitted modulus lines are plotted in black and the 0.2% offset yield is noted with a pink dot.

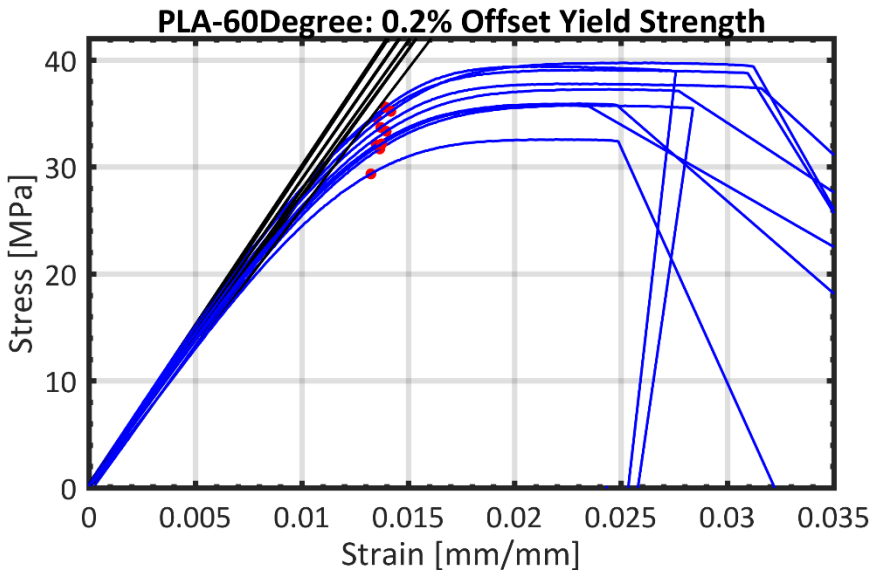

Figure 3.16: Stress-strain curves of all 60-degree coupons overlaid for comparison. Fitted modulus lines are plotted in black and the 0.2% offset yield is noted with a pink dot.

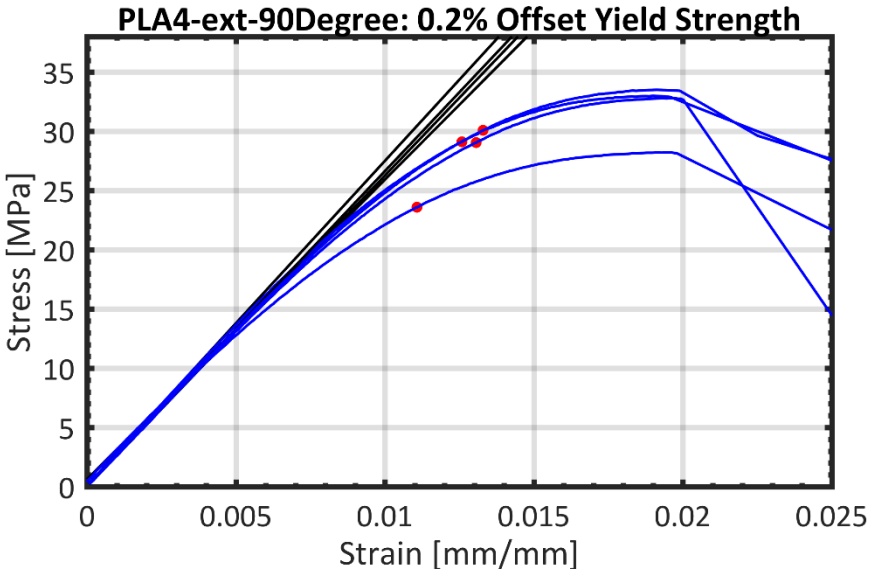

Figure 3.17: Stress-strain curves of all 90-degree coupons with extensometer derived strains overlaid for comparison. Fitted modulus lines are plotted in black and the 0.2% offset yield is noted with a pink dot.

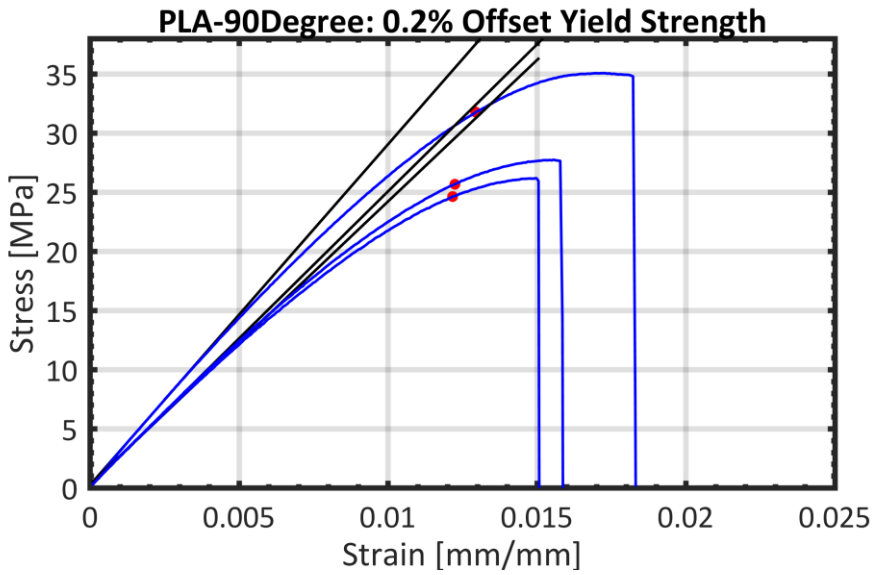

Figure 3.18: Stress-strain curves from of all 90-degree coupons with adjusted crosshead derived strain overlaid for comparison. Fitted modulus lines are plotted in black and the 0.2% offset yield is noted with a pink dot.

Elastic modulus in the direction of loading E_x is plotted for each infill orientation in fig. 3.19 with error bars indicating the extrema. Modulus declined by 23% as the infill orientation was rotated from 0 degrees to 45 degrees. There is a moderate increase in the average modulus between 45 degrees and 60 degrees, though it's not thought to be significant given the large overlap in measured data, followed by the minimum observed modulus at 90 degrees.

This general trend is also evident in the strength data plotted in fig. 3.20. However, the 40% drop in ultimate strength from 0 degrees to 45 degrees is nearly double the respective decrease in stiffness. Ultimate strength in the 90-degree coupons was a marked 47% lower than in the 0-degree coupons. The typical failure modes associated with each specimen are documented fig. 3.21. A planar fracture surface on the 0-degree coupons (fig. 2.21A) indicates a translayer failure in the

filaments. The failure mode shifts to an interlayer sliding/shearing in the 45-degree (fig. 2.21B) and 60-degree (fig. 2.21C) specimens, which is demonstrated by the stepped fracture surface aligned with the infill orientation. Intralayer failure is also dominant in the 90-degree coupons (fig. 2.21D). In this case, failure occurs primarily in the fused region between adjacent filaments.

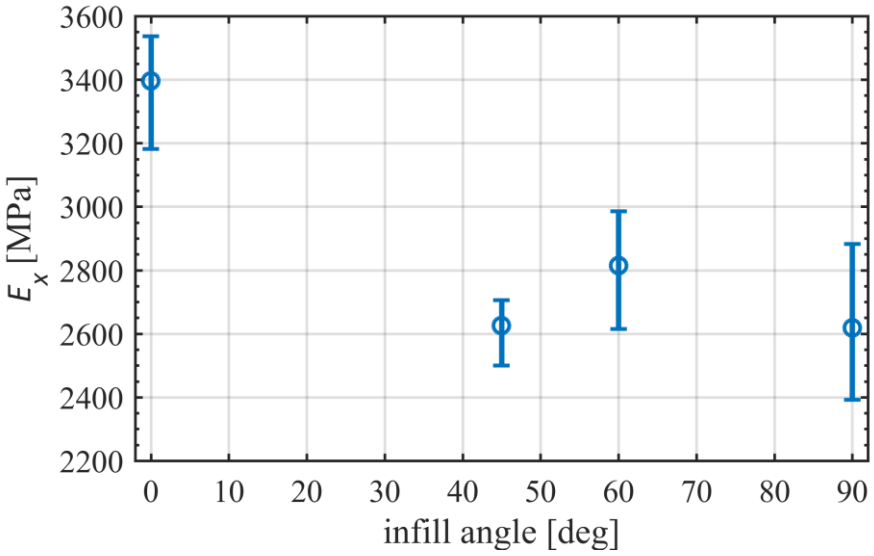

Figure 3.19: Average axial modulus at each tested infill angle. Error bars indicate the minimum and maximum measured values.

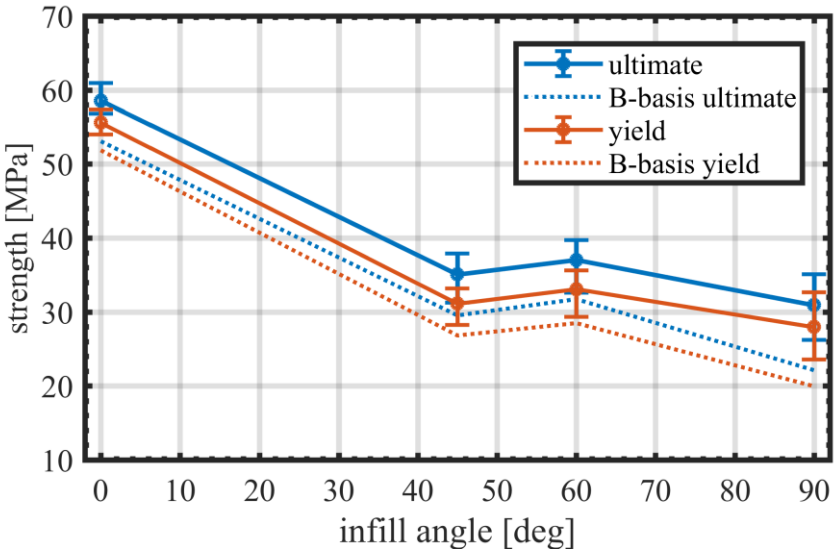

Figure 3.20: Average yield and ultimate strengths at each tested infill angle. Error bars indicate the minimum and maximum measured values.

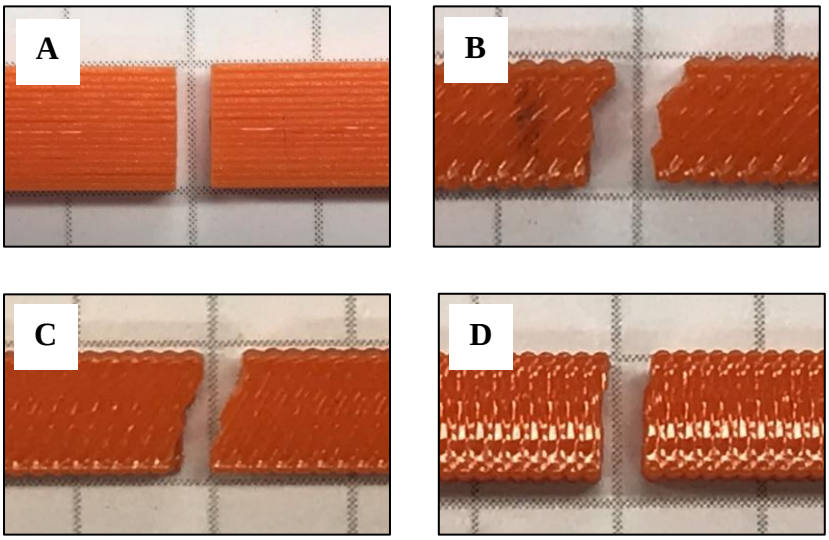

Figure 3.21: Photographs of typical A) 0-degree, B) 45-degree, C) 60-degree, and D) 90-degree coupon failures.

The Poisson's ratio for FDM PLA was found by Casovola et al. [96] to be 0.330. Using the measured moduli E_x with this Poisson's ratio, it's possible to

determine the shear moduli using the following compliance relation for a transversely isotropic material

$$\frac{1}{E_x} = \frac{\cos^4\theta}{E_L} + \frac{\sin^4\theta}{E_T} + \frac{\sin^2\theta\cos^2\theta}{G_{LT}} - \frac{2\nu_{LT}\sin^2\theta\cos^2\theta}{E_L} \tag{3.1}$$

where x references the structural frame. Subscripts L and T refer to the longitudinal and transverse directions respectively within the local filament frame. Measured values of E_x from both the 45-degree and 60-degree coupons were used to calculate the shear modulus G_{LT} in table 3.4.

Table 3.4: In-plane Material Properties

	Minimum [MPa]	Maximum [MPa]	Average [MPa]	Standard Deviation [MPa]
E_L	3181	3536	3396	121
E_T	2392	2882	2618	153
G_{LT}	868	1188	1000	93
ν_{LT}	-	-	0.330	-

3.4 Assessing Stiffness and Strength Properties

Effective in-plane properties are generated for the coupon with $[\pm 45_2/90/0/\overline{90}]_s$ infill to verify the properties developed in the previous section using CLPT. The coupon cross-section is treated as a three-layer laminate with center lamina $[\pm 45_2/90/0/\overline{90}]_s$ sandwiched between the shells oriented at 0-degrees. A diagram of

the coupon cross-section in fig. 3.22 identifies each layer and it's effective in-plane properties.

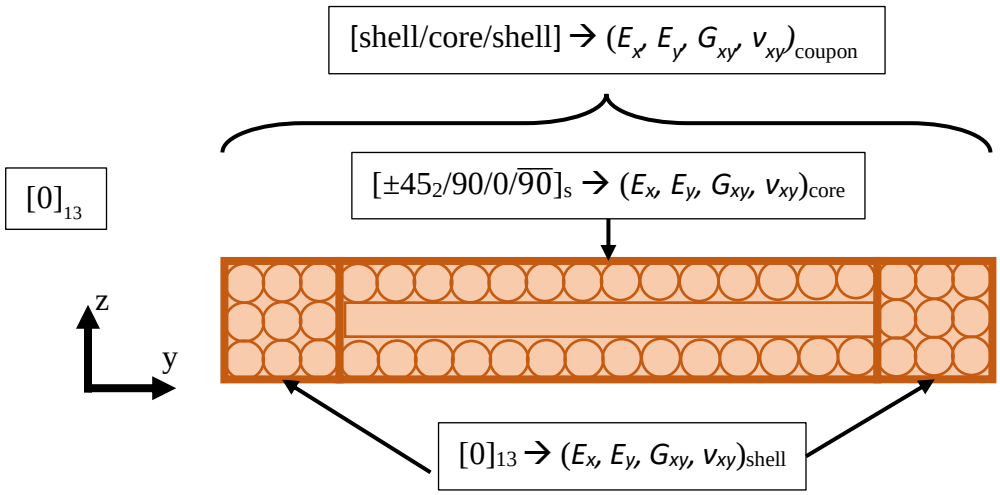

Figure 3.22: A simplified diagram of the discretized coupon cross-section with effective in-plane properties labeled.

An effective modulus in the direction of loading E_x was calculated for the core section alone and then for the entire cross-section using the average cross-sectional geometry for all the coupons. Half of this "laminate" is captured in fig. 3.5. Effective properties for both the nominal coupon infill and the whole coupon are presented in table 3.5. Figure 3.23 is a plot of the recorded stress-strain data overlaid with the calculated coupon effective modulus line.

Table 3.5: Coupon Effective In-plane Properties

		Core: $[\pm45_2/90/0/\overline{90}]_s$	Coupon: [shell/core/shell]
E_x	MPa	2,804	2,979
E_y	MPa	2,862	2,794
G_{xy}	MPa	1,104	1,073
v_{xy}	-	0.326	0.327

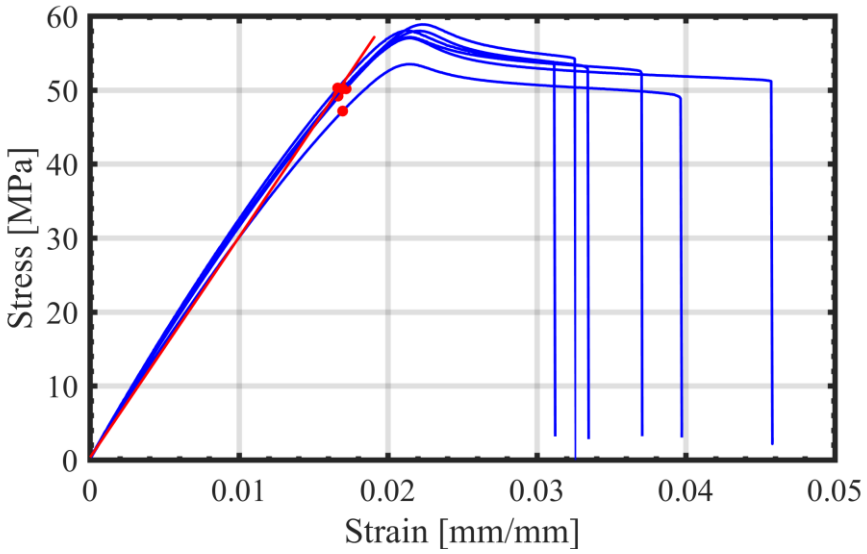

Figure 3.23: Stress-strain curves for 6 PLA $[\pm 45_2/90/0/\overline{90}]_s$ coupons. The red line shows the predicted linear response based on the effective coupon properties in table 3.5. Red dots indicate the 0.2% offset yield strength.

On average, the measured modulus in table 3.2 was 10% greater than the calculated modulus resulting in an overprediction of the strain. However, the strains for this series of coupons are derived from crosshead displacement. It's known that moduli calculated from the crosshead data, for the current machine with PLA, are between 6% and 14% stiffer than those calculated using the extensometer displacements. A comparison of moduli for PLA coupons determined using the crosshead and the much more accurate extensometer is presented in table 3.6. Supporting data is presented in Appendix D. The increased stiffness exhibited in the experimental data can therefore be largely attributed to using the crosshead as the displacement source.

Table 3.6: Average modulus using extensometer and crosshead to calculate strain

Sample Angle [Degree]	E_x - Crosshead [MPa]	E_x - Extensometer [MPa]	% Difference
0	3,620	3,396	6.6
45	2,847	2,626	8.4
60	3,173	2,815	12.7
90	3,004	2,641	13.8

Layer or "lamina" strengths F_{1t} and F_{2t} in table 3.7 are assembled from the average ultimate strengths reported in table 3.3. Shear strength F_s is sourced from [98]. Compressive strengths F_{1c} and F_{2c} were backed out using a first ply failure analysis on the compression coupons ($[0/90]_{20s}$) with the assumption that $F_{1c}=F_{2c}$ based on the findings by Song et al. [99] that the ultimate compressive strength of unidirectional FDM manufactured PLA in the longitudinal direction is approximately equal to the ultimate compressive strength in the transverse direction. An average compressive strength $F_{1c}=F_{2c}$=-93.98 MPa was found to produce the equivalent coupon strength (reported in table 3.3) of -82.37 MPa. The resulting b-basis strength is $F_{1c}=F_{2c}$=-89.05 MPa.

Failure in the coupon is predicted using a progressive ply failure analysis with a maximum stress criterion. Moduli are completely discounted in failed layers until a longitudinal failure occurs in one of the 0-degree layers. Failure analysis was performed on the 0-degree shells and core laminate separately. It was found that the shells failed with midplane strain ε_{xxo}=0.0172 and the core section failed at ε_{xxo}=0.0121. If load is diverted to the shells when the core fails, then the predicted ultimate coupon strain is just ε_{xx}=0.0172. It's evident from fig 3.23, in which the

coupons failed at an average strain of ε_{xx}=0.0366, that the progressive failure model outlined in this section is relatively conservative.

Table 3.7: PLA Average "Lamina" Strengths [MPa]

Property	
F_{1t}	58.56
F_{1c}	-93.98
F_{2t}	30.94
F_{2c}	-93.98
F_s	18.00 [98]

3.5 Relative Anisotropy

Having developed in-plane material properties for PLA manufactured using FDM, it is of interest to compare the relative anisotropy to other common materials. table 3.8 is adapted from Daniel and Ishai [100] with the addition of PLA. The elastic ratios for PLA are of the same order of magnitude as the Silicon Carbide (SiC)/Ceramic and E-glass/Epoxy. There is a greater distinction when it comes to the strength ratio F_{1t}/F_{2t}. This suggests that the anisotropic nature of PLA parts produced using FDM can be leveraged in the same ways that a composite part might be used to reduce weight or lower costs. The specific strength and specific modulus for materials listed in table 3.8 are presented in fig. 3.24 along with a selection of other materials as an additional point of comparison. Material properties are sourced from [89,96,100–102].

Table 3.8: Degrees of Anisotropy [100]

Material	E_L/E_T	E_L/G_{LT}	F_{1t}/F_{2t}
SiC/ceramic	1.09	2.75	17.8
FDM PLA	1.30	3.40	2.4
E-Glass/Epoxy	4.00	9.5	29
Carbon/Epoxy	14.20	21.3	40

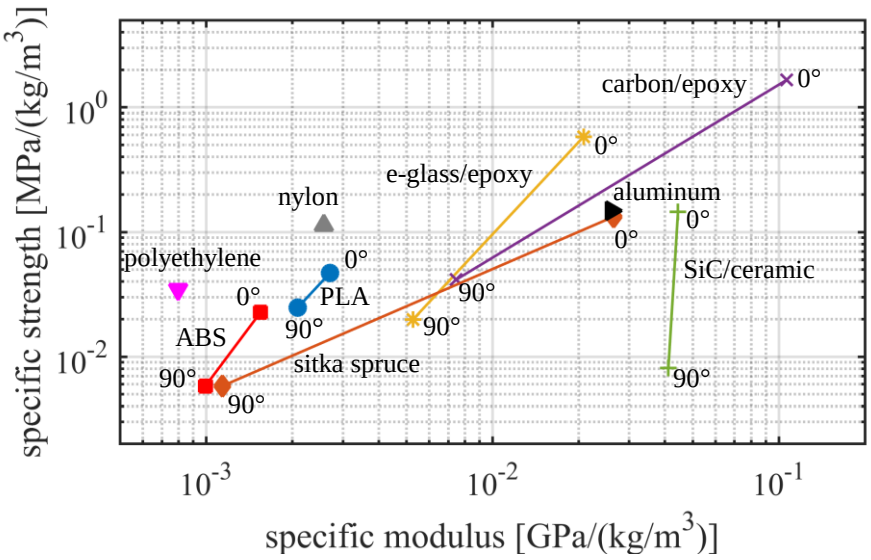

Figure 3.24: A comparison of specific strength and specific modulus for a selection of materials.

Chapter 4. Rotor Model

Blade element momentum theory (BEMT) is a well-established tool for the design of wind turbines [103] that has recently been employed in the analysis of hydrokinetic turbines [104–108]. The low-computational cost relative to computational fluid dynamics (CFD) makes it ideal for rapid design iteration and optimization. A steady BEMT model was modified for application to open-centered turbines. With this model it's possible to calculate the hydrodynamic loads, sum the thrust and torque generated by the rotor, and characterize the performance under various operating conditions. Loads generated from this model were used to establish a safe blade design for water trials.

4.1 Turbine Characterization

Turbines are generally characterized in terms of how much thrust T, torque Q, and power P they produce. Non-dimensional coefficients fundamental to describing rotor performance are introduced in this section. A thrust coefficient C_T is defined as

$$C_T = \frac{T}{\frac{1}{2}\rho A U_o^2}, \tag{4.1}$$

where U_o is the free stream velocity, ρ is the fluid density, and A is the swept area of the turbine. Likewise, the torque coefficient C_Q is defined as

$$C_Q = \frac{Q}{\frac{1}{2}\rho r_o A U_o^2}, \tag{4.2}$$

where r_o is the radius of the turbine. The power coefficient C_P, or efficiency, of a turbine is defined by the ratio of power generated to power available

$$C_P = \frac{P}{\frac{1}{2}\rho A U_o^3}. \tag{4.3}$$

In addition, a tip-speed ratio λ is found from the quotient of the tangential velocity at the blade tip and the free stream velocity

$$\lambda = \frac{\Omega r_o}{U_o}, \tag{4.4}$$

in which Ω is the turbine's angular velocity. A local Reynolds number Re is determined by the ratio of the inertial forces to the viscous forces along the blade,

$$\mathrm{Re} = \frac{\rho u_{rel} c}{\mu}, \tag{4.5}$$

where u_{rel} is the local fluid velocity, c is the local chord, and μ is the dynamic fluid viscosity.

4.2 Momentum Theory

In this section the elements of momentum theory, also known as disk actuator theory, necessary to derive the blade element momentum theory are introduced. The following equation development is based on the approach by Hansen in [54]. Momentum theory models an idealized frictionless-rotor as permeable disc, which

slows the stream velocity by extracting energy from the flow. Several basic relations are developed from consideration an ideal one-dimensional (1-D) rotor. Wake rotation is subsequently introduced in a more general two-dimensional (2-D) model that can be coupled with the effects occurring locally at the blade to form the steady BEMT equations.

Assuming incompressible inviscid-flow, the stream tube around the disc must expand to satisfy mass continuity in the slower moving wake. Figure 4.1 shows the ideal rotor disc in one dimension. It is initially assumed that the rotor imparts no rotational velocity on the wake so that it can operate at the maximum theoretical efficiency, which is known as the Betz Limit [54].

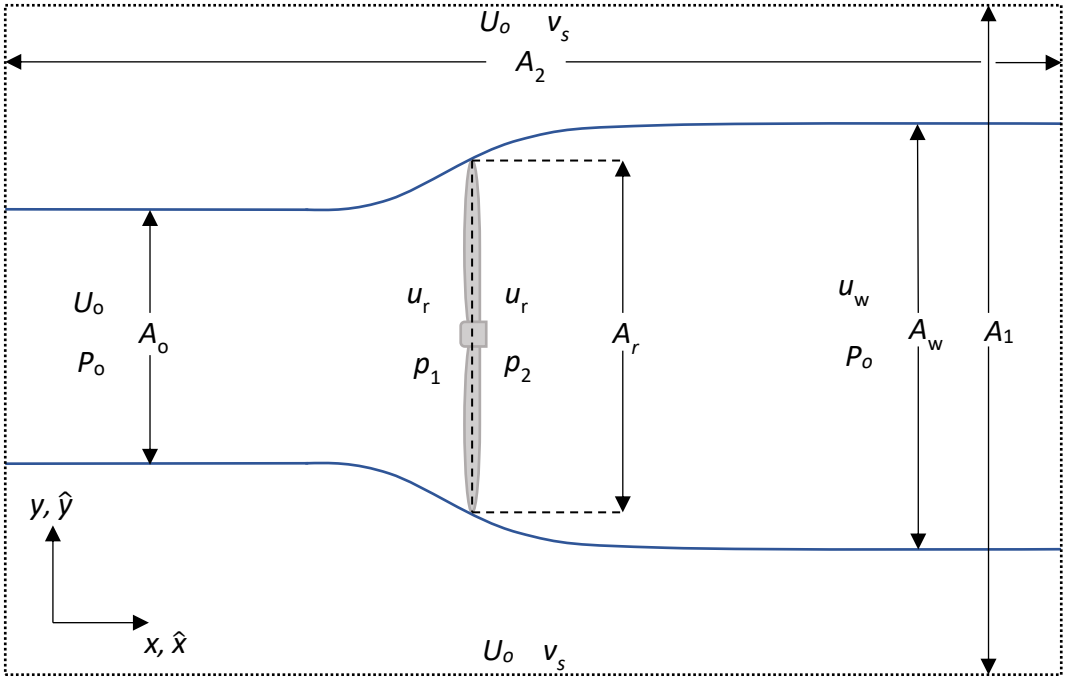

Figure 4.1: Diagram of the ideal rotor model with a streamtube (blue line) and rectangular control volume 1 (black dotted line) that encloses the entire system. Areas (A), pressures ($P,\ p$), stream velocities in the x-direction ($U,\ u$), and stream velocities in the y-direction (v) are shown at points of interest.

The force exerted by the rotor disc to slow down the fluid, or thrust T, can be found from the pressure drop across the turbine as

$$T = A_r\left(p_1 - p_2\right), \tag{4.6}$$

where p_1 is the pressure immediately upstream of the rotor, p_2 is the pressure immediately downstream of the rotor, and A_r is the area of the rotor. It is further assumed that the flow is stable, frictionless, and with no external forces acting on it. Therefore, Bernoulli's Equation can be applied to the upstream side of the rotor

$$P_o + \frac{1}{2}\rho U_o^2 = p_1 + \frac{1}{2}\rho u_r^2 \tag{4.7}$$

and rearranged

$$P_o = p_1 + \frac{1}{2}\rho\left(u_r^2 - U_o^2\right). \tag{4.8}$$

The same principle is applied to the downstream side,

$$p_2 + \frac{1}{2}\rho u_r^2 = P_o + \frac{1}{2}\rho u_w^2 \tag{4.9}$$

and rearranged

$$P_o = p_2 + \frac{1}{2}\rho\left(u_r^2 - u_w^2\right) \tag{4.10}$$

where P_o is the undisturbed stream pressure, U_o is the undisturbed stream velocity, p_1 is the pressure immediately upstream of the rotor, u_r is the stream velocity at the rotor, p_2 is the pressure immediately downstream of the rotor, u_w is the downstream wake velocity where the pressure has recovered to P_o, and ρ is the fluid density.

Equating eq. (4.8) and eq. (4.10) yields an expression for the pressure drop across the rotor

$$\left(p_1 - p_2\right) = \frac{1}{2}\rho\left(U_o^2 - u_w^2\right). \tag{4.11}$$

Substituting eq. (4.11) into eq. (4.6) results in a total thrust equal to

$$T = \frac{1}{2}\rho A_r\left(U_o^2 - u_w^2\right). \tag{4.12}$$

Conservation of linear momentum for steady flow within control volume 1 (CV1), identified in fig. 4.1 with a black dotted line, requires

$$\sum F_x = \int_{CS} \rho u\left(\vec{u}\cdot\hat{n}\right)dA \tag{4.13}$$

where CS is the control surface defined by CV1 and

$$\vec{u} = u\hat{x} + v\hat{y}, \tag{4.14}$$

with $\hat{x}$ and $\hat{y}$ being the unit vectors pointing in the x and y directions respectively. The positive surface normal $\hat{n}$ faces outward from the control surface. The area of the streamtube in the wake is A_w, A_1 is the area of the left and right surfaces of CV1, A_2 is the area of the top and bottom surfaces of CV1. The y-component of the stream velocity along the top and bottom of CV1 is v_s.

Looking at fig. 4.1, the right hand side of eq. (4.13) can be written for the flow coming into the left side of CV1

$$-\rho U_o^{\,2} A_1, \tag{4.15}$$

with $\vec{u}=U_o\hat{x}$ and $\hat{n}=-\hat{x}$, plus the contribution from flow through the top of CV1

$$\rho U_o v_s A_2 \tag{4.16}$$

with $\vec{u}=v_s\hat{y}$ and $\hat{n}=\hat{y}$, plus the contribution from flow through the bottom of CV1

$$\rho U_o v_s A_2 \tag{4.17}$$

with $\vec{u}=-v_s\hat{y}$ and $\hat{n}=-\hat{y}$, and the contribution from the flow exiting CV1 on the right side

$$\rho u_w{}^2 A_w + \rho U_o{}^2 \left(A_1 - A_w\right), \tag{4.18}$$

where $\vec{u}=u_w\,\hat{x}$ and $\hat{n}=\hat{x}$.

Combing and rearranging eqs. (4.15)-(4.18) results in

$$\sum F_x = -\rho U_o{}^2 A_1 + U_o\left(2\rho v_s A_2\right) + \rho u_w{}^2 A_w + \rho U_o{}^2 (A_1 - A_w). \tag{4.19}$$

The mass flow $\dot{m}$ is defined as the product of fluid density ρ, velocity u, and cross-sectional area A

$$\dot{m} = \rho u A \tag{4.20}$$

Conservation of mass within the control volume dictates that the mass flow entering the control volume is equal to the mass flow exiting the control volume, therefore

$$\rho U_o A_1 = 2\rho v_s A_2 + \rho u_w A_w + \rho U_o\left(A_1 - A_w\right) \tag{4.21}$$

which is simplified to give an expression for the unknown mass flow out the top and bottom of CV1,

$$2\rho v_s A_2 = \rho A_w\left(U_o - u_w\right). \tag{4.22}$$

It's assumed that the pressure outside CV1 is at P_o and the external forces all sum to zero in the x-direction. Therefore, the only force acting on the system is the internal thrust T resulting from the pressure drop across the rotor. Substituting this information, along with eq. (4.22), into eq. (4.19) results in the following form of the conservation of linear momentum equation:

$$\sum F_x = -T = -\rho U_o^2 A_1 + \rho A_w U_o \left(U_o - u_w\right) + \rho u_w^2 A_w + \rho U_o^2 \left(A_1 - A_w\right). \tag{4.23}$$

Rearranging and simplifying, the rotor thrust T is equal to

$$T = \rho u_w A_w \left(U_o - u_w\right) . \tag{4.24}$$

Since the conservation of mass applies within the blue stream tube shown in fig 4.1, then;

$$\rho U_o A_o = \rho u_r A_r = \rho u_w A_w \ . \tag{4.25}$$

Using this relationship, thrust can be expressed in terms of rotor area and flow speed at the rotor

$$T = \rho u_r A_r \left(U_o - u_w\right). \tag{4.26}$$

Alternatively, the streamtube can be used as the control volume. Applying the conservation of linear momentum within the streamtube control volume (CV2), which by the definition of a streamline has no flow across the lateral boundaries, yields

$$\sum F_x = -T + F_{ext} = -U_o \left(\rho U_o A_o\right) + u_w \left(\rho u_w A_w\right), \tag{4.27}$$

where F_{ext} is equal to the sum of external forces on the streamtube CV2. Applying the identity in eq. (4.25) results in

$$-T + F_{ext} = \rho u_r A_r \left(-U_o + u_w\right), \tag{4.28}$$

or after rearranging

$$T = \rho u_r A_r \left(U_o - u_w\right) + F_{ext} . \tag{4.29}$$

The pressure at both the entrance and exit of the streamtube is equal to P_o so there is no net force on those surfaces. Furthermore, the thrust generated by the rotor disc doesn't depend on which control volume is used so equations (4.26) and (4.29) must

be equal. This requires that the sum of external forces along the streamlines also equal zero and as a result F_{ext} must also be zero.

Finally, by setting eq. (4.12) equal to eq. (4.26) and solving for flow velocity at the rotor u_r it is seen that

$$u_r = \frac{1}{2}\left(U_o + u_w\right). \tag{4.30}$$

It's convenient to define an axial induction factor a as the fractional decrease between upstream velocity and velocity at the rotor

$$a = \frac{U_o - u_r}{U_o}, \tag{4.31}$$

or

$$u_r = U_o\left(1 - a\right). \tag{4.32}$$

Combining eq. (4.30) and eq. (4.32) results in a useful relation between wake velocity u_w and the free stream velocity U_o in terms of the induction factor

$$u_w = U_o\left(1 - 2a\right). \tag{4.33}$$

A similar exercise can now be performed on an annular control volume, shown in fig. 4.2, of infinitesimal thickness dr. Having established that the external forces on the streamline do not have an x-component, the thrust on an annular rotor section is again found using the conservation of linear momentum

$$-dT = -U_o\left(\rho U_o\right)dA_o + u_w\left(\rho u_w\right)dA_w \tag{4.34}$$

and in terms of mass flow

$$dT = \left(U_o - u_w\right)d\dot{m}, \tag{4.35}$$

where

$$d\dot{m} = \rho U_o dA_o = \rho u_w dA_w = \rho u_r dA_r \,. \tag{4.36}$$

By enforcing mass continuity and substituting in the cross-sectional area of the annular rotor element

$$dT = \left(U_o - u_w\right)\left(\rho u_r 2\pi r dr\right) \tag{4.37}$$

where

$$dA_r = 2\pi r dr \,. \tag{4.38}$$

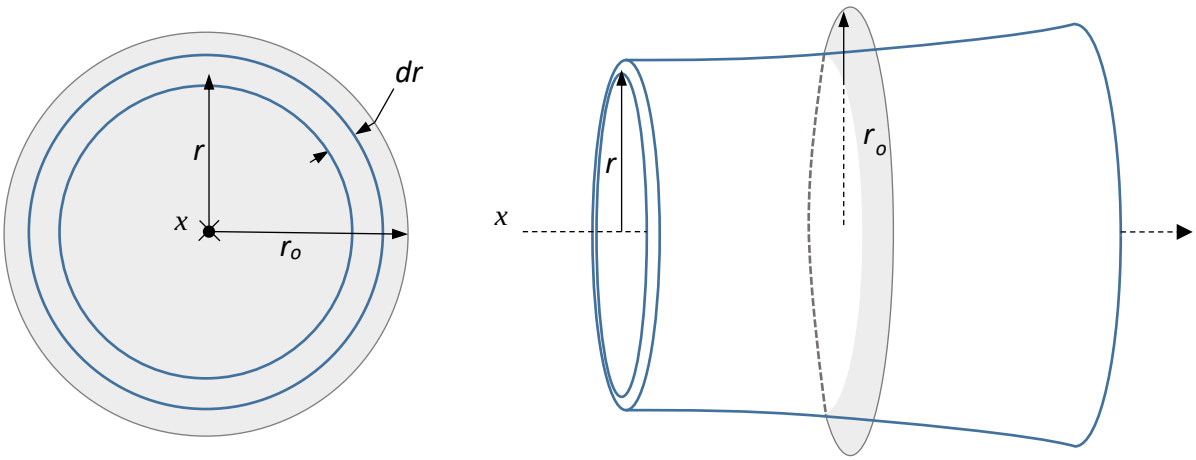

A B

Figure 4.2: An annular control volume of thickness dr defined by streamtubes (blue lines). The control volume is shown from a planar section view A) and an isometric view B) with the rotor represented by a gray disc. Flow is in the x-direction.

Thrust on an annular element of the rotor disc can be expressed in terms of the induction factor a by applying eq. (4.32) and eq. (4.33)

$$dT = 4\pi\rho r U_o^2 a\left(1-a\right)dr \,, \tag{4.39}$$

which can be integrated over the rotor disc of radius r_o to get the total thrust

$$T = \int_0^{r_o} 4\pi\rho r U_o^2 a\left(1-a\right)dr \ . \tag{4.40}$$

Up to this point it was assumed that the rotor disc was not spinning and therefore did not impart rotation on the wake. A spinning rotor disc is now considered to incorporate the angular velocity induced in its wake. Upstream of the rotor there is assumed to be no rotational component to the fluid velocity. To begin, a tangential—with respect to the rotor plane—induction factor a_t is defined as the ratio of the induced fluid rotation at the rotor plane to the angular speed of the rotor

$$a_t = \frac{\omega}{2\Omega} \tag{4.41}$$

where ω is the induced angular speed immediately downstream of the rotor and Ω is the angular speed of the rotor [54]. Figure 4.3 depicts the local fluid velocity vectors near the rotor plane (u_r, u_d), at a radius r, with the added tangential component $r\omega$ resulting from wake rotation.

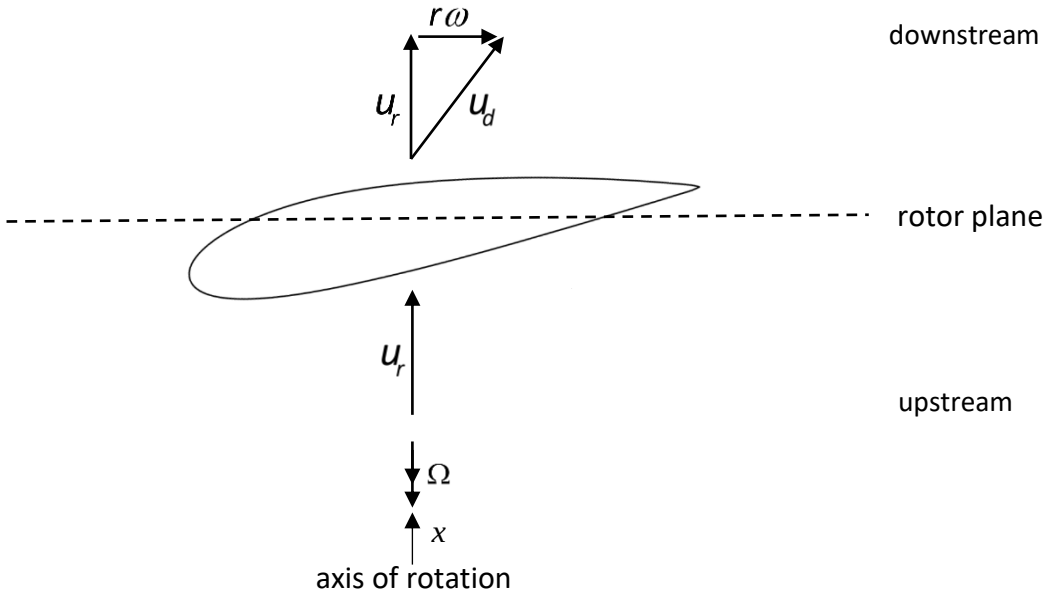

Figure 4.3: A section view of the rotor plane at radius r with fluid velocities indicated on the upstream and downstream side. The velocity u_d on the downstream side has a tangential component with magnitude $r\omega$ induced by the rotor.

Conservation of angular momentum for steady flow requires

$$\sum M_o = \int_{CS} (\vec{r} \times \vec{u}) \rho (\vec{u} \cdot \hat{n}) dA, \tag{4.42}$$

where $\vec{r}$ is the is the position vector from the origin to a mass element on dA and M_o is the sum of applied moments taken about the centroid of the control surface [78]. As there is no angular velocity upstream of the rotor disc, the net moment acting about the x-axis of the annular control volume, or the differential torque dQ, must be equal to the angular momentum in the wake

$$\sum M_x = dQ. \tag{4.43}$$

The angular momentum contained in the wake exiting the annular control volume can be written

$$\rho\left(r^2\omega\right)u_w dA_w\,, \tag{4.44}$$

which is equal to the differential torque dQ on the annular rotor section

$$dQ=\left(r^2\omega\right)\rho u_w dA_w\,. \tag{4.45}$$

Applying mass continuity as expressed in eq. (4.36), the torque can be written in terms of the flow speed at the rotor

$$dQ=\left(r^2\omega\right)\rho u_r dA_r \tag{4.46}$$

and since $dA_r=2\pi r dr$

$$dQ=\left(r^2\omega\right)\rho u_r 2\pi r dr\,. \tag{4.47}$$

Using the definition of the induction factors in eq. (4.32) and eq. (4.41), eq. (4.47) is simplified to

$$dQ=4\pi r^3\rho U_o\left(1-a\right)a_t\Omega dr\,. \tag{4.48}$$

Total torque generated by the spinning rotor disc of radius r_o is equal to

$$Q=\int_0^{r_o}4\pi r^3\rho U_o\left(1-a\right)a_t\Omega dr\,. \tag{4.49}$$

4.3 Blade Element Theory

Expressions for the differential thrust and the differential torque, eq. (4.39) and eq. (4.48) respectively, on an annular section of the rotor have been derived using momentum theory. The current section considers the blade element model of a rotor, which describes the local hydrodynamic forces generated by 2-D flow over the rotor

blades. This blade element theory (BET) will be coupled with the momentum theory equations to form the BEMT equations.

The individual rotor blades are now examined as a series of discrete elements as depicted in fig. 4.4. A superscript i will be used to refer to the local properties of each blade element. It is assumed that the flow over each radial section is isolated. As a result, there is no spanwise interaction between adjacent blade elements. The rotor behavior is analyzed in annular sections of length Δr^i, which encompass the i^{th} element of each blade. A section view of the rotor plane is introduced in fig. 4.5 to show the relative fluid velocity seen by the i^{th} blade element, with midpoint located at radius r^i, and the resulting hydrodynamic forces.

The relative fluid velocity at each blade segment u_{rel}^i is fixed by the freestream velocity, the angular velocity of the rotor, and the corresponding induction factors (a^i, a_t^i). The magnitude normal to the rotor plane is u_r^i, defined in the previous section by eq. (4.32) as the difference of the freestream velocity U_o and the induced axial velocity $a^i U_o$

$$u_r^i = U_o\left(1 - a^i\right). \tag{4.50}$$

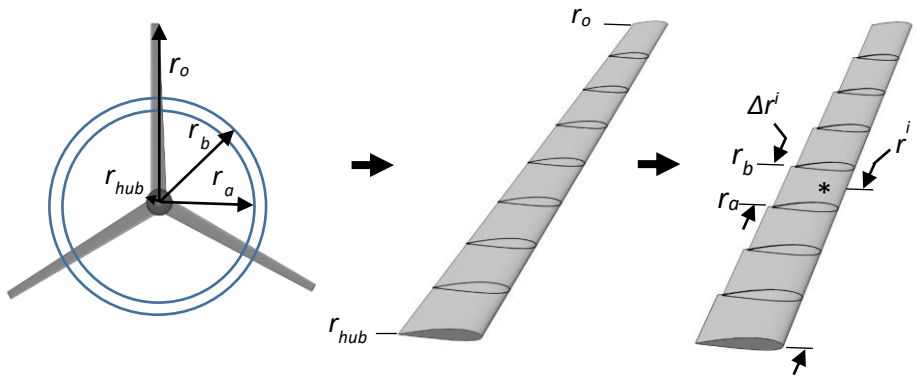

Figure 4.4: A graphic representation of rotor discretization in blade element theory. The rotor, with radius r_o, is modeled in constant geometry sections with a span of Δr^i and midpoint at r^i.

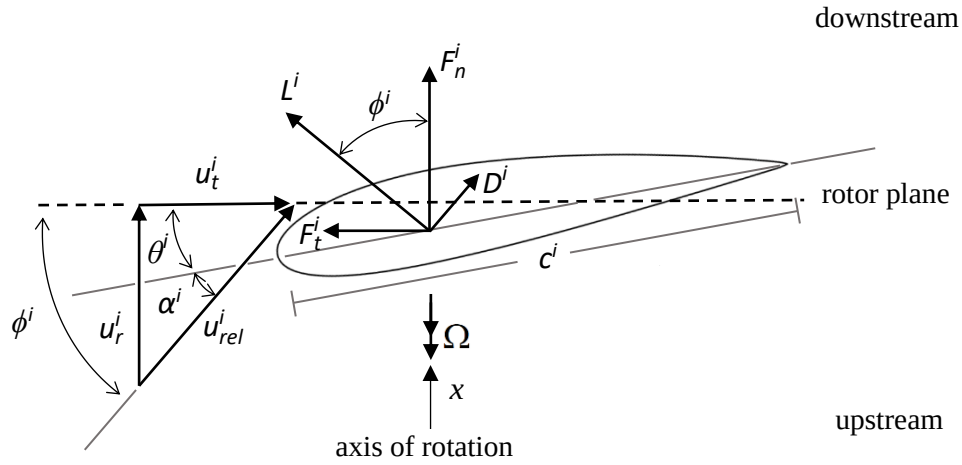

Figure 4.5: A section view of the i^{th} blade element at radius r^i. The relative fluid velocity u_{rel}^i seen by a blade section is depicted along with the magnitude of its normal and tangential components. Hydrodynamic forces generated by u_{rel}^i are shown in both the local blade frame (L^i, D^i) and the rotor frame (F_n^i, F_t^i).

Similarly, the tangential component of the relative velocity on the i^{th} element u_t^i is found by the summing contributions from the angular velocity of the rotor and the induced wake velocity

$$u_t^i = r^i\left(\Omega + \frac{\omega}{2}\right), \tag{4.51}$$

where r^i is the radial location of the i^{th} element's midpoint and the induced angular velocity at the rotor is approximated as the average of the upstream angular velocity, assumed to be zero, and the induced downstream angular velocity ω. Note that, in accordance with Newton's Third Law, the induced fluid rotation moves in the opposite direction of the blade rotation and therefore it increases the relative tangential velocity seen by the blade. Writing u_t^i in terms of the angular induction factor a_t^i defined by eq. (4.41) results in

$$u_t^i = r^i\Omega\left(1 + a_t^i\right). \tag{4.52}$$

The local pitch angle θ^i of the i^{th} element is the sum of blade pitch θ_p and i^{th} element twist angle β^i

$$\theta^i = \theta_p + \beta^i. \tag{4.53}$$

Looking at fig. 4.5, the i^{th} segment angle ϕ^i between the relative velocity u_{rel}^i and the rotor plane can be found by

$$\tan\phi^i = \frac{u_r^i}{u_t^i} = \frac{U_o\left(1 - a^i\right)}{r^i\Omega\left(1 + a_t^i\right)}. \tag{4.54}$$

Angle of attack α^i for the i^{th} element, defined as the angle between the chord line and the relative velocity u_{rel}^i, can be determined by the difference of ϕ^i and local pitch θ^i

$$\alpha^i = \phi^i - \theta^i, \tag{4.55}$$

or after substituting for the relative flow angle ϕ^i

$$\alpha^i = \tan^{-1}\left[\frac{U_o\left(1-a^i\right)}{r^i\Omega\left(1+a_t^i\right)}\right] - \theta^i . \tag{4.56}$$

Two-dimensional flow over the i^{th} blade element generates a lift force L^i that is perpendicular to the relative velocity, a drag force D^i that is parallel to the relative velocity, and a moment M^i about the quarter chord. Only the lift and drag are required at present, as the moment does not directly contribute to either the torque or the thrust on the rotor. The i^{th} segment lift L^i is equal to

$$L^i = q^i c^i C_L^i \Delta r^i , \tag{4.57}$$

where c^i is the blade section chord, C_L^i is the local coefficient of lift at angle of attack α^i, and the i^{th} element dynamic pressure q^i is defined in terms of the density ρ and segment relative velocity u_{rel}^i,

$$q^i = \frac{1}{2}\rho {u_{rel}^i}^2 . \tag{4.58}$$

Drag force on the i^{th} element D^i is

$$D^i = q^i c^i C_D^i \Delta r^i , \tag{4.59}$$

where C_D^i is the local coefficient of drag at angle of attack α^i. The i^{th} element forces are projected onto the reference frame of the rotor using the relative flow angle ϕ^i to produce a normal and tangential force (F_n^i, F_t^i)

$$\begin{Bmatrix} F_n^i \\ F_t^i \end{Bmatrix} = \begin{bmatrix} \cos\phi^i & \sin\phi^i \\ \sin\phi^i & -\cos\phi^i \end{bmatrix} \begin{Bmatrix} L^i \\ D^i \end{Bmatrix} . \tag{4.60}$$

Assuming the rotor consists of a number N_B of identical blades, then the thrust T^i on the i^{th} discrete annular section of the rotor containing the i^{th} element of each blade, is equal to

$$T^i = N_B F_n^i . \tag{4.61}$$

Noting from fig. 4.5 that u_{rel}^i is equivalent to

$$u_{rel}^i = \frac{U_o\left(1-a^i\right)}{\sin\phi^i} , \tag{4.62}$$

and substituting eqs. (4.50)-(4.60) into eq. (4.61) results in an expression for the thrust T^i on i^{th} annular rotor section in terms of the geometric and aerodynamic properties of the i^{th} blade element

$$T^i = \frac{N_B \rho c^i U_o^{\,2}\left(1-a^i\right)^2\left(C_L^i \cos\phi^i + C_D^i \sin\phi^i\right)}{2\sin^2\phi^i}\Delta r^i , \tag{4.63}$$

where element lift C_L^i and element drag C_D^i are both functions of the local angle of attack α^i from eq. (4.56).

The total thrust on the rotor is found by the summation of thrusts from all n_e blade elements

$$T = \sum_{i=1}^{n_e} T^i . \tag{4.64}$$

A thrust efficiency η_T^i can be determined for each blade element by dividing the segment thrust by the total rotor thrust

$$\eta_T^i = \frac{T^i}{T} , \tag{4.65}$$

and thus, the thrust performance of each element can be studied. Finally, a local thrust coefficient C_T^i is determined for the i^{th} element by making use of eq. (4.1)

$$C_T^i = \frac{T^i}{T_o} = \frac{N_B \frac{1}{2}\rho U_o^{\,2}\left(1-a^i\right)^2\left(\sin^{-2}\phi^i\right)c^i\left(C_L^i\cos\phi^i + C_D^i\sin\phi^i\right)\Delta r^i}{\frac{1}{2}\rho A^i U_o^{\,2}}\,, \tag{4.66}$$

where T_o is the total potential thrust on the annular section with area A^i

$$T_o = \frac{1}{2}\rho A^i U_o^{\,2}\,. \tag{4.67}$$

The area of the annular section A^i, as shown in fig. 4.4, is defined as

$$A^i = \pi\left(r_b^{\,2} - r_a^{\,2}\right)\,, \tag{4.68}$$

or given that r_i is just the element midpoint

$$A^i = \frac{2}{2}\pi\left(r_b - r_a\right)\left(r_b + r_a\right) = 2\pi r^i \Delta r^i\,. \tag{4.69}$$

Substituting for the annular area and rearranging results in a convenient expression for local thrust coefficient

$$C_T^i = \left(\frac{N_B c^i}{2\pi r^i}\right)\frac{\left(1-a^i\right)^2\left(C_L^i\cos\phi^i + C_D^i\sin\phi^i\right)}{\sin^2\phi^i}\,, \tag{4.70}$$

of which the first term is called the local solidity ratio σ^i at the i^{th} element

$$\sigma^i = \frac{N_B c^i}{2\pi r^i}\,. \tag{4.71}$$

The torque Q^i on the i^{th} discrete annular section of the rotor, containing the i^{th} element of each blade, is calculated as the tangential force on the elements multiplied by the distance to the element midpoint r^i and the number of blades N_B

$$Q^i = N_B r^i F_t^i\,. \tag{4.72}$$

It's evident from fig. 4.5 that the relative velocity at the i^{th} blade element can be expressed in terms of the tangential induction factor as

$$u_{rel}^{i} = \frac{r^{i}\Omega\left(1+a_{t}^{i}\right)}{\cos\phi^{i}} \ , \tag{4.73}$$

which can be used in addition with eq. (4.62) to express $u_{rel}^{i}{}^{2}$ as

$$u_{rel}^{i}{}^{2} = \frac{r^{i}\Omega\left(1+a_{t}^{i}\right)}{\cos\phi^{i}} \frac{U_{o}\left(1-a^{i}\right)}{\sin\phi^{i}} \ . \tag{4.74}$$

Substituting eqs. (4.50)-(4.60) into eq. (4.72) results an expression for the torque Q^{i} on the i^{th} annular section in terms of the geometric and aerodynamic properties of the i^{th} blade element

$$Q^{i} = \frac{r^{i}\Omega\left(1+a_{t}^{i}\right)}{\cos\phi^{i}} \frac{U_{o}\left(1-a^{i}\right)}{\sin\phi^{i}} \left[\frac{N_{B}\rho c^{i} r^{i}\left(C_{L}^{i}\sin\phi^{i} - C_{D}^{i}\cos\phi^{i}\right)}{2} \right] \Delta r^{i} \ . \tag{4.75}$$

As with the thrust, total torque on the rotor is found by summing the torque on all n_e blade elements

$$Q = \sum_{i=1}^{n_e} Q^{i} \ . \tag{4.76}$$

A torque efficiency η_{Q}^{i} can be determined for each blade element by dividing the element torque by the total rotor torque

$$\eta_{Q}^{i} = \frac{Q^{i}}{Q} \ , \tag{4.77}$$

and thus, the torque performance of each element can be studied. Finally, a local torque coefficient C_{Q}^{i} is determined for the i^{th} element by making use of eq. (4.2)

$$C_{Q}^{i} = \frac{Q^{i}}{Q_{o}} = \frac{\dfrac{r^{i}\Omega\left(1+a_{t}^{i}\right)}{\cos\phi^{i}} \dfrac{U_{o}\left(1-a^{i}\right)}{\sin\phi^{i}} \left[\dfrac{N_{B}\rho c^{i} r^{i}\left(C_{L}^{i}\sin\phi^{i} - C_{D}^{i}\cos\phi^{i}\right)}{2} \right] \Delta r^{i}}{\dfrac{1}{2}\rho r^{i} A^{i} U_{o}^{2}} \tag{4.78}$$

where A^i is again the area annular of the section containing the i^{th} elements

$$A^i = 2\pi r^i \Delta r^i , \tag{4.79}$$

and Q_o is the total potential torque at radius r^i

$$Q_o = \frac{1}{2}\rho r^i A^i U_o^{\,2} . \tag{4.80}$$

After rearranging eq. (4.78) the local torque coefficient is determined by

$$C_Q^i = \left(\frac{N_B c^i}{2\pi r^i}\right)\frac{\Omega r^i \left(1+a_t^i\right)\left(1-a^i\right)\left(C_L^i \sin\phi^i - C_D^i \cos\phi^i\right)}{U_o \cos\phi^i \sin\phi^i} . \tag{4.81}$$

Finally, the power generated by the i^{th} annular section is equal to the product of the torque Q^i on that section and the rotor speed Ω. Thus,

$$P^i = Q^i\Omega = \Omega N_B r^i F_t^i \tag{4.82}$$

and the total rotor power is equal to

$$P = \sum_{i=1}^{n_e} P^i . \tag{4.83}$$

The total rotor power can be expressed in terms of element geometric and aerodynamic parameters by substituting for i^{th} element torque found in eq. (4.75), so that

$$P = \frac{N_B \rho U_o \Omega^2}{2}\sum_{i=1}^{n_e}\frac{c^i \left(r^i\right)^2 \left(1+a_t^i\right)\left(1-a^i\right)\left(C_L^i \sin\phi^i - C_D^i \cos\phi^i\right)}{\cos\phi^i \sin\phi^i}\Delta r^i . \tag{4.84}$$

Element efficiency η_P^i can be calculated by dividing the power generated at each element with the total power generated by the rotor

$$\eta_P^i = \frac{P_i}{P}, \tag{4.85}$$

allowing for the relative power output of each element to be assessed. A local power coefficient C_P^i can also be defined to determine the fraction of theoretically available power that is captured by the annular rotor section containing the i^{th} element. Using eq. (4.3), the local power coefficient is written

$$C_P^i = \frac{P^i}{P_o} = \frac{\Omega \dfrac{r^i \Omega\left(1+a_t^i\right)}{\cos\phi^i} \dfrac{U_o\left(1-a^i\right)}{\sin\phi^i} \left[\dfrac{N_B \rho c^i r^i \left(C_L^i \sin\phi^i - C_D^i \cos\phi^i\right)}{2} \right] \Delta r^i}{\frac{1}{2}\rho A^i U_o^{\,3}}, \tag{4.86}$$

where P_o is the total power available to the i^{th} annular rotor section with area A^i

$$P_o = \frac{1}{2}\rho A^i U_o^{\,3}. \tag{4.87}$$

Rearranging and simplifying eq. (4.86), the local power coefficient is equal to

$$C_P^i = \left(\frac{N_B c^i}{2\pi r^i} \right) \frac{\Omega^2 \left(r^i\right)^2 \left(1+a_t^i\right)\left(1-a^i\right)\left(C_L^i \sin\phi^i - C_D^i \cos\phi^i\right)}{U_o^{\,2} \cos\phi^i \sin\phi^i}. \tag{4.88}$$

4.4 Blade Element Momentum Theory

In this section, the momentum theory is coupled with the blade element theory to produce the fundamental blade element momentum theory (BEMT) equations. The principal purpose of BEMT is to solve for the local induction factors (a^i, a_t^i) that define the flow at the rotor, which can then be used to determine the loads on the

rotor. Theoretical and empirical corrections will be introduced that improve the accuracy of the BEMT model. These corrections are applied to the momentum theory equations through an additional factor F^i. The thrust equation presented as eq. (4.39) is reproduced to describe the differential thrust on the rotor at a radius r^i

$$dT = 4\pi\rho r^i U_o^2 F^i a^i \left(1 - a^i\right) dr \,. \tag{4.89}$$

Similarly, for the differential torque of eq. (4.48)

$$dQ = 4\pi\left(r^i\right)^3 \rho U_o \left(1 - a^i\right) F^i a_t^i \Omega dr \,. \tag{4.90}$$

If a blade element of infinitesimal length is considered, then

$$\Delta r^i \to dr \tag{4.91}$$

and BET equations provide alternative expressions for the differential thrust and torque on the rotor. Setting eq. (4.89), the momentum theory expression for thrust, equal to eq. (4.63) for an element of length dr, the blade element theory equation for thrust, it's possible to solve for the axial induction factor

$$a^i = \frac{1}{\left(\dfrac{4F^i \sin^2\phi^i}{\sigma^i C_n^i} + 1\right)}, \tag{4.92}$$

where

$$C_n^i = C_L^i \cos\phi^i + C_D^i \sin\phi^i \,. \tag{4.93}$$

The two equations for rotor torque, eq. (4.90) and eq. (4.75) for an element length dr, are set equal to each other to find an expression for the tangential induction factor

$$a_t^i = \frac{1}{\left(\frac{4F^i \sin\phi^i \cos\phi^i}{\sigma^i C_t^i} - 1 \right)}, \tag{4.94}$$

where

$$C_t^i = C_L^i \sin\phi^i - C_D^i \cos\phi^i . \tag{4.95}$$

The blade loads and corresponding rotor performance are determined by first solving for the two induction factors.

While deriving the momentum theory equations the rotor was considered to behave like a permeable disc. This assumption is analogous to the rotor having an infinite number of blades. In reality, some fluid particles pass through the rotor without encountering a blade and the force distribution on an annular rotor element is not constant. The vortex system generated by a rotor with a finite number of blades is helical rather than tubular [54]. Figure 4.6 shows this wake structure schematically. Vortices induced at tips from high pressure flow spilling over to the low-pressure side of the blade increase drag and reduce lift at the tips.

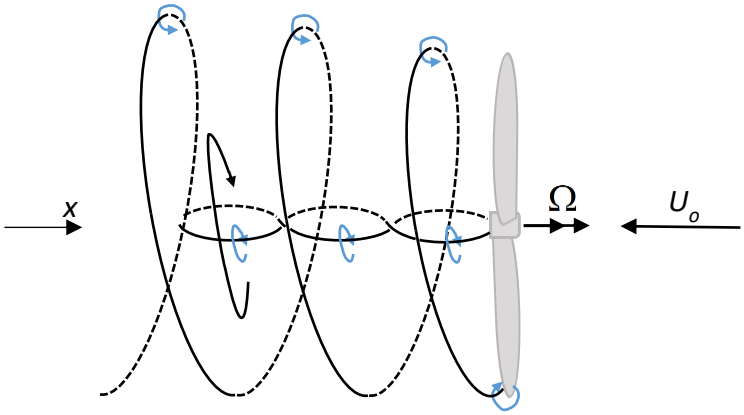

Figure 4.6: Schematic representation of the vortex system induced by a rotor with a finite number of blades. Note that the rotor is shown rotating in the counter-clockwise direction. For clarity, the trailing vortex is only shown for one of the blades.

Prandtl developed a tip-loss function to more closely reflect these differences by modeling the helical wake as series of vortex sheets [109]. Prandtl's tip loss function was later incorporated into BEMT by Glauert as a modification to the local blade section induction factors (a^i, a_t^i) [110,111]. Known as Prandtl's tip loss factor, F_{tip}^i is defined as

$$F_{tip}^i = \frac{2}{\pi}\cos^{-1}\left[\exp\left(-\frac{N_B\left(r_o - r^i\right)}{2r^i \sin\phi^i}\right)\right]. \tag{4.96}$$

The introduction of a shroud or nacelle around the blade tips can prevent the formation of tip vortices and effectively mitigate these tip losses. As with the tip vortices, vortices shed by the rotor hub impact the induced velocity at the blade root and reduce the lift generated in that region. A hub loss factor F_{hub}^i can also be defined from the Prandtl model [112,113]

$$F_{hub}^i = \frac{2}{\pi}\cos^{-1}\left[\exp\left(-\frac{N_B\left(r^i - r_{hub}\right)}{2r^i \sin\phi^i}\right)\right]. \tag{4.97}$$

Total loss factor F^i is found from the product of the tip loss and hub loss factors

$$F^i = F_{tip}^i F_{hub}^i. \tag{4.98}$$

An example loss factor for a rotor with three blades with a constant inflow angle of 8 degrees is plotted in fig. 4.7. In this case, the rotor hub extends from 0 to 5% of the rotor radius.

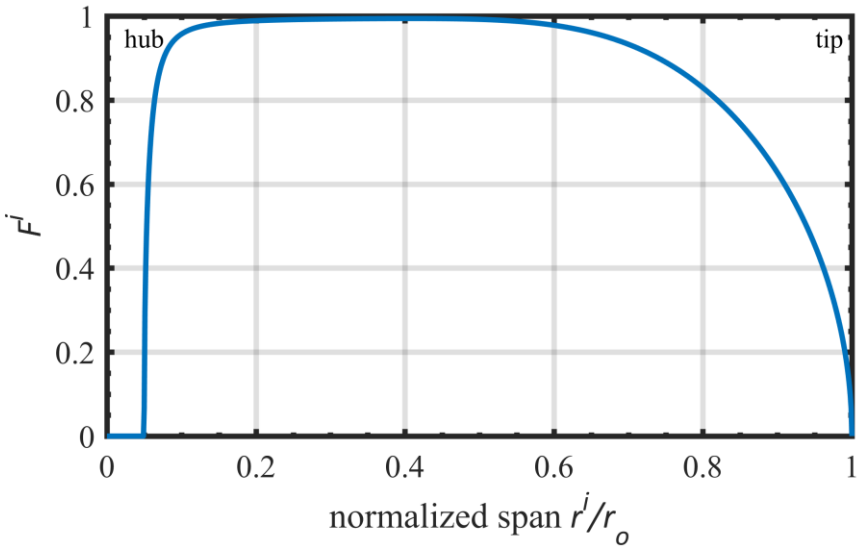

Figure 4.7: Combined loss factor F^i for a 3-bladed rotor operating at constant relative element inflow angle of 8 degrees along the entire span with a hub from 0-5% span.

Momentum theory begins to break down when the axial induction a factor approaches 0.5, at which point eq. (4.33) predicts a negative wake velocity. Rather than reversing direction as predicted, the wake enters a turbulent state. The edge of the wake becomes unstable and eddies develop, transferring energy from the outside stream to the wake [54]. An empirical correction to the analytical rotor thrust, based on experimental data from a rotor operating in the turbulent wake regime, was first introduced by Glauert [114]. Buhl has since developed an improved correction to the thrust coefficient that incorporates the Prandtl tip and hub loss factors [115], if

$$C_T^i \geq 0.96F^i \tag{4.99}$$

then

$$C_T^i = \frac{8}{9} + \left(4F^i - \frac{40}{9}\right)a^i + \left(\frac{50}{9} - 4F^i\right)\left(a^i\right)^2 . \tag{4.100}$$

The axial induction factor is then found to be

$$a^i = \frac{18F^i - 20 - 3\sqrt{C_T^i\left(50 - 36F^i\right) + 12F^i\left(3F^i - 4\right)}}{36F^i - 50}. \tag{4.101}$$

4.5 Solution Procedure

BEMT analysis begins with the discretization of the blades that make up the rotor into a number of elements. Each element is defined by its length, radial location, and airfoil. A rotor speed and a freestream speed are provided as input. The local induction factors are determined for each element independently, as it was assumed that flow over adjacent elements does not interact. A new superscript index m is introduced to describe the iterative procedure to solve for the induction factors at the i^{th} element. Starting values for $a^{i,m}$ and $a_t^{i,m}$ can either be selected based off previous solutions or initialized at 0.

Looking at element $i=i_o$, the relative inflow angle $\phi^{i_o,m}$ and angle of attack $\alpha^{i_o,m}$ are calculated from eq. (4.54) and eq. (4.55) respectively using the assumed induction factors. Coefficients of lift $C_L^{i_o,m}$ and drag $C_D^{i_o,m}$ at the angle of attack $\alpha^{i_o,m}$ are interpolated from tabulated polars. The generation of these polars is detailed in the next section. Once the lift and drag coefficients are known, normal force coefficient $C_n^{i_o,m}$ is calculated from (4.93) and the tangential force coefficient $C_t^{i_o,m}$ is calculated from eq. (4.95). Total loss factor $F^{i_o,m}$ is determined next with eqs. (4.96)-(4.98), followed by local thrust coefficient $C_T^{i_o,m}$ of eq. (4.70) to assess the nature of the element loading. Depending on the magnitude of the local thrust coefficient, under the conditions of eq. (4.99), an updated axial induction factor $a^{i_o,m+1}$ is found by either

the standard BEMT expression of eq. (4.92) or the Buhl form of eq. (4.101). An updated tangential induction factor $a_t^{i_o,m+1}$ is calculated according to eq. (4.94).

A relaxation factor f_r is applied at each update of the induction factors to limit the step change between successive iterations and improve code stability. The relaxation factor is applied to the axial induction factor iterations

$$a^{i_o,m+1} = a^{i_o,m} + f_r\left(a^{i_o,m+1} - a^{i_o,m}\right) \qquad m = 1,2,3\ldots \tag{4.102}$$

and similarly, for the tangential induction factor iterations

$$a_t^{i_o,m+1} = a_t^{i_o,m} + f_r\left(a_t^{i_o,m+1} - a_t^{i_o,m}\right) \qquad m = 1,2,3\ldots \tag{4.103}$$

The relaxation factor is currently initialized at 0.3 and it's slowly reduced if convergence isn't achieved by m=30.

The code developed for this thesis checks first whether the tangential induction factor has converged. If the updated tangential induction factor $a_t^{i_o,m+1}$ is not within 0.05% of the previous value $a_t^{i_o,m}$ then the previous steps are repeated, while holding the axial induction factor fixed, until the updated tangential induction factor has converged. The axial induction factor is then checked for convergence using the same 0.05% criterion. If the axial induction factor has not converged, then the relative inflow angle is updated with the new induction factors ($a^{i_o,m+1}$, $a_t^{i_o,m+1}$) and the whole process repeats again, updating both the axial and tangential induction factors. The solution procedure for a single element is illustrated by the flow chart in fig. 4.8.

Once converged inductions factors are found for all blade elements, relative inflow angle ϕ^i is used to calculate elemental loads F_n^i and F_t^i, defined by eq. (4.60).

Summing these elemental loads along the span of the blade, as in eqs. (4.61)-(4.64) and eqs. (4.72)-(4.76), to gives the total rotor thrust and torque respectively. The overall rotor thrust coefficient C_T, torque coefficient C_Q, and power coefficient C_P are subsequently determined using eqs. (4.1)-(4.3).

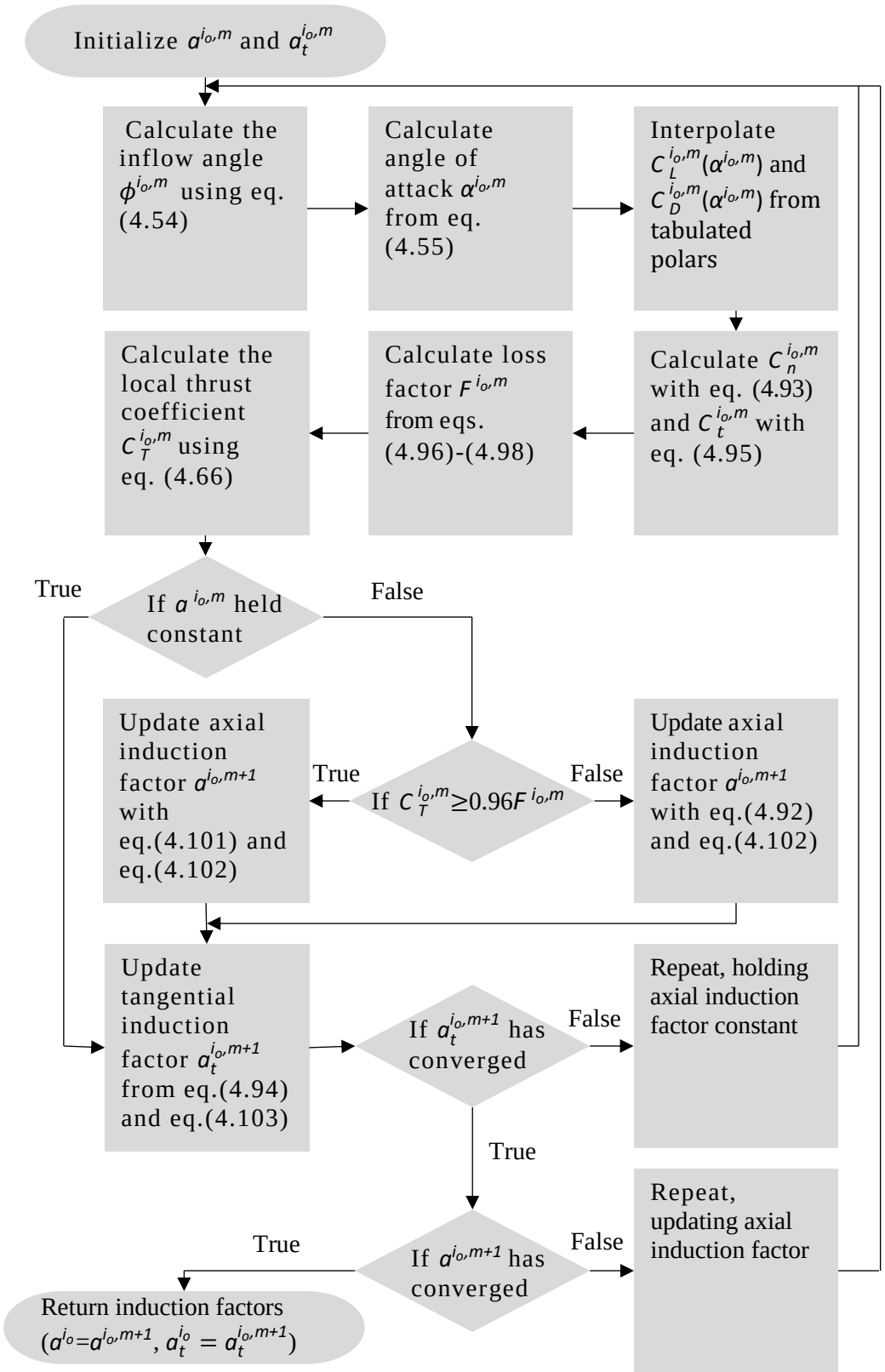

Figure 4.8: Flowchart of underlying BEM solution procedure for a single element ($i=i_o$, m=1,2,3…).

4.6 Airfoil Polars

Implementing the BEMT method described in the previous section requires foil polars containing the lift and drag coefficients as a function of angle of attack. This section details the process of generating these polars, which vary between blade elements as the airfoil and/or local Reynolds number change. Absent experimental data, the 2-D vorticity panel code XFOIL [116] was employed to calculate the lift, drag, and moment coefficients up through the stall angle. For the current blades, this ranges from approximately -10 degrees to 15 degrees. An open source wind turbine design tool called QBlade [117] was used to run a batch analysis on the Oceana foils because it incorporates both the XFOIL source code and a module for 360 degree polar extrapolation.

Each blade (inner and outer) was analyzed using XFOIL's viscous analysis mode at 13 locations—including 0%, 5%, 10%, 20%…90%, 95%, and 100% individual blade span—for Reynolds numbers (Re) of $1.5\text{x}10^5$, $3.0\text{x}10^5$, and $6\text{x}10^5$. These polars can be interpolated as the local Reynolds number along each blade section varies. In general, the turbine operates inside the XFOIL region. However, it can operate in the post-stall region outside this range so the lift and drag coefficients were extrapolated over a full range of 360 degrees, from -180 degrees to 180 degrees, using the Viterna and Corrigan method [118]. This also provides numerical stability if the angle of attack temporarily goes outside the XFOIL range during the iterative solution procedure.

According to Viterna and Corrigan the lift coefficient C_L is found by [118]

$$C_L = \frac{C_{D\max}}{2}\sin 2\alpha + \left[\left(C_{L stall} - C_{D\max}\sin\alpha_{stall}\cos\alpha_{stall}\right)\frac{\sin\alpha_{stall}}{\cos^2\alpha_{stall}}\right]\frac{\cos^2\alpha}{\sin\alpha} \tag{4.104}$$

and the drag coefficient C_D by

$$C_D = C_{D\max}\sin^2\alpha + \left[\frac{C_{D stall} - C_{D\max}\sin^2\alpha_{stall}}{\cos\alpha_{stall}}\right]\cos\alpha, \tag{4.105}$$

where the maximum drag C_{Dmax} is approximated using the blade's aspect ratio AR

$$C_{D\max} \simeq 1.11 + 0.018AR. \tag{4.106}$$

The stall subscript indicates the value of C_D and C_L at the stall angle of attack α_{stall}. The aspect ratio is 2 for the inner blade and 1.6 for the outer blade. Figures 4.9 and 4.10 are examples of extrapolated 360 polars for a NACA 2212 foil (Re=6x10^5) with a maximum drag coefficient of 1.8.

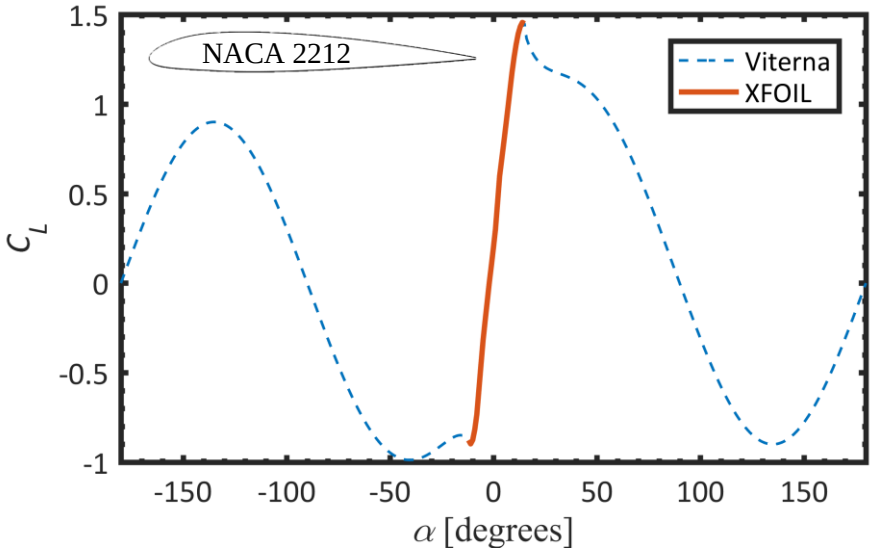

Figure 4.9: Lift coefficient plotted as a function of angle of attack. The orange solid line represents the low-angle of attack data generated by XFOIL and the blue dashed line is the extrapolated lift coefficient according to the Viterna and Corrigan model.

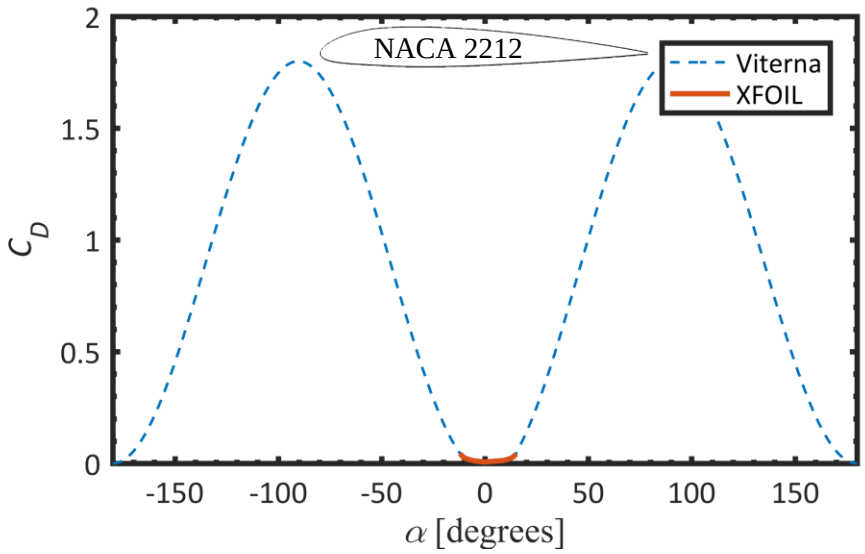

Figure 4.10: Drag coefficient plotted as a function of angle of attack. The orange solid line represents the low-angle of attack data generated by XFOIL and the blue dashed line is the extrapolated drag coefficient according to the Viterna and Corrigan model.

4.7 Cavitation

A cavitation check has been implemented in the BEM algorithm to ensure that cavitation does not occur within the operating limits of the turbine. Cavitation inception occurs when the pressure on a blade is less than or equal to the vapor pressure of the surrounding fluid [104] and results in significant accelerated-wear on the blade surface [107]. A methodology is adopted from [104,107] to predict the inception of cavitation, whereby a cavitation number $\sigma_c{}^i$ is calculated for each blade element

$$\sigma_c^i = \frac{\left(P_{atm} + \rho g h^i\right) - P_V}{\frac{1}{2}\rho u_{rel}^{i\,2}} \tag{4.107}$$

here P_{atm} is atmospheric pressure, ρ is again the fluid density, g is the acceleration due to earth's gravity, P_V is the vapor pressure of the fluid, and u_{rel}^i is the relative inflow velocity on the i^{th} element. The local element depth h^i is dependent on the tip immersion depth h_t, which is measured from the shallowest point, such that

$$h^i = h_t + (r_o - r^i). \tag{4.108}$$

The cavitation number found using eq. (4.107) is compared to the minimum local pressure coefficient C_p^i—determined from the 2D foil analysis in XFOIL—on the i^{th} blade element. If the magnitude of the minimum pressure coefficient is less than the local cavitation number $\sigma_c{}^i$, then cavitation is predicted not to occur. Because of the inherently low operating speeds of an 8-bladed turbine, a tip immersion of 76.2 mm (3 in.) was found to be sufficient for avoiding cavitation at all reasonable operating conditions.

4.8 Code Validation

A Matlab BEMT code based on the theory in sections 4.4 and 4.5 was validated against two established BEMT codes. The current code was used to evaluate the performance of a 5 MW reference turbine, defined by the National Renewable Energy Laboratory (NREL) in [119], over a range of tip-speed ratios. A model of the reference rotor is presented in fig. 4.11A. Results are then compared with NREL's CCBlade [120] and QBlade's rotor BEMT module [117]. QBlade has the option to

implement either a traditional Prandtl tip/hub-loss model or an alternative model proposed by Shen [111] so two separate simulations were run with QBlade.

Simulation parameters are outlined in table 4.1 along with the blade aerodynamic properties. Extrapolated 360 polars for the NREL turbine were prepared by Jonkman in [119] and are reproduced in Appendix E for reference. The lift and drag polars for all the non-circular airfoils are plotted in fig. 4.12. Blade discretization was kept to the 17 elements depicted in fig. 4.11B-C and defined in table 4.1.

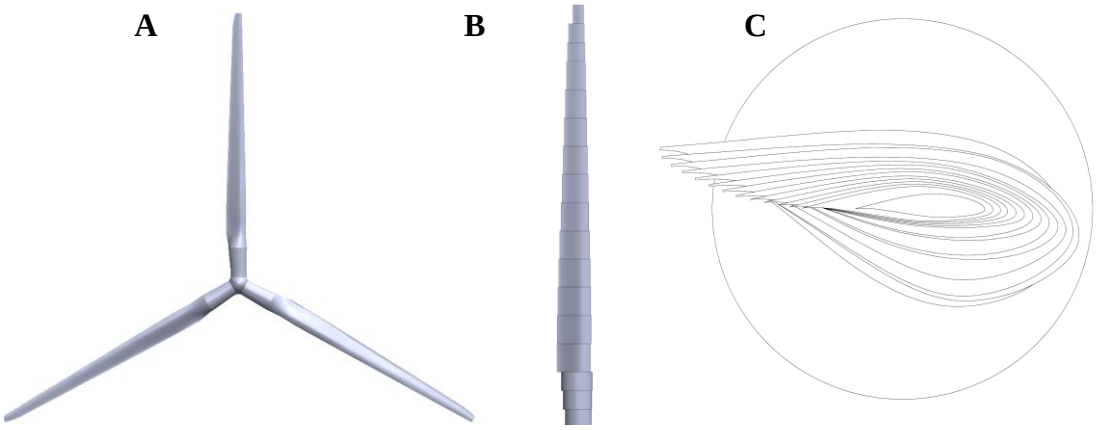

Figure 4.11: Model renderings of A) the 5 MW NREL rotor, B) the discretized reference blade (top view) and C) the stacked element foils (section view).

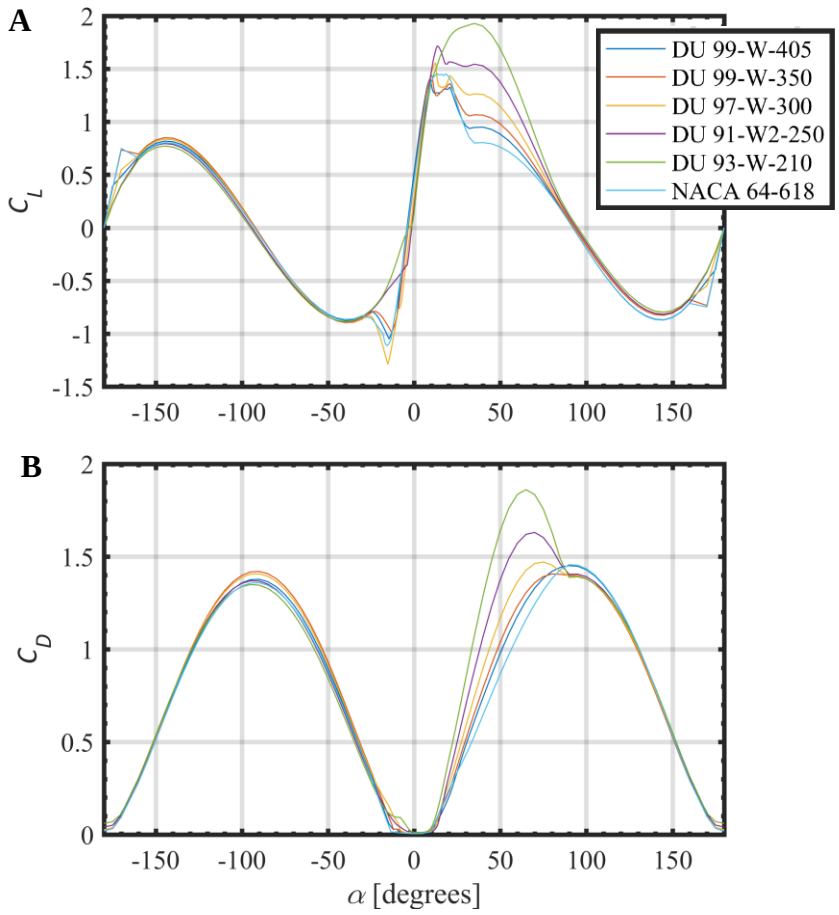

Figure 4.12: A) Lift polars and B) drag polars for NREL 5 MW reference turbine airfoils.

Induction factors were initialized at $a^{(1)}$=0.2 and $a_t^{(1)}$=0.0. On average, the axial induction factor converged after 13 iterations and the tangential induction factor converged in 5 iterations. Converged axial induction factors ranged from $0.026 \leq a \leq 0.777$, while tangential induction factors were found to be between $-0.109 \leq a_t \leq 0.121$. Figure 4.13 demonstrates the convergence behavior of the current BEMT solution procedure for a single tip-speed ratio. The convergence of all 17 blade elements is shown for the axial induction factor in fig. 4.13A, however, for clarity

fig. 4.13B only shows the convergence behavior of the tangential induction factor on a single representative element.

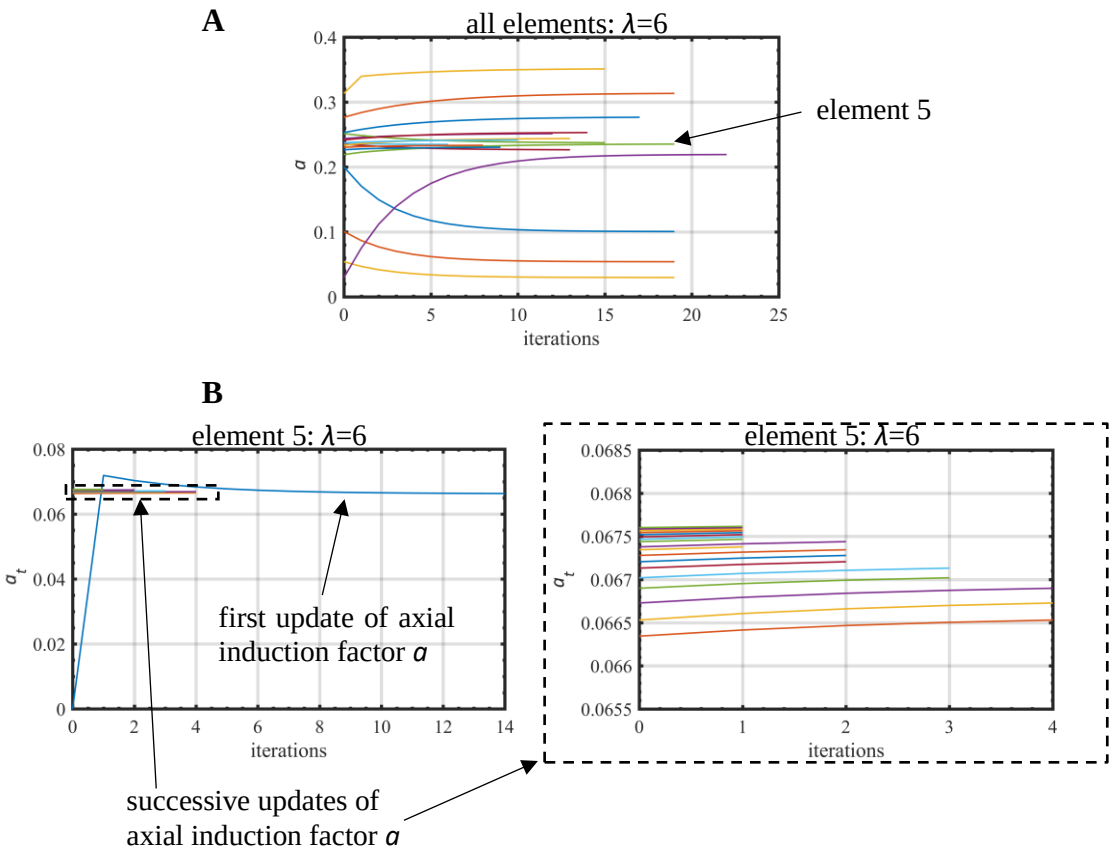

Figure 4.13: Convergence characteristics of A) the axial induction factor for all 17 elements at λ=6 and B) the tangential induction factor at element 5.

Coefficients C_P, C_T, and C_Q were calculated as function of tip-speed ratio using each of the BEMT codes. The code developed in this work is labeled current. Results for C_P, seen in fig. 4.14, closely align at low tip-speed ratios and are all within roughly 5% of each other at peak power coefficient. At higher tip-speed ratios the current model agrees well with CCBlade and QBlade when the Shen loss model is implemented.

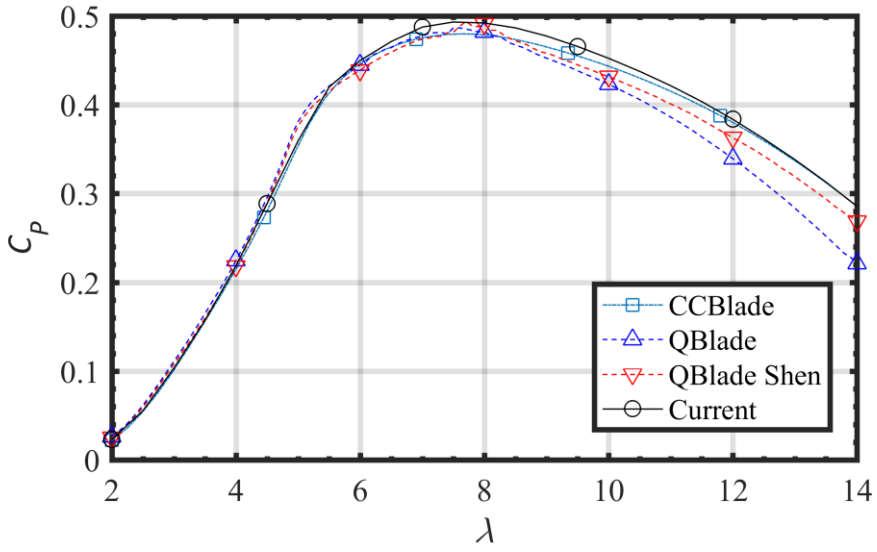

Figure 4.14: Predicted power coefficient C_P as a function of tip speed ratio λ for the 5 MW reference turbine.

There is excellent agreement on C_T among the three codes, plotted in fig. 4.15, at lower tip-speeds but results diverge slightly for QBlade at tip-speed ratios greater than 6. This is thought to be a consequence of QBlade not employing the Buhl correction to element thrust at high induction factors. The Shen loss model in QBlade predicts a significantly lower C_T at high tip-speed ratios. Shen et al. demonstrated a modest improvement in the correlation between predicted thrust and experimental results using their model [111]. Future work should evaluate the performance of the Shen model for incorporation into the current code.

Predicted C_Q curves are plotted in fig. 4.16. While they exhibit the same general trend, with the maximum C_Q being approximately equal across all three codes, there is a slight shift in the QBlade curves that cause peak C_Q to occur at a slower tip-speed ratio. The disparity between QBlade and the other codes in the high tip-speed ratio regime is less pronounced than in the power and thrust curves.

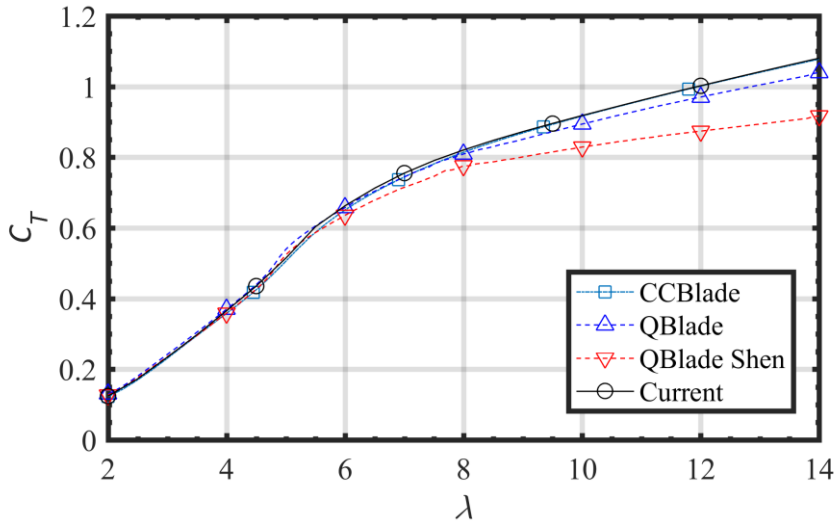

Figure 4.15: Predicted thrust coefficient C_T as a function of tip speed ratio λ for the 5 MW reference turbine.

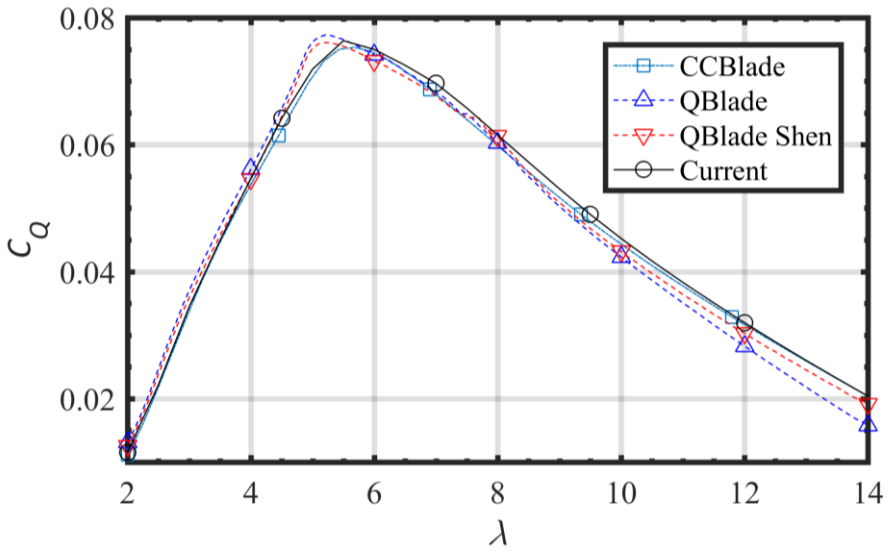

Figure 4.16: Predicted torque coefficient C_Q as a function of tip speed ratio λ for the 5 MW reference turbine.

The current Matlab BEM code produces very similar results to CCBlade over the whole range of tip-speed ratios. This is expected given that the current code employs the same model corrections—though with a very different solution procedure—as CCBlade. Results from the current code also matched up well with QBlade at low tip-speed ratios but diverged in the high tip-speed regime, where

increasing turbulence in the wake causes the basic BEMT to break down. At this point the corresponding correction factors play a more significant role and differing results are not surprising. Overall, the current code correlates well with both CCBlade and QBlade.

Table 4.1: NREL 5MW Reference Turbine Definition

R_{hub} [m]	1.5		
R_{tip} [m]	63		
Number of Blades	3		
ρ [kg/m^3]	1.225		
μ [N-s/m^2]	1.81x10^{-5}		
r [m]	c [m]	θ [deg.]	Foil Name
2.8667	3.542	13.308	Cylinder1
5.6	3.854	13.308	Cylinder1
8.3333	4.167	13.308	Cylinder2
11.75	4.557	13.308	DU 99-W-405
15.85	4.652	11.48	DU 99-W-350
19.95	4.458	10.162	DU 99-W-350
24.05	4.249	9.011	DU 97-W-300
28.15	4.007	7.795	DU 91-W2-250
32.25	3.748	6.544	DU 91-W2-250
36.35	3.502	5.361	DU 93-W-210
40.45	3.256	4.188	DU 93-W-210
44.55	3.01	3.125	NACA 64-618
48.65	2.764	2.319	NACA 64-618
52.75	2.518	1.526	NACA 64-618
56.1667	2.313	0.863	NACA 64-618
58.9	2.086	0.37	NACA 64-618
61.6333	1.419	0.106	NACA 64-618

4.9 Adaptation for Open-Centered Turbines

BEMT has so far been discussed in the context of traditional horizontal-axis turbines where the hub is located at the center of the rotor with blades extending radially outwards. It's thought that relatively minor modifications make the theory applicable to open-centered devices. The adjustments made to the BEM model to calculate the performance of an open-centered turbine are detailed in this section.

One of the core assumptions in BEMT was that the rotor could be broken into annular sections that don't interact with each other. Thus, each blade section can be analyzed independently regardless of its position relative to either the hub or the tip. The presence of a hub—and the effect it has on flow through the rotor—was introduced through the Prandtl tip/hub loss corrections in eq. (4.96)-(4.98). Therefore accommodating an open-centered turbine requires modifying the Prandtl tip/hub loss factors.

Figure 4.17A is a schematic showing the hub (red) and tip (blue) locations between which the loss factor would be applied on a traditional 3-bladed turbine. In fig. 4.17B the analogous locations are indicated for a generic 3-bladed open-centered turbine. Radial locations on the open-centered turbine are defined as r_1 at the tip of the inner blades, r_2 on the inside of the hub, r_3 on the outside of the hub, and r_4 at the tip of the outer blades.

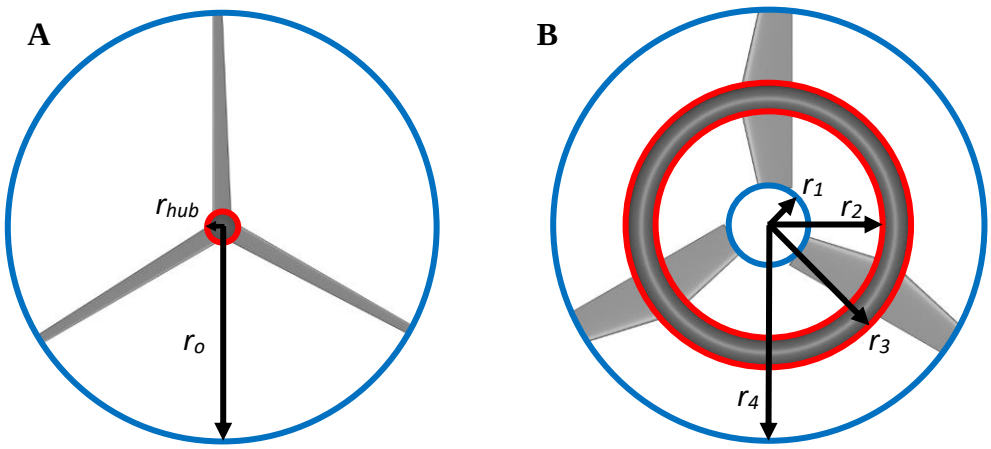

Figure 4.17: Schematic of model regions for A) a traditional 3-bladed turbine and B) the corresponding sections on an open-centered turbine. Radial locations are marked with red circles at the hub and blue circles at the blade tips.

The tip and hub loss factors on the outer blade elements ($r_3<r^i<r_4$) are unchanged from the Prandtl tip/hub loss corrections in eq. (4.96)-(4.98)

$$F_{tip}^{i}=\frac{2}{\pi}\cos^{-1}\left[\exp\left(-\frac{N_B\left(r_4-r^i\right)}{2r^i\sin\phi^i}\right)\right] \tag{4.109}$$

and

$$F_{hub}^{i}=\frac{2}{\pi}\cos^{-1}\left[\exp\left(-\frac{N_B\left(r^i-r_3\right)}{2r^i\sin\phi^i}\right)\right]. \tag{4.110}$$

The loss factors are then mirrored for the inner blade elements ($r^i<r_2$)

$$F_{tip}^{i}=\frac{2}{\pi}\cos^{-1}\left[\exp\left(-\frac{N_B\left(r^i-r_1\right)}{2r^i\sin\phi^i}\right)\right] \tag{4.111}$$

and

$$F_{hub}^{i} = \frac{2}{\pi}\cos^{-1}\left[\exp\left(-\frac{N_B\left(r_2 - r^i\right)}{2r^i \sin\phi^i}\right)\right]. \tag{4.112}$$

The total loss factor on each blade element is still found as the product of the tip and hub loss as

$$F^i = F_{tip}^{i} F_{hub}^{i}. \tag{4.113}$$

Total element loss factor F^i versus normalized span is plotted in fig. 4.18 for a generic 3-bladed open-centered turbine (see fig. 4.17B). A constant relative element inflow angle (ϕ^i=5 degrees) was used for both blades. In this case the radius of the open-center and the radial thickness of the hub were both set to 10% of the rotor span.

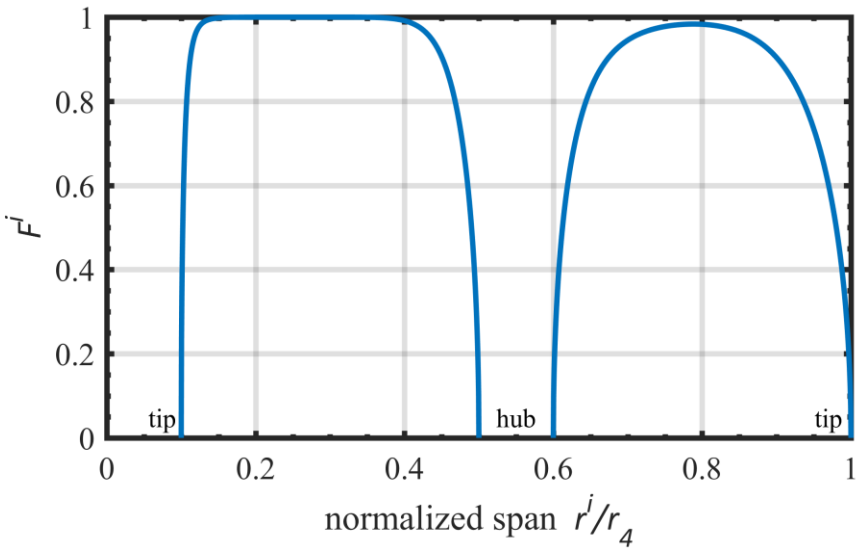

Figure 4.18: Loss factor F^i versus normalized span for an open-centered rotor with 3 blades operating at a constant relative inflow angle of 5 degrees.

4.10 Modeling Performance of an Open-Centered Turbine

The BEMT code detailed was used to predict the performance of the scaled open-centered turbine with Oceana blades. It's noted that the current model does not account for the effects of rake or skew present in the blades. Skew is defined by the angle between the reference line (aligned with the z-axis) and the mid-chord of the blade, while rake characterizes the axial displacement (in the x-direction) of the blade mid-chord from the rotor plane (y-z plane). The blade elements are shown skewed in fig. 4.19 to demonstrate how they capture the blade geometry, recognizing that the radial location remains the same and therefore the results of any BEMT analysis would be unchanged.

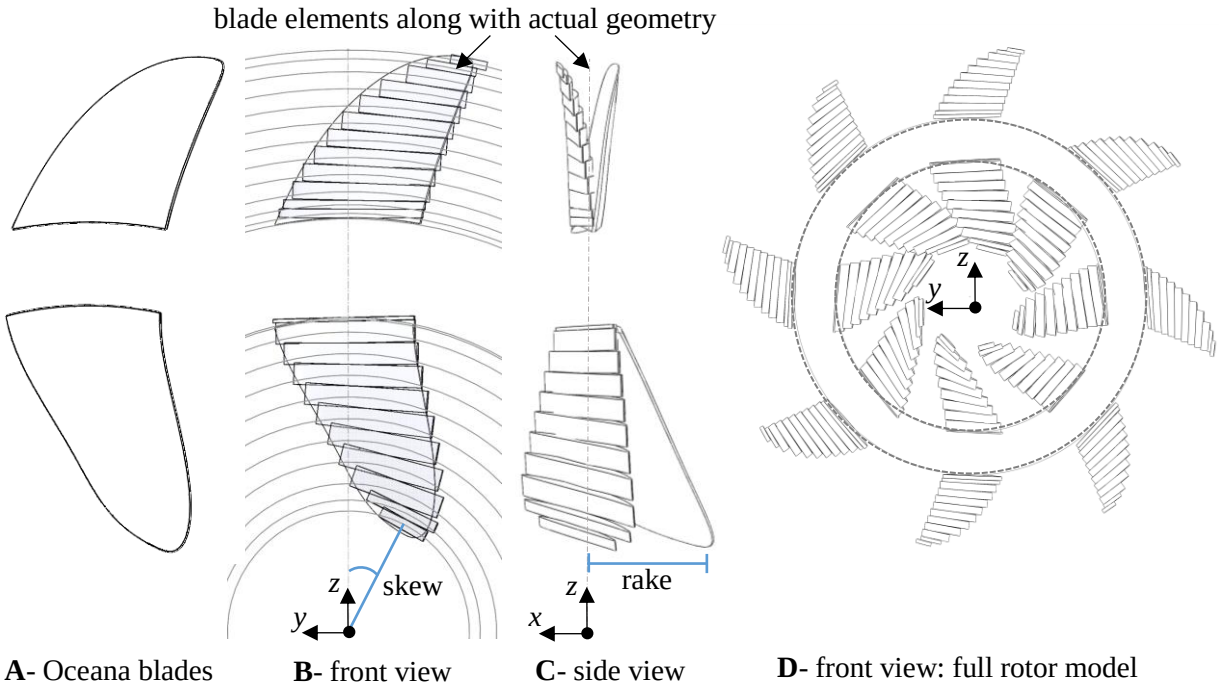

Figure 4.19: Graphic representation of **A)** Oceana blades **B)** overlaid with discrete blade elements shown from the front, **C)** shown from the side, and **D)** assembled into the full rotor open-centered turbine.

The modeling approach described thus far is fundamentally 2-D with corrections applied to account for 3-D effects at the tip and hub of the blades. Skew and rake both invoke radial or spanwise flow between elements, which is excluded in the BEMT derived in this work. Incorporating these additional elements of the blade geometry into the BEMT model with additional correction factors is outside the scope of the current research. While it isn't known how skew and rake would impact the performance predictions, it is expected that their inclusion would improve the cavitation characteristics of the blades.

The total swept area of the open-centered rotor is considered to exclude the area in the center where there are no blades or hub structure, such that

$$A_{rotor} = \pi\left(r_4^2 - r_1^2\right) \tag{4.114}$$

with r_4 and r_1 being the radius of the outer blade tip and the inner blade tip respectively. For the current test bed system with the Oceana blades installed: r_1=55 mm, r_2=150 mm, r_3=197 mm, and r_4=279 mm. Appendix F contains a summary of all the model input parameters along with tabulated output for two different load cases.

Figure 4.20 shows the thrust, torque, and power coefficients for the baseline blade configuration as a function of the dimensionless tip-speed ratio λ of eq. (4.4). The turbine operates near peak efficiency between tip-speed ratios from 1.5 and 2.1, with the peak power coefficient of 0.23 occurring at a tip-speed ratio of 1.8. Meanwhile, the thrust coefficient C_T is maximum at a tip-speed ratio of 1.4, where it's approximately 0.47, and has a negative slope throughout the region of greatest

C_P. A lower thrust coefficient results in lighter loading on the turbine support structure. Peak torque coefficient C_Q occurs near a tip-speed ratio of 1.1.

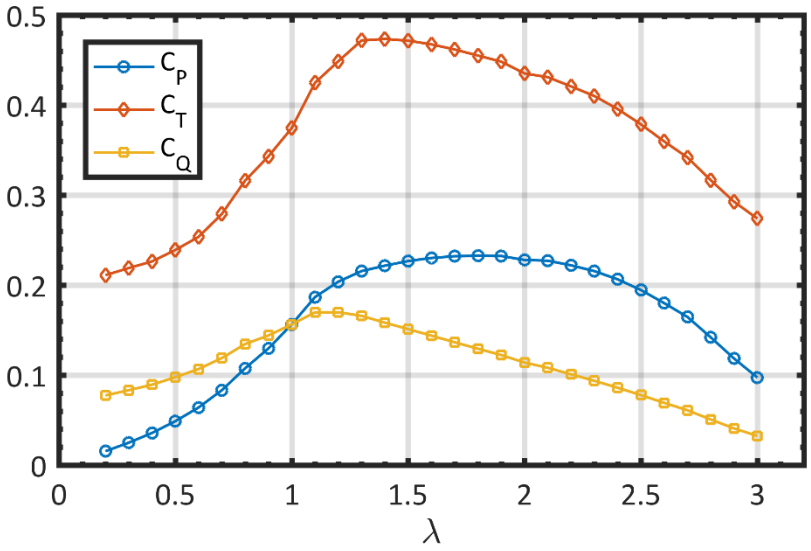

Figure 4.20: Predicted power coefficient C_P, thrust coefficient C_T, and torque coefficient C_Q as a function of tip speed ratio λ for the turbine in its base configuration.

It's also possible to model the effects of different blade pitches, which is of interest for studying future blade designs. Both blades were pitched by the same amount, between -15 degrees and +15 degrees, with the base configuration used as a reference. The resulting characteristic coefficients from each scenario are shown in Figs. 4.21-4.23, where 0 degrees represents the baseline configuration from Fig. 4.20. Decreasing the pitch up to 10 degrees results in an approximate 6% increase in power coefficient at the cost of a 51% increase in thrust loading. At -15 degrees pitch, the efficiency is lower than the reference configuration. A broader peak shifted towards higher tip-speed ratios—roughly spanning tip-speed ratios from 1.6 to 2.5 with a maximum at 2.0—is evident in the power coefficient curve for -10 degrees.

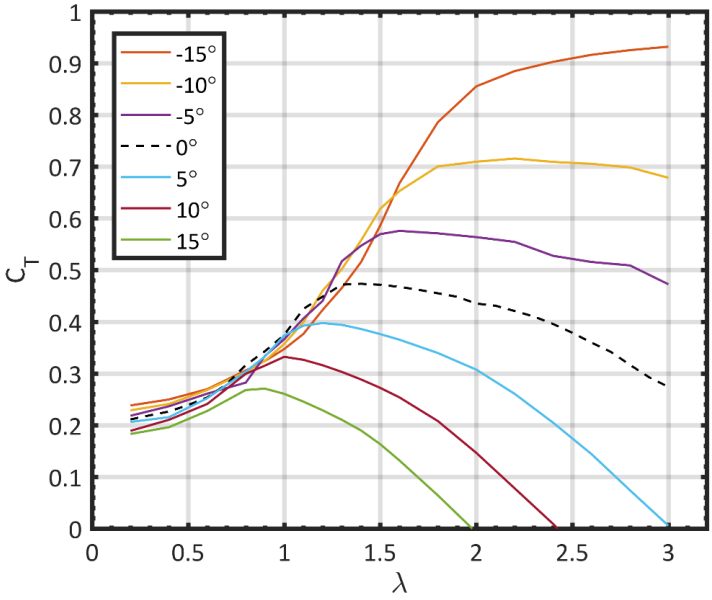

Figure 4.21: Predicted thrust coefficient C_T as a function of tip speed ratio λ for varying blade pitches. The baseline configuration is shown with by a dotted purple line.

Increasing the blade pitch shifts the power coefficient curve toward lower tip-speed ratios. All three coefficients become negative as the tip-speed ratio approaches 3, indicating that the turbine is behaving as a propeller and no longer extracting energy. This significantly restricts the range of tip-speed ratios that the turbine can operate at. Curves plotted in Figs. 4.21-4.23 show only the positive regions in which the turbine extracts energy from the flow. There is an increase in the maximum torque coefficient, but it's accompanied by a significant decline in the maximum power coefficient.

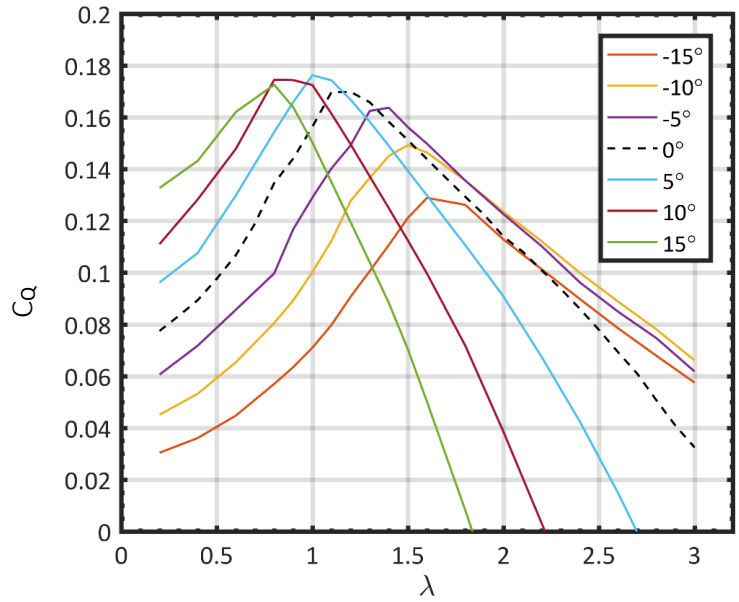

Figure 4.22: Predicted torque coefficient C_Q as a function of tip speed ratio λ for varying blade pitches. The baseline configuration is shown with by a dotted purple line.

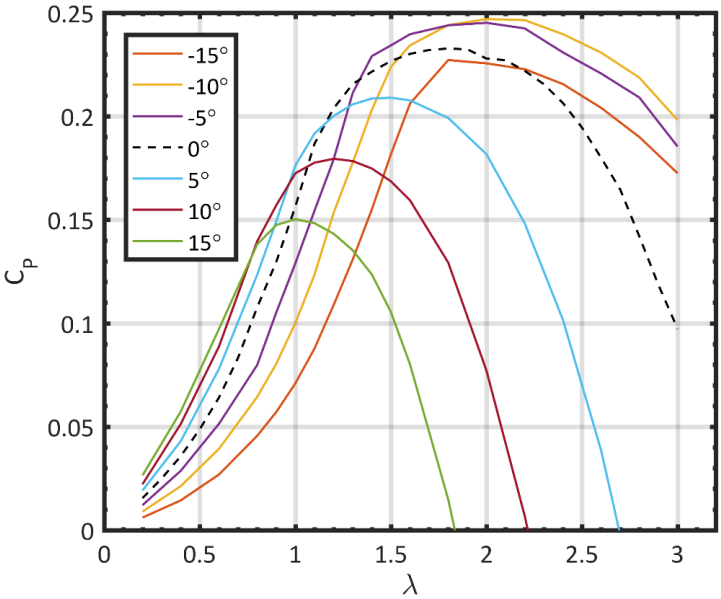

Figure 4.23: Predicted power coefficient C_P as a function of tip speed ratio λ for varying blade pitches. The baseline configuration is shown with by a dotted purple line.

Flow speed was fixed at 3.5 m/s to investigate the spanwise blade loading as function of tip-speed ratio, which can be controlled through the resistive load on the

generator. A representative sample of normal and tangential loads (F_n^i, F_t^i) on each blade element are presented in fig. 4.24. Tip-speed ratios between 0 and 2.8 (~30-340 rpm) were studied to identify the peak load conditions. Maximum loading occurred at a tip-speed ratio of 0.9 (~100 rpm) on the inner blades. Loads continued to increase on the outer blades before peaking at a tip-speed ratio of 1.6 (~190 rpm).

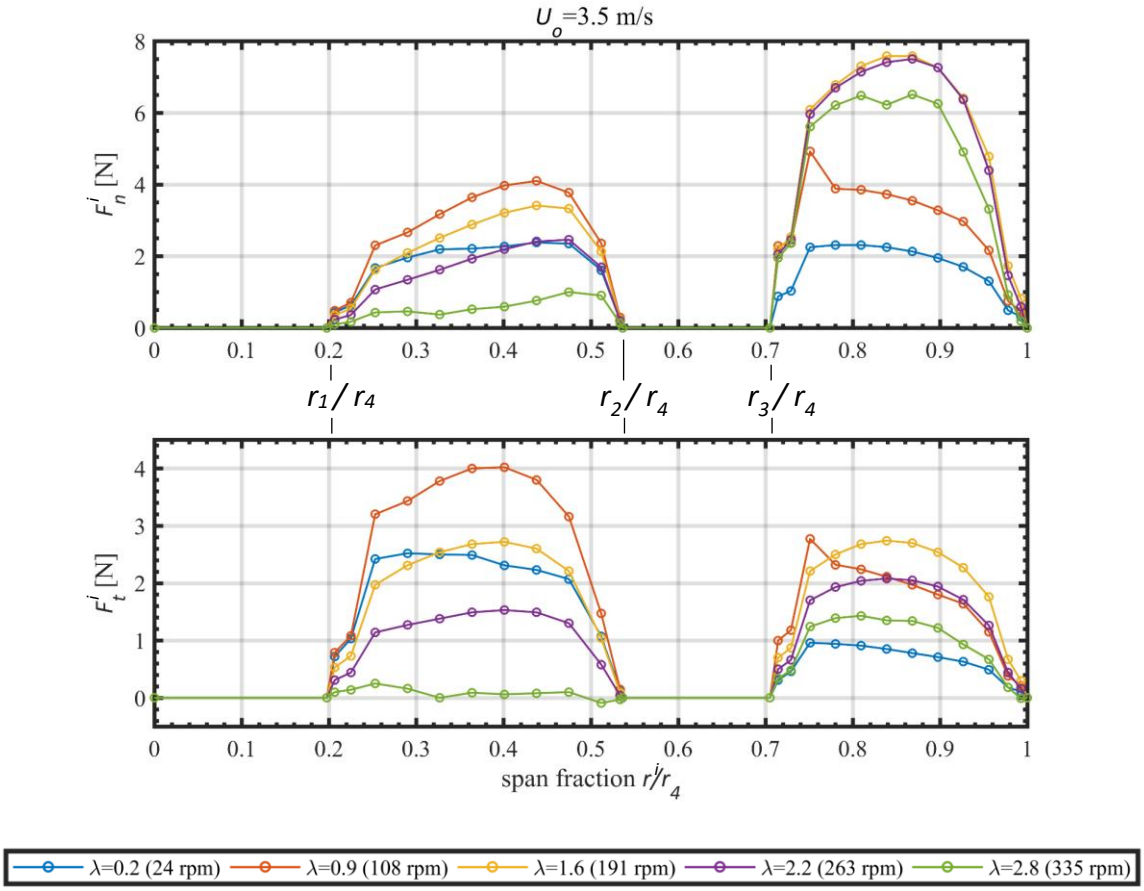

Figure 4.24: Simulated spanwise loads on the inner blades at select rotor speeds. The free stream velocity was fixed at 3.5 m/s.

The element-wise thrust (T^i), torque (Q^i), and power (P^i) are plotted for select tip-speed ratios in fig. 4.25. It's evident that the highly pitched inner blade plays a significant role in torque generation at low speeds (~50% of total rotor torque Q at

λ=0.4) but tapers off as the speed increases (~20% of total rotor torque Q at λ=2.4). At medium to high speeds the outer blade generates significantly more torque (~70% and 80% of total rotor torque Q for λ=1.4 and λ=2.4 respectively), and as a result more power, than the inner blade. Finally, the contributions of each element were summed to find the total rotor thrust (T), rotor torque (Q), and rotor power (P) at all simulated rotor speeds and plotted in fig. 4.26.

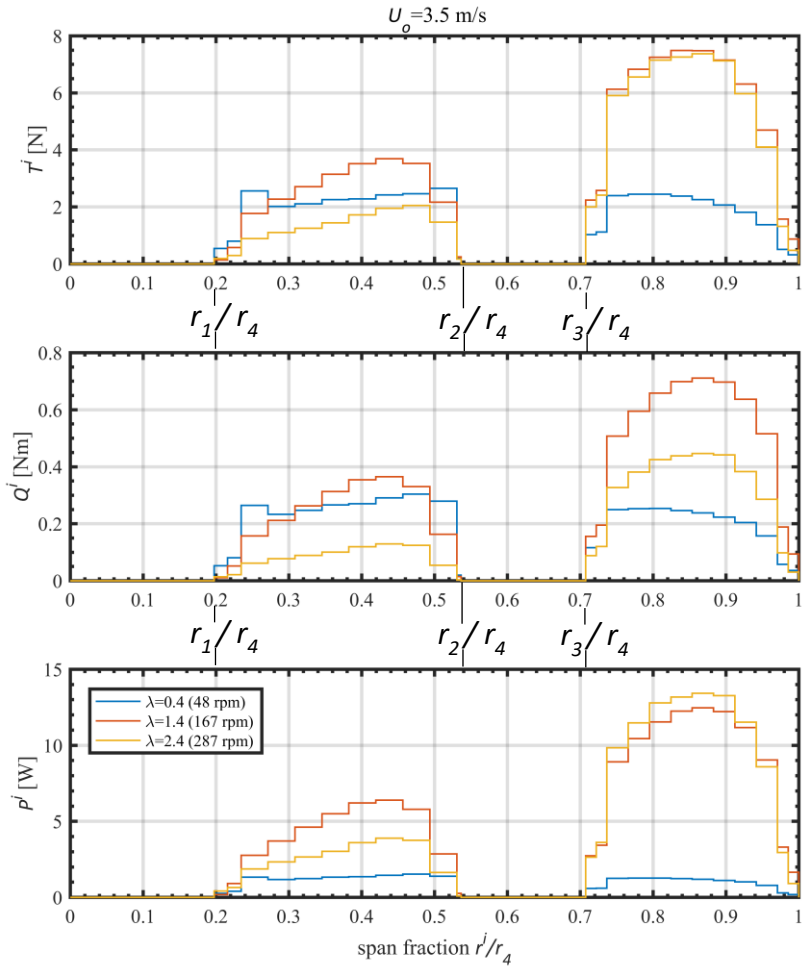

Figure 4.25: Blade element thrust (T^i), torque (Q^i), and power (P^i) distribution at selected tip-speed ratios with a constant free stream velocity of 3.5 m/s.

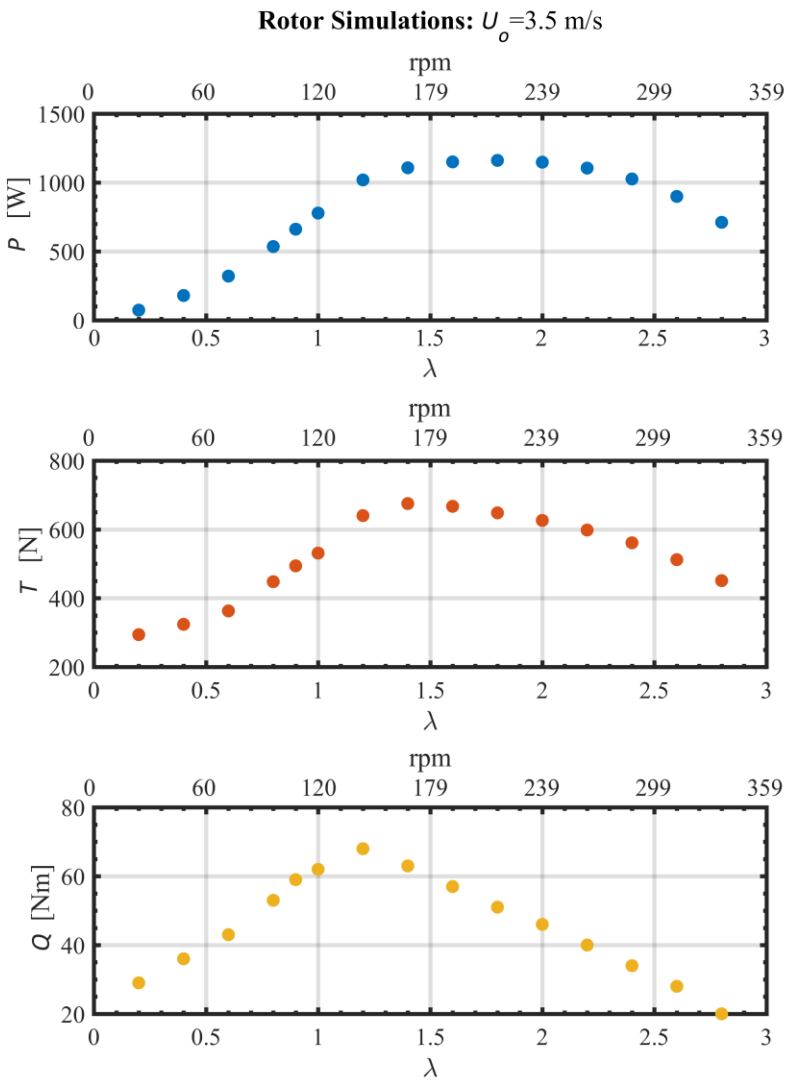

Figure 4.26: Variation in rotor power (P), thrust (T), and torque (Q) over a range of rotor speeds with a constant free stream velocity of 3.5 m/s. Equivalent speed in units of rpm is given along the top axis.

Chapter 5. Rotor Blade Analysis

A set of PLA blades was fabricated by FDM to validate the turbine test rig and measure the performance of the scaled Oceana blades. This chapter details the structural design process for the blades. Hydrodynamic loads found in the chapter 4 are applied to finite element models (FEM) of the blades to study stresses at the root. Results from static proof tests are used to correlate model displacement, and in conjunction with fatigue tests validate the blade's structural integrity.

5.1 Load Cases

Two primary load cases were considered to ensure safe operation: a maximum normal operating condition and an emergency stop. Maximum normal operating loads were established using the BEMT code described in chapter 4. A maximum flow speed of 3.5 m/s was assumed—providing sufficient range for testing the turbine at most naturally occurring flow speeds—and a range of tip-speed ratios from 0.2 to 2.8 were studied. A maximum load case was determined for each blade according to the rotational speed at which the greatest blade-root bending moment was generated. Root moments, M_n due to normal forces and M_t due to tangential forces, are plotted in fig. 5.1 for both blades as function of rotor speed (at U_o=3.5 m/s). The inner blades experience greater loads at low tip-speeds, with its heaviest loading at a tip-speed ratio of 0.9. Forces are greatest on the outer blade at a tip-speed ratio of 1.6.

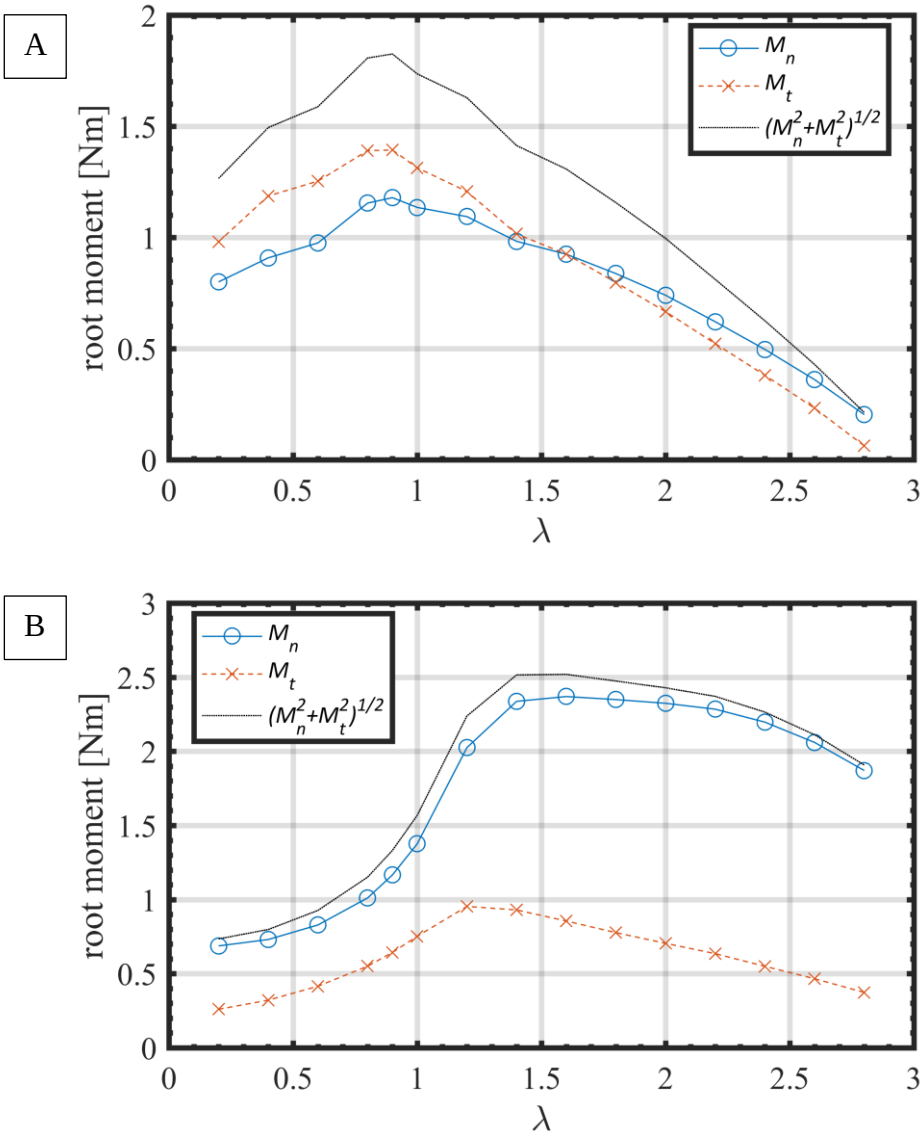

Figure 5.1: Maximum root bending moments for the A) inner blade and B) outer blade plotted as a function of tip-speed ratio at a free stream velocity of 3.5 m/s.

Converged forces and hydrodynamic moments for each element are plotted in fig. 5.2 and fig. 5.3 with respect to the rotor axis. Moments are calculated about the quarter chord of the foil section with a positive moment pitching the leading upwards (increasing the angle of attack). Despite being relatively small compared to the hydrodynamic loads at speeds below 200 rpm, centripetal forces were included in the

analysis of both blades at their maximum operating condition. Total centripetal forces summed about the centroid of the blade root have a magnitude of 2.97 N on the outer blade and 0.74 N on the inner blade.

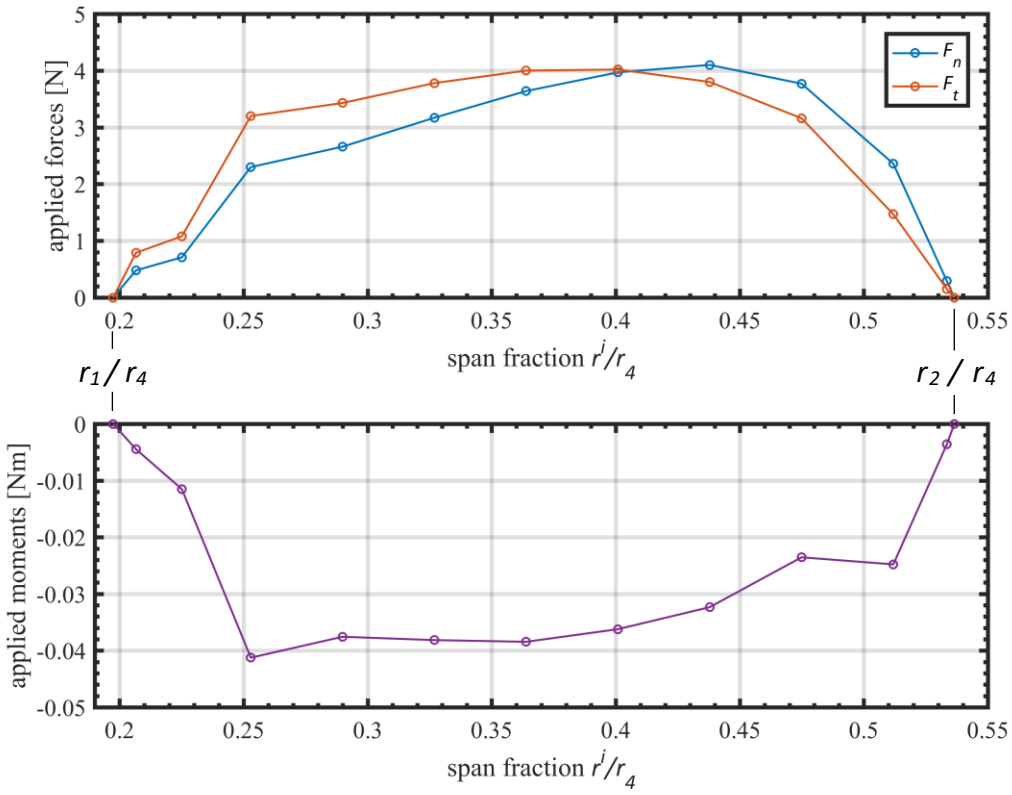

Figure 5.2: Maximum operating loads case for the inner blades at 3.5 m/s and λ=0.9. Normal (flapwise bending) and tangential (edgewise bending) loads reference the rotor plane. Applied hydrodynamic moments (torsion) are calculated about the quarter chord.

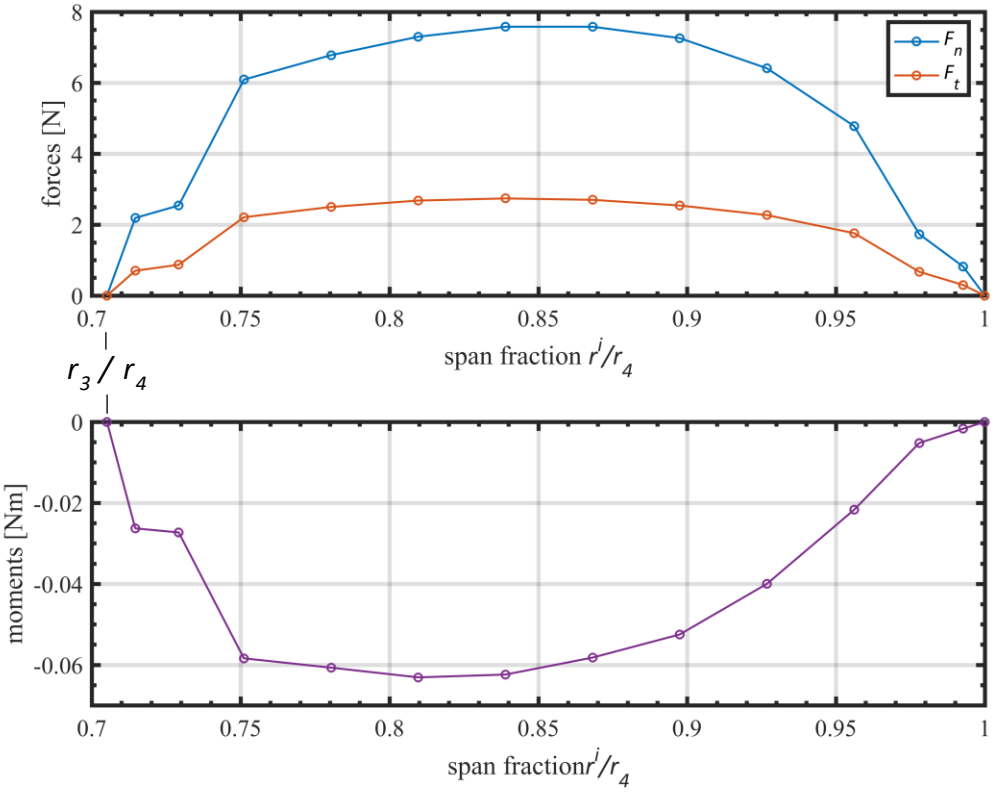

Figure 5.3: Maximum operating load case for the outer blades at 3.5 m/s and λ=1.6. Normal (flapwise bending) and tangential (edgewise bending) loads reference the rotor plane. The applied hydrodynamic moments (torsion) are calculated about the local quarter chord.

An emergency stop resulting from bearing or gear malfunction was considered in addition to the case of normal operation. The maximum flow speed at the stop is again 3.5 m/s. When the blades are locked from rotation they generate a drag load found by

$$D = qSC_{D\max} \tag{5.1}$$

where q is the dynamic pressure

$$q = \frac{1}{2}\rho U_o^2, \tag{5.2}$$

S is the blade area, and C_{Dmax} is approximated using eq. (4.106). Total drag force D is 38 N on each inner blade and 30 N on each outer blade. A tabular summary of each load case is included in Appendix F.

5.2 Effective Material Properties

Material properties used in constructing finite element models of the blades are introduced in this section. The FDM manufactured blades are composed of 10-layer "sub-laminate" $[0_2/\pm45/90]_s$ that repeats through the thickness of the blade. Effective elastic constants can be calculated for the sub-laminate to represent the overall blade as an equivalent homogenous-orthotropic material [121].

These smeared elastic constants are assembled from the stiffness matrices of the individual FDM layers or lamina. The stiffness matrix of the k^{th} lamina $[c]^{(k)}$ in the material reference frame is calculated by taking the inverse of the compliance matrix $[s]^{(k)}$

$$[c]^{(k)} = \left([s]^{(k)}\right)^{-1} \tag{5.3}$$

Where the compliance matrix is equal to

$$[s]^{(k)} = \begin{bmatrix} 1/E_1 & -\nu_{12}/E_1 & -\nu_{13}/E_1 & 0 & 0 & 0 \\ -\nu_{12}/E_1 & 1/E_2 & -\nu_{23}/E_2 & 0 & 0 & 0 \\ -\nu_{13}/E_1 & -\nu_{23}/E_2 & 1/E_3 & 0 & 0 & 0 \\ 0 & 0 & 0 & 1/G_{23} & 0 & 0 \\ 0 & 0 & 0 & 0 & 1/G_{13} & 0 \\ 0 & 0 & 0 & 0 & 0 & 1/G_{12} \end{bmatrix}. \tag{5.4}$$

The stiffness matrix is transformed into the structural frame ($\left[\bar{c}\right]^{(k)}$) through the product

$$\left[\bar{c}\right]^{(k)} = \left[T\right]^{(k)}\left[c\right]^{(k)}\left(\left[T\right]^{(k)}\right)^{T} \tag{5.5}$$

where the transformation matrix $[T]^{(k)}$ is determined by the angle of the k^{th} lamina $\theta^{(k)}$

$$\left[T\right]^{(k)} = \begin{bmatrix} \cos^2\theta^{(k)} & \sin^2\theta^{(k)} & 0 & 0 & 0 & -2\sin\theta^{(k)}\cos\theta^{(k)} \\ \sin^2\theta^{(k)} & \cos^2\theta^{(k)} & 0 & 0 & 0 & 2\sin\theta^{(k)}\cos\theta^{(k)} \\ 0 & 0 & 1 & 0 & 0 & 0 \\ 0 & 0 & 0 & \cos\theta^{(k)} & \sin\theta^{(k)} & 0 \\ 0 & 0 & 0 & -\sin\theta^{(k)} & \cos\theta^{(k)} & 0 \\ \sin\theta^{(k)}\cos\theta^{(k)} & -\sin\theta^{(k)}\cos\theta^{(k)} & 0 & 0 & 0 & \cos^2\theta^{(k)} - \sin^2\theta^{(k)} \end{bmatrix}. \tag{5.6}$$

A smeared stiffness matrix for the sub-laminate $\left[\bar{\bar{c}}\right]$ is then assembled according to [121]

$$\bar{\bar{c}}_{ij} = \begin{cases} \sum_{k=1}^{N} v^{(k)}\left(\bar{c}_{ij}^{(k)}\right) & i,j = 1,2,3,6 \\ \frac{1}{\Delta}\sum_{k=1}^{N}\frac{v^{(k)}\left(\bar{c}_{pq}^{(k)}\right)}{\Delta^{(k)}} & i,j = 4,5 \end{cases} \tag{5.7}$$

where

$$\Delta^{(k)} = c_{44}^{(k)}c_{55}^{(k)} - \left(c_{45}^{(k)}\right)^2 \tag{5.8}$$

and

$$\Delta = \left(\sum_{k=1}^{N}\frac{v^{(k)}c_{44}^{(k)}}{\Delta^{(k)}}\right)\left(\sum_{k=1}^{N}\frac{v^{(k)}c_{55}^{(k)}}{\Delta^{(k)}}\right) - \left(\sum_{k=1}^{N}\frac{v^{(k)}c_{45}^{(k)}}{\Delta^{(k)}}\right)^2. \tag{5.9}$$

Here N is the total number of layers within the sub-laminate and the volume fraction of the k^{th} lamina, $v^{(k)}$, is found by

$$v^{(k)} = \frac{t^{(k)}}{h} \tag{5.10}$$

where $t^{(k)}$ is the thickness of the of the k^{th} layer and h is the total thickness of the sub-laminate (h=2.5 mm). In this case, all layers have the same thickness so $v^{(k)}$=0.1.

Equivalent elastic coefficients are found from the smeared compliance matrix $\left[\bar{\bar{s}}\right]$, where $\left[\bar{\bar{s}}\right] = \left[\bar{\bar{c}}\right]^{-1}$,

$$E_x = \frac{1}{\bar{\bar{s}}_{11}},\ E_y = \frac{1}{\bar{\bar{s}}_{22}},\ E_z = \frac{1}{\bar{\bar{s}}_{33}}$$

$$G_{yz} = \frac{1}{\bar{\bar{s}}_{44}},\ G_{xz} = \frac{1}{\bar{\bar{s}}_{55}},\ G_{xy} = \frac{1}{\bar{\bar{s}}_{66}}$$

$$\nu_{yz} = -\frac{\bar{\bar{s}}_{23}}{\bar{\bar{s}}_{22}},\ \nu_{xz} = -\frac{\bar{\bar{s}}_{31}}{\bar{\bar{s}}_{11}},\ \nu_{xy} = -\frac{\bar{\bar{s}}_{21}}{\bar{\bar{s}}_{11}}. \tag{5.11a-i}$$

A summary of the mechanical properties derived from eqs. (5.3)-(5.11a-i) for the finite element model is provided in table 5.1. Transverse isotropy has been assumed at the lamina level. Thus E_2=E_3, ν_{13}=ν_{12}, G_{13}=G_{12}, and

$$G_{23} = \frac{E_2}{2\left(1+\nu_{23}\right)}. \tag{5.12}$$

Young's modulus E_1 and E_2 (E_L and E_T from table 3.4) were measured experimentally, while G_{12} (G_{LT} from table 3.4) was calculated using eq. (3.1). Values for the Poisson's ratios ν_{23} and ν_{12} (ν_{LT} from table 3.4) come from the sources [122] and [96] respectively.

Table 5.1: Elastic Constants [MPa]

Lamina			$[0_2/\pm45/90]_s$	
E_1	3,396	Table 3.4	E_x	2,981
E_2	2,618	Table 3.4	E_y	2,828
E_3	2,618	Table 3.4	E_z	2,619
G_{23}	1,064	Eq. (5.12)	G_{yz}	1,038
G_{13}	1,000	Table 3.4	G_{xz}	1,025
G_{12}	1,000	Table 3.4	G_{xy}	1,071
ν_{23}	0.23	[122]	ν_{23}	0.26
ν_{13}	0.33	[96]	ν_{13}	0.28
ν_{12}	0.33	[96]	ν_{12}	0.32

Effective strength properties in the x-y plane were developed by applying unit loads to the built up sub-laminate and performing a progressive failure analysis. A yield SF of 1.1 and an ultimate SF of 1.5 were used along with the B-basis properties from table 3.3. Normal tensile strength in the z-direction F_{zt} is set to the lamina tensile strength at 90 degrees while the compressive strength F_{zc} was computed in section 3.4. Additional out of plane shear strengths F_{yz} and F_{xz} are assumed to be the same as the in-plane lamina shear F_{xy} (F_s), meaning the shear strength between adjacent filaments is equivalent to the interlaminar shear strength. Table 5.2 contains a summary of allowable strength components.

The effective material properties defined in this section are representative of regions in the blade with integer numbers of the sub-laminate $[0_2/\pm45/90]_{ns}$ (n=1,2,3…). Between those regions, the properties are more of an approximation. Locations with an integer number of sub-laminates are documented in fig. 5.4 with thickness contours.

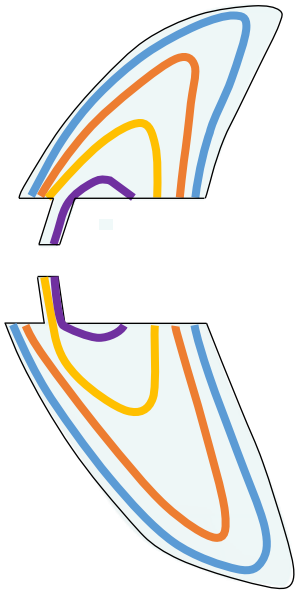

Figure 5.4: Blade thickness contours indicating regions with integer multiples of the sub-laminate $[0_2/\pm45/90]_{ns}$. Blue lines represent n=1, orange n=2, yellow n=3, and purple n=4.

Table 5.2: Strength Allowables [MPa]

Lamina			$[0_2/\pm45/90]_s$	
F_{1t}	35.38	Table 3.3	F_{xt}	20.14
F_{1c}	-59.37	Section 3.4	F_{xc}	-36.20
F_{2t}	14.75	Table 3.3	F_{yt}	16.19
F_{2c}	-59.37	Section 3.4	F_{yc}	-33.36
F_s	10.18	[98]	F_{zt}	14.75
			F_{zc}	-59.37
			F_{xy}	10.87
			F_{yz}	10.18
			F_{zx}	10.18

5.3 Model Construction

This section describes the construction of the global finite element models used to predict stress at the blade roots. Ten-node tetrahedral elements were used to capture the blade geometry without introducing excessive degrees of freedom. Blades were fabricated with a rectangular root and subsequently bonded to interlocking cylindrical adapters shown in fig. 5.5. The adapters were meshed separately from the blade bodies. Glued contacts were defined between the bonded surfaces to connect the two bodies.

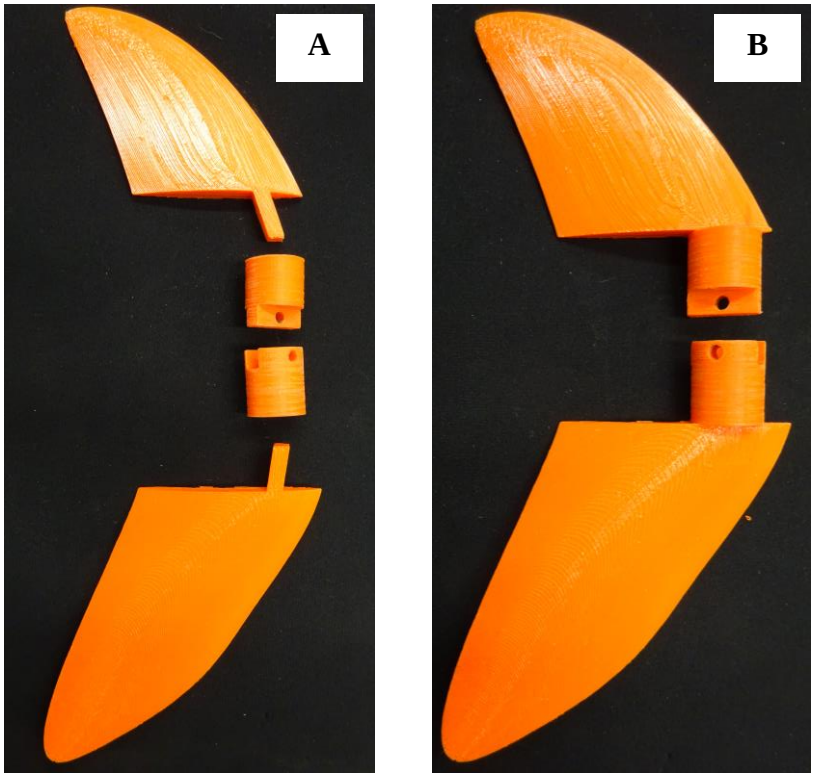

Figure 5.5: Photographs of blade assembly process showing the blades A) before and B) after bonding the interlocking hubs to the blade root.

Hydrodynamic loads at maximum operating conditions are applied through the local quarter-chord, at the center of each BEMT blade element listed in Appendix F, as a series of concentrated nodal forces and moments. Rigid RBE3 elements are used to transfer load to surrounding nodes. The drag force in the emergency stop load case is distributed uniformly to the upstream face of the blade. Figure 5.6 shows the basic elements of the model for the operating load case. Point loads are depicted with green arrows, constraints are shown with blue triangles, and glued contact surfaces are colored orange. The global model coordinate system is depicted in the lower-left corner and the material coordinate system is identified near the root of the blade. The rotor plane is perpendicular to the global x-axis with flow in the positive x-direction.

The initial mesh was sized to generate multiple elements through the thickness of the blade. It was subsequently refined until tip displacement and stress at the root of the blade converged. Stresses in the small filleted regions at the blade edges, highlighted in fig. 5.7, are not fully resolved in these global models.

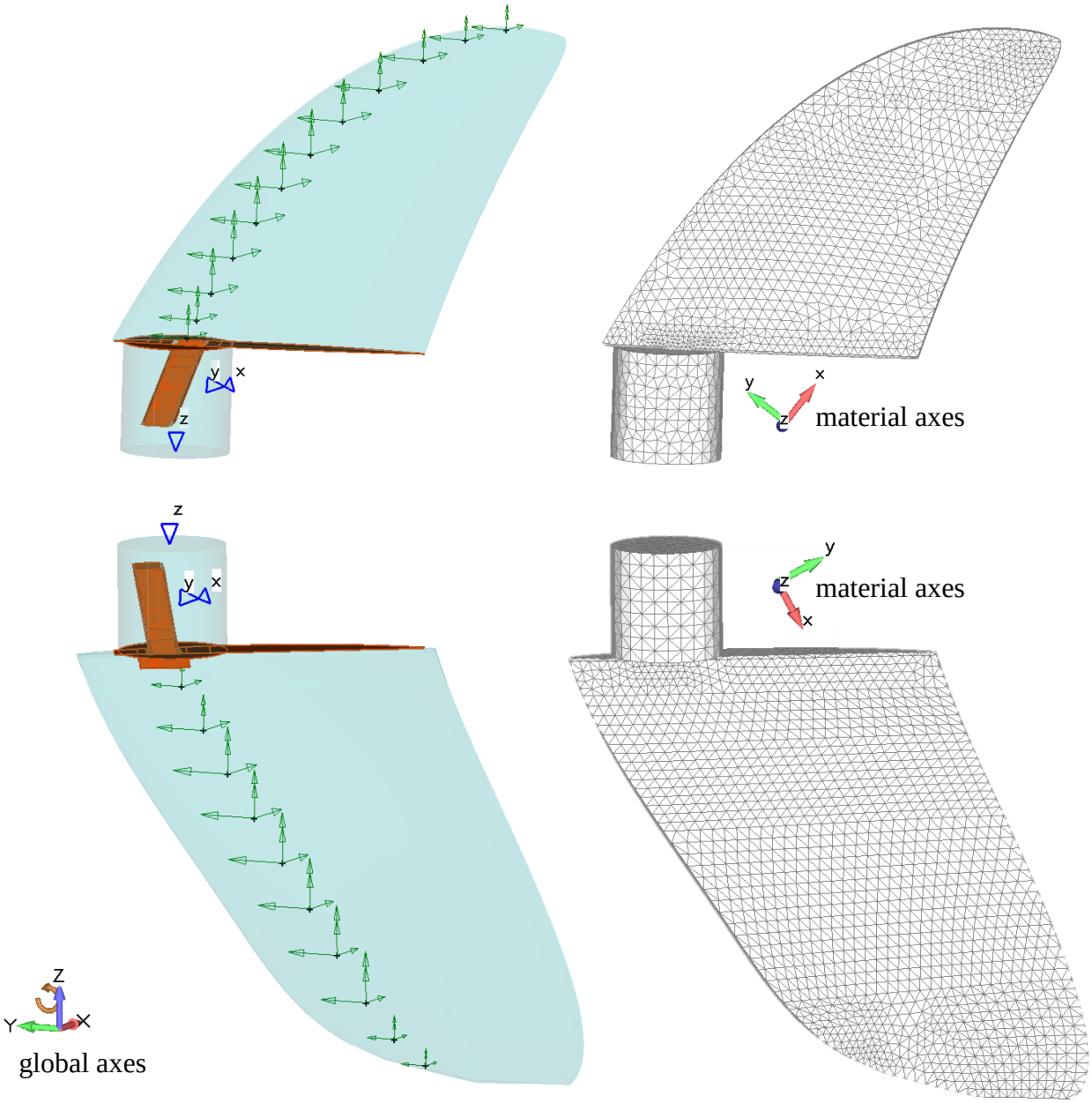

Figure 5.6: FEM of both blades. Load vectors appear as green arrows. Surface boundary conditions are identified with a blue triangle and labeled by the corresponding degree of freedom. Glued contact regions between the blade root and hub attachment are orange.

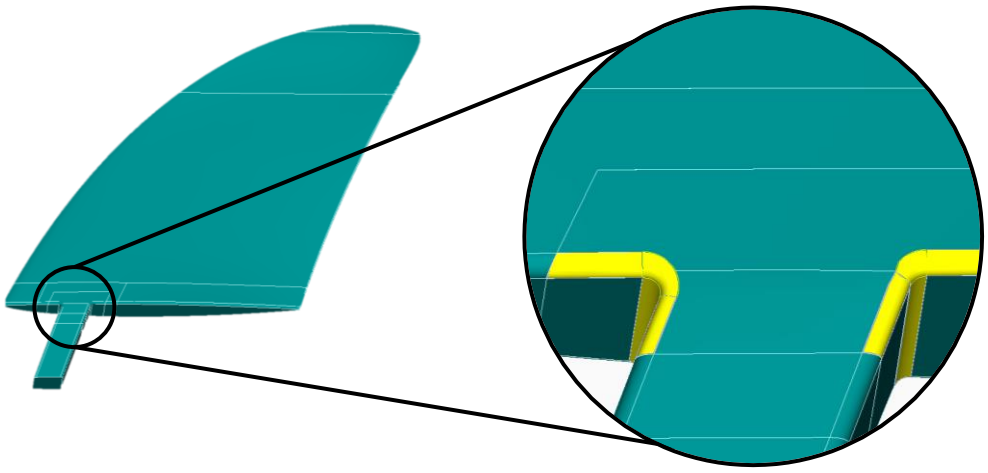

Figure 5.7: Edge geometry at the blade roots.

5.4 FEA Results

This section includes a short summary of the important FEA results. Margins of safety (MS) are calculated using a maximum stress failure criterion according to the strength allowables listed in table 5.2. Stress contours have been deliberately scaled to illustrate the stress field across the entire blade without outsize influence from errant edge elements. For the Von Mises stress contours the scale is set from 0 to 26 MPa.

Contours of tensile normal stress are scaled from 0 to 22 MPa with the second highest level set to the relevant allowable strength. Thus any element shaded red has exceeded the allowable. A similar approach was applied to compressive normal stress contours, which are scaled from -40 to 0 MPa with the second lowest level set such that any element shaded fuchsia has exceeded the allowable strength. The local regions of excessive stress at the blade root attachment are a consequence of local

mesh density and the stress singularity at the sharp corners. Further detailed modeling with mesh refinement shows local yielding of the material in these areas.

The maximum operating load produced a total tip deflection 1.92 mm in the outer blade. A contour of the Von Mises stress is plotted in fig. 5.8 on both the face (upstream side) and the back (downstream side) of the blades. The largest stress components, with respect to the material axes, are the normal stress σ_{xx} and the transverse shear stress τ_{zx} at the glued contact. The material axes and normal stress contours are plotted in fig. 5.9. Excluding elements in the highlighted regions of fig 5.7, which are not accurately resolved in the present model, the minimum MS is 0.03. Note that elements forming the glued hub attachments, shown in fig 5.6, were included in the analysis but are hidden in the following stress contours to highlight results on the blade.

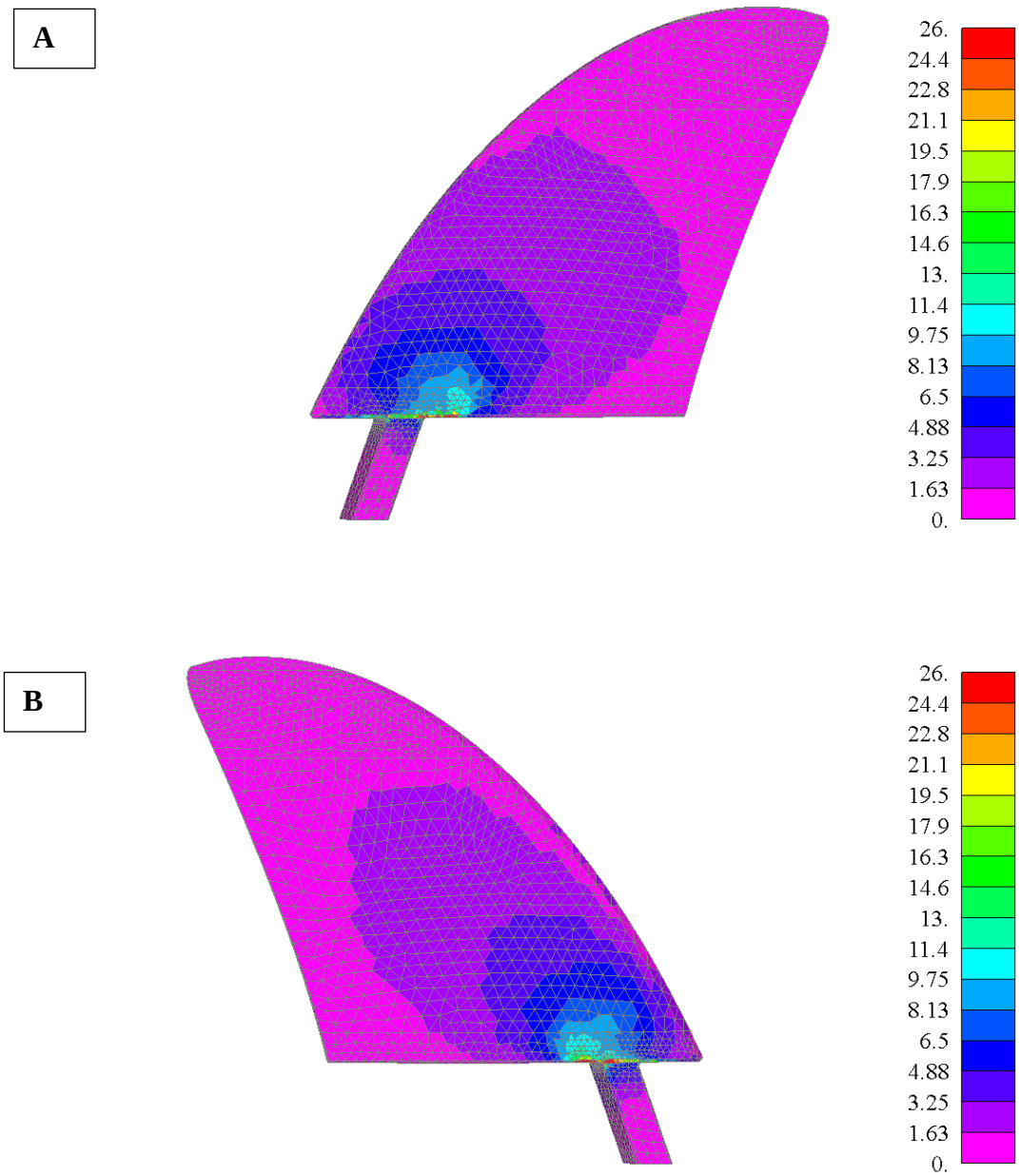

Figure 5.8: Von Mises stress in MPa on the outer blade A) face and B) back at maximum operating load. No elemental averaging has been applied. Elements composing the cylindrical hub have been hidden.

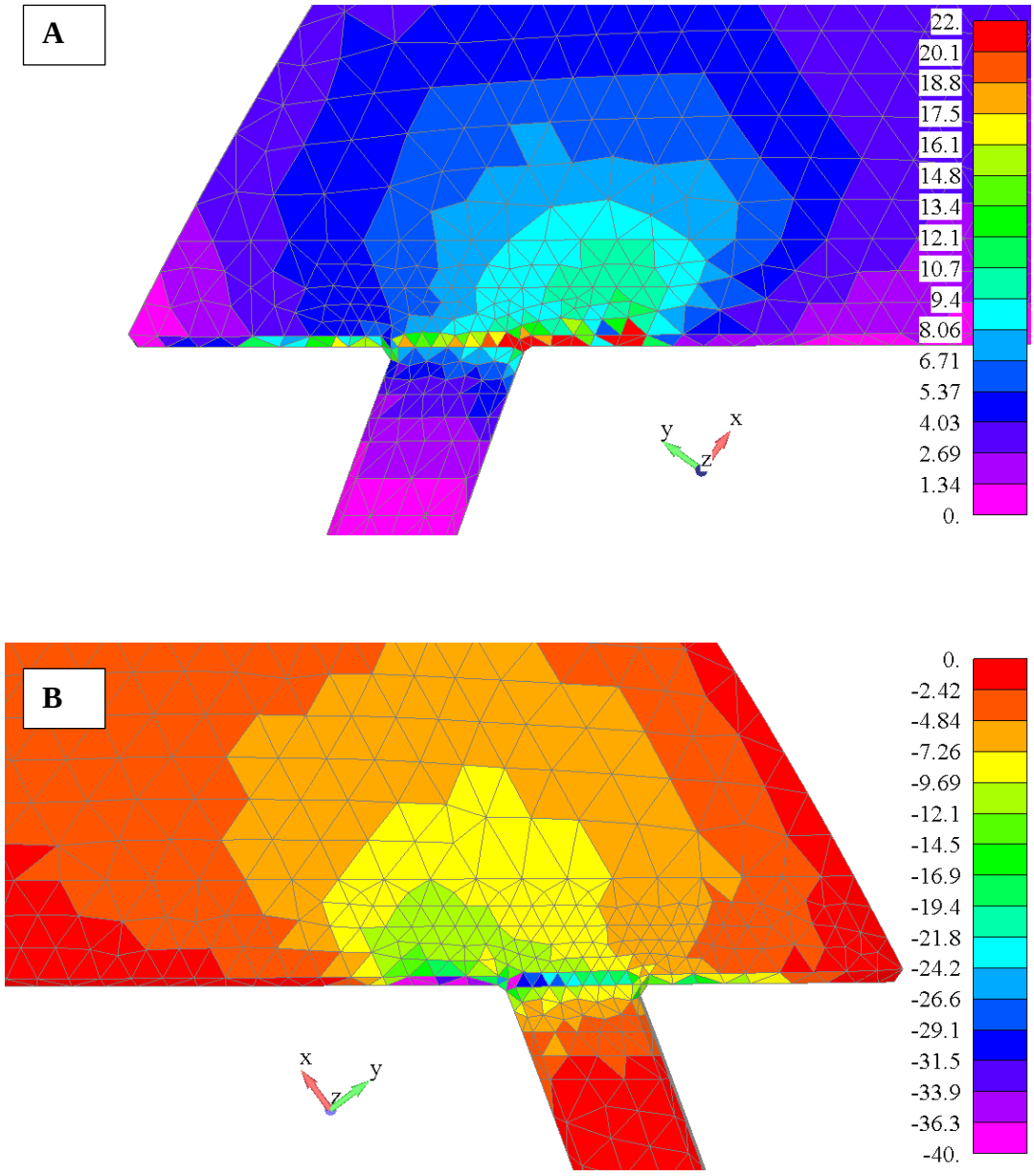

Figure 5.9: Maximum A) and minimum B) x-direction normal stress at the blade root, in MPa, for the maximum operating load. The material axis is shown beside the root of the blade. No elemental averaging has been applied.

The inner blades undergo a tip displacement of 1.40 mm when subject to the maximum operating load. Resulting Von Mises stress is shown in fig 5.10. It's apparent in fig. 5.8 that the significantly stressed portion of the outer blade extends to about 50% span. Equivalent stress levels only extend to about 30% span in the inner blade. This suggests that future efforts to tailor print parameters like print density or layer orientation out towards the blade tip should start with the inner blades. The largest component of stress is in the material x-direction. A contour of the x-direction normal stress σ_{xx} is presented in fig. 5.11. Excluding the edge regions identified in fig. 5.7 the minimum MS is 0.6.

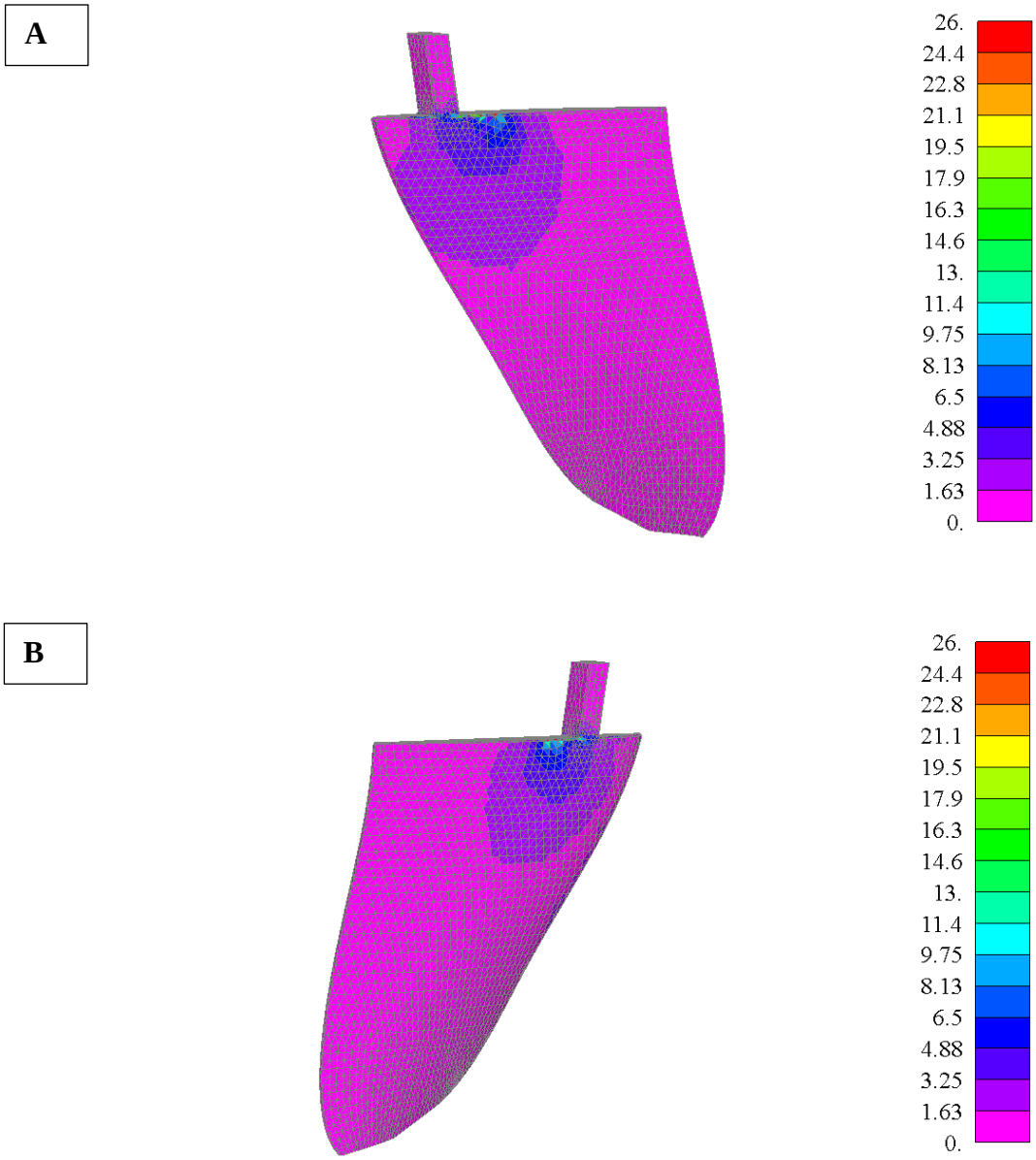

Figure 5.10: Von Mises stress in MPa on the inner blade A) face and B) back at maximum operating load. No elemental averaging has been applied. Elements composing the cylindrical hub have been hidden.

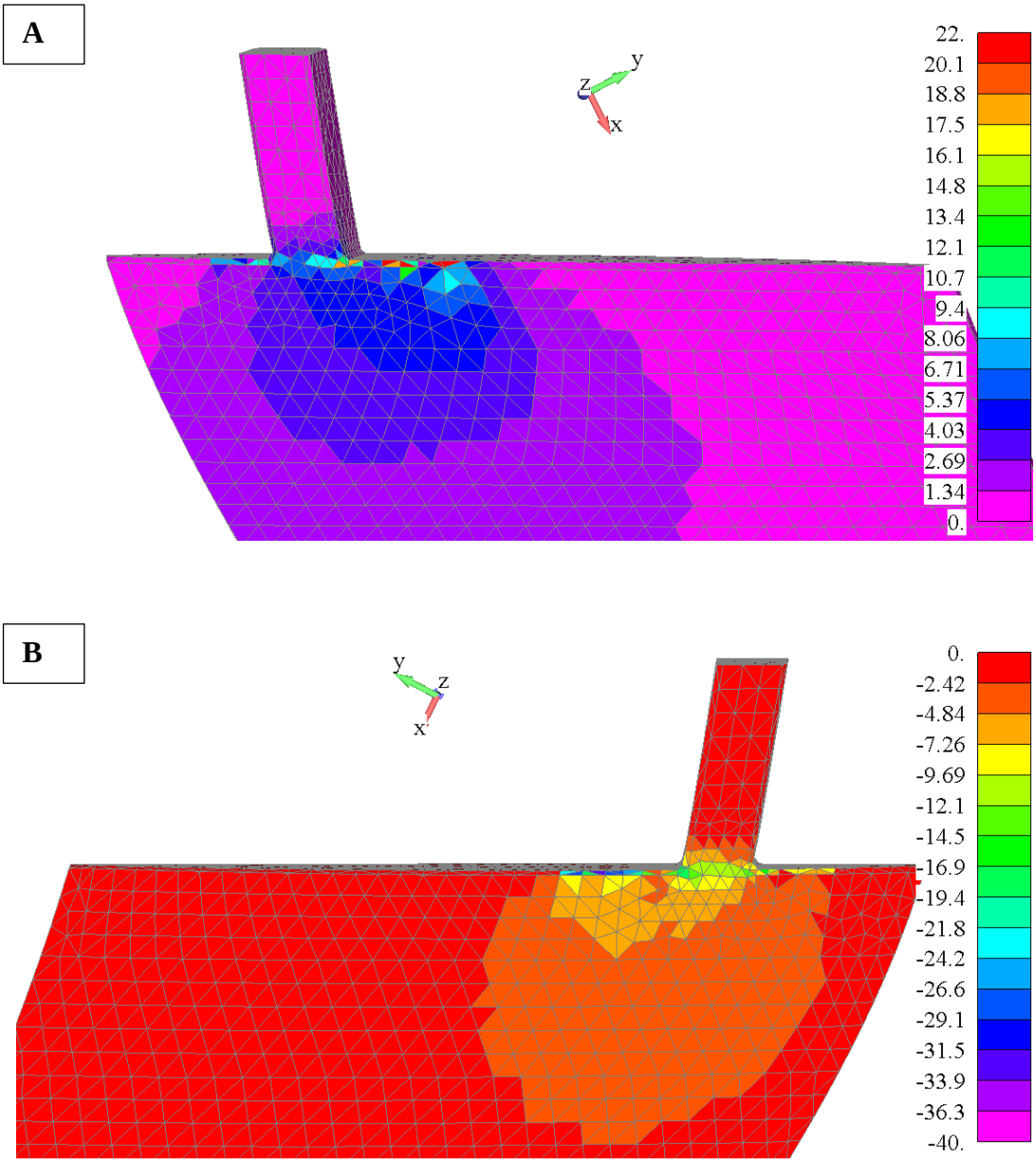

Figure 5.11: Maximum A) and minimum B) x-direction normal stress in MPa for the maximum operating load. The material axis is shown at the root of the blade. No elemental averaging has been applied.

Analysis of the emergency stop scenario generally yielded lower stresses than the maximum operating load case. Von Mises stress contours are presented for the inner and outer blades in fig. 5.12 and fig. 5.13 respectively. Minimum MS's (outside the unresolved edges) occur on the blade face, 0.88 on the inner blade and 0.97 on the outer blade, due tensile stress in the x-direction. Normal stress contours in the material's x-direction are displayed in fig. 5.14 and fig. 5.15. A summary of all margins of safety for both load cases is provided in table 5.3.

Table 5.3: Minimum Margins of Safety

		Max Operating Load	Emergency Stop
	Dir.	MS	MS
Inner Blade	x	0.60	0.88
	y	1.90	2.29
	z	1.40	2.09
	xy	1.26	0.94
	yz	2.81	2.81
	zx	1.47	2.02
Outer Blade	x	0.07	0.97
	y	0.60	3.71
	z	0.34	2.60
	xy	0.77	2.20
	yz	0.88	4.64
	zx	0.03	1.59

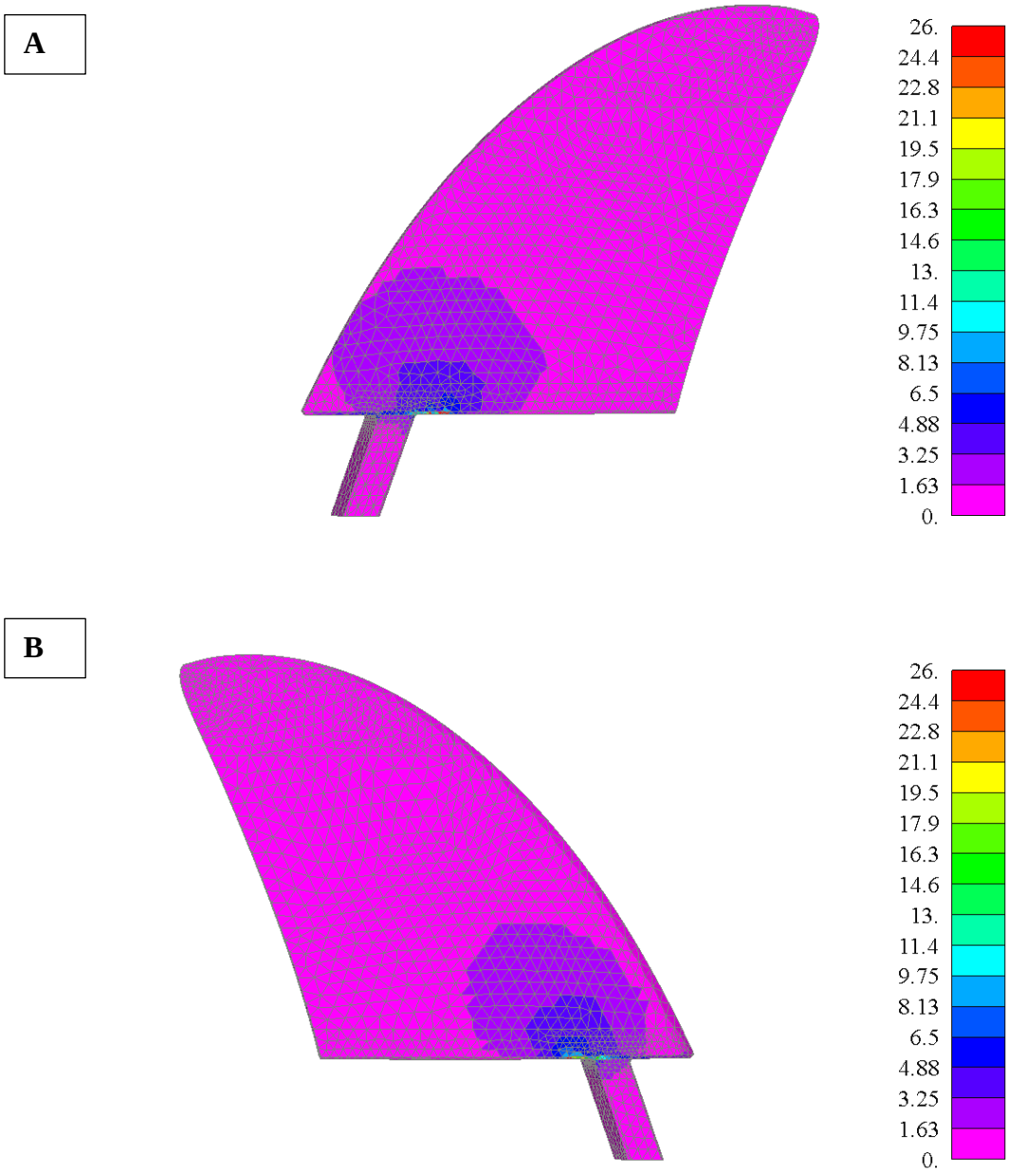

Figure 5.12: Von Mises Stress in MPa on the outer blade A) face and B) back for the emergency stop load case. No elemental averaging has been applied. Elements composing the cylindrical hub have been hidden.

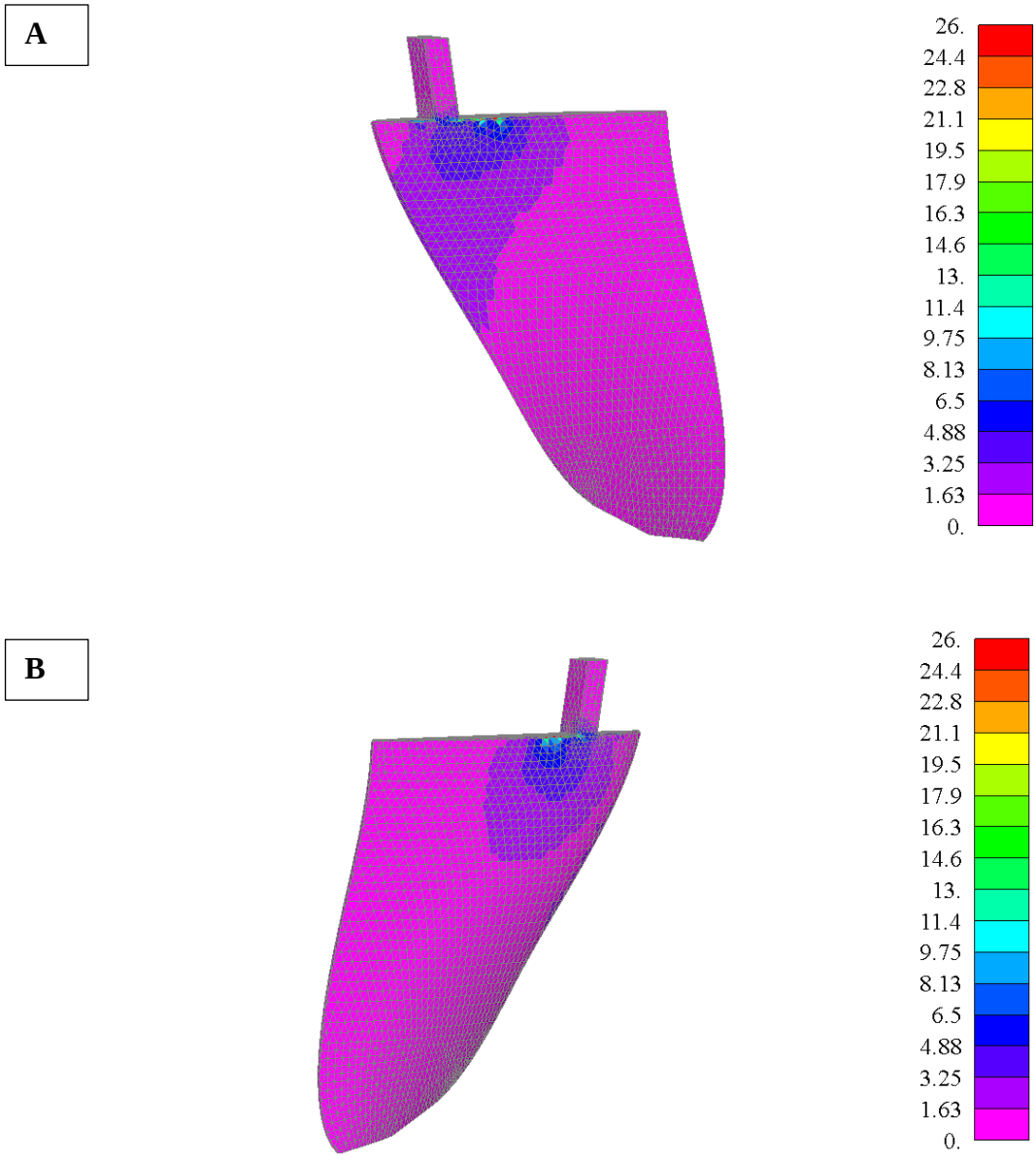

Figure 5.13: Von Mises Stress in MPa on the inner blade A) face and B) back for the emergency stop load case. No elemental averaging has been applied. Elements composing the cylindrical hub have been hidden.

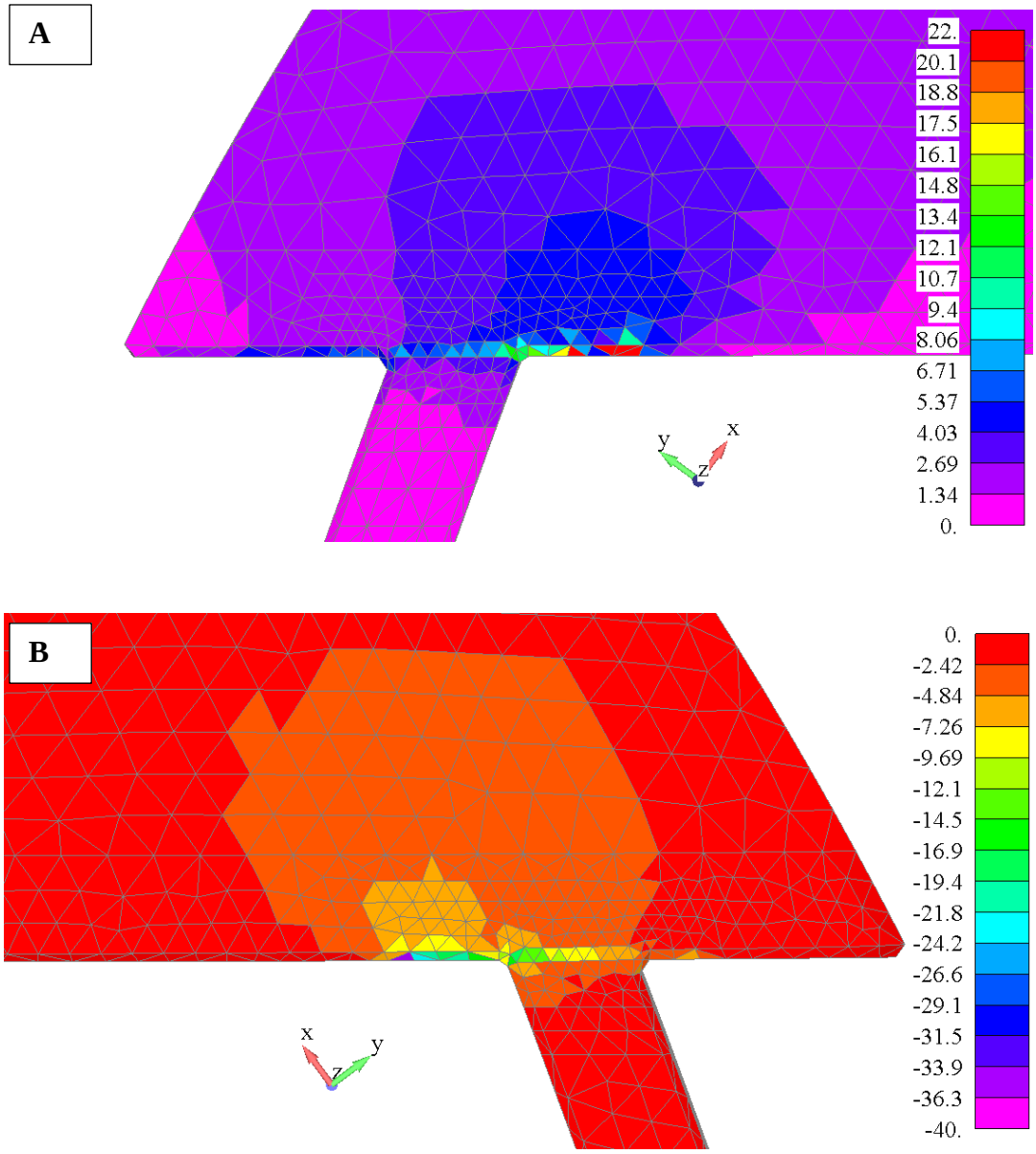

Figure 5.14: Outer blade maximum A) and minimum B) x-direction normal stress in MPa for the emergency stop load case. The material axis is shown at the root of the blade. No elemental averaging has been applied.

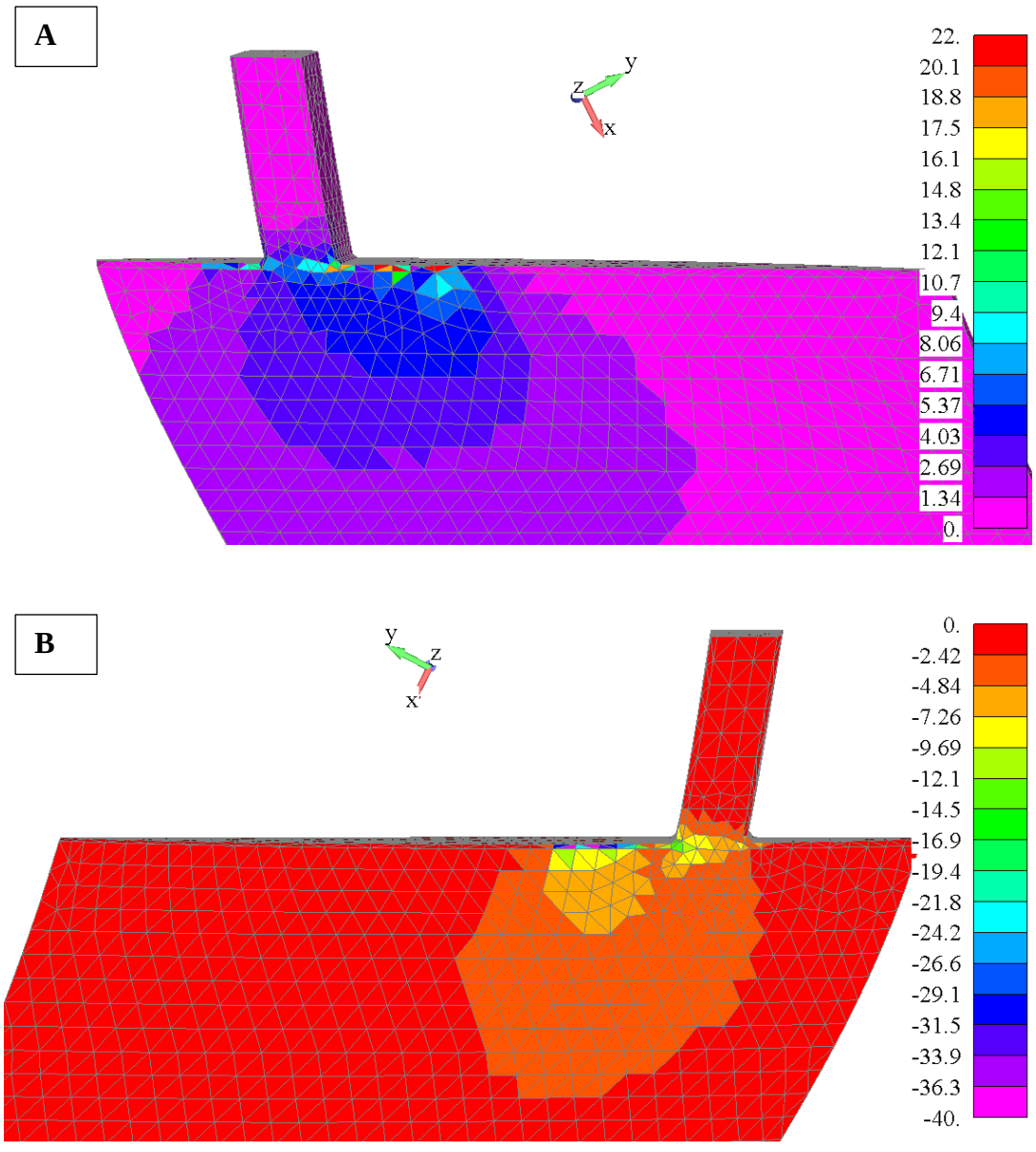

Figure 5.15: Inner blade maximum A) and minimum B) x-direction normal stress in MPa for the emergency stop load case. The material axis is shown at the root of the blade. No elemental averaging has been applied.

5.5 Blade Proof Testing

Three blade sets were manufactured for proof testing. Static and fatigue tests were conducted to ensure adequate blade performance. The results from those tests are described in this section. A two-part fixture was machined from aluminum to clamp the root of the blade and simulate the boundary condition at the blade hubs. Figure 5.16 is a photograph of the fixture in different stages of assembly. A Delrin ball was used to apply a point load to the blade quarter-chord at 50% span.

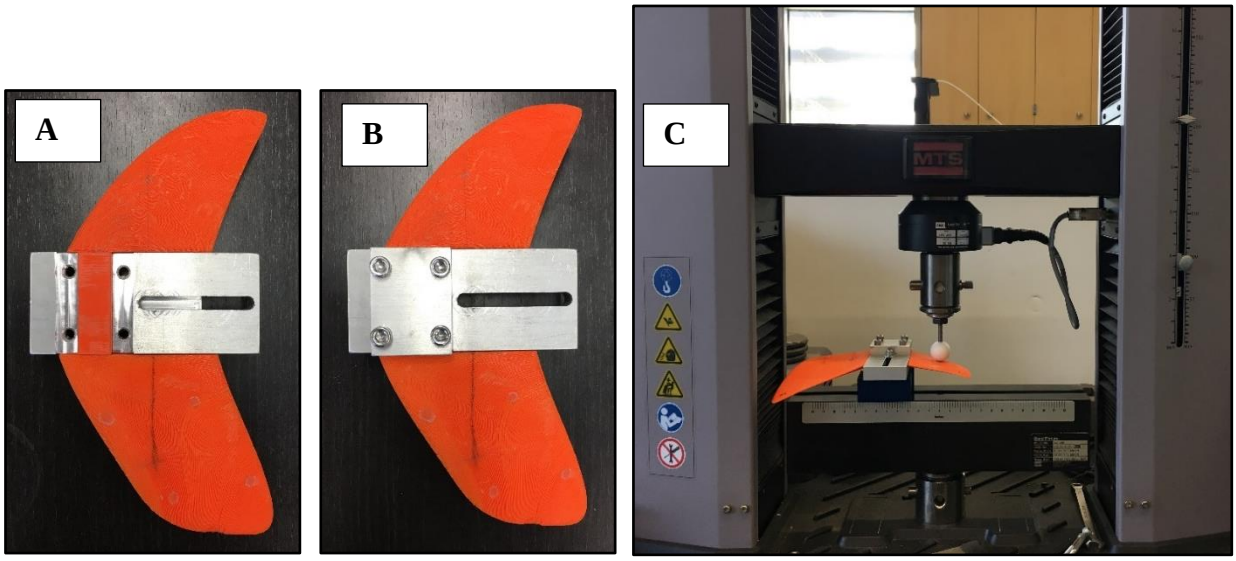

Figure 5.16: Two-piece blade fixture A) without top half and B) with top secured. The c-shaped lid is secured with four bolts that provide clamping pressure. A slot allows the fixture position to be adjusted within the MTS machine to precisely locate the applied load. A photograph C) of the blade fixture positioned in MTS machine. The white Delrin sphere is used to approximate a point load on the blade.

Blade sets one and two were loaded to failure to ensure they exceeded maximum predicted loads. No strain gauges were applied to the blades. Root moment versus crosshead displacement is plotted for the inner blades in fig. 5.18A and the

outer blades in fig. 5.18B. Average ultimate failure loads—123 N for the inner blade and 243 N for the outer blade—were extracted from the load-displacement plots to calculate a maximum failure moment.

Reaction moments for each test were summed about the root centroid at the root-blade interface and reported with respect to the rotor plane in table 5.4A. The rotor plane aligns with the x-y plane of the global model axes in fig. 5.6 so that $M_x=M_t$ and $M_y=M_n$. Reaction moments are also reported with respect to local blade axes (see fig. 5.17) in table 5.4B, in which the two load cases considered in the FEM have been scaled by their corresponding minimum MS for comparison with the test load.

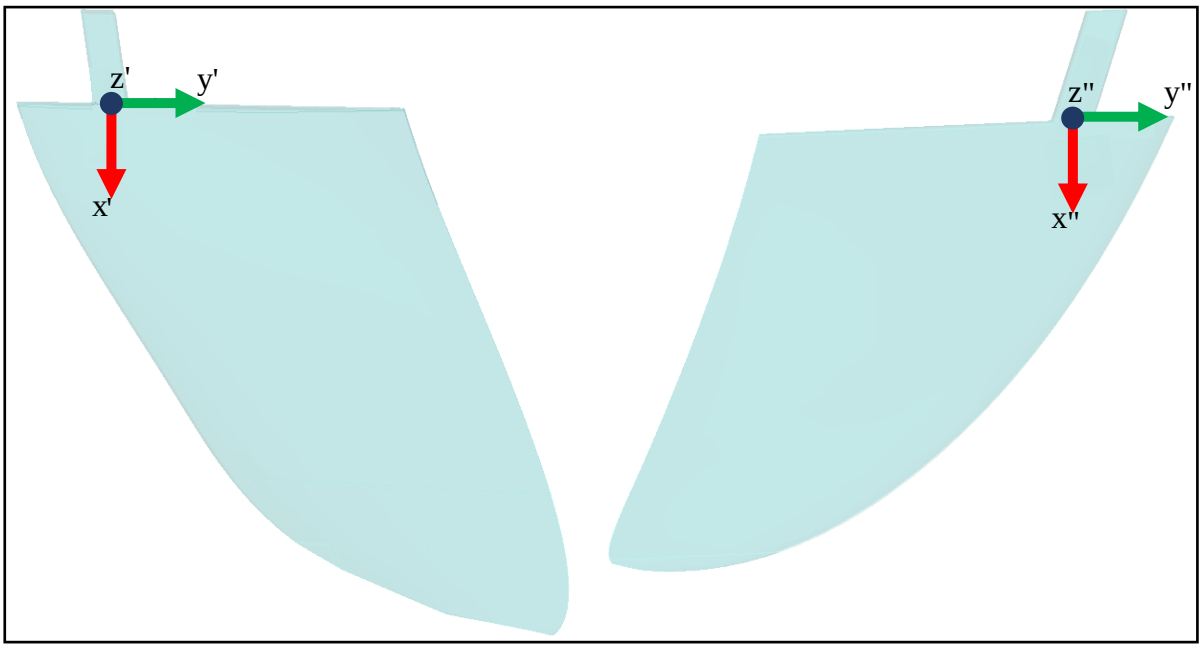

Figure 5.17: Blade axes used to report reaction forces and moments.

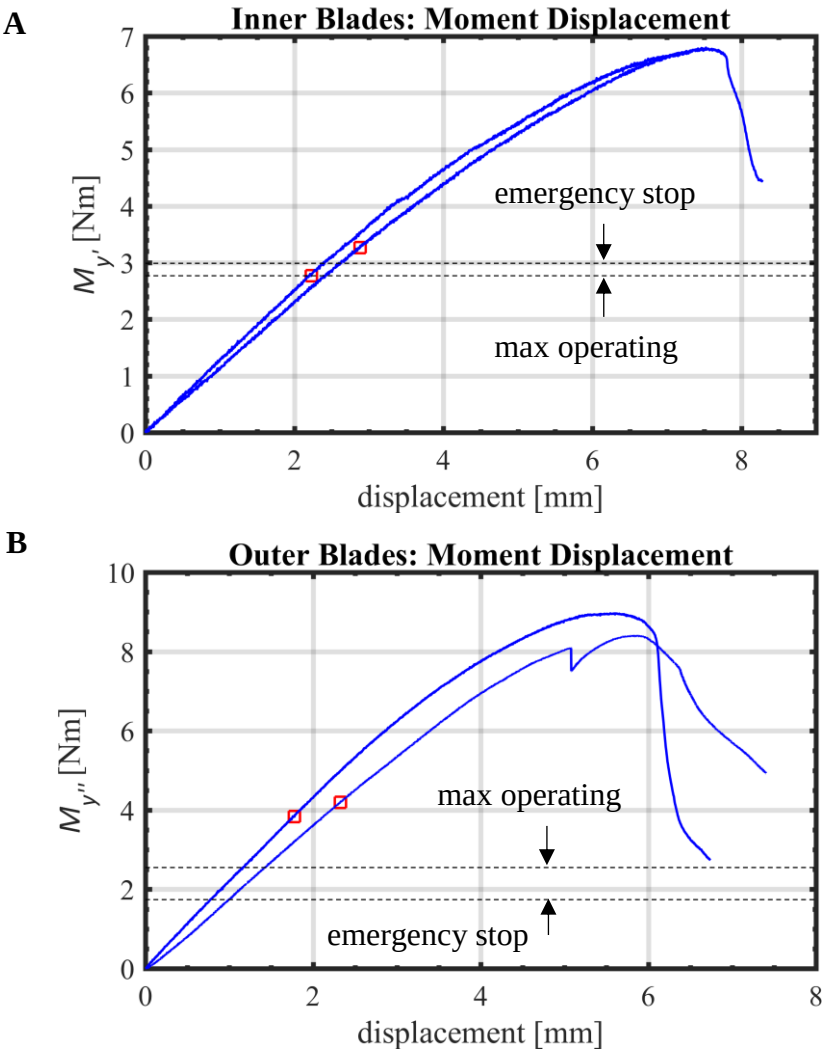

Figure 5.18: Moment-displacement data from A) inner blade tests and B) outer blade tests. The proportional limit is indicated with a red square. The discontinuity in one outer blade curve is the result of apparent yielding during a brief pause in the test.

A proportional limit—considered here to be a proxy for yield strength—was determined for each blade based on the initial linear portion of the load-displacement plots. Proportional limits are indicated with square markers in fig. 5.18A-B. Predicted loads, in terms of root moments (M_n, M_t), are well below the measured failure loads of each blade in table 5.4A. Failure moments predicted by the FEM compare favorably

with the average proportional limits in table 5.4B. It's apparent that the FEM is fairly conservative with respect to the ultimate failure load.

Table 5.4: Root Moment Reactions

			FEM		Experimental	
A			Maximum Operating Load	Emergency Stop	Proportional Limit	Failure
Inner	M_t	[Nm]	-1.39	0.00	-1.48	-3.30
	M_n	[Nm]	1.21	1.82	2.66	5.95
Outer	M_t	[Nm]	0.92	0.00	1.20	2.59
	M_n	[Nm]	-2.30	-0.93	-3.74	-8.09
B			Maximum Operating Load Scaled by Min. MS	Emergency Stop Scaled by Min. MS	Proportional Limit	Failure
Inner	$M_{y'}$	[Nm]	-2.77	-2.99	-3.04	-6.81
Outer	$M_{y''}$	[Nm]	-2.55	-1.74	-3.93	-8.50

Fatigue tests were also performed to assess the impact of cyclic loading on the FDM PLA blades. The gear housing on the turbine stator is located immediately downstream of the blades. Flow blockage by the gear housing is expected to temporarily reduce the hydrodynamic forces on each outer blade as it passes by. Load was again applied with a Delrin ball on the quarter-chord at 50% span. A range of 10 N to 100 N was chosen to stay within the linear portion of the previously established load-displacement response of the outer blade. The blade was subjected to 10,000 cycles at a frequency of 1 Hz. Select cycles plotted in fig. 5.20 demonstrate a gradually softening blade with permanent deformation of 0.7 mm.

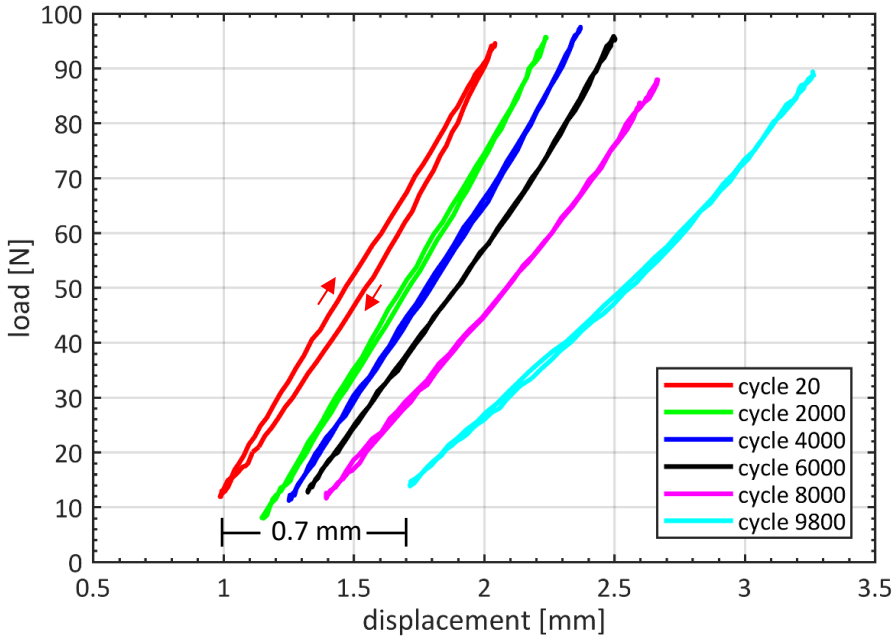

Figure 5.20: Hysteresis curves for a PLA blade loaded between 10 N and 100 N at rate of 1 Hz. Permanent deformation and loss of stiffness is increasingly evident as the blade approaches 9,800 cycles. Arrows indicate the direction of the load cycles.

Static proof tests confirm that the blades meet the strength requirements to operate in flow speeds up to 3.5 m/s and survive a sudden stop. The modeling approach described in this chapter appears to provide a conservative framework for analysis of future blade designs, though elements at the blade edges warrant more detailed study. Although only one fatigue test was performed, significant permanent deformation after 10,000 load cycles suggests a severely limited effective blade lifetime (1.7 hours at 100 rpm). Further investigation of blade fatigue behavior is warranted to weigh the questionable long-term viability of PLA blades. Addition of an outer structural coating, such as a spray or laminate ply layer, could be used to improve the environmental stability and fatigue life of PLA blades.

Chapter 6. Experimental Demonstration

This chapter covers all experimental work performed to demonstrate the turbine's capabilities. A combination of laboratory bench tests and open-water tow tests were conducted to measure the performance of the turbine and its various components. Performance measurements are compared with BEMT predictions to assess model accuracy.

6.1 System Efficiency

Bench tests were performed on the turbine assembly pictured in fig. 6.1 to quantify the efficiency of the bearings, gears, chain drive, and generator that make up the powertrain. Powertrain efficiency is used to isolate the conversion efficiency of the blades from the rest of the system, facilitating direct comparison of future blade designs. This section summarizes the test procedure and results used to identify energy loss at each stage of the powertrain.

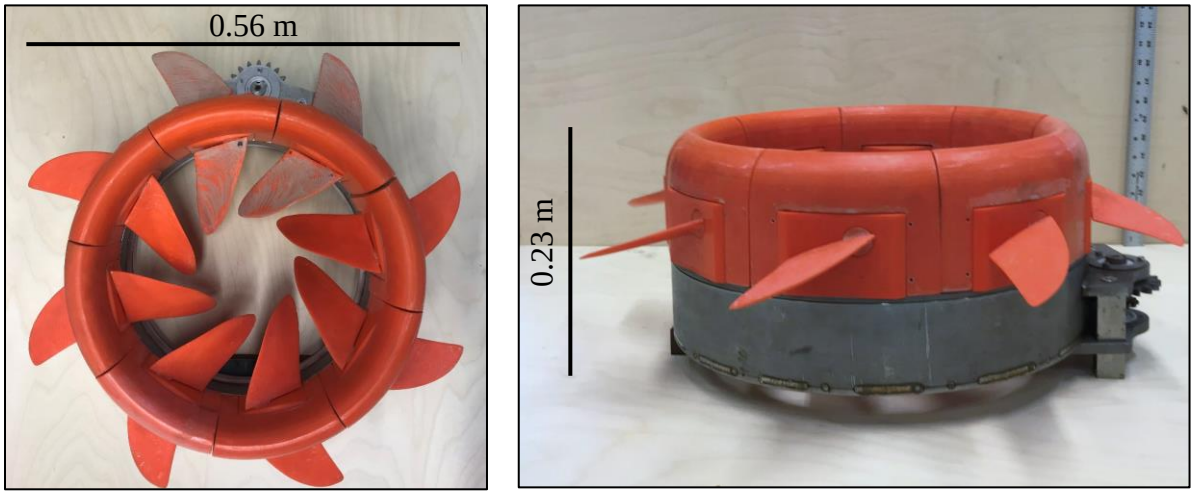

Figure 6.1: Photographs of the completed rotor assembly.

During operation the axial rollers bear the primary (thrust) load while the radials mostly serve to maintain rotor alignment within the stator. The turbine support frame was therefore secured in a horizontal position, shown in fig. 6.2, to actively engage the thrust bearings with the weight of the rotor. A handheld drill was used to the drive the system through a nut on the generator shaft.

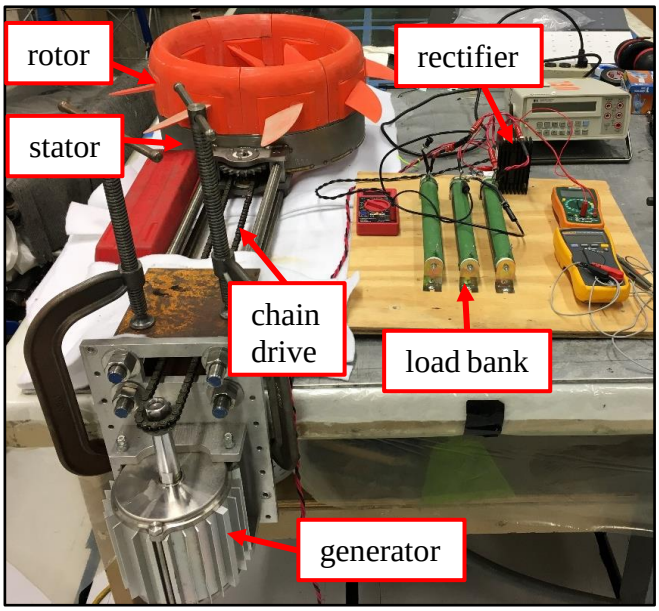

Figure 6.2: Experimental set-up for powertrain bench tests.

Input torque was monitored with an ACDelco ARM602-4 model torque cell located between the drill and the generator shaft. Generator shaft rotational speed was measured using a DT-2236C model laser tachometer. A bank of three Uxcell 200 W power resistors, each variable between 0 Ω and 100 Ω, was used for a dummy load. Voltage and current through the load were monitored to determine output power P_o from the system. Input power from the drill P_i is calculated from the product of applied torque τ and angular velocity ω at the generator shaft

$$P_i = \tau\omega \tag{5.13}$$

Measurements were recorded with the system in various stages of assembly: 1) the generator by itself, 2) the generator with the chain attached and no rotor, 3) the generator fully coupled with the rotor but no blades, and finally 4) the fully assembled turbine. Energy loss in the three-phase rectifier is incorporated into the measurement of every stage. The load was varied from 2-16 Ω for each system configuration while the generator was driven at speeds up to 600 rpm, which translates to rotor speeds of up to 120 rpm. System efficiency is defined as the ratio of electrical power out P_o to mechanical power in P_i.

Recorded efficiencies for each stage of assembly are plotted as a function of generator rpm in fig. 6.3. Shaded color bands show the 95% confidence interval for the quadratic best fit lines. The maximum generator efficiency, based on the average at each sampled speed, is 75% at approximately 500 rpm. There was no discernable decline in efficiency with the inclusion of the chain drive uncoupled from the rotor, so it has been omitted from fig. 6.3 for clarity. However, introduction of the rotor (with gearing) and rotor bearings reduced the overall efficiency by about 6% near

peak efficiency. Maximum efficiency for the full powertrain ($\eta_{powertrain}$) assembly was found to be 67%.

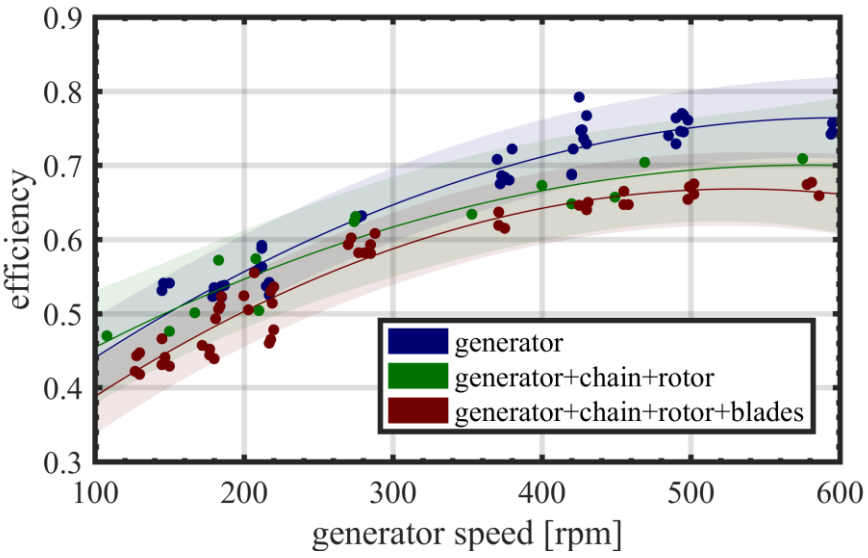

Figure 6.3: Efficiency of the generator (blue), the assembly with no blades (green), and the full assembly (red) at different rotational speeds. Shaded color bands show 95% confidence interval for quadratic fit line.

System efficiency doesn't decline appreciably until the bearings are engaged. It's likely that they are the greatest source of energy loss within the turbine powertrain. Any future effort to improve the powertrain should focus on reducing friction in the bearings. The powertrain efficiency $\eta_{powertrain}$ will be used to isolate hydrodynamic performance of the rotor from the complete test-rig system

$$C_{Q-adjusted} = \frac{C_{Q-measured}}{\eta_{powertrain}} \tag{5.14}$$

and

$$C_{P-adjusted} = \frac{C_{P-measured}}{\eta_{powertrain}} \tag{5.15}$$

where C_Q is the torque coefficient and C_P is the power coefficient.

6.2 Tow Testing

Tow testing was conducted in San Diego's Mission Bay to evaluate the completed turbine and characterize its performance. A motor boat was used to drive the test bed system through a wide range of operating conditions while a custom-built data acquisition system documented turbine functionality. Details of how the turbine was towed, instrumented, and operated during testing are described in this section.

A pontoon boat was able to tow the turbine up to a speed of 3.2 m/s. Figure 6.4A shows the front of the boat where the turbine was mounted. It's located in the center of the pontoons so that a clean uniform flow is produced across the front of the turbine and no downstream obstruction. As seen in fig. 6.4B, a 2"x6" board was clamped to the deck as mounting surface for the turbine. Testing was conducted on a calm day, in a sheltered section of Mission Bay, to minimize the effects of any surface waves on turbine.

Two separate Arduino Microcontrollers were used to log data during testing. One was used to record voltage, current, and generator rpm. The other was used to monitor boat/current speed. Water speed measurements were taken intermittently with a propeller-type current meter made by Vernier. Voltage was measured across the load bank using a basic voltage divider circuit sampled with a 16-bit ADC. A hall-effect based Allegro Microsystems ACS712 sensor was used to monitor current through the load.

Generator shaft rpm was measured with a Uxcell optical sensor, which combines a Vishay TCRT5000 infrared (IR) sensor with Texas Instruments LM393 comparator, mounted above the generator shaft to detect strips of reflective tape. Shaft rpm was determined from the frequency of passing strips. The position of the IR rpm sensor is noted in fig. 6.4B. Figure 6.5 is a photograph of the primary data acquisition package identifying important components. It's fitted in a plastic container to protect the electronics from water.

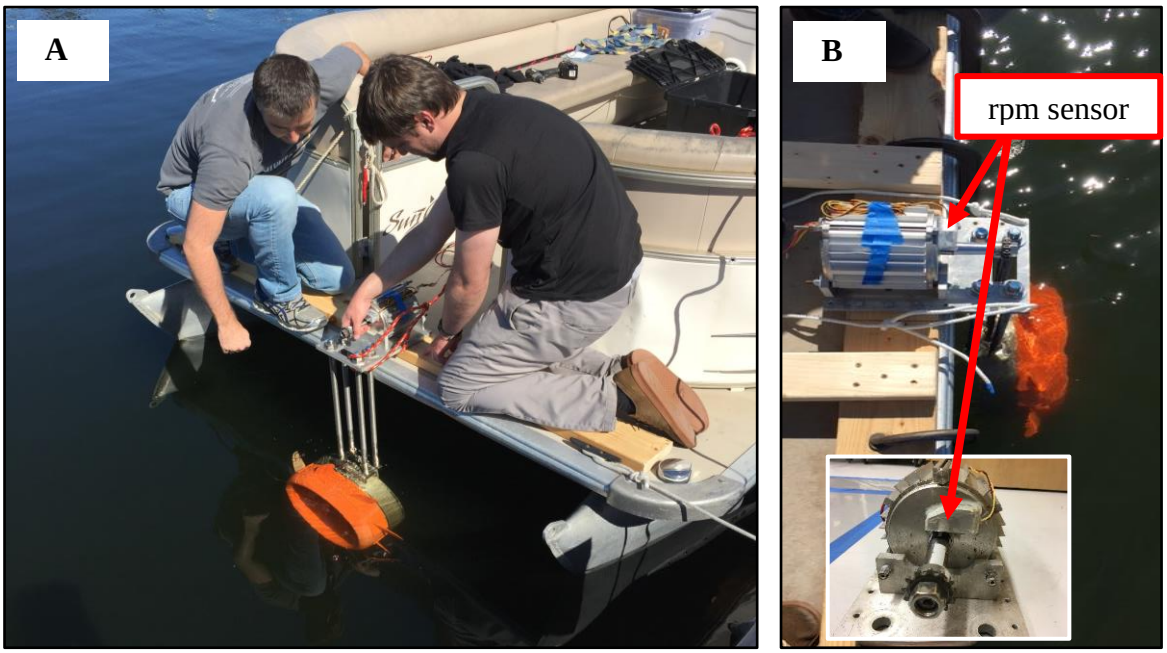

Figure 6.4: A) A photograph of the turbine being prepared for mounting at the front of the pontoon boat. B) Close-up images of the generator frame after being bolted to the 2"x6" and of the generator shaft showing placement of IR rpm sensor (indicated with an arrow).

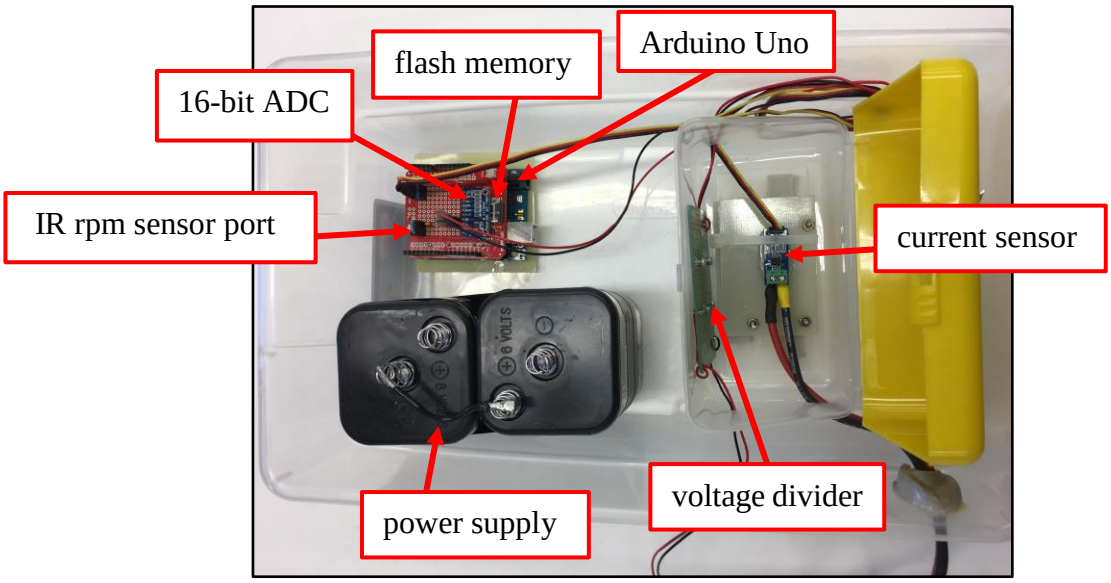

Figure 6.5: The self-contained data acquisition system prior to tow tests. Lantern batteries were used to power the Arduino Uno. Data was logged to an external flash drive. The IR rpm sensor was disconnected in this image, but the 3-pin input port (with signal filter) are still indicated.

Tow tests were executed at 1 m/s, 2 m/s, 2.5 m/s, 3 m/s, and 3.2 m/s. Except for one run, all tests were performed with a nominal load of 20 Ω. The load was set to 10 Ω for the run exceeding 3 m/s to control the rotational speed of the turbine and reduce the output voltage from the generator. Table 6.1 outlines the combinations of load and flow speed that were studied. Test durations were between 1 and 2 minutes to capture the steady-state turbine behavior at each flow speed.

Table 6.1: Nominal Tow Test Parameters

Run	Load [Ω]	Flow Speed [m/s]
1	20	1
2	20	2
3	20	2
4	20	2.5
5	20	3
6	20	3
7	10	3.2

6.3 Turbine Performance

Data acquired during the tow tests are presented in this section. Voltage and current measurements are used to calculate the turbine power coefficient for each run. The observed power coefficients (C_p) and torque coefficients (C_Q) are expressed in terms of tip-speed ratio (λ) and compared to the predicted performance curves in chapter 4. Correlation of the results with the hydrodynamic model improves dramatically after taking into consideration the powertrain efficiency.

Figures 6.6-6.10 present time series of generator rpm, current, and voltage from each test run. Data are organized by test speed with the test load noted in the legend. A moving average filter with a 16-point window has been applied to eliminate some of the higher frequency noise. Reported mean values are all calculated from the quasi-steady region between the ramp up and ramp down.

The processed data for run 1, for which the measured boat speed was 0.94 m/s, are plotted in fig. 6.6. Average values were calculated based on the period ranging from 27-100 seconds. The resulting mean current and voltage, 0.5 A and 9.8 V respectively, occurred at an average rotor speed of 19.5 rpm (λ=0.60). Corresponding power output was 4.9 W.

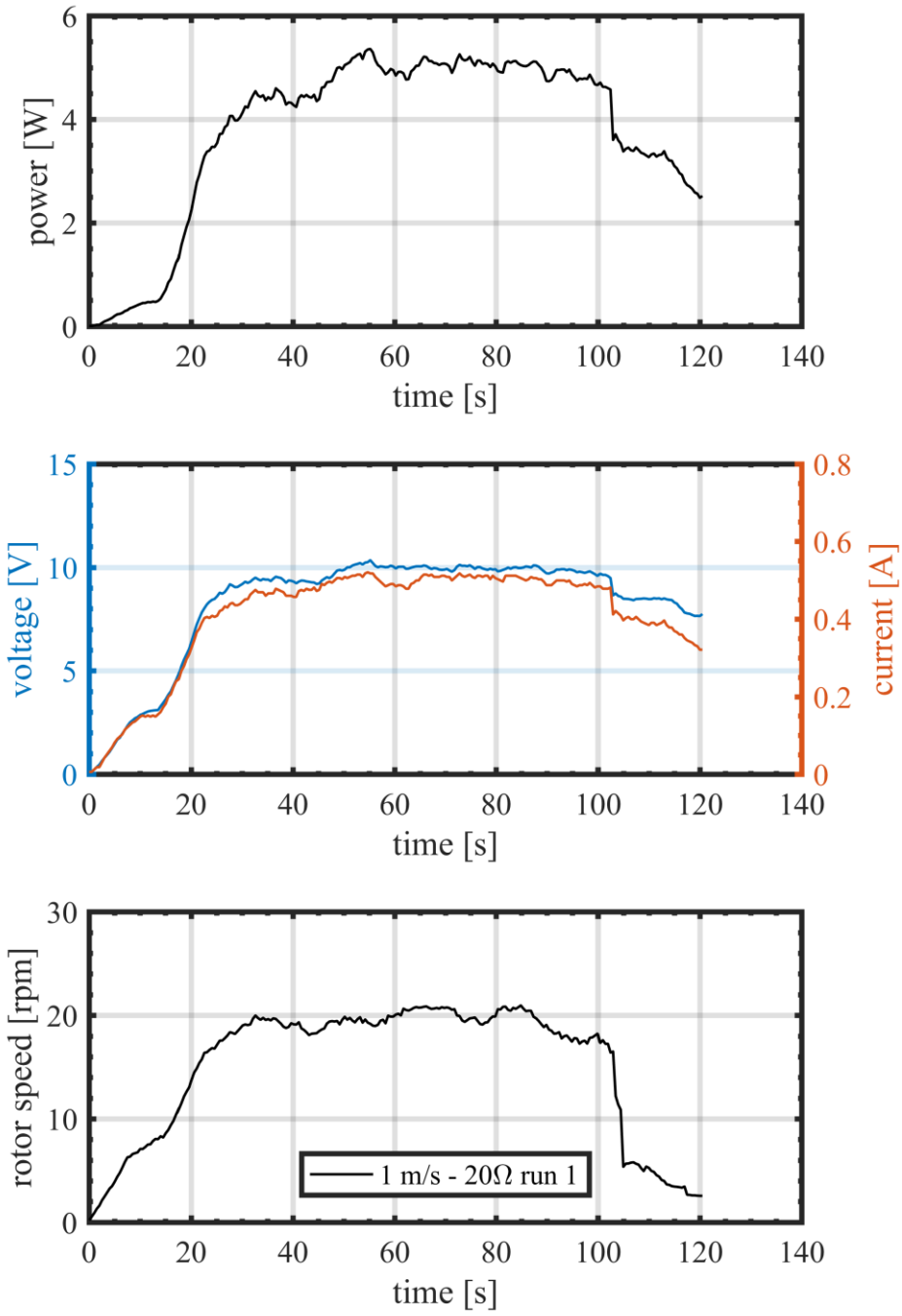

Figure 6.6: Processed output voltage, current, and rotor rpm at an average flow speed of 0.94 m/s for run 1. The nominal load on the generator was 20 Ω.

Figure 6.7 presents the processed data from runs 2 and 3. The recorded boat speed during run 2 was 1.97 m/s. Run 2 data from 75-250 seconds were used to calculate an average output of 49.9 V, 2.8 A, and 139 W. Rotor speed was an average 76 rpm (λ=1.13) over that same period. The boat speed drifted slightly during the middle of run 3 so it was analyzed as two separate parts; one ranging from 40-90 seconds with a boat speed of 1.90 m/s and the other from 120-220 seconds with a boat speed of 2.06 m/s. Output during the first half of the run 3 (40-90 seconds) was 46.6 V, 2.7 A, and 126 W with an average rotor speed of 91 rpm (λ=1.42). Meanwhile, output voltage, current, and rotor speed all increased slightly during the latter half of run 3 (120-220 seconds) to 55.5 V, 3.0 A, and 102 rpm (λ=1.44). There was consequently an increase in power output to 166 W.

A temporary malfunction in the rpm sensor during run 4 corrupted a portion of the rpm data plotted in fig. 6.8. Average rpm was therefore determined from the range 150-180 seconds, at which point the boat speed was 2.51 m/s. It's assumed, due to the steady voltage and current exhibited throughout the run, that the generator rpm was relatively stable and that the average of 138 rpm (λ=1.61) from the end of the sample (150-180 seconds) is representative of the whole run. Average generator output over that 30 second period was 74.3 V, 4.1 A, and 303 W.

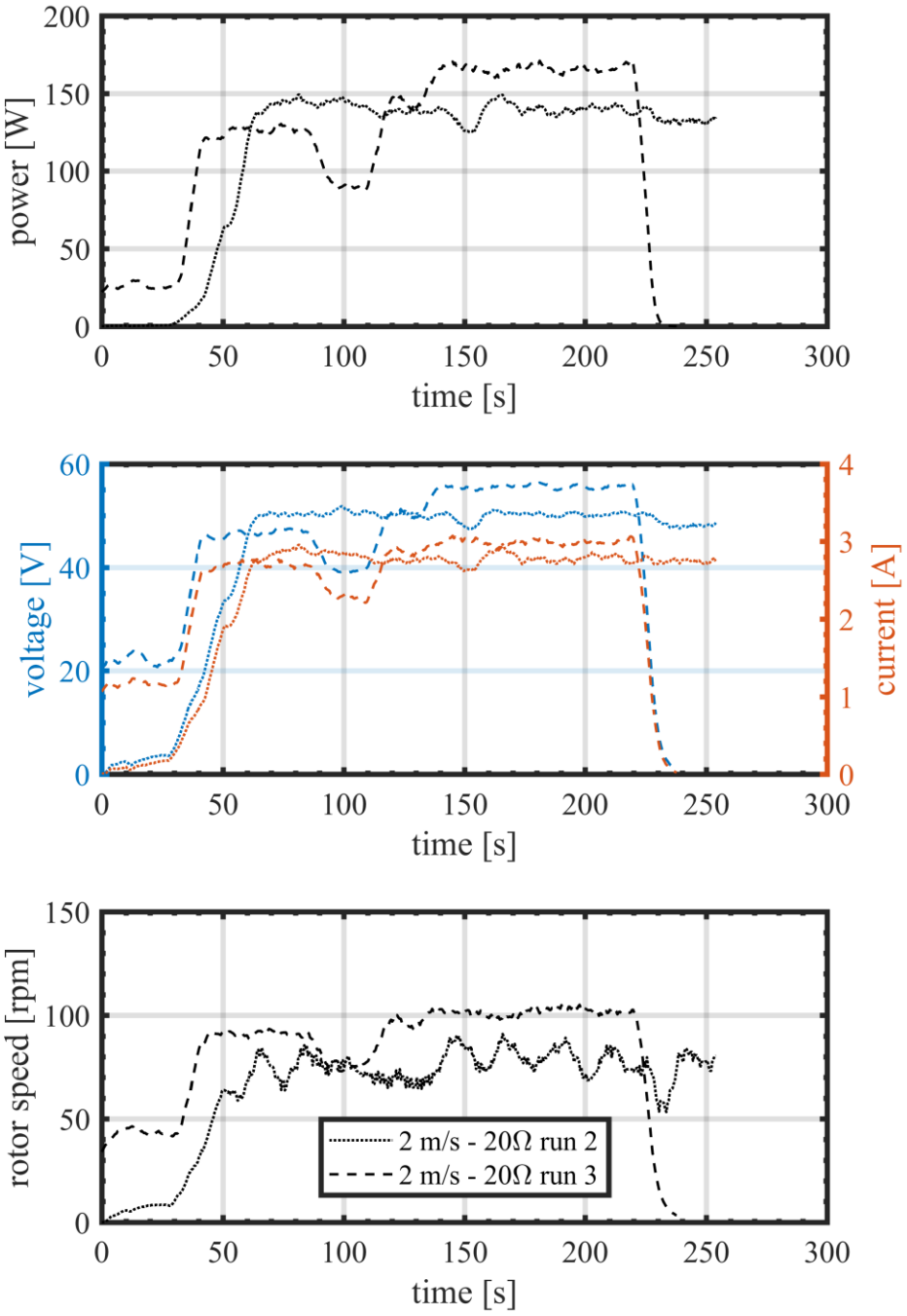

Figure 6.7: Processed output voltage, current, and rotor rpm at average flow speed of 1.97 m/s for run 2 and 1.96 m/s for run 3. The nominal load on the generator was 20 Ω for both runs.

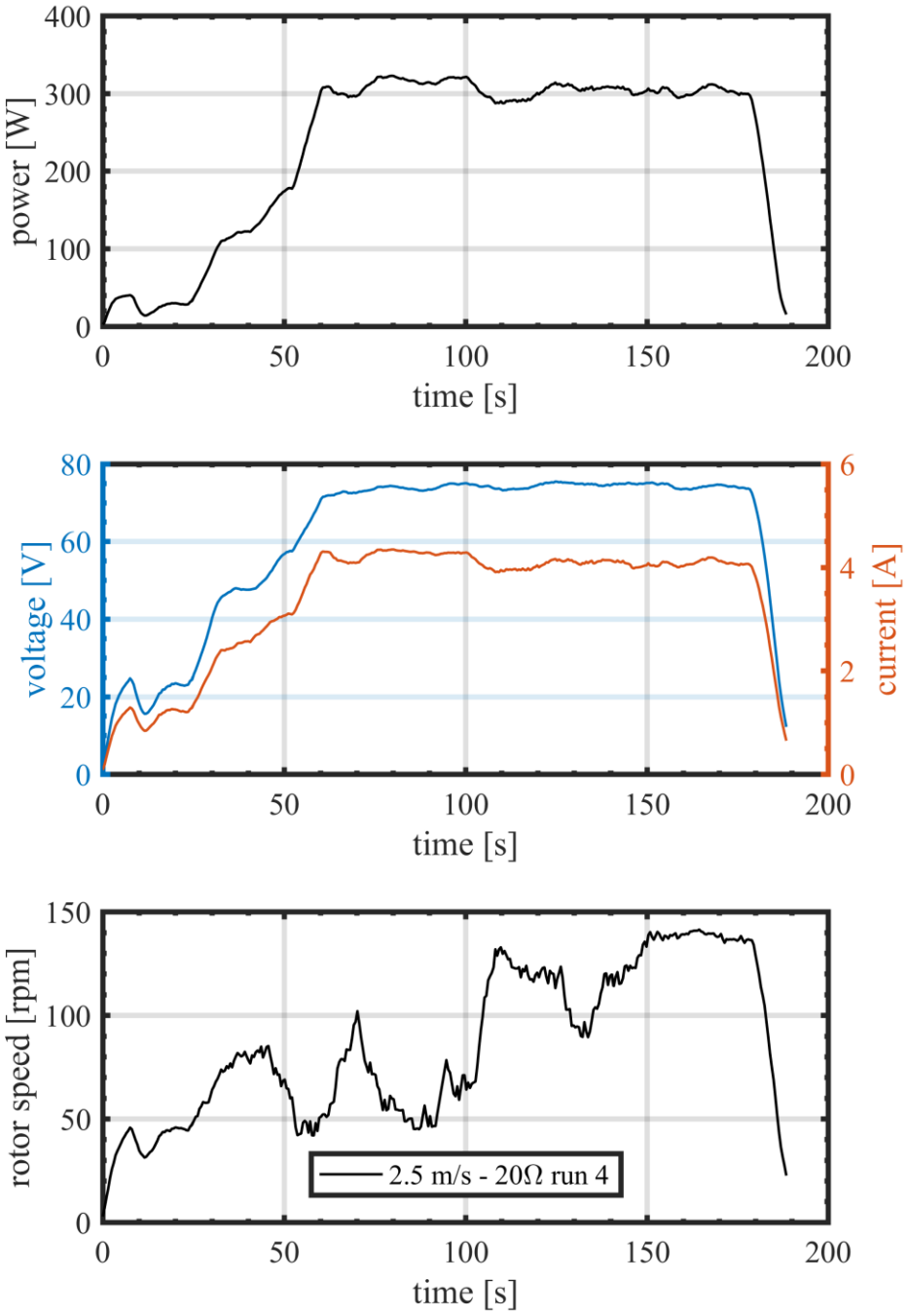

Figure 6.8: Processed output voltage, current, and rotor rpm at an average flow speed of 2.51 m/s for run 4. The nominal load on the generator was 20 Ω.

Processed results from runs 5-7 are plotted together in fig. 6.9. Runs 5 and 6 were analyzed from 23-62 seconds and 23-100 seconds respectively. During both runs the observed voltage temporarily exceeded the range of the voltage sensor. For these instances the peak voltage was reconstructed from the known current and load resistance. Average output parameters for run 5, conducted at a boat speed of 2.96 m/s, were 96.1 V, 5.3 A, and 510 W with a rotor speed of 183 rpm (λ=1.82). Likewise, in run 6 the average output parameters occurring at a boat speed of 2.91 m/s were 98.7 V, 4.5 A, and 449 W with a rotor speed of 183 rpm (λ=1.84).

Finally, run 7 was originally intended to be a short dwell at 3 m/s before ramping to 3.5 m/s and holding. However, the boat began to pitch excessively, and the test was abruptly stopped after achieving a maximum speed 3.18 m/s. Data from the short dwell at 2.95 m/s, plotted in fig. 6.9, were analyzed from 11 to 26 seconds. During this time the turbine produced an average 60.0 V, 5.8 A, and 349 W with a rotor speed of 87 rpm (λ=0.87). The short ramp to 3.18 m/s, shown in fig. 6.10, was not incorporated into the calculations of power or torque coefficient because it never reached a steady state. It is still noted that at peak 597 W of power was generated.

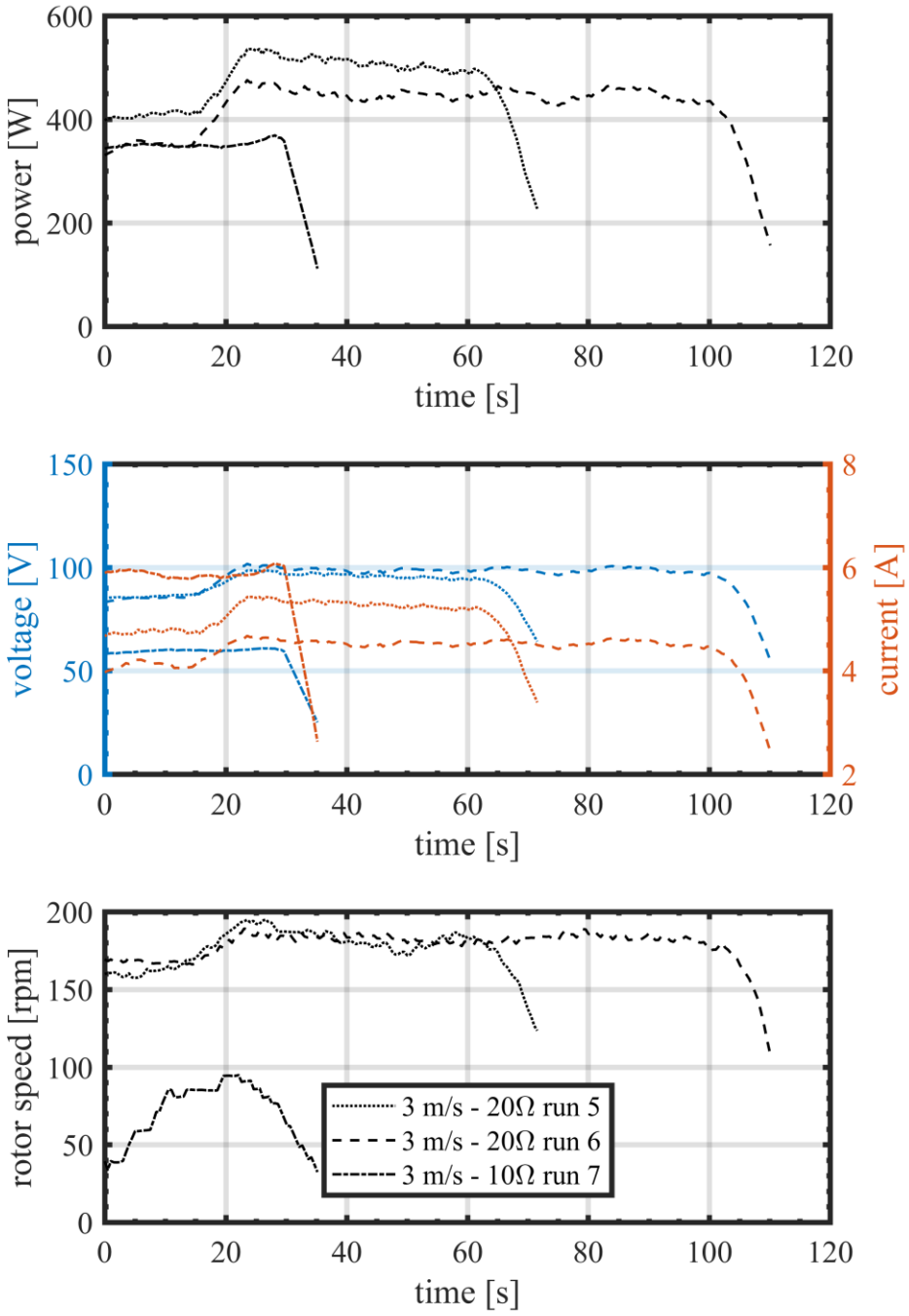

Figure 6.9: Processed output voltage, current, and rotor rpm for runs 5-7. Average flow speed was 2.96 m/s for run 5, 2.91 m/s for run 6, and 2.95 m./s for run 7. The nominal load on the generator was 20 Ω for runs 5-6 and 10 Ω for runs 7.

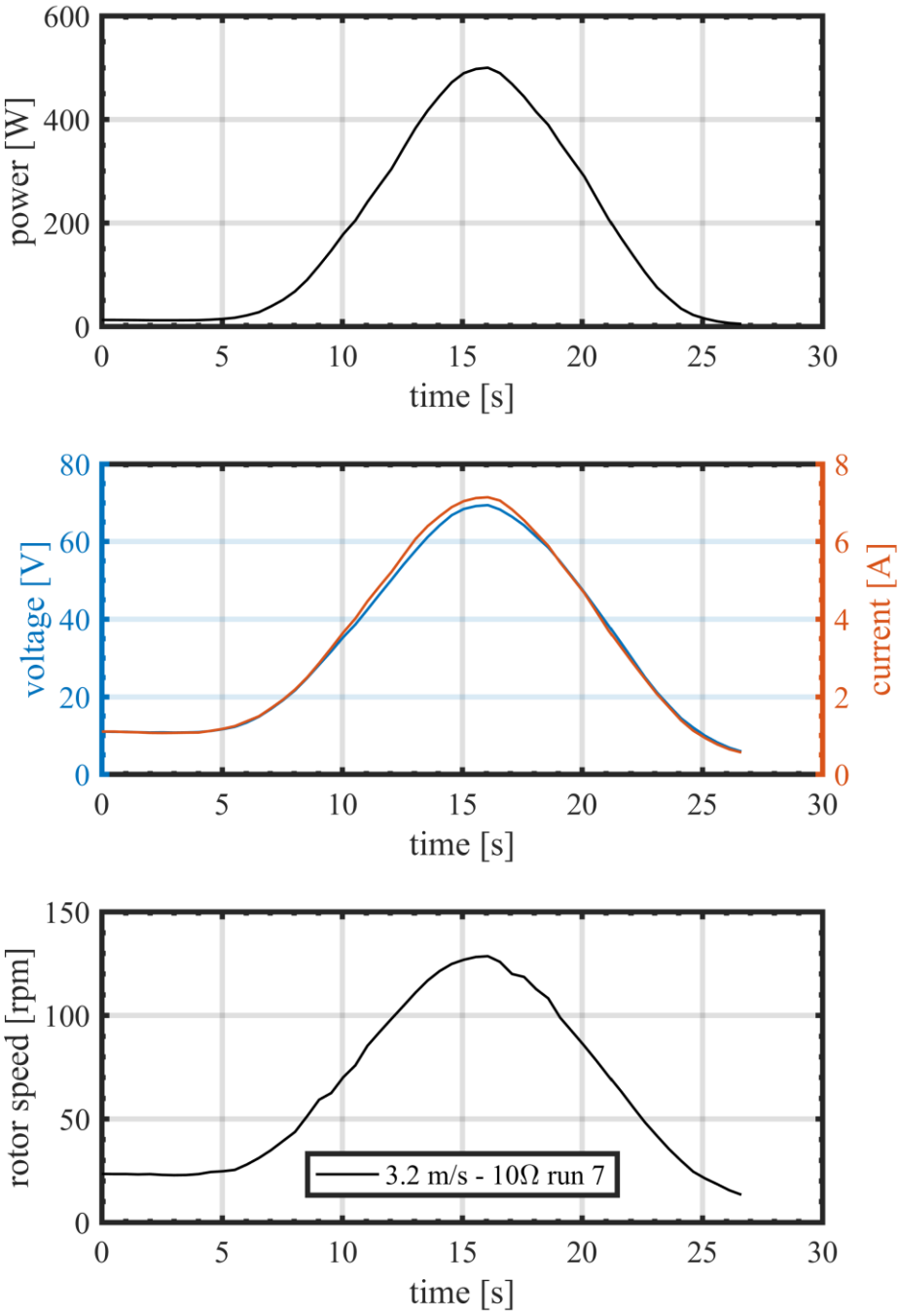

Figure 6.10: Processed output voltage, current, and rotor rpm at an average flow speed of 3.18 m/s for run 7. The nominal load on the generator was 10 Ω.

Less than 10 W of power was generated in the 1 m/s flow. Performance in this regime was hindered by the low generator efficiency around 100 rpm, which could be mitigated by optimizing the load. Hydrodynamic efficiency is evidently also low at that tip-speed ratio of 0.60. Increasing the flow to 2.0 m/s and approximately doubling the tip-speed ratio raised the average power production to 140 W. Further power production scaled rapidly from 300 W at 2.5 m/s to 480 W at 3.0 m/s before peaking at 600 W under a 3.2 m/s flow.

Turbine power density is plotted as a function of flow speed in fig. 6.11. Also plotted as a means of basic data validation is a least squares fit to the data using the model $f(x)=ax^3$, where a is a constant. The underlying assumption that C_P (embedded in the parameter a) is uniform across all sample points is an approximation. This simplified model of eq. (4.3) demonstrates that the power data correctly behave as a cubic function of flow speed. Data that deviate significantly from the fitted line do so because the turbine was operating with a much lower relative C_P when those measurements were taken.

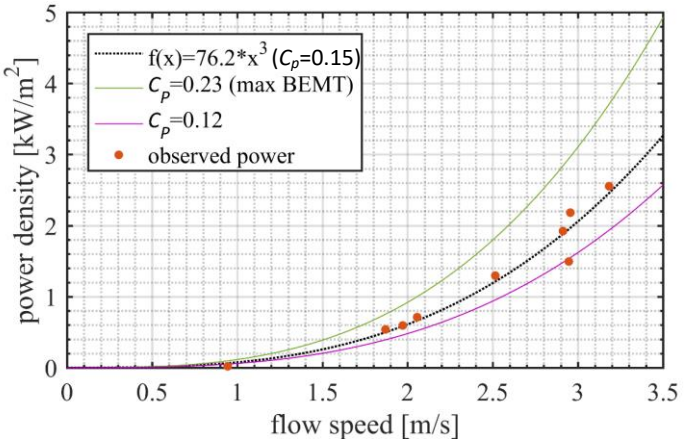

Figure 6.11: Average turbine power production plotted as a function of flow speed. Fitted power function shown with dotted line.

Average torque coefficients, according to eq. (4.2), were found for each test run in which steady state was achieved and plotted as a function of tip-speed ratio in fig. 6.12. The maximum observed torque coefficient of 0.136 occurred at a tip-speed ratio of 1.14. In fig. 6.13, the experimental torque coefficients are shown along with the BEMT model predictions (fig. 4.20) for direct comparison. While the experimental turbine consistently produced less torque than the model turbine, both exhibited the same general trend and peaked near a tip-speed ratio of 1.1. Torque coefficients were adjusted using eq. (5.14), with powertrain efficiency equal to 0.67, and plotted in fig. 6.13. Adjusted values correlate more closely with the BEMT model at all tip-speed ratios except 0.9 and 1.1.

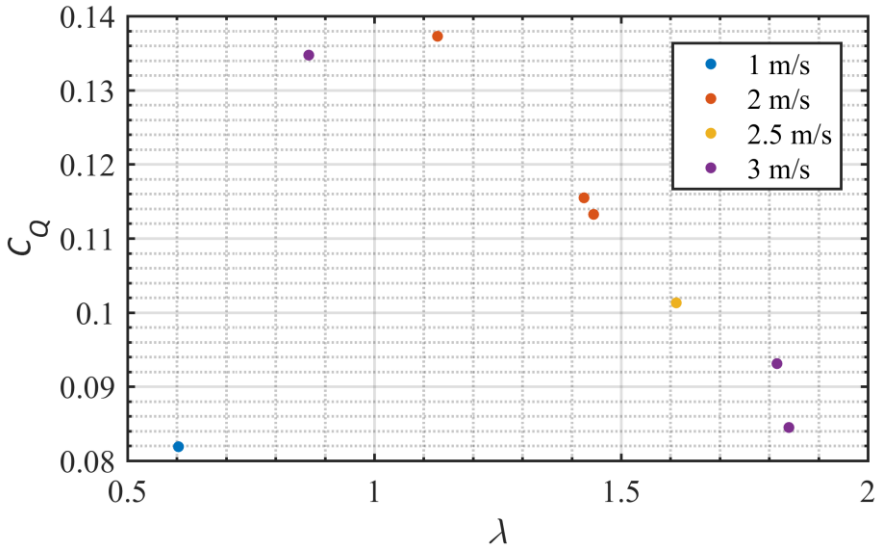

Figure 6.12: Calculated torque coefficients plotted as a function of tip-speed ratio.

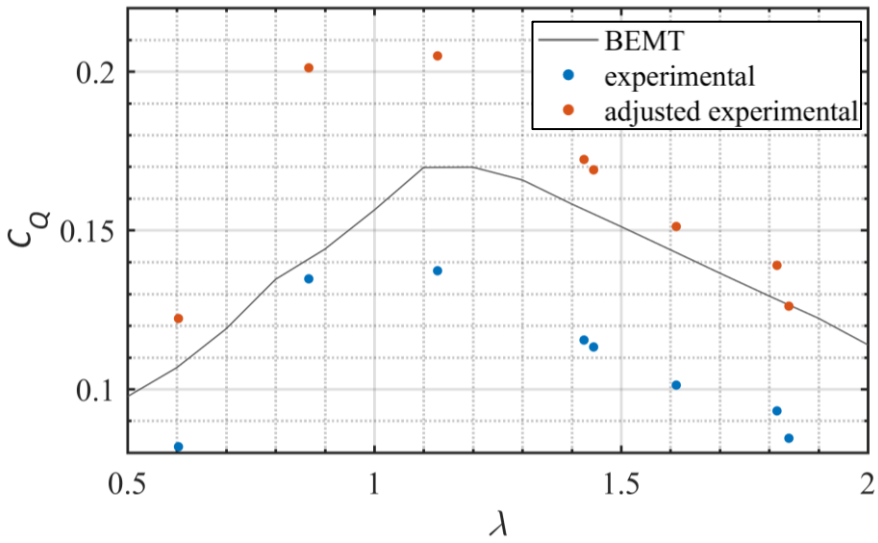

Figure 6.13: Calculated torque coefficients, including powertrain loss adjusted and BEMT model values, plotted as a function of tip-speed ratio.

Average power coefficients for each test were calculated with eq. (4.3). Figure 6.14 is a plot of power coefficient versus tip-speed ratio for the test runs that achieved steady state. Turbine efficiency increases rapidly from the tip-speed ratio 0.6 to 0.9, reaching 90% of the maximum power coefficient by a tip-speed ratio of 1.1. The maximum power coefficient 0.169 was observed at a tip-speed ratio of 1.82.

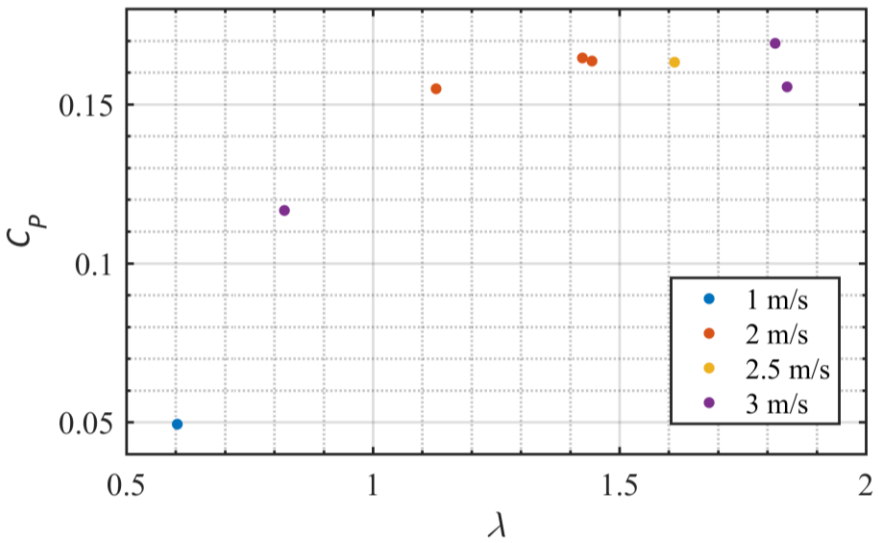

Figure 6.14: Calculated power coefficients plotted as a function of tip-speed ratio.

Experimental efficiencies were also compared to the BEMT predicted power coefficients. Figure 6.15 displays the power coefficient curve produced with the BEMT model (fig. 4.20) overlaid with the tow test results. It's evident from fig. 6.15 that the experimental efficiency is roughly 30% lower than the BEMT efficiency. The experimental data was again adjusted according to eq. (5.15), with powertrain efficiency equal to 0.67, to isolate the hydrodynamic efficiency of the turbine. Resulting power coefficients generally align more closely with the model predictions. In the region around peak efficiency the discrepancy is reduced to about 8%. Performance data for tip-speed ratios greater than 2 were not collected and further testing with faster rotor speeds and/or slower boat speeds is required to study this regime.

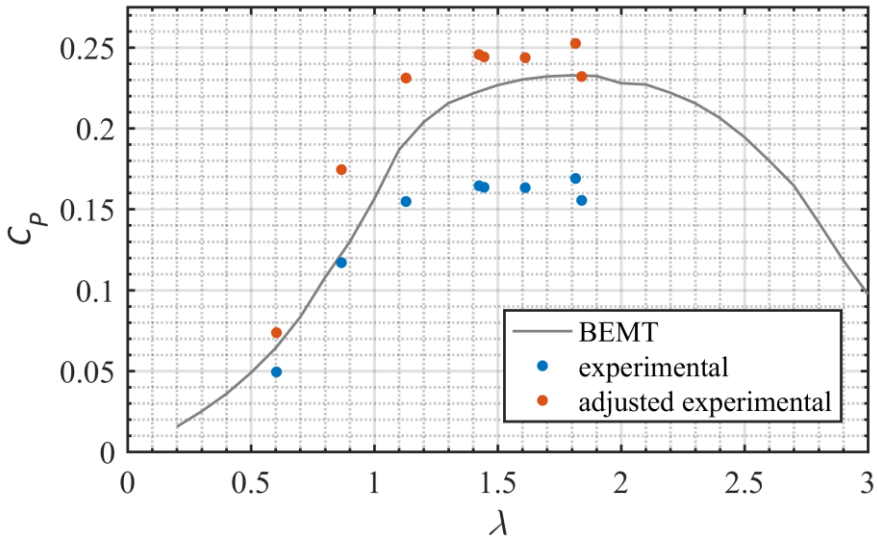

Figure 6.15: Calculated power coefficients, including powertrain loss adjusted and BEMT model values, plotted as a function of tip-speed ratio.

Chapter 7. Conclusion

A pico-scale hydrokinetic turbine test bed was developed and demonstrated experimentally. Efficient hydrodynamic analysis with BEMT was successfully employed in the design of FDM manufactured PLA blades, laying the groundwork for future research on open-centered hydrokinetic turbines.

7.1 Summary

There is growing scientific and political consensus on the need reduce greenhouse gas emissions. Meanwhile, energy demand is projected to increase rapidly in the next few decades. The kinetic energy stored in moving water has a tremendous potential to help meet this demand around the world. Hydrokinetic turbines can deliver consistent and highly predictable power from these flows with minimal added infrastructure. Pico scale turbines are a promising avenue for rural electrification in developing countries with limited grid infrastructure. Such mobile turbines also have application in temporary military encampments or emergency power generation.

A unique open-centered hydrokinetic turbine originally designed by Oceana Energy Company has been scaled down to a pico-class system. The scaled turbine is designed to be a testbed for development of a new portable Oceana device. It's manufactured from corrosion resistant materials to enable testing in marine environments. With a robust, modular design it can be fully assembled and disassembled in the field using only a limited number of common tools. Blade hubs

are designed so that the blade pitch can be adjusted, or new blades can be installed in minutes.

Fusion deposition modeling (FDM) was employed to manufacture the turbine blades, blade hubs, and cowling. Material property testing established PLA as a suitable structural material for blade prototyping and performance evaluation, though fatigue tests of blades indicate that fatigue life will limit long duration tests. It was shown that the FDM coupon behavior could be described with classical laminate theory and strength could be predicted with a progressive failure model.

A steady blade element momentum (BEMT) code has been modified for open-centered turbines. Power, thrust, and torque coefficients were calculated to predict turbine performance over a range of tip-speed ratios from 0 to 3. Maximum power coefficient was found to be 0.23 at a tip-speed ratio of 1.8. The BEMT code was used to determine static loads on the turbine blades at maximum operating speed. Loads were applied to finite element models of the blades to evaluate margins of safety. Proof testing confirmed that the PLA blades exceeded design load by satisfactory margin.

Tow testing was conducted to measure the turbine performance experimentally. The turbine was successfully operated in flows up to 3.2 m/s, where it generated nearly 600 W of electrical power. A maximum power coefficient of 0.169 was observed at a tip-speed ratio of 1.82, during which the boat speed was 2.96 m/s and the rotor speed was 183 rpm. Tip-speed ratio at maximum efficiency corresponds well with the model value. However, experimental power coefficients at their peak are approximately 30% lower than the BEMT predictions. This discrepancy is reduced to

roughly 8% if the data are adjusted to remove the known energy loss in the powertrain.

7.2 Future Work

Baseline modulus and strength properties (E_1, E_2, F_{1t}, F_{2t}) of FDM manufactured PLA were measured in this thesis. Remaining properties used in the finite element models of the blades were backed out from published data. Future work should include a more complete material characterization to directly measure all relevant properties. The impacts of layer height, infill density, and print temperature on material performance are also worth consideration. A structural coating, such as polyurethane or a lamina ply, should be considered to improve the environmental stability and fatigue life of PLA.

In addition to incorporating more accurate material properties, fidelity of the finite element models could be improved by switching from a smeared representation of the blade as an orthotropic solid to one that treats the material as a laminate. Smeared equivalent properties represent a specific print sequence that's repeated through the thickness of the blade. Blade geometry forces certain regions to contain only fractional portions of that sequence, resulting in a less accurate representation of the material response in those areas. Layered solid elements that model the actual printed layers could be used to alleviate this problem.

Tow testing revealed a maximum efficiency of 25% after controlling for electro-mechanical loss in the testbed powertrain, which is near the 30% to 40% efficiency range of the full-scale Oceana turbine. An outline has been established for designing turbine blades for manufacture with FDM, wherein BEMT is used to evaluate hydrodynamics and influence basic structural analysis. Future work should leverage this process to optimize blade geometry for the scaled turbine. Performance improvement has been noted from cursory pitch studies, warranting experimental investigation. Physical blade testing would benefit from the use of strain gauges, along with the creation of custom blade jig to assess any permanent deformations.

The tow tests performed in this work were limited to tip-speed ratios less than 2. Additional test should be conducted in the higher tip-speed ratio regime from 2 to 3, by increasing the rotor speed and/or decreasing the flow speed, so that the remainder of the C_P and C_Q curves can be demonstrated. Load cells should be included in all future testing to measure rotor torque—as opposed to calculating it indirectly from the power output and rotor speed—and rotor thrust directly. The capability to measure thrust, and subsequently C_T, would allow for a more complete characterization of the rotor behavior. The IR rpm sensor used for tow testing was unreliable at times. An alternative contactless method such as a magnet and Hall Effect sensor may perform better.

Development of an unsteady BEMT algorithm and coupling it with a structural model of the turbine would significantly improve modeling capabilities. Turbulence in natural flows results in transient turbine behavior not captured by the current BEMT model. Dynamic engineering models can be incorporated to track time

dependent loads (dynamic inflow models) and time dependent aerodynamic coefficients (dynamic stall models). A coupled aeroelastic model can be created by combining unsteady BEMT with a structural model of the turbine, yielding insight into the dynamic behavior of the turbine structure under realistic operating conditions. Future code development should also seek to incorporate the effects of rake and skew within the hydrodynamic analysis. A new set of blades could be manufactured with the rake and skew removed to evaluate the impact of these parameters on overall performance. An enhanced BEMT model would serve as a good benchmark for detailed CFD simulations of the turbine.

Vibration testing and modal analysis of the open-centered turbine is necessary to further establish safe operating speeds. Natural frequencies of the blades and support structures should be measured to develop a Campbell Diagram for the system. Identification of any resonant conditions ensures they can be avoided during future experimental tests.

Appendix A: Marin Equation for Calculating Endurance Strength

A Marin equation was used to incorporate the effects of surface conditions, size, load types, operating temperature, and reliability into the published endurance on a laboratory specimen. Reduced endurance strength F_E is calculated as function of reported endurance strength F_e' according to [67]

$$F_E = k_a k_b k_c k_d k_e F_e' \ . \tag{A.16}$$

Surface condition factor k_a reduces the endurance strength according to the surface condition. For a machined or cold-drawn surface it's determined using the following relationship in [67]

$$k_a = 4.51 F_{ut}^{-0.265} \tag{A.17}$$

where F_{ut} is the ultimate tensile strength of the material.

The size modification factor k_b for a rectangular cross-section is found by [67]

$$k_b = \left(\frac{d_e}{7.62} \right)^{-0.107} \tag{A.18}$$

when d_e is an effective diameter equal to

$$d_e = 0.808\sqrt{bt} \tag{A.19}$$

where b and t are the cross-sectional dimensions in mm. This effective diameter encloses the same area that is stressed at levels greater than or equal to 95% the maximum stress in the rectangular section [67,123]. For a circular cross-section normal diameter d is used in place of d_e in eq. (A.18) [67].

Load modification factor k_c is equal to 1 for cases of pure bending as well as combined torsion and bending [67]. Operation of the turbine is at or near room temperature so the temperature factor k_d is unity [67]. Reliability factor k_e approximates material reliability by incorporating a standard deviation for the reported mean endurance limit. It's found that a k_e equal to 0.814 results in a 99% part reliability [67]. A summary of the Marin factors is presented in table A.1.

Table A.1: Marin Factors for Endurance Strength

	Variable	Value	Unit	Source
Surface factor	k_a	0.74		
Size factor- gear	k_b	1.02		
Size factor- pinion	k_b	1.04		
Size factor- shaft	k_b	0.91		
Load factor	k_c	1		
Temperature factor	k_d	1		
Reliability factor	k_e	0.814		
Ultimate Tensile Strength	F_{ut}	889	MPa	[72]
Endurance strength	F_e'	269	MPa	[71]

Appendix B: Stress-Strain Plots for Material Performance Studies

PLA Filament

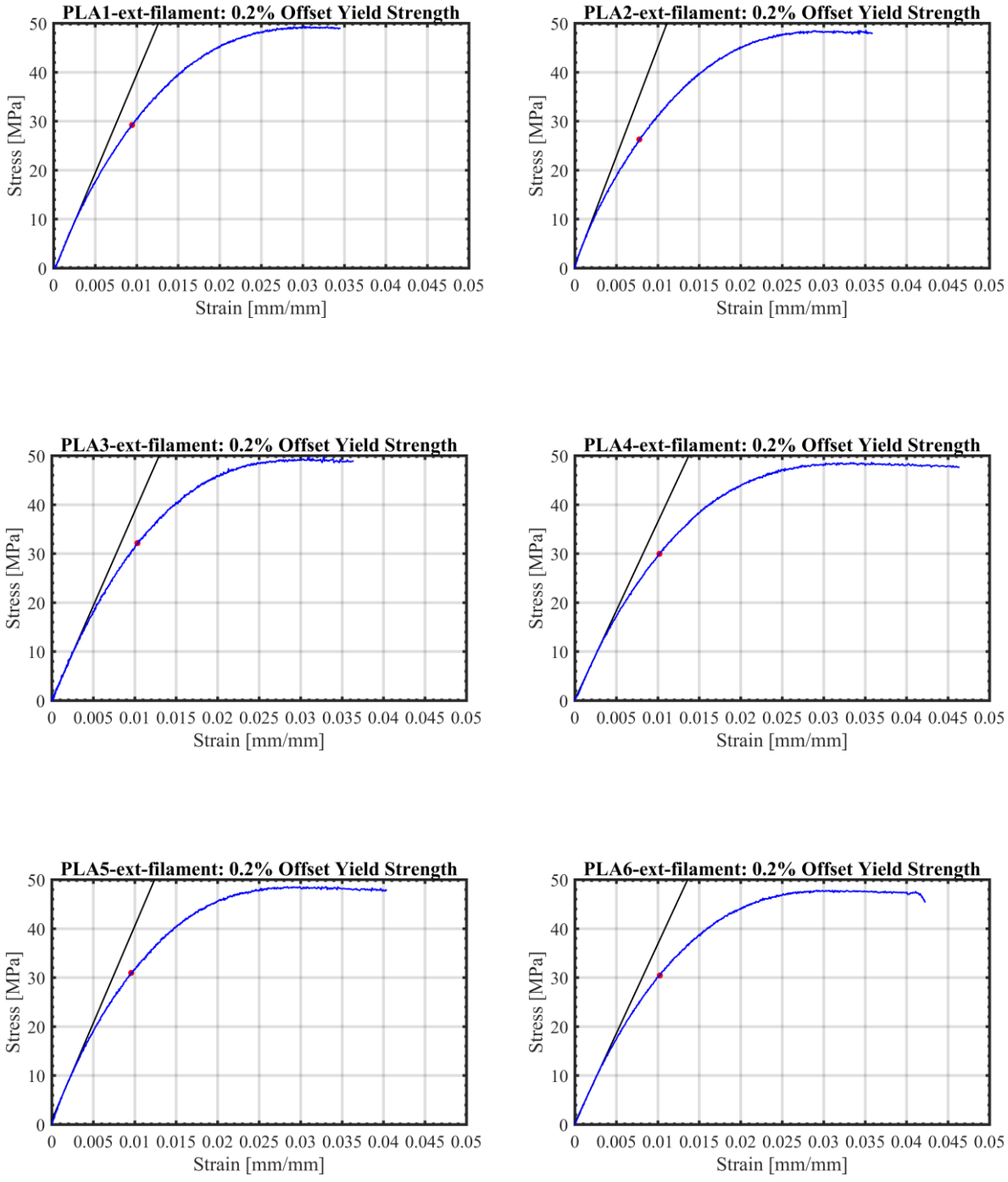

Figure B.1: Stress-strain curves for PLA filament samples with fitted modulus line (black) and 0.2% offset yield identified (pink dot).

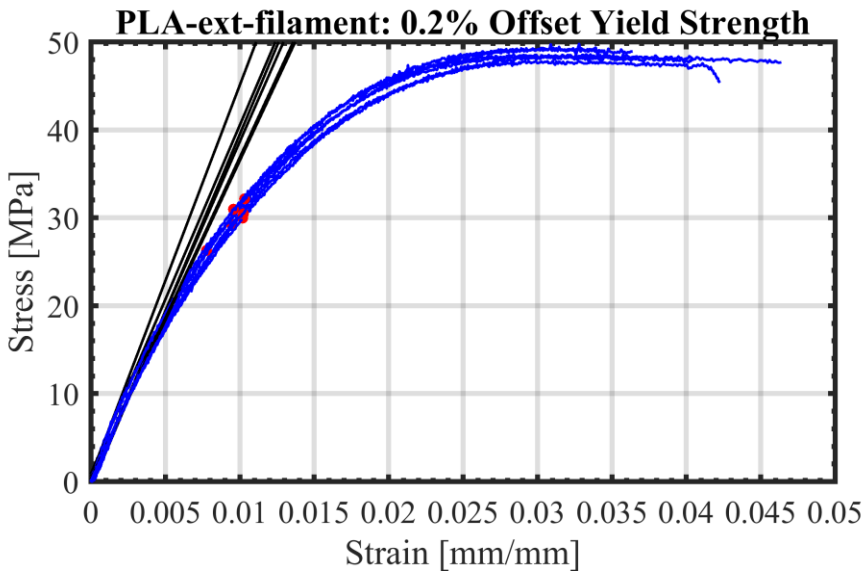

Figure B.2: Stress-strain curves from fig. B.1 overlaid for comparison. As above, the fit modulus lines are plotted in black and the 0.2% offset yield is noted with a pink dot.

ABS Filament

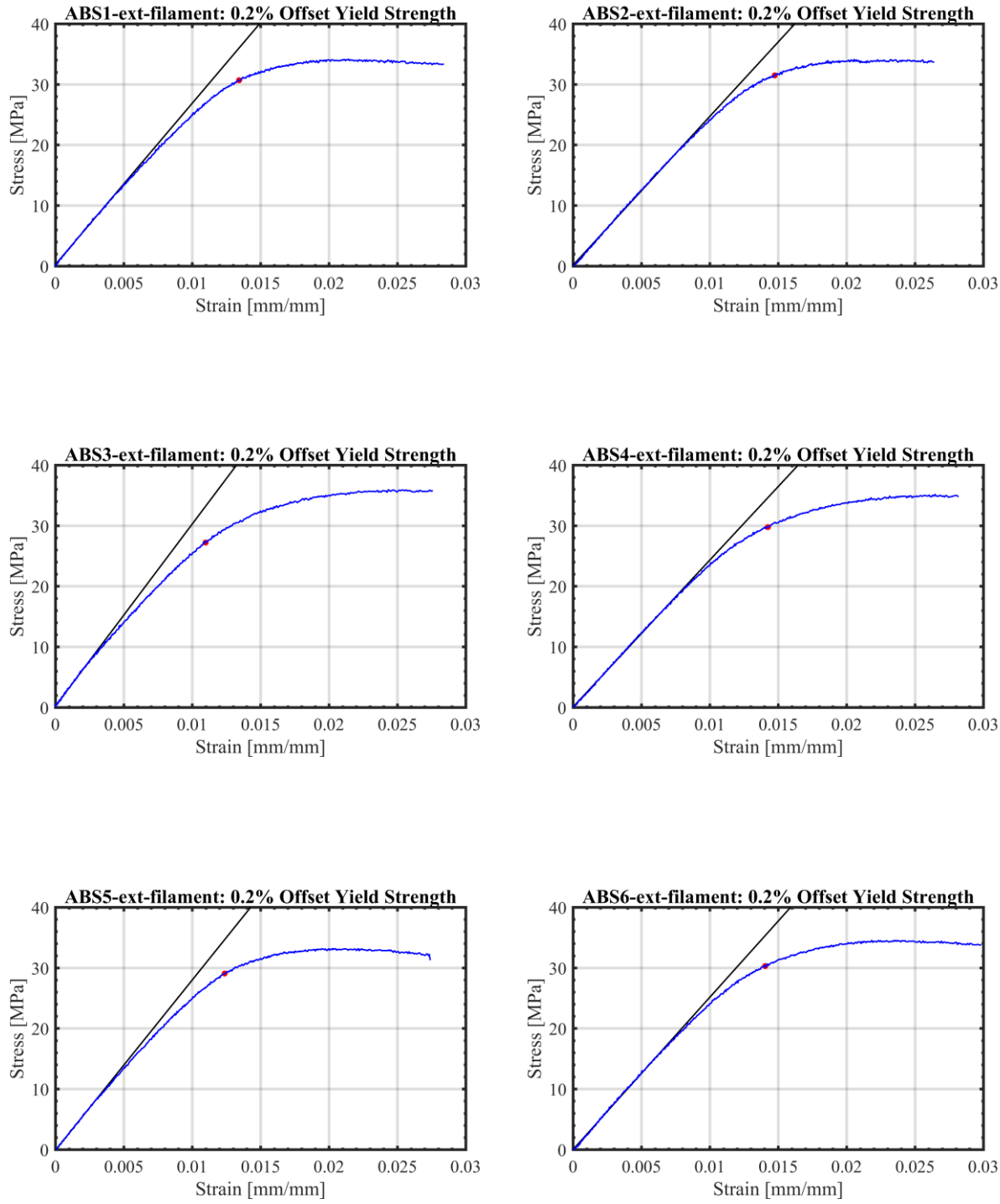

Figure B.3: Stress-strain curves for ABS filament samples with fitted modulus line (black) and 0.2% offset yield identified (pink dot).

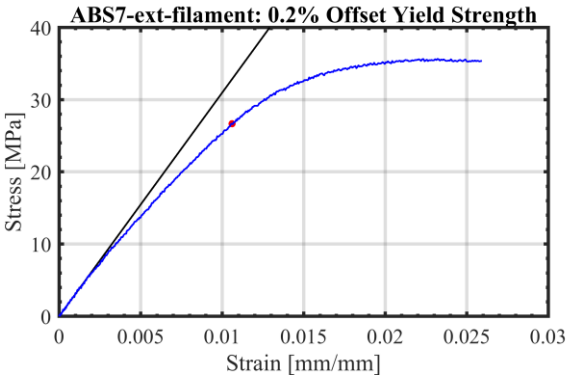

Figure B.3: Stress-strain curves for ABS filament samples with fitted modulus line (black) and 0.2% offset yield identified (pink dot), continued.

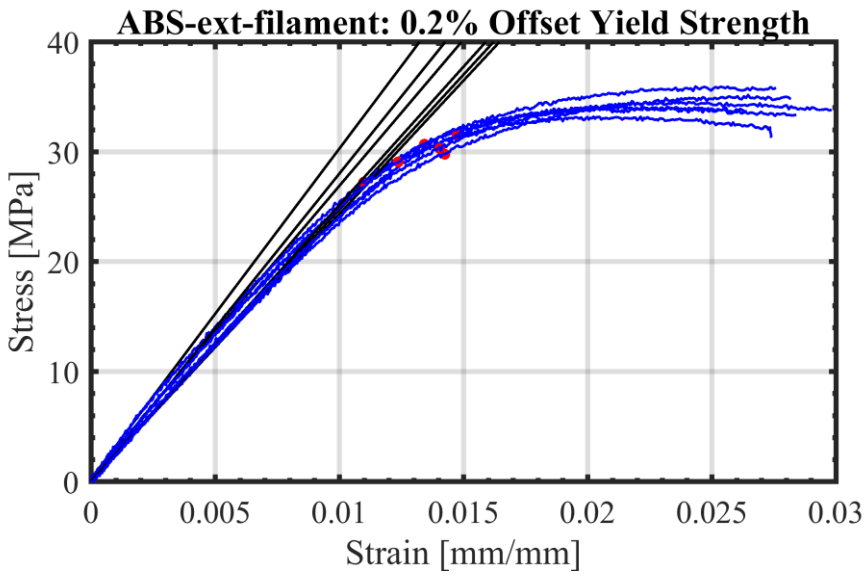

Figure B.4: Stress-strain curves from fig. B.3 overlaid for comparison. As above, the fit modulus lines are plotted in black and the 0.2% offset yield is noted with a pink dot.

PLA Tension

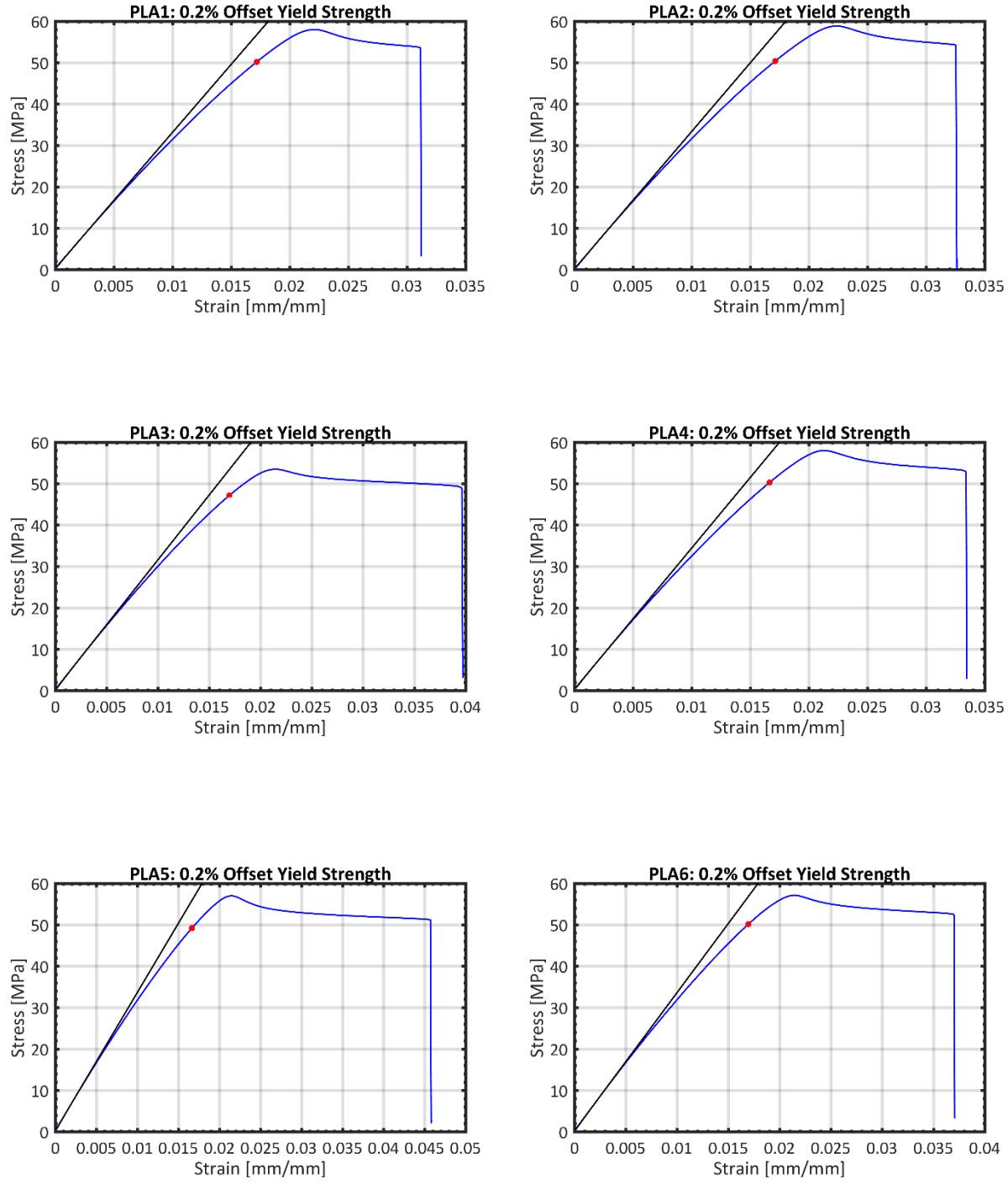

Figure B.5: Stress-strain curves for 6 PLA $[\pm 45_2/90/0/\overline{90}]_s$ coupons with fitted modulus line (black) and 0.2% offset yield identified (pink dot).

ABS Tension

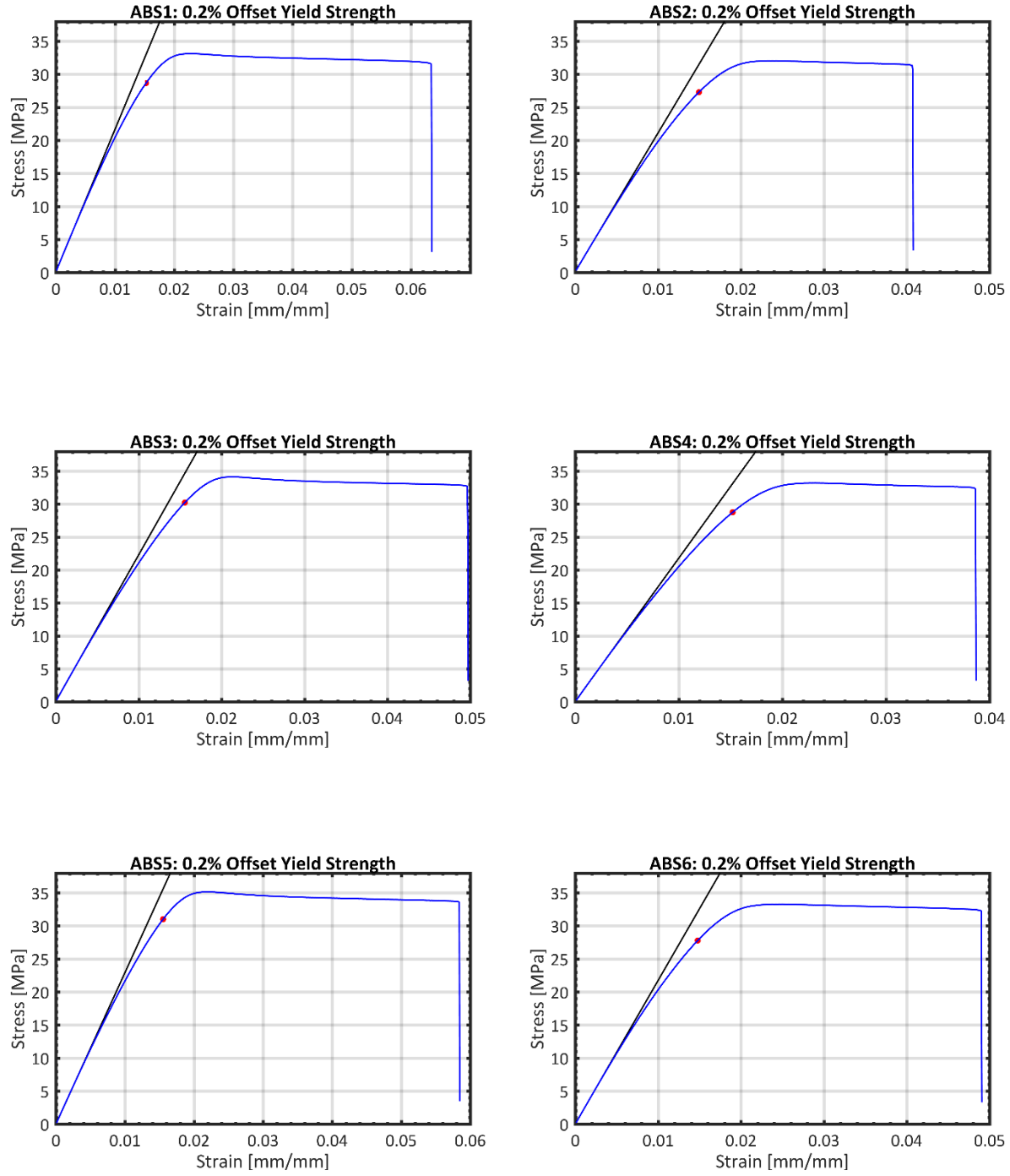

Figure B.6: Stress-strain curves for 6 $[\pm 45_3/\overline{45}]_s$ ABS coupons with fitted modulus line (black) and 0.2% offset yield identified (pink dot).

PLA Compression

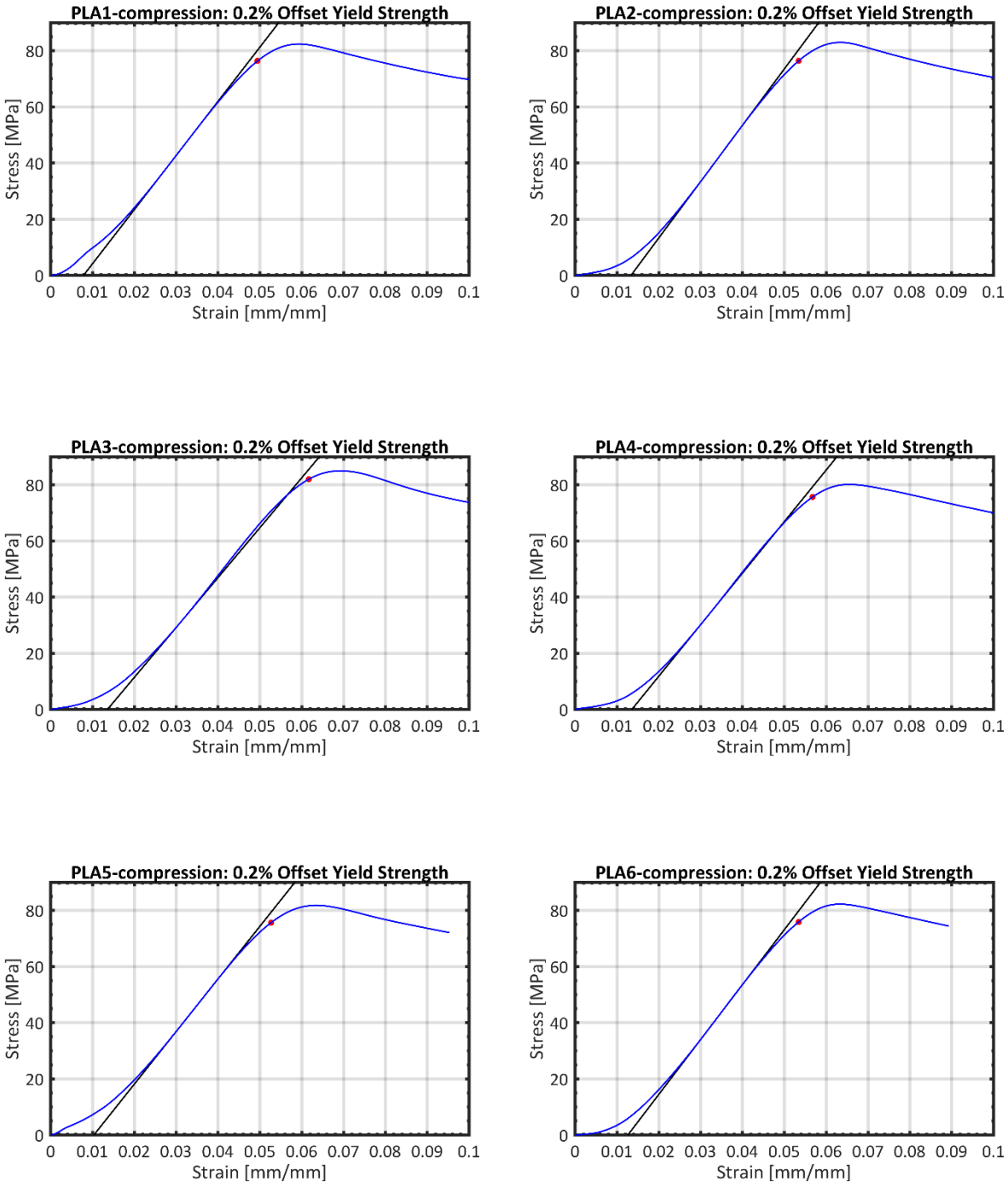

Figure B.7: Stress-strain curves for PLA compression specimens with $[0/90]_{20s}$ infill orientation and 5 shells.

ABS Compression

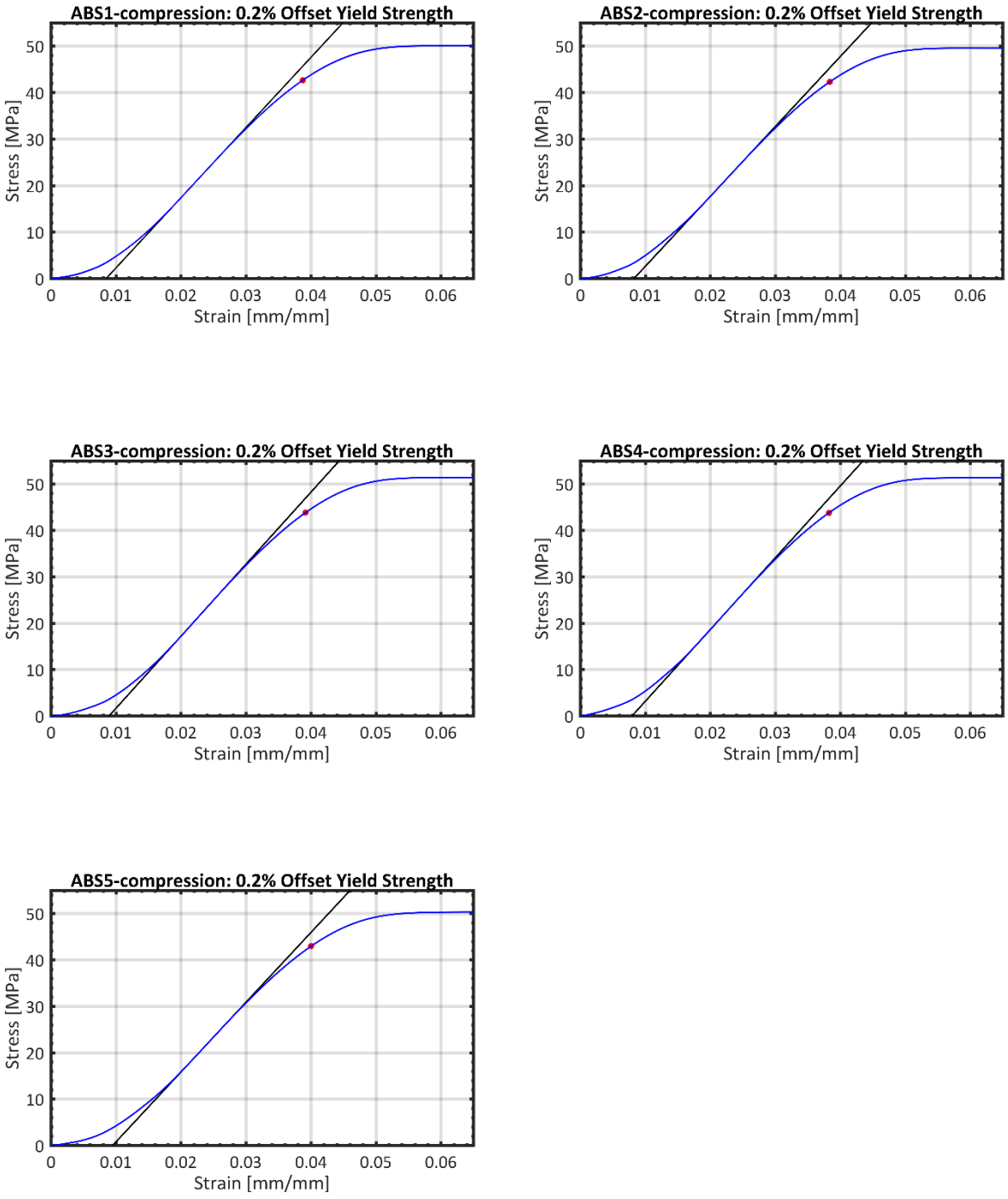

Figure B.8: Stress-strain curves for ABS compression specimens with $[\pm 45]_{23s}$ infill orientation and 1 shell.

Appendix C: Stress-Strain Plots for Infill Orientation Study

0 Degree Coupons

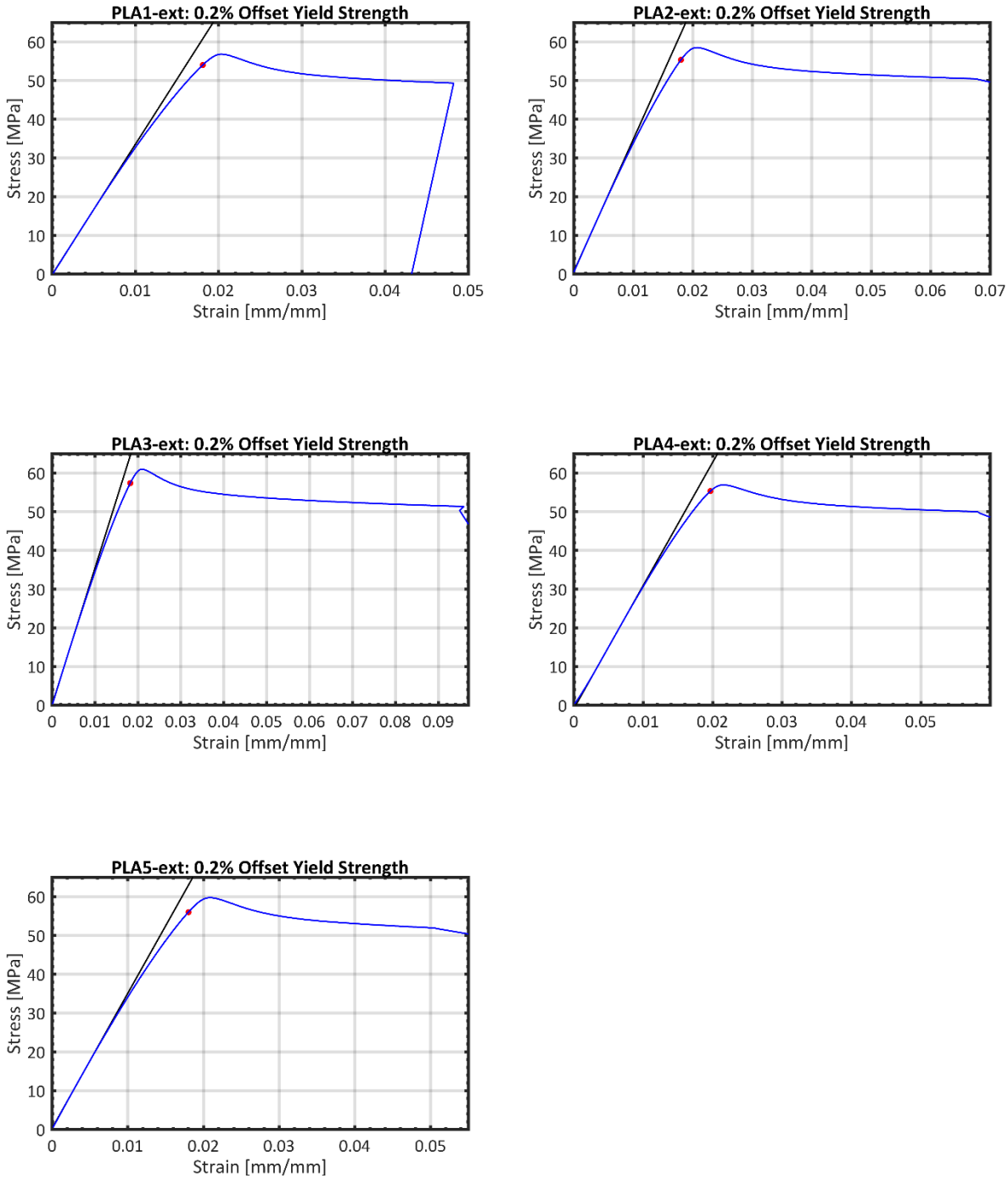

Figure C.1: Stress-strain curves for PLA coupons with 0-degree infill orientation.

45 Degree Coupons

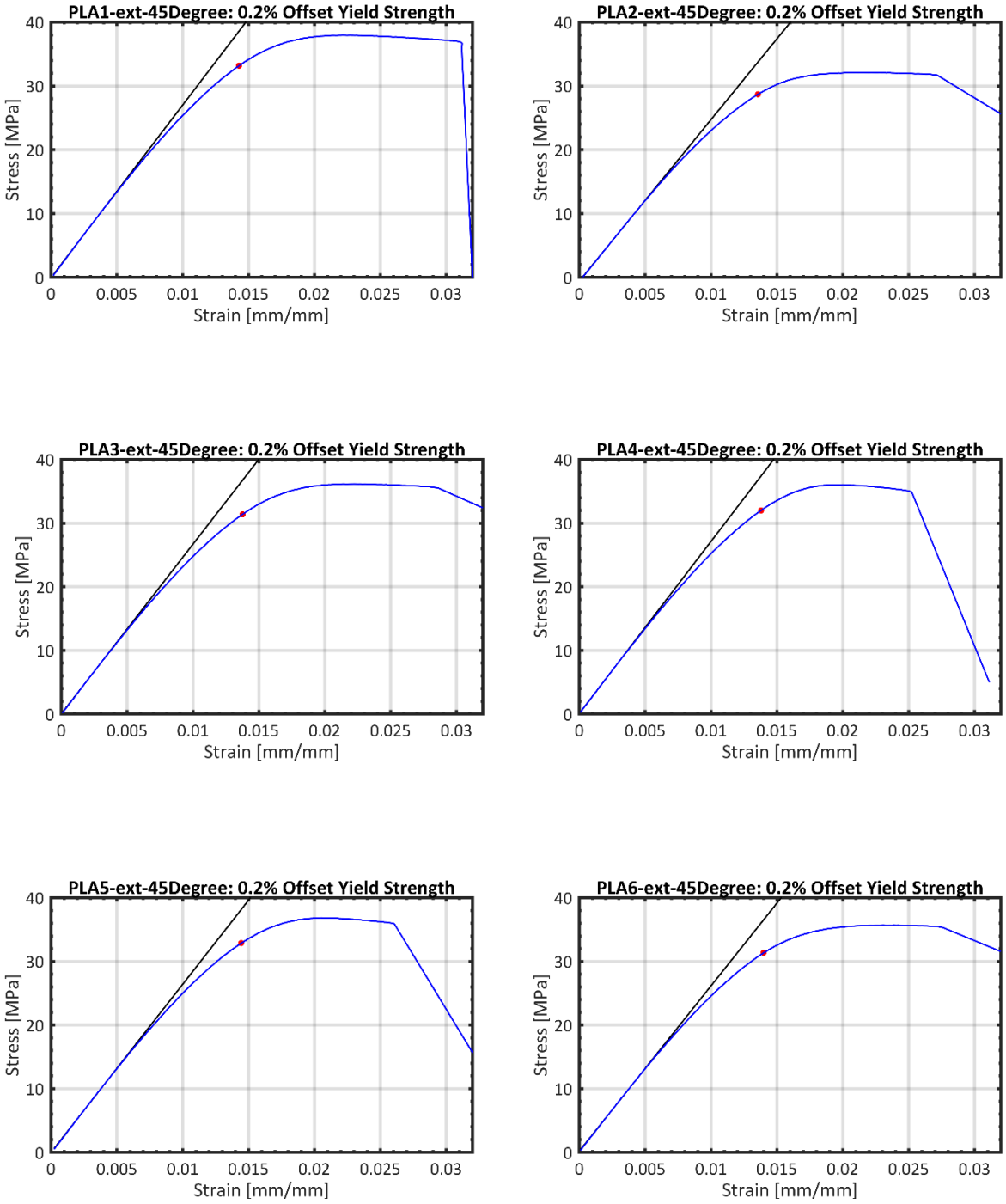

Figure C.2: Stress-strain curves for PLA coupons with 45-degree infill orientation.

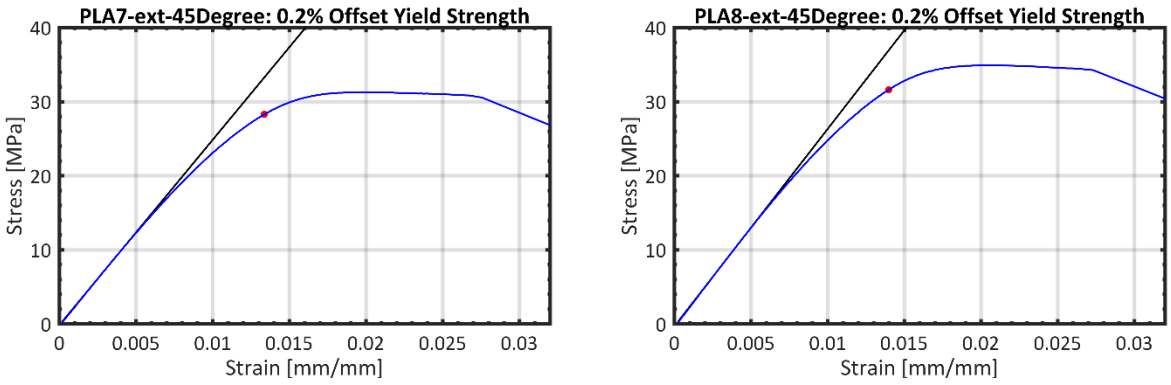

Figure C.2: Stress-strain curves for PLA coupons with 45-degree infill orientation, continued.

60 Degree Coupons

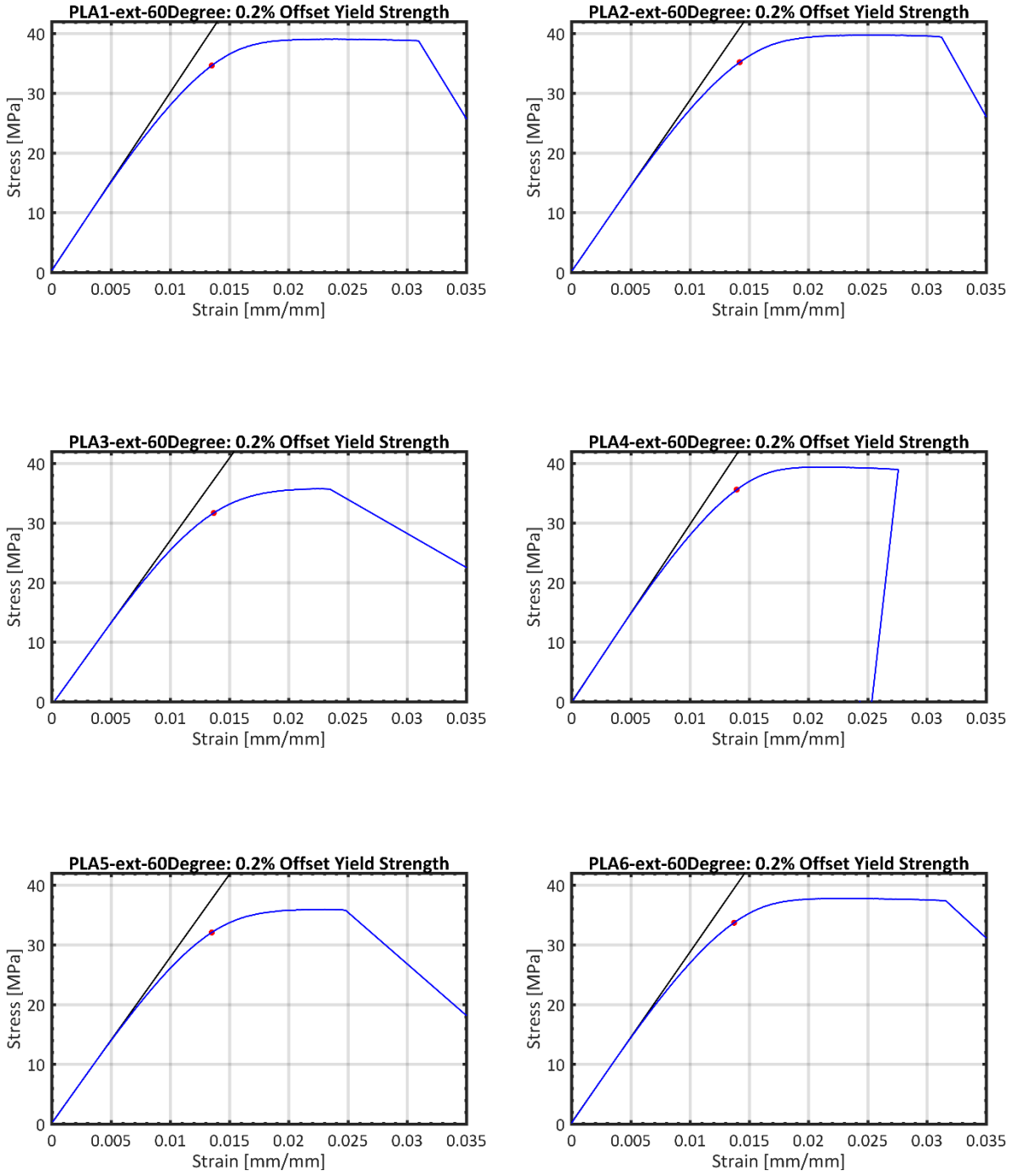

Figure C.3: Stress-strain curves for PLA coupons with 60-degree infill orientation.

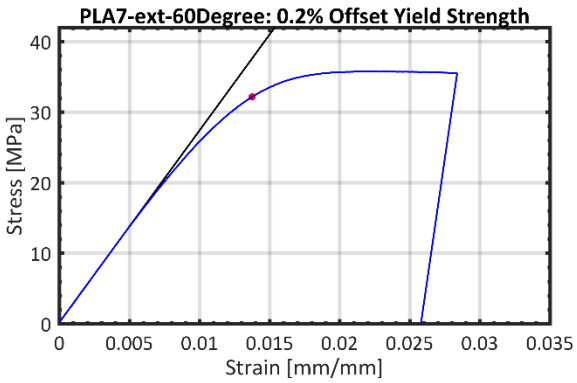

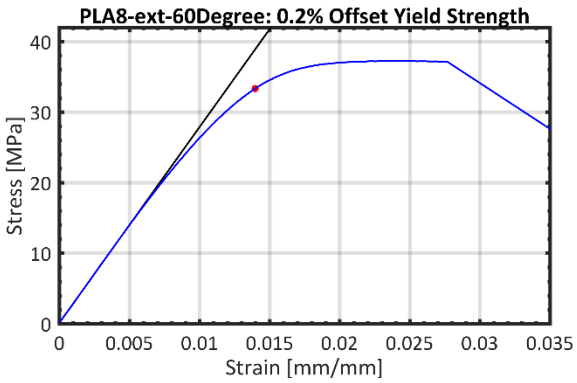

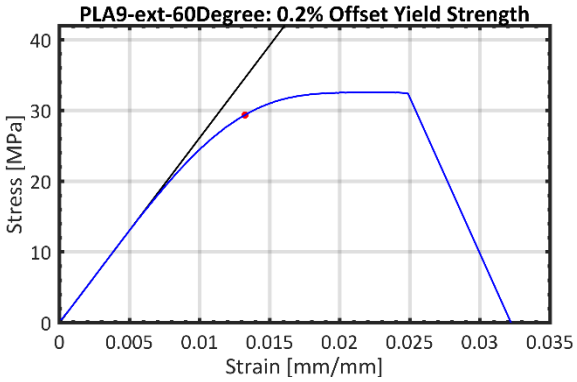

Figure C.3: Stress-strain curves for PLA coupons with 60-degree infill orientation, continued.

90 Degree Coupons

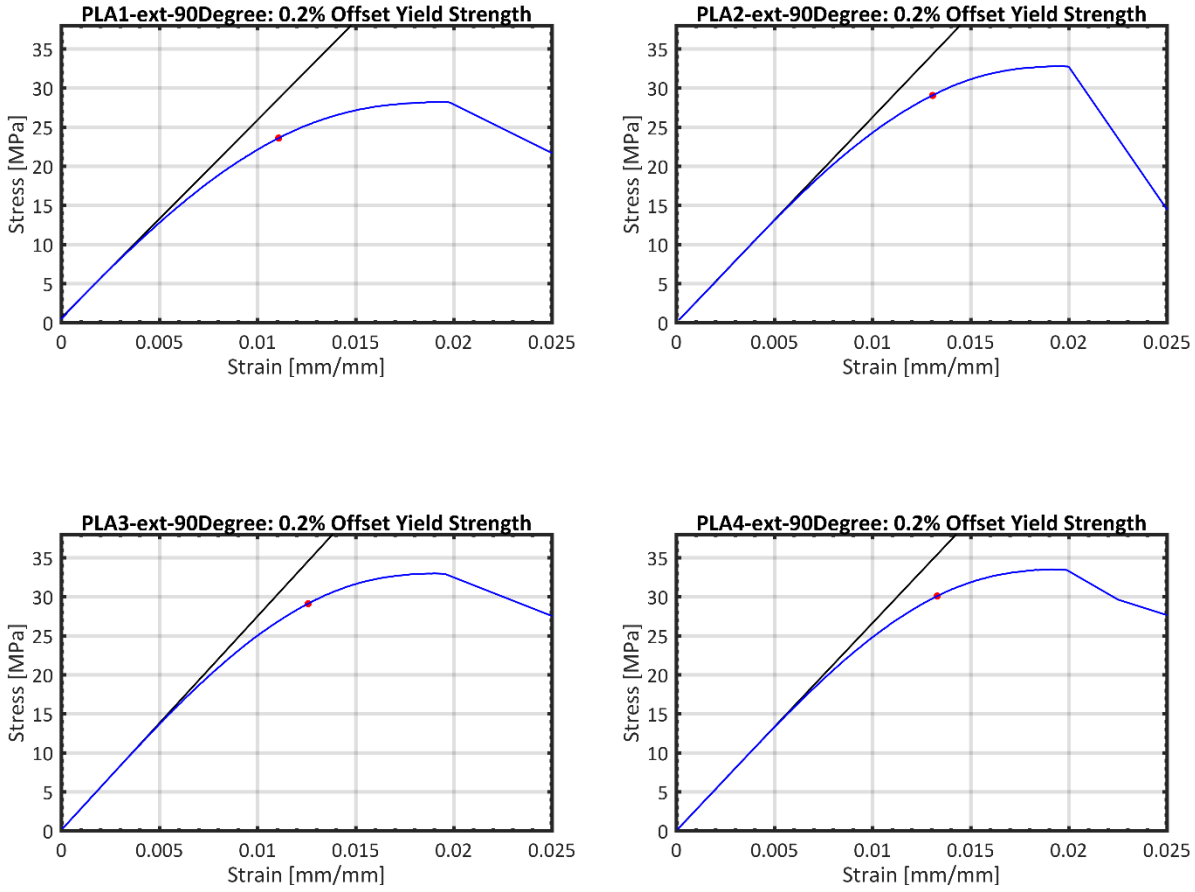

Figure C.4: Stress-strain curves for PLA coupons with 90-degree infill orientation.

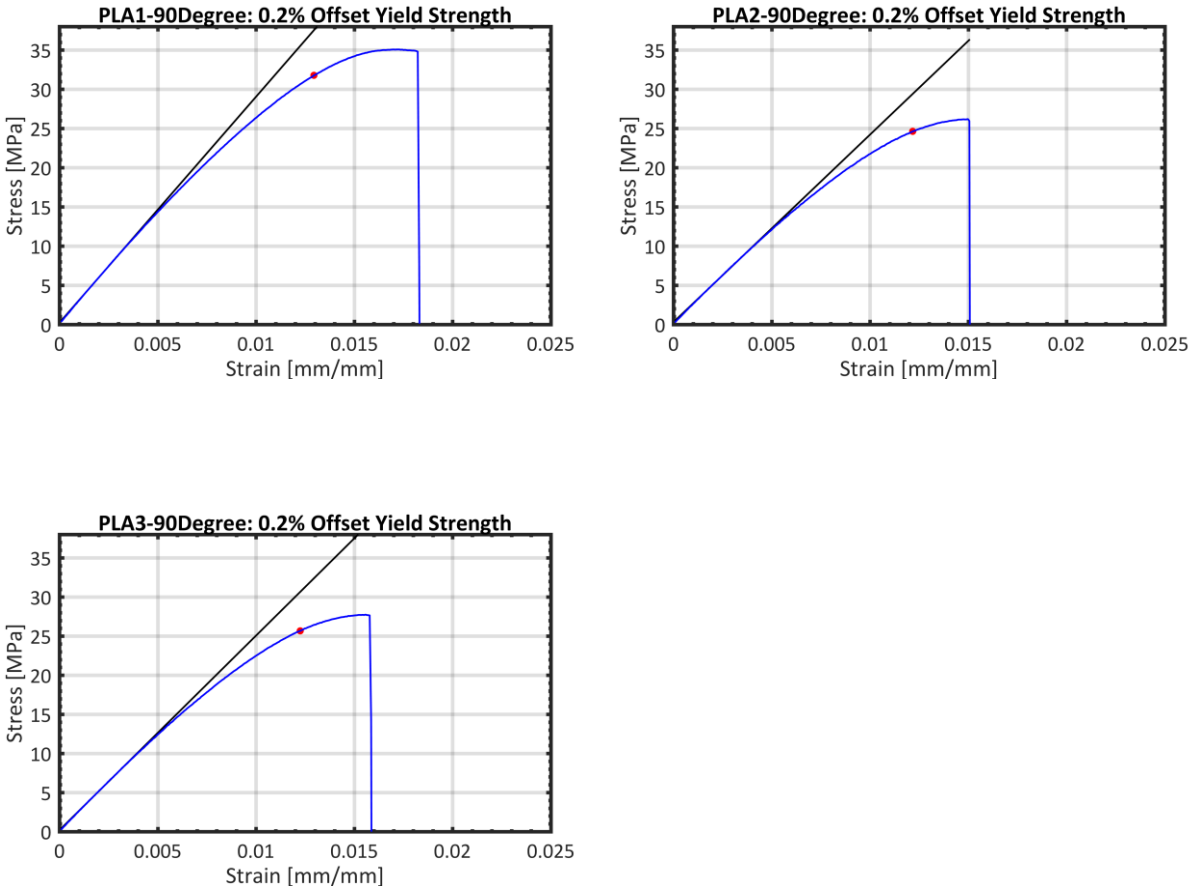

Figure C.5: Stress-strain curves for PLA coupons with 90-degree infill orientation. Strains for these three test runs were calculated from crosshead displacement and adjusted based on average modulus.

Appendix D: Stress-Strain Plots Comparing Crosshead and Extensometer Data

0 Degree Coupons

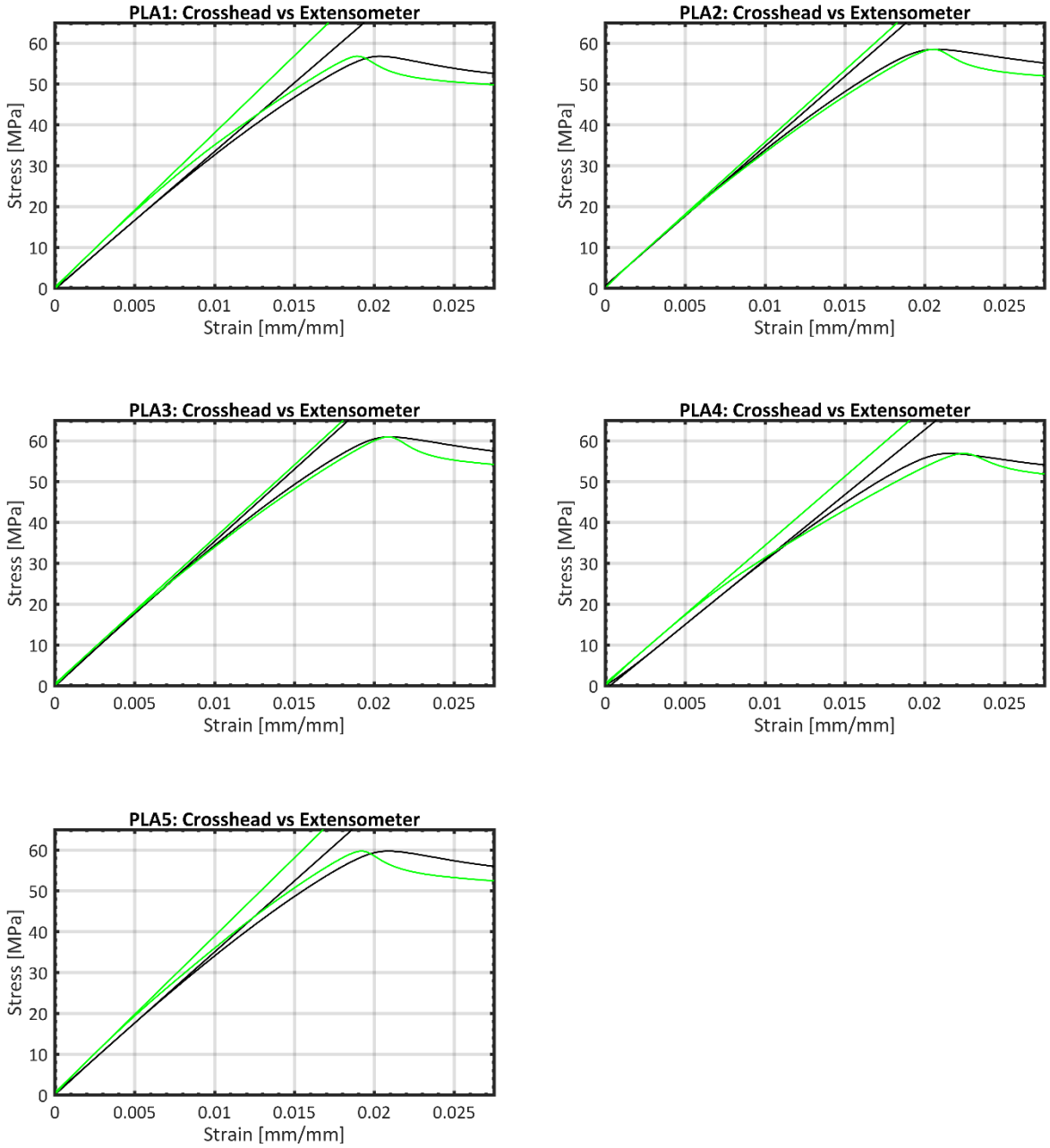

Figure D.1: A comparison of stress-strain curves for PLA samples with 0-degree infill orientation. The green lines are derived from crosshead deflections while the black lines are derived from the simultaneous extensometer deflection. On average, the stiffness calculated from the crosshead data was 6.6% greater the stiffness based on the extensometer data.

45 Degree Coupons

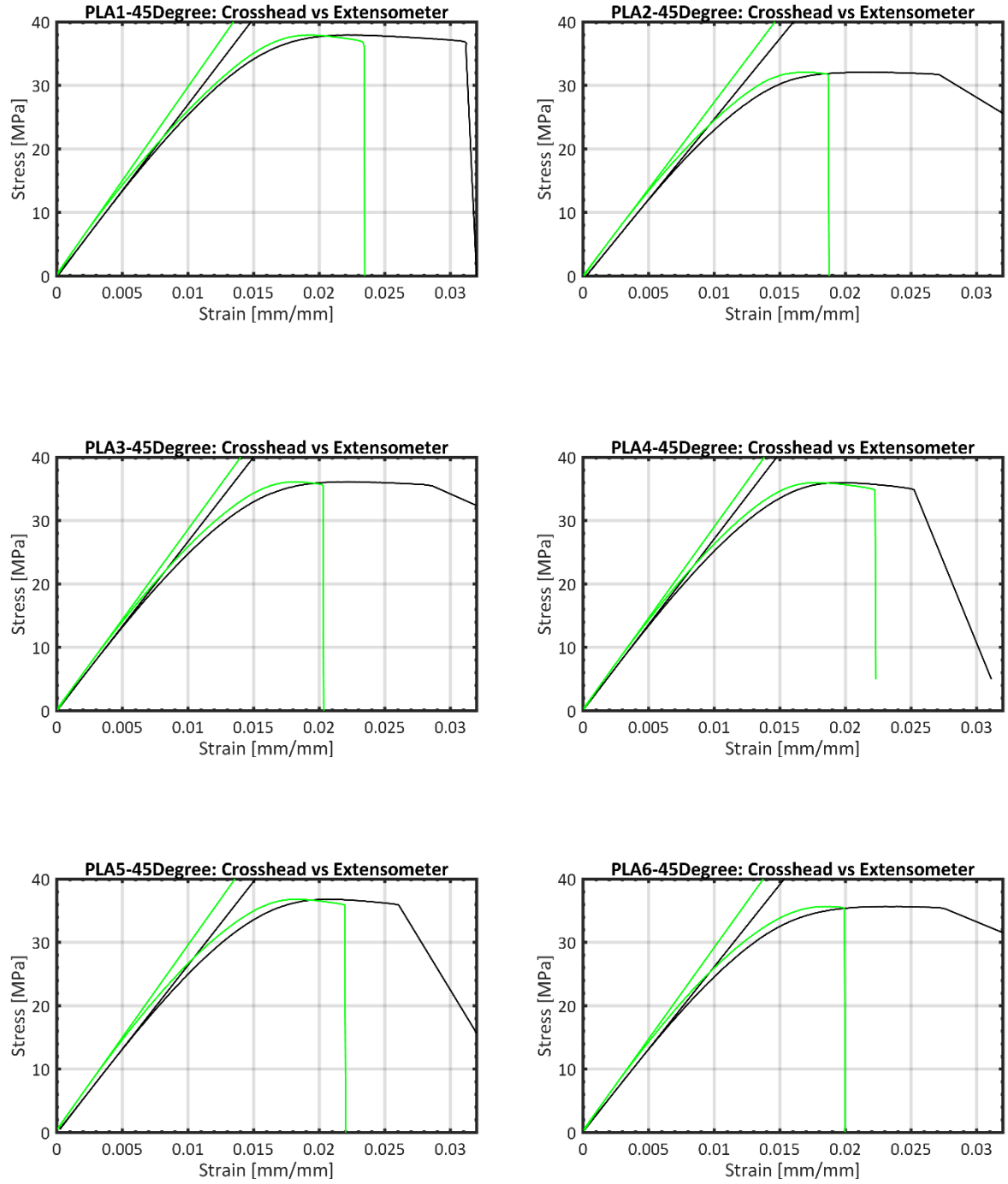

Figure D.2: A comparison of stress-strain curves for PLA samples with 45-degree infill orientation. The green lines are derived from crosshead deflections while the black lines are derived from the simultaneous extensometer deflection. On average, the stiffness calculated from the crosshead data was 8.4% greater the stiffness based on the extensometer data.

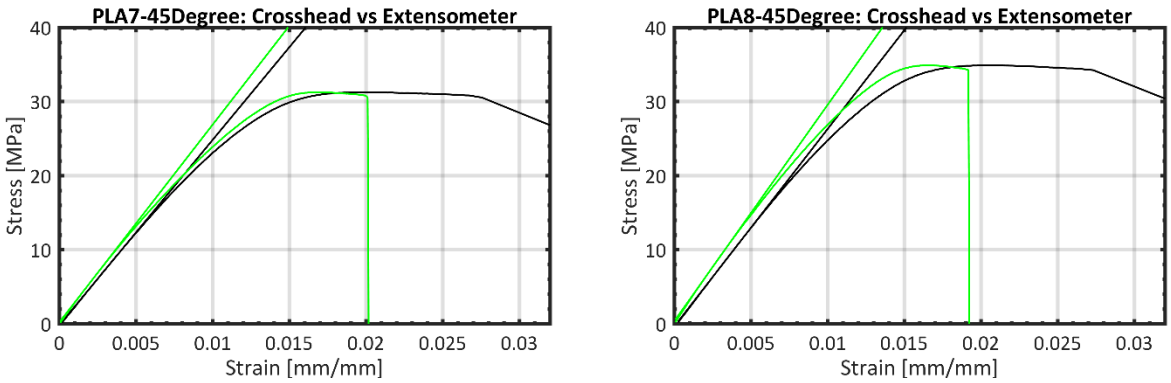

Figure D.2: A comparison of stress-strain curves for PLA samples with 45-degree infill orientation. The green lines are derived from crosshead deflections while the black lines are derived from the simultaneous extensometer deflection. On average, the stiffness calculated from the crosshead data was 8.4% greater the stiffness based on the extensometer data, continued.

60 Degree Coupons

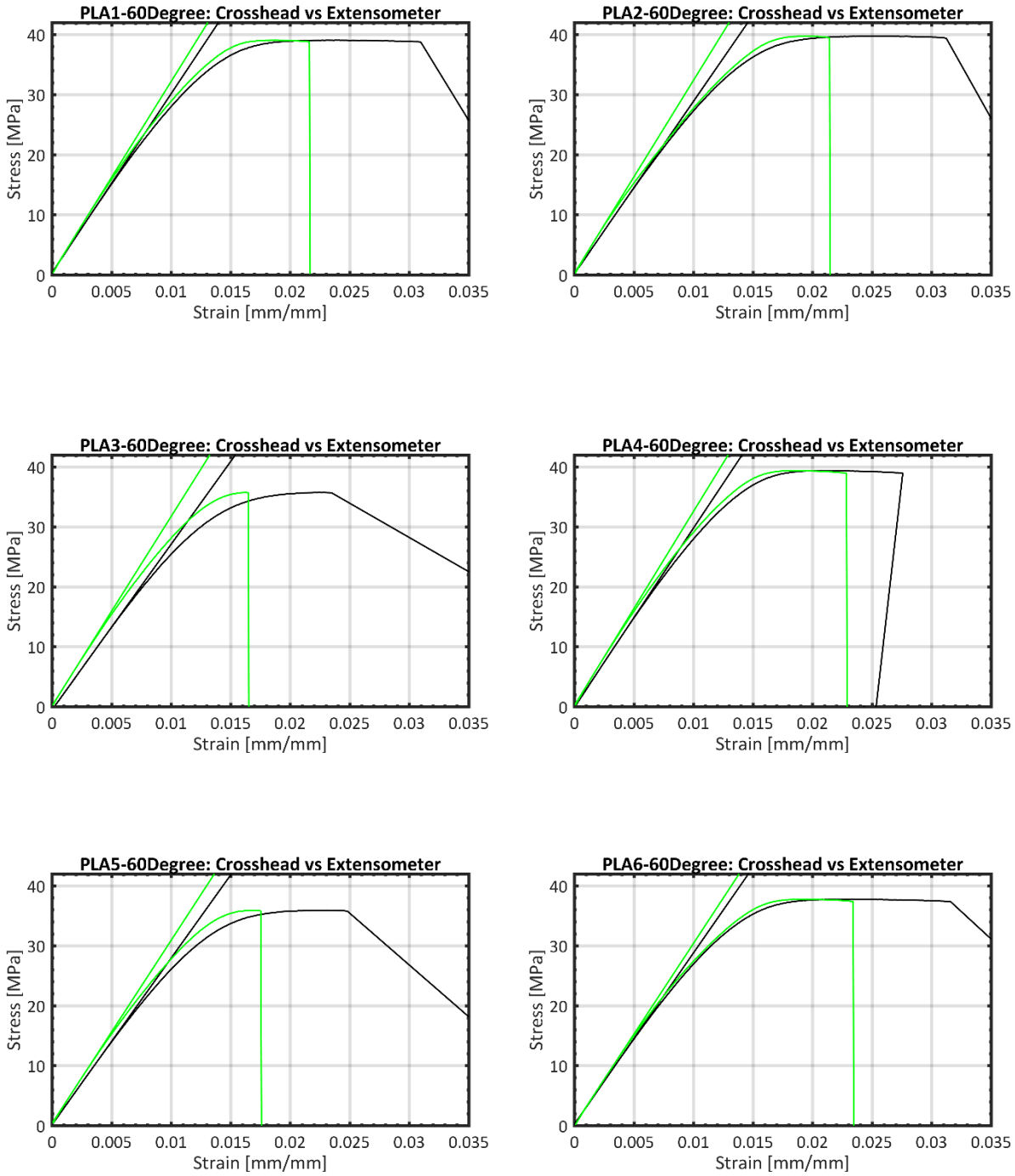

Figure D.3: A comparison of stress-strain curves for PLA samples with 60-degree infill orientation. The green lines are derived from crosshead deflections while the black lines are derived from the simultaneous extensometer deflection.

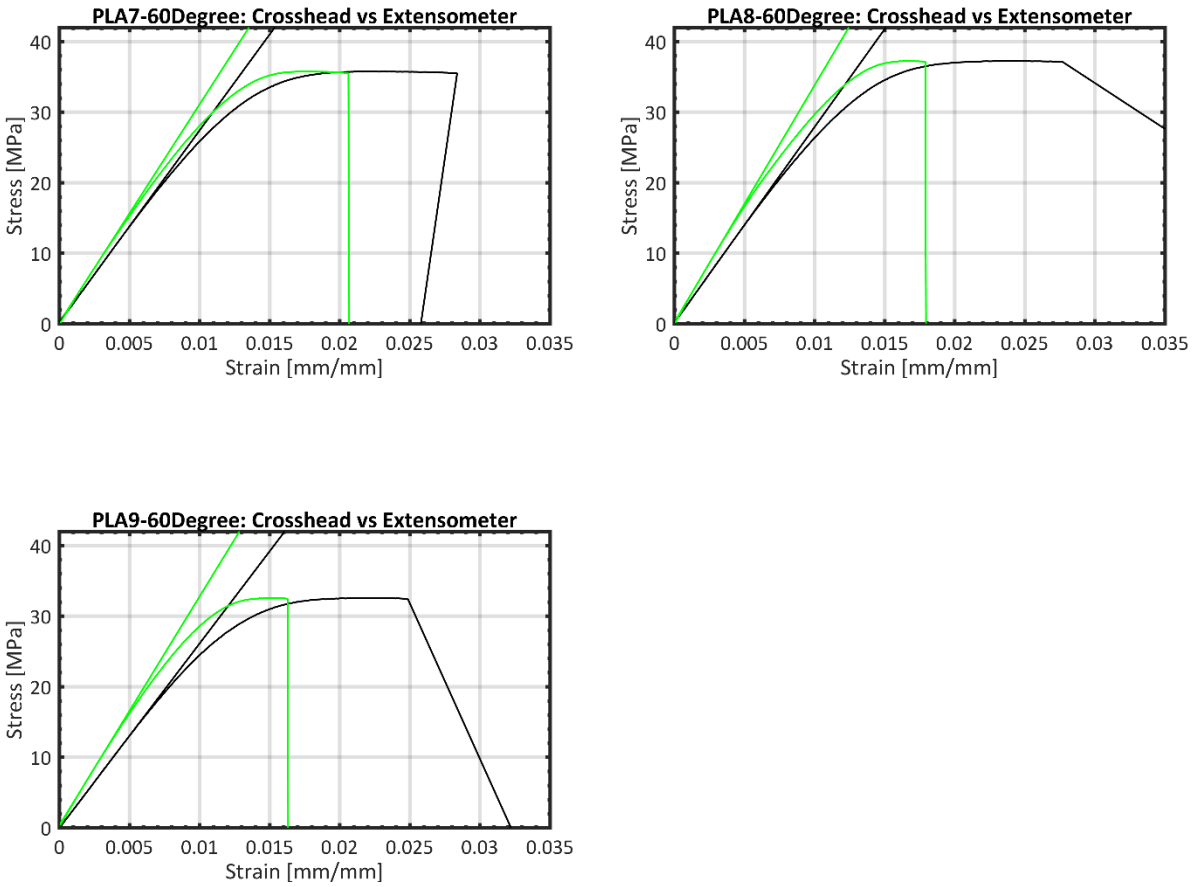

Figure D.3: A comparison of stress-strain curves for PLA samples with 60-degree infill orientation. The green lines are derived from crosshead deflections while the black lines are derived from the simultaneous extensometer deflection. On average, the stiffness calculated from the crosshead data was 12.7% greater the stiffness based on the extensometer data, continued.

90 Degree Coupons

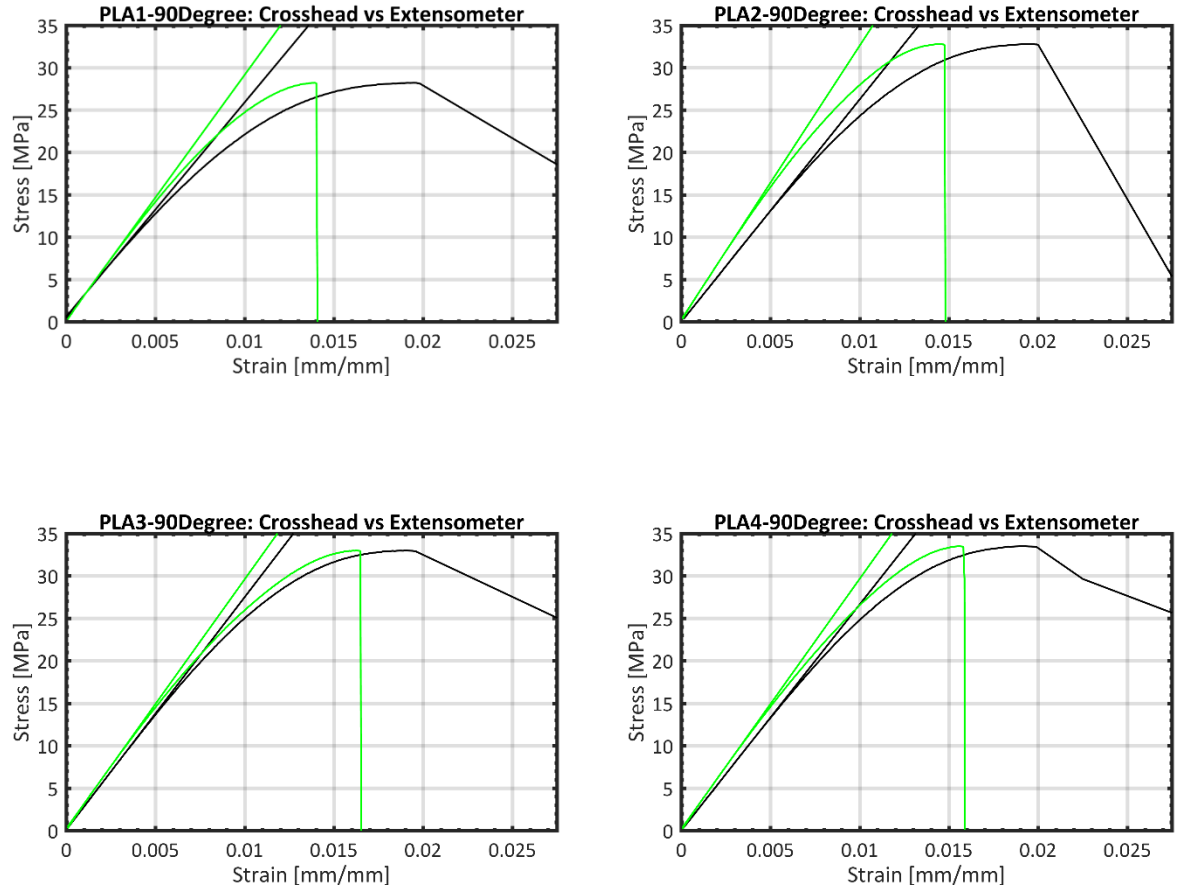

Figure D.4: A comparison of stress-strain curves for PLA samples with 90-degree infill orientation. The green lines are derived from crosshead deflections while the black lines are derived from the simultaneous extensometer deflection. On average, the stiffness calculated from the crosshead data was 13.8% greater the stiffness based on the extensometer data.

Appendix E. Reference Turbine 360 Polars

The following 360 polars were prepared by Jason Jonkman [119]. They are reproduced from [119], which contains more information on the source data and assumptions used to generate them. Lift (C_L), drag (C_D), and moment (C_M) coefficients are listed as a function of angle of attack (α).

Table E.1: Cylinder1 360 Polar

Round root section with a Cd of 0.50			
1	Number of airfoil tables in this file		
1	Reynolds numbers in millions		
0	Control setting		
0	Stall angle (deg)		
0	Zero lift angle of attack (deg)		
0	Cn slope for zero lift (dimensionless)		
0	Cn at stall value for positive angle of attack		
0	Cn at stall value for negative angle of attack		
0	Angle of attack for minimum CD (deg)		
0.5	Minimum CD value		
α	CL	CD	CM
-180	0	0.5	0
0	0	0.5	0
180	0	0.5	0
EOT			

Table E.2: Cylinder2 360 Polar

Round root section with a Cd of 0.35			
line			
1	Number of airfoil tables in this file		
1	Reynolds numbers in millions		
0	Control setting		
0	Stall angle (deg)		
0	Zero lift angle of attack (deg)		
0	Cn slope for zero lift (dimensionless)		
0	Cn at stall value for positive angle of attack		
0	Cn at stall value for negative angle of attack		
0	Angle of attack for minimum CD (deg)		
0.35	Minimum CD value		
α	CL	CD	CM
-180	0	0.35	0
0	0	0.35	0
180	0	0.35	0
EOT			

Table E.3: DU 99-W-405 **(**DU40) 360 Polar

1	Number of airfoil tables in this file
1	Reynolds numbers in millions
0	Control setting
9	Stall angle (deg)
-1.343	Zero Cn angle of attack (deg)
7.4888	Cn slope for zero lift (dimensionless)
1.3519	Cn extrapolated to value at positive stall angle of attack
-0.3226	Cn at stall value for negative angle of attack
0	Angle of attack for minimum CD (deg)
0.0113	Minimum CD value

α	CL	CD	CM
-180	0	0.0602	0
-175	0.218	0.0699	0.0934
-170	0.397	0.1107	0.1697
-160	0.642	0.3045	0.2813
-155	0.715	0.4179	0.3208
-150	0.757	0.5355	0.3516
-145	0.772	0.6535	0.3752
-140	0.762	0.7685	0.3926
-135	0.731	0.8777	0.4048
-130	0.68	0.9788	0.4126
-125	0.613	1.07	0.4166
-120	0.532	1.1499	0.4176
-115	0.439	1.2174	0.4158
-110	0.337	1.2716	0.4117
-105	0.228	1.3118	0.4057
-100	0.114	1.3378	0.3979
-95	-0.002	1.3492	0.3887
-90	-0.12	1.346	0.3781
-85	-0.236	1.3283	0.3663
-80	-0.349	1.2964	0.3534
-75	-0.456	1.2507	0.3394
-70	-0.557	1.1918	0.3244
-65	-0.647	1.1204	0.3084
-60	-0.727	1.0376	0.2914
-55	-0.792	0.9446	0.2733
-50	-0.842	0.8429	0.2543
-45	-0.874	0.7345	0.2342
-40	-0.886	0.6215	0.2129
-35	-0.875	0.5067	0.1906
-30	-0.839	0.3932	0.167
-25	-0.777	0.2849	0.1422
-24	-0.761	0.2642	0.1371

Table E.3: DU-99-W-405 (DU40) 360 Polar, continued.

α	CL	CD	CM
-23	-0.744	0.244	0.132
-22	-0.725	0.2242	0.1268
-21	-0.706	0.2049	0.1215
-20	-0.685	0.1861	0.1162
-19	-0.662	0.1687	0.1097
-18	-0.635	0.1533	0.1012
-17	-0.605	0.1398	0.0907
-16	-0.571	0.1281	0.0784
-15	-0.534	0.1183	0.0646
-14	-0.494	0.1101	0.0494
-13	-0.452	0.1036	0.033
-12	-0.407	0.0986	0.0156
-11	-0.36	0.0951	-0.0026
-10	-0.311	0.0931	-0.0213
-8	-0.208	0.093	-0.06
-6	-0.111	0.0689	-0.05
-5.5	-0.09	0.0614	-0.0516
-5	-0.072	0.0547	-0.0532
-4.5	-0.065	0.048	-0.0538
-4	-0.054	0.0411	-0.0544
-3.5	-0.017	0.0349	-0.0554
-3	0.003	0.0299	-0.0558
-2.5	0.014	0.0255	-0.0555
-2	0.009	0.0198	-0.0534
-1.5	0.004	0.0164	-0.0442
-1	0.036	0.0147	-0.0469
-0.5	0.073	0.0137	-0.0522
0	0.137	0.0113	-0.0573
0.5	0.213	0.0114	-0.0644
1	0.292	0.0118	-0.0718
1.5	0.369	0.0122	-0.0783
2	0.444	0.0124	-0.0835
2.5	0.514	0.0124	-0.0866
3	0.58	0.0123	-0.0887
3.5	0.645	0.012	-0.09
4	0.71	0.0119	-0.0914
4.5	0.776	0.0122	-0.0933
5	0.841	0.0125	-0.0947
5.5	0.904	0.0129	-0.0957
6	0.967	0.0135	-0.0967
6.5	1.027	0.0144	-0.0973
7	1.084	0.0158	-0.0972

Table E.3: DU-99-W-405 (DU40) 360 Polar, continued.

α	CL	CD	CM
7.5	1.14	0.0174	-0.0972
8	1.193	0.0198	-0.0968
8.5	1.242	0.0231	-0.0958
9	1.287	0.0275	-0.0948
9.5	1.333	0.0323	-0.0942
10	1.368	0.0393	-0.0926
10.5	1.4	0.0475	-0.0908
11	1.425	0.058	-0.089
11.5	1.449	0.0691	-0.0877
12	1.473	0.0816	-0.087
12.5	1.494	0.0973	-0.087
13	1.513	0.1129	-0.0876
13.5	1.538	0.1288	-0.0886
14.5	1.587	0.165	-0.0917
15	1.614	0.1845	-0.0939
15.5	1.631	0.2052	-0.0966
16	1.649	0.225	-0.0996
16.5	1.666	0.2467	-0.1031
17	1.681	0.2684	-0.1069
17.5	1.699	0.29	-0.111
18	1.719	0.3121	-0.1157
19	1.751	0.3554	-0.1242
19.5	1.767	0.3783	-0.1291
20.5	1.798	0.4212	-0.1384
21	1.81	0.4415	-0.1416
22	1.83	0.483	-0.1479
23	1.847	0.5257	-0.1542
24	1.861	0.5694	-0.1603
25	1.872	0.6141	-0.1664
26	1.881	0.6593	-0.1724
28	1.894	0.7513	-0.1841
30	1.904	0.8441	-0.1954
32	1.915	0.9364	-0.2063
35	1.929	1.0722	-0.222
40	1.903	1.2873	-0.2468
45	1.82	1.4796	-0.2701
50	1.69	1.6401	-0.2921
55	1.522	1.7609	-0.3127
60	1.323	1.836	-0.3321
65	1.106	1.8614	-0.3502
70	0.88	1.8347	-0.3672
75	0.658	1.7567	-0.383

Table E.3: DU-99-W-405 (DU40) 360 Polar, continued.

α	CL	CD	CM
80	0.449	1.6334	-0.3977
85	0.267	1.4847	-0.4112
90	0.124	1.3879	-0.4234
95	0.002	1.3912	-0.4343
100	-0.118	1.3795	-0.4437
105	-0.235	1.3528	-0.4514
110	-0.348	1.3114	-0.4573
115	-0.453	1.2557	-0.461
120	-0.549	1.1864	-0.4623
125	-0.633	1.1041	-0.4606
130	-0.702	1.0102	-0.4554
135	-0.754	0.906	-0.4462
140	-0.787	0.7935	-0.4323
145	-0.797	0.675	-0.4127
150	-0.782	0.5532	-0.3863
155	-0.739	0.4318	-0.3521
160	-0.664	0.3147	-0.3085
170	-0.41	0.1144	-0.1858
175	-0.226	0.0702	-0.1022
180	0	0.0602	0

EOT

Table E.4: DU 99-W-350 (DU35) 360 Polar

1	Number of airfoil tables in this file
1	Reynolds numbers in millions
0	Control setting
11.5	Stall angle (deg)
-1.833	Zero Cn angle of attack (deg)
7.1838	Cn slope for zero lift (dimensionless)
1.6717	Cn extrapolated to value at positive stall angle of attack
-0.3075	Cn at stall value for negative angle of attack
0	Angle of attack for minimum CD (deg)
0.0094	Minimum CD value

α	CL	CD	CM
-180	0	0.0407	0
-175	0.223	0.0507	0.0937
-170	0.405	0.1055	0.1702
-160	0.658	0.2982	0.2819
-155	0.733	0.4121	0.3213
-150	0.778	0.5308	0.352
-145	0.795	0.6503	0.3754
-140	0.787	0.7672	0.3926
-135	0.757	0.8785	0.4046
-130	0.708	0.9819	0.4121
-125	0.641	1.0756	0.416
-120	0.56	1.158	0.4167
-115	0.467	1.228	0.4146
-110	0.365	1.2847	0.4104
-105	0.255	1.3274	0.4041
-100	0.139	1.3557	0.3961
-95	0.021	1.3692	0.3867
-90	-0.098	1.368	0.3759
-85	-0.216	1.3521	0.3639
-80	-0.331	1.3218	0.3508
-75	-0.441	1.2773	0.3367
-70	-0.544	1.2193	0.3216
-65	-0.638	1.1486	0.3054
-60	-0.72	1.066	0.2884
-55	-0.788	0.9728	0.2703
-50	-0.84	0.8705	0.2512

Table E.4: DU 99-W-350 (DU35) 360 Polar, continued.

α	CL	CD	CM
-45	-0.875	0.7611	0.2311
-40	-0.889	0.6466	0.2099
-35	-0.88	0.5299	0.1876
-30	-0.846	0.4141	0.1641
-25	-0.784	0.303	0.1396
-24	-0.768	0.2817	0.1345
-23	-0.751	0.2608	0.1294
-22	-0.733	0.2404	0.1243
-21	-0.714	0.2205	0.1191
-20	-0.693	0.2011	0.1139
-19	-0.671	0.1822	0.1086
-18	-0.648	0.164	0.1032
-17	-0.624	0.1465	0.0975
-16	-0.601	0.13	0.0898
-15	-0.579	0.1145	0.0799
-14	-0.559	0.1	0.0682
-13	-0.539	0.0867	0.0547
-12	-0.519	0.0744	0.0397
-11	-0.499	0.0633	0.0234
-10	-0.48	0.0534	0.006
-5.54	-0.385	0.0245	-0.08
-5.04	-0.359	0.0225	-0.08
-4.54	-0.36	0.0196	-0.08
-4.04	-0.355	0.0174	-0.08
-3.54	-0.307	0.0162	-0.08
-3.04	-0.246	0.0144	-0.08
-3	-0.24	0.024	-0.0623
-2.5	-0.163	0.0188	-0.0674
-2	-0.091	0.016	-0.0712
-1.5	-0.019	0.0137	-0.0746
-1	0.052	0.0118	-0.0778
-0.5	0.121	0.0104	-0.0806
0	0.196	0.0094	-0.0831
0.5	0.265	0.0096	-0.0863
1	0.335	0.0098	-0.0895
1.5	0.404	0.0099	-0.0924
2	0.472	0.01	-0.0949
2.5	0.54	0.0102	-0.0973
3	0.608	0.0103	-0.0996

Table E.4: DU 99-W-350 (DU35) 360 Polar, continued.

α	CL	CD	CM
3.5	0.674	0.0104	-0.1016
4	0.742	0.0105	-0.1037
4.5	0.809	0.0107	-0.1057
5	0.875	0.0108	-0.1076
5.5	0.941	0.0109	-0.1094
6	1.007	0.011	-0.1109
6.5	1.071	0.0113	-0.1118
7	1.134	0.0115	-0.1127
7.5	1.198	0.0117	-0.1138
8	1.26	0.012	-0.1144
8.5	1.318	0.0126	-0.1137
9	1.368	0.0133	-0.1112
9.5	1.422	0.0143	-0.11
10	1.475	0.0156	-0.1086
10.5	1.523	0.0174	-0.1064
11	1.57	0.0194	-0.1044
11.5	1.609	0.0227	-0.1013
12	1.642	0.0269	-0.098
12.5	1.675	0.0319	-0.0953
13	1.7	0.0398	-0.0925
13.5	1.717	0.0488	-0.0896
14	1.712	0.0614	-0.0864
14.5	1.703	0.0786	-0.084
15.5	1.671	0.1173	-0.083
16	1.649	0.1377	-0.0848
16.5	1.621	0.16	-0.088
17	1.598	0.1814	-0.0926
17.5	1.571	0.2042	-0.0984
18	1.549	0.2316	-0.1052
19	1.544	0.2719	-0.1158
19.5	1.549	0.2906	-0.1213
20	1.565	0.3085	-0.1248
21	1.565	0.3447	-0.1317
22	1.563	0.382	-0.1385
23	1.558	0.4203	-0.1452
24	1.552	0.4593	-0.1518
25	1.546	0.4988	-0.1583
26	1.539	0.5387	-0.1647
28	1.527	0.6187	-0.177

Table E.4: DU 99-W-350 (DU35) 360 Polar, continued.

α	CL	CD	CM
30	1.522	0.6978	-0.1886
32	1.529	0.7747	-0.1994
35	1.544	0.8869	-0.2148
40	1.529	1.0671	-0.2392
45	1.471	1.2319	-0.2622
50	1.376	1.3747	-0.2839
55	1.249	1.4899	-0.3043
60	1.097	1.5728	-0.3236
65	0.928	1.6202	-0.3417
70	0.75	1.6302	-0.3586
75	0.57	1.6031	-0.3745
80	0.396	1.5423	-0.3892
85	0.237	1.4598	-0.4028
90	0.101	1.4041	-0.4151
95	-0.022	1.4053	-0.4261
100	-0.143	1.3914	-0.4357
105	-0.261	1.3625	-0.4437
110	-0.374	1.3188	-0.4498
115	-0.48	1.2608	-0.4538
120	-0.575	1.1891	-0.4553
125	-0.659	1.1046	-0.454
130	-0.727	1.0086	-0.4492
135	-0.778	0.9025	-0.4405
140	-0.809	0.7883	-0.427
145	-0.818	0.6684	-0.4078
150	-0.8	0.5457	-0.3821
155	-0.754	0.4236	-0.3484
160	-0.677	0.3066	-0.3054
170	-0.417	0.1085	-0.1842
175	-0.229	0.051	-0.1013
180	0	0.0407	0

EOT

Table E.5: DU 97-W-300 (DU30) 360 Polar

1	Number of airfoil tables in this file
1	Reynolds numbers in millions
0	Control setting
9	Stall angle (deg)
-2.322	Zero Cn angle of attack (deg)
7.3326	Cn slope for zero lift (dimensionless)
1.449	Cn extrapolated to value at positive stall angle of attack
-0.6138	Cn at stall value for negative angle of attack
0	Angle of attack for minimum CD (deg)
0.0087	Minimum CD value

α	CL	CD	CM
-180	0	0.0267	0
-175	0.274	0.037	0.1379
-170	0.547	0.0968	0.2778
-160	0.685	0.2876	0.274
-155	0.766	0.4025	0.3118
-150	0.816	0.5232	0.3411
-145	0.836	0.6454	0.3631
-140	0.832	0.7656	0.3791
-135	0.804	0.8807	0.3899
-130	0.756	0.9882	0.3965
-125	0.69	1.0861	0.3994
-120	0.609	1.173	0.3992
-115	0.515	1.2474	0.3964
-110	0.411	1.3084	0.3915
-105	0.3	1.3552	0.3846
-100	0.182	1.3875	0.3761
-95	0.061	1.4048	0.3663
-90	-0.061	1.407	0.3551
-85	-0.183	1.3941	0.3428
-80	-0.302	1.3664	0.3295
-75	-0.416	1.324	0.3153
-70	-0.523	1.2676	0.3001
-65	-0.622	1.1978	0.2841
-60	-0.708	1.1156	0.2672
-55	-0.781	1.022	0.2494
-50	-0.838	0.9187	0.2308
-45	-0.877	0.8074	0.2113
-40	-0.895	0.6904	0.1909
-35	-0.889	0.5703	0.1696
-30	-0.858	0.4503	0.1475
-25	-0.832	0.3357	0.1224

Table E.5: DU 97-W-300 (DU30) 360 Polar, continued.

α	CL	CD	CM
-24	-0.852	0.3147	0.1156
-23	-0.882	0.2946	0.1081
-22	-0.919	0.2752	0.1
-21	-0.963	0.2566	0.0914
-20	-1.013	0.2388	0.0823
-19	-1.067	0.2218	0.0728
-18	-1.125	0.2056	0.0631
-17	-1.185	0.1901	0.0531
-16	-1.245	0.1754	0.043
-15.25	-1.29	0.1649	0.0353
-14.24	-1.229	0.1461	0.024
-13.24	-1.148	0.1263	0.01
-12.22	-1.052	0.1051	-0.009
-11.22	-0.965	0.0886	-0.023
-10.19	-0.867	0.074	-0.0336
-9.7	-0.822	0.0684	-0.0375
-9.18	-0.769	0.0605	-0.044
-8.18	-0.756	0.027	-0.0578
-7.19	-0.69	0.018	-0.059
-6.65	-0.616	0.0166	-0.0633
-6.13	-0.542	0.0152	-0.0674
-6	-0.525	0.0117	-0.0732
-5.5	-0.451	0.0105	-0.0766
-5	-0.382	0.0097	-0.0797
-4.5	-0.314	0.0092	-0.0825
-4	-0.251	0.0091	-0.0853
-3.5	-0.189	0.0089	-0.0884
-3	-0.12	0.0089	-0.0914
-2.5	-0.051	0.0088	-0.0942
-2	0.017	0.0088	-0.0969
-1.5	0.085	0.0088	-0.0994
-1	0.152	0.0088	-0.1018
-0.5	0.219	0.0088	-0.1041
0	0.288	0.0087	-0.1062
0.5	0.354	0.0087	-0.1086
1	0.421	0.0088	-0.1107
1.5	0.487	0.0089	-0.1129
2	0.554	0.009	-0.1149
2.5	0.619	0.0091	-0.1168
3	0.685	0.0092	-0.1185
3.5	0.749	0.0093	-0.1201
4	0.815	0.0095	-0.1218

Table E.5: DU 97-W-300 (DU30) 360 Polar, continued.

α	CL	CD	CM
4.5	0.879	0.0096	-0.1233
5	0.944	0.0097	-0.1248
5.5	1.008	0.0099	-0.126
6	1.072	0.0101	-0.127
6.5	1.135	0.0103	-0.128
7	1.197	0.0107	-0.1287
7.5	1.256	0.0112	-0.1289
8	1.305	0.0125	-0.127
9	1.39	0.0155	-0.1207
9.5	1.424	0.0171	-0.1158
10	1.458	0.0192	-0.1116
10.5	1.488	0.0219	-0.1073
11	1.512	0.0255	-0.1029
11.5	1.533	0.0307	-0.0983
12	1.549	0.037	-0.0949
12.5	1.558	0.0452	-0.0921
13	1.47	0.063	-0.0899
13.5	1.398	0.0784	-0.0885
14	1.354	0.0931	-0.0885
14.5	1.336	0.1081	-0.0902
15	1.333	0.1239	-0.0928
15.5	1.326	0.1415	-0.0963
16	1.329	0.1592	-0.1006
16.5	1.326	0.1743	-0.1042
17	1.321	0.1903	-0.1084
17.5	1.331	0.2044	-0.1125
18	1.333	0.2186	-0.1169
18.5	1.34	0.2324	-0.1215
19	1.362	0.2455	-0.1263
19.5	1.382	0.2584	-0.1313
20	1.398	0.2689	-0.1352
20.5	1.426	0.2814	-0.1406
21	1.437	0.2943	-0.1462
22	1.418	0.3246	-0.1516
23	1.397	0.3557	-0.157
24	1.376	0.3875	-0.1623
25	1.354	0.4198	-0.1676
26	1.332	0.4524	-0.1728
28	1.293	0.5183	-0.1832
30	1.265	0.5843	-0.1935
32	1.253	0.6492	-0.2039
35	1.264	0.7438	-0.2193

Table E.5: DU 97-W-300 (DU30) 360 Polar, continued.

α	CL	CD	CM
40	1.258	0.897	-0.244
45	1.217	1.0402	-0.2672
50	1.146	1.1686	-0.2891
55	1.049	1.2779	-0.3097
60	0.932	1.3647	-0.329
65	0.799	1.4267	-0.3471
70	0.657	1.4621	-0.3641
75	0.509	1.4708	-0.3799
80	0.362	1.4544	-0.3946
85	0.221	1.4196	-0.4081
90	0.092	1.3938	-0.4204
95	-0.03	1.3943	-0.4313
100	-0.15	1.3798	-0.4408
105	-0.267	1.3504	-0.4486
110	-0.379	1.3063	-0.4546
115	-0.483	1.2481	-0.4584
120	-0.578	1.1763	-0.4597
125	-0.66	1.0919	-0.4582
130	-0.727	0.9962	-0.4532
135	-0.777	0.8906	-0.4441
140	-0.807	0.7771	-0.4303
145	-0.815	0.6581	-0.4109
150	-0.797	0.5364	-0.3848
155	-0.75	0.4157	-0.3508
160	-0.673	0.3	-0.3074
170	-0.547	0.1051	-0.2786
175	-0.274	0.0388	-0.138
180	0	0.0267	0
EOT			

Table E.6: DU 91-W2-250 360 Polar

1	Number of airfoil tables in this file
1	Reynolds numbers in millions
0	Control setting
8.5	Stall angle (deg)
-4.2422	Zero Cn angle of attack (deg)
6.4462	Cn slope for zero lift (dimensionless)
1.4336	Cn extrapolated to value at positive stall angle of attack
-0.6873	Cn at stall value for negative angle of attack
0	Angle of attack for minimum CD (deg)
0.0065	Minimum CD value

α	CL	CD	CM
-180	0	0.0202	0
-175	0.368	0.0324	0.1845
-170	0.735	0.0943	0.3701
-160	0.695	0.2848	0.2679
-155	0.777	0.4001	0.3046
-150	0.828	0.5215	0.3329
-145	0.85	0.6447	0.354
-140	0.846	0.766	0.3693
-135	0.818	0.8823	0.3794
-130	0.771	0.9911	0.3854
-125	0.705	1.0905	0.3878
-120	0.624	1.1787	0.3872
-115	0.53	1.2545	0.3841
-110	0.426	1.3168	0.3788
-105	0.314	1.365	0.3716
-100	0.195	1.3984	0.3629
-95	0.073	1.4169	0.3529
-90	-0.05	1.4201	0.3416
-85	-0.173	1.4081	0.3292
-80	-0.294	1.3811	0.3159
-75	-0.409	1.3394	0.3017
-70	-0.518	1.2833	0.2866
-65	-0.617	1.2138	0.2707
-60	-0.706	1.1315	0.2539
-55	-0.78	1.0378	0.2364
-50	-0.839	0.9341	0.2181
-45	-0.879	0.8221	0.1991
-40	-0.898	0.7042	0.1792
-35	-0.893	0.5829	0.1587
-30	-0.862	0.4616	0.1374
-25	-0.803	0.3441	0.1154

Table E.6: DU 91-W2-250 (DU25) 360 Polar, continued.

α	CL	CD	CM
-24	-0.792	0.3209	0.1101
-23	-0.789	0.2972	0.1031
-22	-0.792	0.273	0.0947
-21	-0.801	0.2485	0.0849
-20	-0.815	0.2237	0.0739
-19	-0.833	0.199	0.0618
-18	-0.854	0.1743	0.0488
-17	-0.879	0.1498	0.0351
-16	-0.905	0.1256	0.0208
-15	-0.932	0.102	0.006
-14	-0.959	0.0789	-0.0091
-13	-0.985	0.0567	-0.0243
-13	-0.985	0.0567	-0.0243
-12.01	-0.953	0.0271	-0.0349
-11	-0.9	0.0303	-0.0361
-9.98	-0.827	0.0287	-0.0464
-8.98	-0.753	0.0271	-0.0534
-8.47	-0.691	0.0264	-0.065
-7.45	-0.555	0.0114	-0.0782
-6.42	-0.413	0.0094	-0.0904
-5.4	-0.271	0.0086	-0.1006
-5	-0.22	0.0073	-0.1107
-4.5	-0.152	0.0071	-0.1135
-4	-0.084	0.007	-0.1162
-3.5	-0.018	0.0069	-0.1186
-3	0.049	0.0068	-0.1209
-2.5	0.115	0.0068	-0.1231
-2	0.181	0.0068	-0.1252
-1.5	0.247	0.0067	-0.1272
-1	0.312	0.0067	-0.1293
-0.5	0.377	0.0067	-0.1311
0	0.444	0.0065	-0.133
0.5	0.508	0.0065	-0.1347
1	0.573	0.0066	-0.1364
1.5	0.636	0.0067	-0.138
2	0.701	0.0068	-0.1396
2.5	0.765	0.0069	-0.1411
3	0.827	0.007	-0.1424
3.5	0.89	0.0071	-0.1437
4	0.952	0.0073	-0.1448
4.5	1.013	0.0076	-0.1456
5	1.062	0.0079	-0.1445

Table E.6: DU 91-W2-250 (DU25) 360 Polar, continued.

α	CL	CD	CM
6	1.161	0.0099	-0.1419
6.5	1.208	0.0117	-0.1403
7	1.254	0.0132	-0.1382
7.5	1.301	0.0143	-0.1362
8	1.336	0.0153	-0.132
8.5	1.369	0.0165	-0.1276
9	1.4	0.0181	-0.1234
9.5	1.428	0.0211	-0.1193
10	1.442	0.0262	-0.1152
10.5	1.427	0.0336	-0.1115
11	1.374	0.042	-0.1081
11.5	1.316	0.0515	-0.1052
12	1.277	0.0601	-0.1026
12.5	1.25	0.0693	-0.1
13	1.246	0.0785	-0.098
13.5	1.247	0.0888	-0.0969
14	1.256	0.1	-0.0968
14.5	1.26	0.1108	-0.0973
15	1.271	0.1219	-0.0981
15.5	1.281	0.1325	-0.0992
16	1.289	0.1433	-0.1006
16.5	1.294	0.1541	-0.1023
17	1.304	0.1649	-0.1042
17.5	1.309	0.1754	-0.1064
18	1.315	0.1845	-0.1082
18.5	1.32	0.1953	-0.111
19	1.33	0.2061	-0.1143
19.5	1.343	0.217	-0.1179
20	1.354	0.228	-0.1219
20.5	1.359	0.239	-0.1261
21	1.36	0.2536	-0.1303
22	1.325	0.2814	-0.1375
23	1.288	0.3098	-0.1446
24	1.251	0.3386	-0.1515
25	1.215	0.3678	-0.1584
26	1.181	0.3972	-0.1651
28	1.12	0.4563	-0.1781
30	1.076	0.5149	-0.1904
32	1.056	0.572	-0.2017
35	1.066	0.6548	-0.2173
40	1.064	0.7901	-0.2418
45	1.035	0.919	-0.265

Table E.6: DU 91-W2-250 (DU25) 360 Polar, continued.

α	CL	CD	CM
50	0.98	1.0378	-0.2867
55	0.904	1.1434	-0.3072
60	0.81	1.2333	-0.3265
65	0.702	1.3055	-0.3446
70	0.582	1.3587	-0.3616
75	0.456	1.3922	-0.3775
80	0.326	1.4063	-0.3921
85	0.197	1.4042	-0.4057
90	0.072	1.3985	-0.418
95	-0.05	1.3973	-0.4289
100	-0.17	1.381	-0.4385
105	-0.287	1.3498	-0.4464
110	-0.399	1.3041	-0.4524
115	-0.502	1.2442	-0.4563
120	-0.596	1.1709	-0.4577
125	-0.677	1.0852	-0.4563
130	-0.743	0.9883	-0.4514
135	-0.792	0.8818	-0.4425
140	-0.821	0.7676	-0.4288
145	-0.826	0.6481	-0.4095
150	-0.806	0.5264	-0.3836
155	-0.758	0.406	-0.3497
160	-0.679	0.2912	-0.3065
170	-0.735	0.0995	-0.3706
175	-0.368	0.0356	-0.1846
180	0	0.0202	0

EOT

Table E.7: DU 93-W-210 (DU21) 360 Polar

1	Number of airfoil tables in this file
1	Reynolds numbers in millions
0	Control setting
8	Stall angle (deg)
-5.0609	Zero lift angle of attack (deg)
6.2047	Cn slope for zero lift (dimensionless)
1.4144	Cn at stall value for positive angle of attack
-0.5324	Cn at stall value for negative angle of attack
-1.5	Angle of attack for minimum CD (deg)
0.005	7 Minimum CD value

α	CL	CD	CM
-180	0	0.0185	0
-175	0.394	0.0332	0.1978
-160	0.67	0.2809	0.2738
-155	0.749	0.3932	0.3118
-150	0.797	0.5112	0.3413
-145	0.818	0.6309	0.3636
-140	0.813	0.7485	0.3799
-135	0.786	0.8612	0.3911
-130	0.739	0.9665	0.398
-125	0.675	1.0625	0.4012
-120	0.596	1.1476	0.4014
-115	0.505	1.2206	0.399
-110	0.403	1.2805	0.3943
-105	0.294	1.3265	0.3878
-100	0.179	1.3582	0.3796
-95	0.06	1.3752	0.37
-90	-0.06	1.3774	0.3591
-85	-0.179	1.3648	0.3471
-80	-0.295	1.3376	0.334
-75	-0.407	1.2962	0.3199
-70	-0.512	1.2409	0.3049
-65	-0.608	1.1725	0.289
-60	-0.693	1.0919	0.2722
-55	-0.764	1.0002	0.2545
-50	-0.82	0.899	0.2359
-45	-0.857	0.79	0.2163
-40	-0.875	0.6754	0.1958
-35	-0.869	0.5579	0.1744
-30	-0.838	0.4405	0.152
-25	-0.791	0.3256	0.1262
-24	-0.794	0.3013	0.117

Table E.7: DU 93-W-210 (DU21) 360 Polar, continued.

α	CL	CD	CM
-23	-0.805	0.2762	0.1059
-22	-0.821	0.2506	0.0931
-21	-0.843	0.2246	0.0788
-20	-0.869	0.1983	0.0631
-19	-0.899	0.172	0.0464
-18	-0.931	0.1457	0.0286
-17	-0.964	0.1197	0.0102
-16	-0.999	0.094	-0.0088
-15	-1.033	0.0689	-0.0281
-14.5	-1.05	0.0567	-0.0378
-12.01	-0.953	0.0271	-0.0349
-11	-0.9	0.0303	-0.0361
-9.98	-0.827	0.0287	-0.0464
-8.12	-0.536	0.0124	-0.0821
-7.62	-0.467	0.0109	-0.0924
-7.11	-0.393	0.0092	-0.1015
-6.6	-0.323	0.0083	-0.1073
-6.5	-0.311	0.0089	-0.1083
-6	-0.245	0.0082	-0.1112
-5.5	-0.178	0.0074	-0.1146
-5	-0.113	0.0069	-0.1172
-4.5	-0.048	0.0065	-0.1194
-4	0.016	0.0063	-0.1213
-3.5	0.08	0.0061	-0.1232
-3	0.145	0.0058	-0.1252
-2.5	0.208	0.0057	-0.1268
-2	0.27	0.0057	-0.1282
-1.5	0.333	0.0057	-0.1297
-1	0.396	0.0057	-0.131
-0.5	0.458	0.0057	-0.1324
0	0.521	0.0057	-0.1337
0.5	0.583	0.0057	-0.135
1	0.645	0.0058	-0.1363
1.5	0.706	0.0058	-0.1374
2	0.768	0.0059	-0.1385
2.5	0.828	0.0061	-0.1395
3	0.888	0.0063	-0.1403
3.5	0.948	0.0066	-0.1406
4	0.996	0.0071	-0.1398
4.5	1.046	0.0079	-0.139
5	1.095	0.009	-0.1378
5.5	1.145	0.0103	-0.1369

Table E.7: DU 93-W-210 (DU21) 360 Polar, continued.

α	CL	CD	CM
6	1.192	0.0113	-0.1353
6.5	1.239	0.0122	-0.1338
7	1.283	0.0131	-0.1317
7.5	1.324	0.0139	-0.1291
8	1.358	0.0147	-0.1249
8.5	1.385	0.0158	-0.1213
9	1.403	0.0181	-0.1177
9.5	1.401	0.0211	-0.1142
10	1.358	0.0255	-0.1103
10.5	1.313	0.0301	-0.1066
11	1.287	0.0347	-0.1032
11.5	1.274	0.0401	-0.1002
12	1.272	0.0468	-0.0971
12.5	1.273	0.0545	-0.094
13	1.273	0.0633	-0.0909
13.5	1.273	0.0722	-0.0883
14	1.272	0.0806	-0.0865
14.5	1.273	0.09	-0.0854
15	1.275	0.0987	-0.0849
15.5	1.281	0.1075	-0.0847
16	1.284	0.117	-0.085
16.5	1.296	0.127	-0.0858
17	1.306	0.1368	-0.0869
17.5	1.308	0.1464	-0.0883
18	1.308	0.1562	-0.0901
18.5	1.308	0.1664	-0.0922
19	1.308	0.177	-0.0949
19.5	1.307	0.1878	-0.098
20	1.311	0.1987	-0.1017
20.5	1.325	0.21	-0.1059
21	1.324	0.2214	-0.1105
22	1.277	0.2499	-0.1172
23	1.229	0.2786	-0.1239
24	1.182	0.3077	-0.1305
25	1.136	0.3371	-0.137
26	1.093	0.3664	-0.1433
28	1.017	0.4246	-0.1556
30	0.962	0.4813	-0.1671
32	0.937	0.5356	-0.1778
35	0.947	0.6127	-0.1923
40	0.95	0.7396	-0.2154
45	0.928	0.8623	-0.2374

Table E.7: DU 93-W-210 (DU21) 360 Polar, continued.

α	CL	CD	CM
50	0.884	0.9781	-0.2583
55	0.821	1.0846	-0.2782
60	0.74	1.1796	-0.2971
65	0.646	1.2617	-0.3149
70	0.54	1.3297	-0.3318
75	0.425	1.3827	-0.3476
80	0.304	1.4202	-0.3625
85	0.179	1.4423	-0.3763
90	0.053	1.4512	-0.389
95	-0.073	1.448	-0.4004
100	-0.198	1.4294	-0.4105
105	-0.319	1.3954	-0.4191
110	-0.434	1.3464	-0.426
115	-0.541	1.2829	-0.4308
120	-0.637	1.2057	-0.4333
125	-0.72	1.1157	-0.433
130	-0.787	1.0144	-0.4294
135	-0.836	0.9033	-0.4219
140	-0.864	0.7845	-0.4098
145	-0.869	0.6605	-0.3922
150	-0.847	0.5346	-0.3682
155	-0.795	0.4103	-0.3364
160	-0.711	0.2922	-0.2954
175	-0.394	0.0334	-0.1978
180	0	0.0185	0

EOT

Table E.8: NACA 64-618 (NACA64) 360 Polar

1	Number of airfoil tables in this file
1	Reynolds numbers in millions
0	Control setting
9	Stall angle (deg)
4.432	Zero Cn angle of attack (deg)
6.0031	Cn slope for zero lift (dimensionless)
1.4073	Cn extrapolated to value at positive stall angle of attack
-0.7945	Cn at stall value for negative angle of attack
-1	Angle of attack for minimum CD (deg)
0.0052	Minimum CD value

α	CL	CD	CM
-180	0	0.0198	0
-175	0.374	0.0341	0.188
-170	0.749	0.0955	0.377
-160	0.659	0.2807	0.2747
-155	0.736	0.3919	0.313
-150	0.783	0.5086	0.3428
-145	0.803	0.6267	0.3654
-140	0.798	0.7427	0.382
-135	0.771	0.8537	0.3935
-130	0.724	0.9574	0.4007
-125	0.66	1.0519	0.4042
-120	0.581	1.1355	0.4047
-115	0.491	1.207	0.4025
-110	0.39	1.2656	0.3981
-105	0.282	1.3104	0.3918
-100	0.169	1.341	0.3838
-95	0.052	1.3572	0.3743
-90	-0.067	1.3587	0.3636
-85	-0.184	1.3456	0.3517
-80	-0.299	1.3181	0.3388
-75	-0.409	1.2765	0.3248
-70	-0.512	1.2212	0.3099
-65	-0.606	1.1532	0.294
-60	-0.689	1.0731	0.2772
-55	-0.759	0.9822	0.2595
-50	-0.814	0.882	0.2409
-45	-0.85	0.7742	0.2212
-40	-0.866	0.661	0.2006
-35	-0.86	0.5451	0.1789
-30	-0.829	0.4295	0.1563
-25	-0.853	0.3071	0.1156

Table E.8: NACA 64-618 (NACA64) 360 Polar, continued.

α	CL	CD	CM
-24	-0.87	0.2814	0.104
-23	-0.89	0.2556	0.0916
-22	-0.911	0.2297	0.0785
-21	-0.934	0.204	0.0649
-20	-0.958	0.1785	0.0508
-19	-0.982	0.1534	0.0364
-18	-1.005	0.1288	0.0218
-17	-1.082	0.1037	0.0129
-16	-1.113	0.0786	-0.0028
-15	-1.105	0.0535	-0.0251
-14	-1.078	0.0283	-0.0419
-13.5	-1.053	0.0158	-0.0521
-13	-1.015	0.0151	-0.061
-12	-0.904	0.0134	-0.0707
-11	-0.807	0.0121	-0.0722
-10	-0.711	0.0111	-0.0734
-9	-0.595	0.0099	-0.0772
-8	-0.478	0.0091	-0.0807
-7	-0.375	0.0086	-0.0825
-6	-0.264	0.0082	-0.0832
-5	-0.151	0.0079	-0.0841
-4	-0.017	0.0072	-0.0869
-3	0.088	0.0064	-0.0912
-2	0.213	0.0054	-0.0946
-1	0.328	0.0052	-0.0971
0	0.442	0.0052	-0.1014
1	0.556	0.0052	-0.1076
2	0.67	0.0053	-0.1126
3	0.784	0.0053	-0.1157
4	0.898	0.0054	-0.1199
5	1.011	0.0058	-0.124
6	1.103	0.0091	-0.1234
7	1.181	0.0113	-0.1184
8	1.257	0.0124	-0.1163
8.5	1.293	0.013	-0.1163
9	1.326	0.0136	-0.116
9.5	1.356	0.0143	-0.1154
10	1.382	0.015	-0.1149
10.5	1.4	0.0267	-0.1145
11	1.415	0.0383	-0.1143
11.5	1.425	0.0498	-0.1147
12	1.434	0.0613	-0.1158

Table E.8: NACA 64-618 (NACA64) 360 Polar, continued.

α	CL	CD	CM
12.5	1.443	0.0727	-0.1165
13	1.451	0.0841	-0.1153
13.5	1.453	0.0954	-0.1131
14	1.448	0.1065	-0.1112
14.5	1.444	0.1176	-0.1101
15	1.445	0.1287	-0.1103
15.5	1.447	0.1398	-0.1109
16	1.448	0.1509	-0.1114
16.5	1.444	0.1619	-0.1111
17	1.438	0.1728	-0.1097
17.5	1.439	0.1837	-0.1079
18	1.448	0.1947	-0.108
18.5	1.452	0.2057	-0.109
19	1.448	0.2165	-0.1086
19.5	1.438	0.2272	-0.1077
20	1.428	0.2379	-0.1099
21	1.401	0.259	-0.1169
22	1.359	0.2799	-0.119
23	1.3	0.3004	-0.1235
24	1.22	0.3204	-0.1393
25	1.168	0.3377	-0.144
26	1.116	0.3554	-0.1486
28	1.015	0.3916	-0.1577
30	0.926	0.4294	-0.1668
32	0.855	0.469	-0.1759
35	0.8	0.5324	-0.1897
40	0.804	0.6452	-0.2126
45	0.793	0.7573	-0.2344
50	0.763	0.8664	-0.2553
55	0.717	0.9708	-0.2751
60	0.656	1.0693	-0.2939
65	0.582	1.1606	-0.3117
70	0.495	1.2438	-0.3285
75	0.398	1.3178	-0.3444
80	0.291	1.3809	-0.3593
85	0.176	1.4304	-0.3731
90	0.053	1.4565	-0.3858
95	-0.074	1.4533	-0.3973
100	-0.199	1.4345	-0.4075
105	-0.321	1.4004	-0.4162
110	-0.436	1.3512	-0.4231
115	-0.543	1.2874	-0.428

Table E.8: NACA 64-618 (NACA64) 360 Polar, continued.

α	CL	CD	CM
120	-0.64	1.2099	-0.4306
125	-0.723	1.1196	-0.4304
130	-0.79	1.0179	-0.427
135	-0.84	0.9064	-0.4196
140	-0.868	0.7871	-0.4077
145	-0.872	0.6627	-0.3903
150	-0.85	0.5363	-0.3665
155	-0.798	0.4116	-0.3349
160	-0.714	0.2931	-0.2942
170	-0.749	0.0971	-0.3771
175	-0.374	0.0334	-0.1879
180	0	0.0198	0

EOT

Appendix F. Supplemental Loads Data

Table F.1: BEMT Input Parameters

	Units	Inner Blade	Outer Blade
TSR	[-]	0.9	1.6
Rotor Speed	[rpm]	107.7	191.4
Flow Speed	[m/s]	3.5	3.5
Fluid density	[kg/m^3]	1,000	1,000
Dynamic Viscosity	[N-s/m^2]	0.0012	0.0012
Vapor Pressure	[Pa]	1,823	1,823
Atmospheric Pressure	[Pa]	101,325	101,325
Gravity	[m/s^2]	9.8	9.8
Minimum Tip Depth	[m]	0.0762	0.0762
Tangential induction factor initial	[-]	1.4	0.5
Axial Induction Factor initial	[-]	0.2	0.2
Convergence Criteria	[%]	0.05	0.05

Table F.2: Inner Blade BEMT Data

Element Centroid	r [m]	0.058	0.063	0.071	0.081	0.091	0.102	0.112	0.122	0.133	0.143	0.149
	x [m]	0.04	0.03	0.02	0.02	0.01	0.01	0.00	0.00	0.00	-0.01	-0.01
Element Quarter-Chord	y [m]	-0.02	-0.02	-0.01	-0.01	-0.01	0.00	0.00	0.01	0.01	0.02	0.02
	z [m]	0.05	0.06	0.07	0.08	0.09	0.10	0.11	0.12	0.13	0.14	0.15
Element Width	dr [m]	0.0052	0.0052	0.0103	0.0103	0.0103	0.0103	0.0103	0.0103	0.0103	0.0103	0.0017
Normal Force	F_n [N]	0.48	0.71	2.30	2.66	3.17	3.64	3.97	4.10	3.77	2.36	0.29
Tangential Force	F_t [N]	0.79	1.08	3.20	3.43	3.78	4.00	4.02	3.80	3.16	1.47	0.15
Hydrodynamic Moment	M_{hydro} [N-m]	-0.004	-0.012	-0.041	-0.038	-0.038	-0.038	-0.036	-0.032	-0.024	-0.025	-0.004
Relative Inflow velocity	u_{rel} [m/s]	3.34	3.33	3.44	3.37	3.39	3.40	3.42	3.44	3.45	3.31	3.31
Minimum Pressure Coefficient	C_p [-]	-2.62	-1.91	-2.37	-3.07	-3.62	-3.95	-4.13	-4.02	-3.26	-0.89	-0.58
Cavitation Number	σ_c [-]	18.08	18.20	17.10	17.81	17.58	17.38	17.16	16.96	16.89	18.26	18.28
Converged Angle of Attack	α [degrees]	3.86	3.72	4.23	5.45	6.47	7.20	7.84	8.19	8.10	4.90	3.66

Table F.3: Outer Blade BEMT Data

Element Centroid	r [m]	0.200	0.204	0.210	0.218	0.226	0.234	0.243	0.251	0.259	0.267	0.273	0.277
	x [m]	-0.01	0.00	0.00	0.00	0.00	0.00	0.01	0.01	0.01	0.02	0.02	0.02
Element Quarter-Chord	y [m]	0.02	0.02	0.01	0.01	0.00	0.00	-0.01	-0.01	-0.02	-0.03	-0.04	-0.05
	z [m]	0.20	0.20	0.21	0.22	0.23	0.23	0.24	0.25	0.26	0.27	0.27	0.27
Element Width	dr [m]	0.0041	0.0041	0.0082	0.0082	0.0082	0.0082	0.0082	0.0082	0.0082	0.0082	0.0041	0.0041
Normal Force	F_n [N]	2.19	2.54	6.09	6.78	7.30	7.58	7.58	7.26	6.41	4.78	1.73	0.82
Tangential Force	F_t [N]	0.70	0.87	2.21	2.50	2.68	2.74	2.70	2.54	2.27	1.76	0.67	0.30
Hydrodynamic Moment	M_{hydro} [N-m]	-0.026	-0.027	-0.058	-0.061	-0.063	-0.062	-0.058	-0.052	-0.040	-0.022	-0.005	-0.002
Relative Inflow velocity	u_{rel} [m/s]	5.00	5.07	5.24	5.39	5.54	5.69	5.83	5.98	6.14	6.31	6.41	6.46
Minimum Pressure Coefficient	C_p [-]	-0.81	-0.88	-0.96	-1.03	-1.08	-1.11	-1.11	-1.10	-1.06	-1.23	-1.81	-1.30
Cavitation Number	σ_c [-]	8.09	7.86	7.36	6.94	6.56	6.23	5.92	5.63	5.34	5.04	4.89	4.81
Converged Angle of Attack	α [degrees]	2.47	3.17	3.93	4.33	4.48	4.57	4.65	4.45	4.37	4.25	4.39	3.15

Table F.4: Emergency Stop Parameters

		Inner Blade	Outer Blade
Blade Area	[m^2]	0.00542	0.00432
Blade Span	[m]	0.103	0.082
Aspect Ratio *A*R	[-]	1.97	1.55
C_{Dmax}	[-]	1.15	1.14
Flow Speed	[m/s]	3.50	3.50
Fluid Density	[kg/m^3]	1000	1000
Total Drag Force	[N]	38.02	30.13

References

[1] Verdant, “Verdant Power” [Online]. Available: http://www.verdantpower.com/.

[2] Corp., N. E., “New Energy Corporation” [Online]. Available: http://www.newenergycorp.ca/.

[3] Atlantis, “Atlantis Resources Ltd.” [Online]. Available: https://www.atlantisresourcesltd.com/.

[4] ORPC, 2017, “Ocean Renewable Power Company” [Online]. Available: http://www.orpc.co.

[5] Vermaak, H. J., Kusakana, K., and Koko, S. P., 2014, “Status of Micro-Hydrokinetic River Technology in Rural Applications: A Review of Literature,” Renew. Sustain. Energy Rev., **29**, pp. 625–633.

[6] Cape Sharp Tidal, “OpenHydro.”

[7] Oceana, “Oceana Energy Company” [Online]. Available: https://www.oceanaenergy.com/.

[8] Asian Phoenix Resources Ltd., “PowerPal” [Online]. Available: http://www.powerpal.com/index.html.

[9] SHP, “Smart Hydro Power” [Online]. Available: http://www.smart-hydro.de/.

[10] Khan, M. J., Bhuyan, G., Iqbal, M. T., and Quaicoe, J. E., 2009, “Hydrokinetic Energy Conversion Systems and Assessment of Horizontal and Vertical Axis Turbines for River and Tidal Applications: A Technology Status Review,” Appl. Energy, **86**(10), pp. 1823–1835.

[11] IEA, 2016, “World Energy Outlook 2016,” p. 684.

[12] Pasternak, A., 2000, “Global Energy Futures and Human Development: A Framework for Analysis,” US Dep. Energy Rep. UCRL-ID, (October).

[13] Sheffield, J., 1998, "World Population Growth and the Role of Annual Energy Use per Capita," Technol. Forecast. Soc. Change, **59**(1), pp. 55–87.

[14] IPCC, 2014, *Climate Change 2014: Mitigation of Climate Change*.

[15] Stocker, and T.F., D. Qin, G.-K. Plattner, M. Tignor, S.K. Allen, J. Boschung, A. Nauels, Y. Xia, V. B. and P. M. M. (eds. ., 2015, "Summary for Policymakers. In: Climate Change 2013: The Physical Science Basis. Contribution of Working Group I to the Fifth Assessment Report of the Intergovernmental Panel on Climate Change," CEUR Workshop Proc., **1542**, pp. 33–36.

[16] Ravens, T., Cunningham, K., and Scott, G., 2012, "Assessment and Mapping of the Riverine Hydrokinetic Resource in the Continental United States," p. 80.

[17] Haas, K. A., Fritz, H. M., French, S. P., and Neary, V. S., 2013, "Assessment of Energy Production Potential from Ocean Currents along the United States Coastline."

[18] Hass, K. A., Fritz, H. M., French, S. P., Smith, B. T., and Neary, V. S., 2011, "Assessment of Energy Production Potential from Tidal Streams in the United States Final Project Report Award Number : DE-FG36-08GO18174," pp. 1–109.

[19] Independent Statistics & Analysis (EIA), 2017, "Electric Power Monthly: With Data for August 2017," U.S. Energy Inf. Adm., (October), p. 237.

[20] Kelly, A. C., and Merritt, J. A., 2014, "Hybrid Systems: A Review of Current and Future Feasibility," Electr. J., **27**(9), pp. 97–104.

[21] Yuce, M. I., and Muratoglu, A., 2015, "Hydrokinetic Energy Conversion Systems: A Technology Status Review," Renew. Sustain. Energy Rev., **43**, pp. 72–82.

[22] Gaden, D. L. F., and Bibeau, E. L., 2010, "A Numerical Investigation into the Effect of Diffusers on the Performance of Hydro Kinetic Turbines Using a Validated Momentum Source Turbine Model," Renew. Energy, **35**(6), pp. 1152–1158.

[23] Jamieson, P., 2008, "Generalized Limits for Energy Extraction in a Linear Constant Velocity Flow Field," Wind Energy, **11**(5), pp. 445–457.

[24] Huang, B., Zhu, G. J., and Kanemoto, T., 2016, "Design and Performance Enhancement of

a Bi-Directional Counter-Rotating Type Horizontal Axis Tidal Turbine," Ocean Eng., **128**(October), pp. 116–123.

[25] OpenHydro Group Ltd., "OpenHydro."

[26] Williams, Herbert L, ., 2003, "HYDROELECTRIC TURBINE FOR PRODUCING ELECTRICITY FROM A WATER CURRENT."

[27] Belloni, C., 2013, "Hydrodynamics of Ducted and Open-Centre Tidal Turbines," p. 230.

[28] Power III, D. E., and Hansen, N. R., 2017, "HYDROELECTRICTURBINES, ANCHORING STRUCTURES, AND RELATED METHODS OFASSEMBLY."

[29] Power III, D. E., Hansen, N. R., Bachtar, D., and Schilke, A., 2008, "SYSTEM FOR GENERATING ELECTRICITY FROM FLUID CURRENTS."

[30] Power III, D. E., and Hansen, N. R., 2011, "SYSTEMS AND METHODS FOR SUPPORTING UNDERWATER ENERGY CONVERSION DEVICES."

[31] Davey, K., Hansen, N. R., and Power III, D. E., 2012, "ENERGY CONVERSION SYSTEMS AND METHODS."

[32] Davey, K., 2014, "MAGNETIC BEARINGS AND RELATED SYSTEMIS AND METHODS."

[33] Paish, O., 2002, "Small Hydro Power: Technology and Current Status," Renew. Sustain. Energy Rev., **6**(6), pp. 537–556.

[34] Khan, M. J., Iqbal, M. T., and Quaicoe, J. E., 2008, "River Current Energy Conversion Systems: Progress, Prospects and Challenges," Renew. Sustain. Energy Rev., **12**(8), pp. 2177–2193.

[35] U.S. Energy Information Administration, 2018, *2015 Residential Energy Consumption Survey: Energy Consumption and Expenditure Tables*.

[36] Ashok, S., 2007, "Optimised Model for Community-Based Hybrid Energy System," Renew. Energy, **32**(7), pp. 1155–1164.

[37] Bekele, G., and Tadesse, G., 2012, "Feasibility Study of Small Hydro/PV/Wind Hybrid System for off-Grid Rural Electrification in Ethiopia," Appl. Energy, **97**, pp. 5–15.

[38] Lal, D. K., Dash, B. B., and Akella, a K., 2011, "Optimization of PV / Wind / Micro-Hydro / Diesel Hybrid Power System in HOMER for the Study Area," Int. J. Electr. Eng. Informatics, **3**(3), pp. 307–325.

[39] Urban, B., Shmakova, V., Lim, B., and Roth, K., 2014, *Energy Consumption of Consumer Electronics in U.S. Homes in 2013*.

[40] O'Brien, G., Keefe, P. O., Rose, J., and Wisner, B., 2006, "Climate Change and Disaster Management," Disasters, **30**(1), pp. 64–80.

[41] Pinon, G., Mycek, P., Germain, G., and Rivoalen, E., 2012, "Numerical Simulation of the Wake of Marine Current Turbines with a Particle Method," Renew. Energy, **46**, pp. 111–126.

[42] Williams, A. A., and Simpson, R., 2009, "Pico Hydro - Reducing Technical Risks for Rural Electrification," Renew. Energy, **34**(8), pp. 1986–1991.

[43] Lahimer, A. A., Alghoul, M. A., Sopian, K., Amin, N., Asim, N., and Fadhel, M. I., 2012, "Research and Development Aspects of Pico-Hydro Power," Renew. Sustain. Energy Rev., **16**(8), pp. 5861–5878.

[44] Williamson, S. J., Stark, B. H., and Booker, J. D., 2014, "Low Head Pico Hydro Turbine Selection Using a Multi-Criteria Analysis," Renew. Energy, **61**, pp. 43–50.

[45] Maher, P., Smith, N. P. A., and Williams, A. A., 2003, "Assessment of Pico Hydro as an Option for off-Grid Electrification in Kenya," Renew. Energy, **28**(9), pp. 1357–1369.

[46] Haidar, A. M. A., Senan, M. F. M., Noman, A., and Radman, T., 2012, "Utilization of Pico Hydro Generation in Domestic and Commercial Loads," Renew. Sustain. Energy Rev., **16**(1), pp. 518–524.

[47] Seamap, "Ampair UW100" [Online]. Available: http://www.seamap.com/.

[48] Watt&Sea, "Watt&Sea" [Online]. Available: https://www.wattandsea.com/en/.

[49] Idenergie, “Idenergie” [Online]. Available: http://idenergie.ca/en/.

[50] Ibasei, “Cappa” [Online]. Available: http://earthmilk.jp/english/cappa/.

[51] Blue Freedom, “Portable Turbine” [Online]. Available: https://blue-freedom.net/.

[52] Seaformatics, “WaterLily” [Online]. Available: https://waterlilyturbine.com/.

[53] DuPont, *Design Guide-Module III*.

[54] Hansen, M. O. L., 2008, *Aerodynamics of Wind Turbines*, Earthscan, London.

[55] Bohannon, R. W., 1997, “Comfortable and Maximum Walking Speed of Adults Aged 20-79 Years: Reference Values and Determinants,” Age Ageing, **26**(1), pp. 15–19.

[56] Mann, R. A., Moran, G. T., and Dougherty, S. E., 1986, “Comparative Electromyography of the Lower Extremity in Jogging, Running, and Sprinting,” Am. J. Sports Med., **14**(6), pp. 501–510.

[57] Kusakana, K., and Vermaak, H. J., 2013, “Hydrokinetic Power Generation for Rural Electricity Supply: Case of South Africa,” Renew. Energy, **55**, pp. 467–473.

[58] Gunawan, B., Roberts, J., and Neary, V., 2015, “HYDRODYNAMIC EFFECTS OF HYDROKINETIC TURBINE DEPLOYMENT IN AN IRRIGATION CANAL,” *3rd Marine Energy Technology Symposium*, Washington D.C., pp. 1–6.

[59] Punys, P., Adamonyte, I., Kvaraciejus, A., Martinaitis, E., Vyciene, G., and Kasiulis, E., 2015, “Riverine Hydrokinetic Resource Assessment. A Case Study of a Lowland River in Lithuania,” Renew. Sustain. Energy Rev., **50**, pp. 643–652.

[60] Gunawan, B., Neary, V. S., and Colby, J., 2014, “Tidal Energy Site Resource Assessment in the East River Tidal Strait, near Roosevelt Island, New York, New York,” Renew. Energy, **71**, pp. 509–517.

[61] Blumberg, A. F., and Pritchard, D. W., 1997, “Estimates of the Transport through the East River , New York about,” J. Geophys. Res., **102**, pp. 5685–5703.

[62] Toniolo, H., Duvoy, P., Anlesberg, S. V., and Johnson, J., 2010, "Modelling and Field Measurements in Support of the Hydrokinetic Resource Assessment for the Tanana River at Nenana, Alaska," Proc. Inst. Mech. Eng. Part A J. Power Energy, **224**(8), pp. 1127–1139.

[63] U.S. Geological Survey, 2018, "National Water Information System Data Available on the World Wide Web (USGS Water Data for the Nation)."

[64] Duerr, A. E. S., and Dhanak, M. R., 2012, "An Assessment of the Hydrokinetic Energy Resource of the Florida Current," IEEE J. Ocean. Eng., **37**(2), pp. 281–293.

[65] Schmitz, W. J., and Richardson, W. S., 1968, "On the Transport of the Florida Current," Deep. Res. Oceanogr. Abstr., **15**(6), pp. 679–693.

[66] American Gear Manufactures Association, 2004, "ANSI/AGMA 2001-D04 Fundamental Rating Factors and Calculation Metrhods for Involute Spur and Helical Gear Teeth," **4**, p. 66.

[67] Shigley, J. E., Mischke, C. R., and Budynas, R. G., 2004, *Mechanical Engineering Design*.

[68] Radzevich, S. P., and Dudley, D. W., 2016, *Dudley's Handbook of Practical Gear Design and Manufacture*, CRC Press, Boca Raton.

[69] American Gear Manufactures Association, 1993, *ANSI/AGMA 2000-A88 Gear Classification and Inspection Handbook.*

[70] Childs, P. R. N., 2014, *Spur and Helical Gear Stressing*.

[71] ASM, 1996, *ASM Handbook -Fatigue and Fracture*.

[72] Institute, B. M., 2016, *Metallic Materials Properties Development and Standardization (MMPDS-11)*, Battelle Memorial Institute.

[73] Gale, W. F., and Totemeir, T. C., 2004, "Smithells Metals Reference Book," Smithells Met. Ref. B., pp. 1–2072.

[74] HKK Chain Corporation, "Product Catalog."

[75] Elements, F. M., 2004, “Flexible Machine Elements.”

[76] Young, W. C., and Budynas, R. G., 2002, *Roark’s Formulas for Stress and Strain*.

[77] Harnoy, A., 2002, *Bearing Design In Machinery Engineering Tribology and Lubrication*, Marcel Dekker, New York.

[78] White, F. M., 2011, *Fluid Mechanics*, New York.

[79] Huang, S. H., Liu, P., Mokasdar, A., and Hou, L., 2013, “Additive Manufacturing and Its Societal Impact: A Literature Review,” Int. J. Adv. Manuf. Technol., **67**(5–8), pp. 1191–1203.

[80] Thompson, M. K., Moroni, G., Vaneker, T., Fadel, G., Campbell, R. I., Gibson, I., Bernard, A., Schulz, J., Graf, P., Ahuja, B., and Martina, F., 2016, “Design for Additive Manufacturing: Trends, Opportunities, Considerations, and Constraints,” CIRP Ann. - Manuf. Technol., **65**(2), pp. 737–760.

[81] Tymrak, B. M., Kreiger, M., and Pearce, J. M., 2014, “Mechanical Properties of Components Fabricated with Open-Source 3-D Printers under Realistic Environmental Conditions,” Mater. Des., **58**, pp. 242–246.

[82] Li, L., Sun, Q., Bellehumeur, C., and Gu, P., 2002, “Composite Modeling and Analysis for Fabrication of FDM Prototypes with Locally Controlled Properties,” J. Manuf. Process., **4**(2), pp. 129–141.

[83] Afrose, M. F., Masood, S. H., Nikzad, M., and Iovenitti, P., 2014, “Effects of Build Orientations on Tensile Properties of PLA Material Processed by FDM,” Adv. Mater. Res., **1044**–**1045**, pp. 31–34.

[84] Lanzotti, A., Grasso, M., Staiano, G., and Martorelli, M., 2015, “The Impact of Process Parameters on Mechanical Properties of Parts Fabricated in PLA with an Open-Source 3-D Printer,” Rapid Prototyp. J., **21**(5), pp. 604–617.

[85] Melenka, G. W., Schofield, J. S., Dawson, M. R., and Carey, J. P., 2015, “Evaluation of Dimensional Accuracy and Material Properties of the Makerbot 3D Desktop Printer,” Rapid Prototyp. J., **21**(5).

[86] Forster, A. M., 2015, "Materials Testing Standards for Additive Manufacturing of Polymer Materials :," Nist.Ir.8059.

[87] Makerbot, "Makerbot" [Online]. Available: https://store.makerbot.com/filament/pla.

[88] Bassett, K., Carriveau, R., and Ting, D. S. K., 2015, "3D Printed Wind Turbines Part 1: Design Considerations and Rapid Manufacture Potential," Sustain. Energy Technol. Assessments, **11**, pp. 186–193.

[89] Farah, S., Anderson, D. G., and Langer, R., 2016, "Physical and Mechanical Properties of PLA, and Their Functions in Widespread Applications — A Comprehensive Review," Adv. Drug Deliv. Rev., **107**, pp. 367–392.

[90] Bergström, J. S., and Hayman, D., 2016, "An Overview of Mechanical Properties and Material Modeling of Polylactide (PLA) for Medical Applications," Ann. Biomed. Eng., **44**(2), pp. 330–340.

[91] Li, X., Chu, C. L., Liu, L., Liu, X. K., Bai, J., Guo, C., Xue, F., Lin, P. H., and Chu, P. K., 2015, "Biodegradable Poly-Lactic Acid Based-Composite Reinforced Unidirectionally with High-Strength Magnesium Alloy Wires," Biomaterials, **49**, pp. 135–144.

[92] Wittbrodt, B., and Pearce, J. M., 2015, "The Effects of PLA Color on Material Properties of 3-D Printed Components," Addit. Manuf., **8**, pp. 110–116.

[93] Bellini, A., and Guceri, S., 2003, "Mechanical Characterization of Parts Fabricated Using Fused Deposition," Rapid Prototyp. J., **9**(4), pp. 252–264.

[94] Sood, A. K., Ohdar, R. K., and Mahapatra, S. S., 2010, "Parametric Appraisal of Mechanical Property of Fused Deposition Modelling Processed Parts," Mater. Des., **31**(1), pp. 287–295.

[95] ASTM International, 2010, "ASTM D695-10 Standard Test Method for Compressive Properties of Rigid Plastics."

[96] Casavola, C., Cazzato, A., Moramarco, V., and Pappalettere, C., 2016, "Orthotropic Mechanical Properties of Fused Deposition Modelling Parts Described by Classical Laminate Theory," Mater. Des., **90**, pp. 453–458.

[97] ASTM International, 2014, "ASTM D638-14 Standard Test Method for Tensile Properties

of Plastics."

[98] Ferreira, R. T. L., Amatte, I. C., Dutra, T. A., and Bürger, D., 2017, "Experimental Characterization and Micrography of 3D Printed PLA and PLA Reinforced with Short Carbon Fibers," Compos. Part B Eng., **124**, pp. 88–100.

[99] Song, Y., Li, Y., Song, W., Yee, K., Lee, K. Y., and Tagarielli, V. L., 2017, "Measurements of the Mechanical Response of Unidirectional 3D-Printed PLA," Mater. Des., **123**, pp. 154–164.

[100] Daniel, I. M., and Ishai, O., 2006, "Engineering Mechanics of Composite Materials," Mech. Compos. Mater.

[101] Ashby, M. F., 2011, *Materials Selection in Mechanical Design*, Elsevier Ltd.

[102] Ross, R. J., 2010, *Wood Handbook : Wood as an Engineering Material*, Madison.

[103] Lanzafame, R., and Messina, M., 2007, "Fluid Dynamics Wind Turbine Design: Critical Analysis, Optimization and Application of BEM Theory," Renew. Energy, **32**(14), pp. 2291–2305.

[104] Batten, W. M. J., Bahaj, A. S., Molland, A. F., and Chaplin, J. R., 2008, "The Prediction of the Hydrodynamic Performance of Marine Current Turbines," Renew. Energy, **33**(5), pp. 1085–1096.

[105] Lee, J. H., Park, S., Kim, D. H., Rhee, S. H., and Kim, M. C., 2012, "Computational Methods for Performance Analysis of Horizontal Axis Tidal Stream Turbines," Appl. Energy, **98**, pp. 512–523.

[106] Goundar, J. N., and Ahmed, M. R., 2013, "Design of a Horizontal Axis Tidal Current Turbine," Appl. Energy, **111**, pp. 161–174.

[107] Grogan, D. M., Leen, S. B., Kennedy, C. R., and Ó Brádaigh, C. M., 2013, "Design of Composite Tidal Turbine Blades," Renew. Energy, **57**, pp. 151–162.

[108] Masters, I., Chapman, J. C., Willis, M. R., and Orme, J. A. C., 2011, "A Robust Blade Element Momentum Theory Model for Tidal Stream Turbines Including Tip and Hub Loss Corrections," J. Mar. Eng. Technol., **10**(1), pp. 25–35.

[109] Prandtl, L., and Betz, A., 1927, "Vier Abhandlungen Zur Hydrodynamik Und Aerodynamik," III. Int. Methmatker Kongresses zu Heidelb., **3**.

[110] Glauert, H., 1935, "Airplane Propellers," Aerodyn. Theory, **75**, pp. 169–360.

[111] Shen, W. Z., Mikkelsen, R., Sørensen, J. N., and Bak, C., 2005, "Tip Loss Corrections for Wind Turbine Computations," Wind Energy, **8**(4), pp. 457–475.

[112] Moriarty, P. J., and Hansen, a C., 2005, "AeroDyn Theory Manual," Renew. Energy, **15**(January), pp. 500–36313.

[113] Wilson, R. E., and Lissaman, P. B. S., 1974, "Applied Aerodynamics of Wind Power Machines," NASA STI/Recon Tech. Rep. N, **75**, p. 22669.

[114] Glauert, H., 1926, "The Analysis of Experimental Results in the Windmill Brake and Vortex Ring States of an Airscrew," Gt. Britain Aeronaut. Res. Comm., **1026**, p. 8.

[115] Buhl, M. L., and Buhl, M. L., 2005, "A New Empirical Relationship between Thrust Coefficient and Induction Factor for the Turbulent Windmill State A New Empirical Relationship between Thrust Coefficient and Induction Factor for the Turbulent Windmill State," Tech. Rep. NREL/TP-500-36834, (August).

[116] Drela, M., 1989, "XFOIL: An Analysis and Design System for Low Reynolds Number Airfoils," Conf. Low Reynolds Number Airfoil Aerodyn., **Volume 54**, p. pp 1-12.

[117] Marten, D., and Wendler, J., 2013, "QBLADE: An Open Source Tool for Design and Simulation of Horizontal and Vertical Axis Wind Turbines," Int. J. Emerg. Technol. Adv. Eng., **3**(3), pp. 264–269.

[118] Viterna, L. a, and Corrigan, R. D., 1982, "Fixed Pitch Rotor Performance of Large Horizontal Axis Wind Turbines," NASA, Cleveland, Ohio.

[119] Jonkman, J., Butterfield, S., Musial, W., and Scott, G., 2009, "Definition of a 5-MW Reference Wind Turbine for Offshore System Development," (February).

[120] Ning, S. A., 2013, "CCBlade."

[121] Sun, C. T., and Sijian Li, 1988, "Three-Dimensional Effective Elastic Constants for Thick

Laminates," J. Compos. Mater., **22**(7), pp. 629–639.

[122] Poissenot-Arrigoni, B., Scheyer, A., and Anton, S. R., 2017, "Determination of Orthotropic Mechanical Properties of 3D Printed Parts for Structural Health Monitoring," **10168**, p. 101681D.

[123] Kuguel, R., 1961, "A Relation between Theoretical Stress Concentration Factor and Fatigue Notch Factor Deduced from the Concept of Highly Stressed Volume," *Proc. ASTM*, pp. 732–748.